Devendra Singh Bundela

Influence of Digital Elevation Models Derived from Remote Sensing on Spatio-Temporal Modelling of Hydrologic and Erosion Processes

National Soil Resources Institute

PhD Thesis

Cranfield University

National Soil Resources Institute

PhD Thesis

Academic Year 2004-2005

Devendra Singh Bundela

Influence of Digital Elevation Models Derived from Remote Sensing on Spatio-Temporal Modelling of Hydrologic and Erosion Processes

Supervisor: Prof J. C. Taylor

4 November 2004

This thesis is submitted in fulfilment of the requirements for the Degree of Doctor of Philosophy

Influence of Digital Elevation Models Derived from Remote Sensing on Spatio-Temporal Modelling of Hydrologic and Erosion Processes

Abstract

LISEM, a physically-based distributed and dynamic erosion model within the PCRaster GIS, is used to investigate the influence of different spatial representations of input parameters on surface hydrologic and erosion processes at three antecedent soil moisture levels for a 6-hour heavy storm at catchment scale.

Two derived DEMs viz. Cartometric and PulSAR DEMs and three public domain DEMs viz. Landmap, ASTER and SRTM were used in this study. These five DEMs of various original resolutions along with a land use and land cover map and a soil map of the Saltdean catchment were resampled into five spatial representations at 20, 40, 60, 80 and 100 m grid-cell sizes to create input parameters at each resolution. Spaceborne radar interferometry was investigated for generating a suitable DEM for modelling in the context of developing countries having poor availability of quality DEMs. The land use and land cover map was derived from SPOT-1 data and the infiltration parameters were estimated from the 1:250 000 soil map using pedotransfer functions. Crop, soil and soil surface parameters were estimated for possible field conditions in the catchment. Subsequently, twenty-five LISEM databases of 30 input parameters each were created in PCRaster and tested in the model.

The results show that at increasing the grid-cell size of a DEM, the slope gradient flattens and the drainage length shortens. Both of these have competing effects on runoff and sediment flow routing. The catchment area also increases at larger grid-cell sizes and influences these processes, which are then normalised for the comparison of various resolution results.

In the absence of observed runoff and average soil loss data, a relative evaluation across resolutions and DEMs was carried out in the context of developing

countries. The results indicate that the PulSAR and Landmap DEMs have higher variations in runoff and average soil loss than the ASTER DEM, Cartometric DEM, and SRTM DEM at coarser resolutions at all three moisture levels with respect to their result at 20 m. The SRTM DEM has lower variability than other DEMs at finer resolutions. It is demonstrated that resampling a medium resolution SRTM DEM at smaller grid-cell sizes does not improve the prediction of runoff and soil erosion. At 100 m resolution, the runoff is over predicted as compared to an 80 m resolution. Hence, high resolution DEMs should be resampled to 80 m grid-cell size, but the resampling reduces the spatial variability drastically.

The results also indicate that the prediction of runoff is improved for the PulSAR DEM and Landmap DEM, and is slightly improved for the ASTER DEM as compared to the Cartometric DEM, but it is not improved for the SRTM DEM. It is related with their slope gradients.

The results support that the average soil loss is improved for the PulSAR DEM and Landmap DEM and is slightly degraded for the SRTM DEM as compared to the Cartometric DEM. It also suggests that both are suitable for erosion prediction due to higher slope gradient mapped by remote sensing. The ASTER DEM did not produce reliable soil losses at all the moisture levels. Therefore, it should not be used for the prediction of soil erosion.

The results also indicate that small grid-cell size produces detailed soil erosion and deposition outputs, which help in identifying the exact location of sediment source and sink areas necessary for planning the effective conservation strategy in the catchment.

Acknowledgements

I wish to express my sincere gratitude to:

Prof J. C. Taylor, my supervisor for his guidance, and for his review and comments on the thesis for the successful completion of the study,

Dr. G. Thomas, the Chairman of the thesis committee and the former supervisor for keen interest, constant encouragement, guidance and useful suggestions,

Dr. C. S. Sannier, my second supervisor and the member of the thesis committee for his valuable suggestions, discussions and support for radar interferometry on Linux environment and GPS data processing, and

Mr T. Brewer for his support, useful discussions and valuable suggestions on digital photogrammetry.

I wish to acknowledge and appreciate contribution from:

Dr. S. Hobbs, School of Aeronautics, Cranfield Campus, for useful discussions on radar interferometry and sparing SAR SLC data for testing of InSAR processors,

Dr. R. P. C. Morgan for useful suggestions for modelling and providing useful information on the Eastern South Downs study area,

Dr. J. H. Hollis and Dr. S. Hallett for providing pedotransfer functions for the UK soils,

Dr. T. Hess for providing the FEH parameters for the Saltdean catchment,

Dr. P. R. Chitty, University of Sussex, Falmer, Brighton for providing daily and hourly rainfall data,

Mr. R. Burton, National Soil Resource Institute for providing NATMAP soil data of the Eastern South Downs,

My appreciation and thanks are also extended to:

The Commonwealth Award administrator at the Commonwealth Scholarship Commission, London, for providing an excellent support during the study,

The staff of the British Council in Manchester, Cambridge and New Delhi,

The staff of the Department of Agricultural Research and Education (DARE) and Indian Council of Agricultural Research (ICAR), New Delhi, and the Ministry of Human Resources Development, Govt of India, New Delhi for granting the permission for undertaking this study at Silsoe,

The Director, The Head (Division of Agricultural Engineering) and the Staff of ICAR Research Complex for North Eastern Hills Region, Barapani (Umiam) for granting the study leave for my studies at Silsoe,

the colleagues in Engineering Division especially, Dr. A K Mishra, Er. C. S. Sahay, Er. K. N. Agrawal, Er. R. K Singh and others for kind help during the study,

Elizabeth Farmer, Mark Stephens, Simon Pettifer, Dr. Gavin Wood and Sandra Pires for kind help and useful discussions, and

Dharminder Sharma and Grace Lhouvum for useful suggestions.

My appreciation is also extended to:

my wife for her support and encouragement and for bearing my absence while completing this study,

my parents and parents-in law for kind support and for bearing my long absence, and

my two loving children for missing me a lot during my absence.

Table of Contents

List of Tables

Chapter 1

Chapter 2

Chapter 3

Chapter 4

Chapter 5

Chapter 6

List of Figures

Chapter 1

Chapter 2

Chapter 3

Chapter 4

Chapter 5

Chapter 6

List of Appendices

Appendix A

Appendix B

Appendix C

Appendix F

1

Introduction

This chapter introduces approaches to event-based distributed and dynamic erosion modelling within a GIS. It also identifies the role of remote sensing and GIS in the generation of key spatial data and model input parameters and the need to test their sensitivity at different resolutions to model predictive capacity.

1.1 Background of the Study

Soil erosion is one of the major threats to sustainable land management (Lal, 2001). It needs to be modelled spatio-temporally at catchment scale not only to quantify surface runoff and erosion, but also to identify sediment source and sink areas in a catchment. This will enable an effective conservation strategy for a catchment, for an example, by encouraging stakeholders to adopt the best management practices.

Soil erosion models should capture the presence of physical control of topography, vegetation and soils of a catchment on hydrologic and erosion processes within a catchment. Therefore, physically-based models are preferred over empirical and conceptual models due to their wider applicability to multiple situations. Integration of physically-based models into a GIS provides a useful modelling environment for predicting the surface runoff and sediment movement in space and time across a catchment and helps in locating sediment source and sink areas. However, these models require large amounts of spatial data and input parameters, which can be expensive and

time consuming to collect through traditional methods. Therefore, optical and radar remote sensing technology can be exploited as timely and cost effective tools for generating high resolution and quality DEMs (digital elevation models) and land use and land cover maps using radar interferometry and multispectral classification respectively. These spatial data can further be used to derive input parameters with minimal field surveys. In developing countries, requisite quality DEMs required for distributed modelling are rarely available. Therefore, spaceborne radar interferometry is explored for generating the quality DEMs required in this study. At the same time, the usefulness of public domain DEMs also needs to be assessed for distributed modelling.

Spatial variability of catchment characteristics is integrated into a model either by hydrological response unit (HRU) or by grid-cell representation (Engel, 1996). HRU-based polygons use larger computational elements based on hydrologically similar characteristics, which make the identification of source and sink areas in a catchment difficult. Therefore, HRU representation is more applicable to larger catchments and river basins to reduce the requirement of computation resource (Kite and Pietroniro, 1996). Grid-cell representation uses smaller computational elements and is better to locate the sediment source and sink areas in a catchment. Therefore, grid-cell representation can be applied to smaller catchments. Although there has been a huge improvement in computational power and storage, this approach still has a limitation for larger catchments. The spatial variability of input parameters over the grid-cell is assumed to be uniform. The grid-cell size is mainly determined by the inherent spatial variability of catchment characteristics and affects the routing of hydrologic and erosion processes in a distributed manner. Moreover, grid-cell based spatial data can be obtained from remotely sensed data for model parameterisation. The original resolution of spatial data and measurement scale on input parameters influence the model outputs. Therefore, the influence of different resolutions, spatial variability representations and data sources on the performance of a physically-based distributed and dynamic erosion model needs to be investigated for a single event at catchment scale.

1.2 Aim and Objectives

1.2.1 Overall Aim

The overall aim of the study was to investigate the influence of spatial representations of terrain, vegetation and soil on the performance of GIS-based dynamic modelling of surface runoff and erosion processes for a single storm event, at catchment scale in order to identify guidelines for catchment scale modelling.

1.2.2 Objectives

The specific objectives of the study were to:

1) explore the application of radar interferometry for generating quality DEMs for distributed modelling,
2) assess the usefulness of public domain DEMs for distributed modelling,
3) create different spatial representations of input parameters from key spatial data using remote sensing and GIS,
4) generate model outputs for a single storm at three antecedent soil moisture levels using different levels of spatial representations for sensitivity analysis, and
5) identify guidelines for the representation of spatial variability in catchment modelling.

1.3 Approaches to Hydrologic and Erosion Process Modelling

A mathematical erosion model consists of a formulation of physical processes, their spatial and temporal structure, and the scale of application (Figure 1.1). Hydrological and erosion processes can be modelled by an empirically, a conceptually or a physically-based formulation (Singh, 2002; Chow, 1964). Physically-based models use equations of conservation of mass, momentum and energy to model both runoff and sediment production and their routing in a linked manner. They simulate a more realistic approximation of a catchment system. These models can be applied to multiple situations, but they require extensive data collection for the estimation of large numbers of input parameters. Their application was constrained in the past by inadequate availability of input data and powerful computers. Instead empirically based models were used, but their applications were limited to the data range from which they were

originally developed. At the same time, conceptually based models were also applied because they are based on a simplification of the underlying physical processes relying either on water or sediment balance concept or both for model formulation. These models did not require large computation power, but the runoff and sediment production and their routing were not closely linked. Therefore, they produced some realistic and skewed outputs in time. Of late, physically-based models are gaining popularity due to advances in spatial data collection technology and computational power.

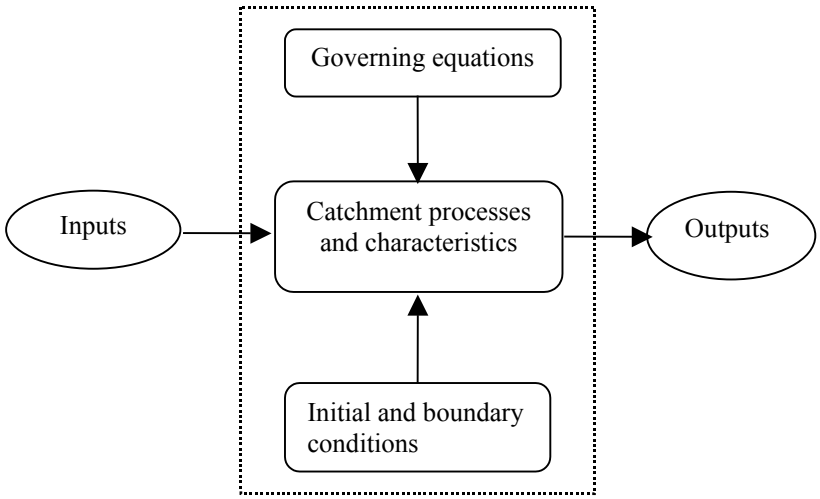

Figure 1.1: Conceptual description of an erosion model (reproduced from Singh, 2002)

Spatial and temporal representations of a process are modelled by discretisation of space and time in order to provide a more realistic approximation across a catchment. Space can be discretised either as a series of contiguous grid-cells or as a series of elements such as hydrological response units (HRUs). Grid-cell based representation allows integration of remotely sensed data through a GIS for model parameterisation. The spatial structure of a model can be determined from Table 1.1. Temporal discretisation can be represented in the models either as a single event or a continuous event. Single event models simulate processes for a single rainstorm event and run over a short period that includes the rainstorm duration and time to drain the runoff from a catchment while continuous models run for longer periods like a crop season, a year or longer (Pullar and Springer, 2000). Single event based models provide a more realistic prediction of processes, but they require precise initial conditions of the processes to be modelled, which require a thorough understanding and knowledge of a physical system.

Continuous models adjust the initial condition of each parameter over time during the simulation. These models can either be static or dynamic on the basis of flow condition. Static models such as WEPP or CREAMS simulate a steady state flow condition while dynamic models simulate more or less a realistic unsteady state flow condition that occurs in a catchment. It can be modelled by assigning a time step as an independent variable in a model. According to the nature of outputs, these models can further be classified as deterministic, stochastic or mixed. The scale of application of a model often determines important physical processes to be included and formulated for a catchment as the dominance of hydrologic and erosion processes varies with scales. For this modelling study, a physically-based deterministic, dynamic and distributed model was to be selected.

Table 1.1: Definition of a model type on the basis of spatial structure (reproduced from Singh, 2002)

Input	Catchment characteristics	Component process	Governing equations	Output	Model type
Lumped	Lumped	Lumped	Ordinary differential	Lumped	Lumped
Lumped	Lumped	Distributed	Partial differential	Distributed	Distributed
Distributed	Lumped	Distributed	Partial differential	Distributed	Distributed
Distributed	Distributed	Distributed	Partial differential	Distributed	Distributed

1.4 Role of Remote Sensing and GIS in Distributed Modelling

With the advent of powerful desktop computers, more physically-based distributed erosion models have been applied for a realistic simulation of catchment processes. This has led to an increased demand for spatial data to derive input parameters at catchment scale. However, collection of large amounts of spatial data through traditional methods is expensive and time consuming and has been a deterrent in the application of these models. Remote sensing technologies can be exploited as cost effective and timely spatial data collection tools to improve the availability of spatial information on physiographic characteristics of a catchment, which can further be used for the model parameterisation. Land use and land cover and topography, and

biophysical parameters have successfully been derived at catchment scale from remotely sensed data (Müschen et al, 1999; Olivieri et al, 1995; Schultz, 1988).

The role of a GIS in modelling is to provide an environment for integration of spatial data at multi scale collected from multi sources such as ground, air and space borne sensors to create key spatial data of catchment characteristics. These data are further used to derive spatial input parameters for distributed and dynamic modelling. A GIS with spatial data management and analysis tools in addition to other standard functionality provides an excellent environment to create the database of input parameters at a particular scale or resolution. A GIS can be used for data creation and management, visualisation, querying and analysing spatially referenced objects and their non spatial attributes (Burrough and McDonnell, 1998). A GIS can also be integrated with catchment scale distributed models or vice versa to simplify the process of data exchange between a GIS and models.

1.5 Dynamic Erosion Modelling within a GIS

Hydrologic and erosion processes are spatially varied and dynamic in nature. Erosion models have been integrated into a GIS to provide a powerful environment for modelling these processes in a realistic spatio-temporal manner at catchment scale (Pullar and Springer, 2000). Integration between models and a GIS can be achieved in three ways: loose coupling, tight coupling and embedded coupling (Wesseling et al, 1996; De Roo, 1998) (Figure 1.2). In loose coupling (Figure 1.2a), a data conversion program is involved to convert data between a model and a GIS for manipulation and display of model inputs and outputs (De Roo et al, 1996; De Roo, 1998). Loose coupling has few disadvantages such as time consuming data conversion and difficulty in tracing errors in input parameter files. Development in GIS-based modelling languages permits a move towards a tighter coupling (Figure 1.2b) where an interface program written in a GIS macro language has been used to input data from a GIS to a model and to display the model outputs (Brooks and MacDonald, 1999; De Roo, 1998).

Further development in tighter integration has resulted in a form of embedded coupling either by adding simple GIS functionality to a model to provide an interactive control to extract parameters and to display results (Figure 1.2c), for example,

EROSION-3D (Schmidt, 2000; Werner, 2002) or by building up a model within a GIS-based programming language (Wesseling et al, 1996) (Figure 1.2d), for example, PCRaster. GIS-based models have advantages that models can be improved as and when required and avoid the database programming. Dynamic modelling languages have been introduced and incorporated into three GIS packages namely; PCRaster (Wesseling et al, 1996), GRASS (Geographic resources analysis support system) (GRASS, 2002) and IDRISI (Clark Lab, 2004). PCRaster and GRASS are gaining popularity because of their capabilities for dynamic modelling. Functionality in IDRISI is still limited. However, most commercial GIS packages provide the catchment analysis tools for delineation of catchments and definition of drainage networks. A few GIS packages have some more modelling capabilities, such as the grid-cell based AML modelling language in ArcInfo. These are not sufficient for dynamic modelling. However, the commercial GIS packages still lack dynamic functionality such as flow routing required for spatio-temporal modelling (Wesseling et al, 1996).

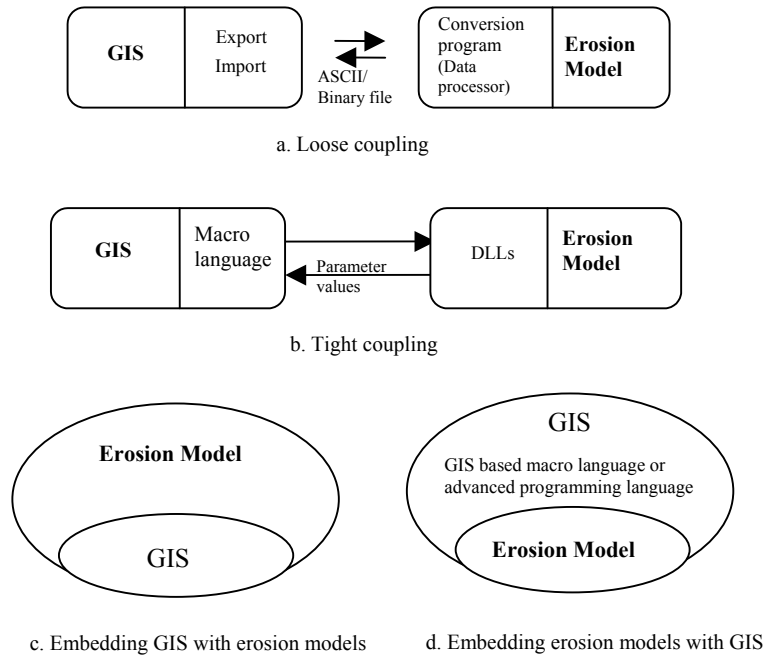

Figure 1.2: Approaches of integrating erosion models with a GIS (adapted from Sui and Maggio, 1999)

1.6 Layout of the Thesis

Chapter 1 introduced the approaches to event-based distributed and dynamic erosion modelling within a GIS environment, role of remote sensing and GIS in generation of digital elevation models, land use and land cover maps, and model input parameters, and the need to test their sensitivity at different resolutions to model predictive capacity. It included the background of the study with problem identification, overall aim and objectives. It presents layout of the thesis, description of the study area with present and future problems, identification and description of the Saltdean catchment. The selection of a suitable erosion model within a GIS environment is described in next Chapter.

Chapter 2 presents the selection of an event based distributed and dynamic model, description and theory of the LISEM model, input parameter requirement and model outputs. It also includes the PCRaster capabilities for dynamic modelling with a description of its functionality and limitations, and generic structure of its dynamic database. Non-remotely sensed data such as rainfall and soil data for estimation of a few model parameters are described in next Chapter.

Chapter 3 deals with non-remotely sensed data such as rainfall and soil data for estimation of model input parameters. It firstly reports a procedure proposed for identification of heavy rainstorms from daily and hourly rainfall, and secondly, describes a methodology for extraction of infiltration parameters for a single layer Green and Ampt model from the 1:250 000 scale National Soil Data using pedotransfer functions. It also includes characteristics and analysis of October 2000 storms, and description of soil and geology of the Eastern South Downs. The landuse and land cover mapping is described in next Chapter.

Chapter 4 deals with remotely sensed data for landuse and land cover mapping. It treats hybrid classification methodology of SPOT-1 multispectral data for mapping of land use and land cover for a historical event. Generation of suitable interferometric synthetic aperture radar (InSAR) DEMs for modelling is described in next chapter.

Chapter 5 reviews elevation mapping technologies in terms of their capabilities and limitations and identifies spaceborne radar interferometry for generation of high resolution and quality DEMs from an ERS-1 and ERS-2 tandem data pair, equally

suitable for developing countries. It also includes generation of DEM validation data using digital aerial photogrammetry and quality assessment of InSAR DEMs against reference data. The model sensitivity analysis for different resolutions and DEMs is described in next Chapter.

Chapter 6 deals with the creation of LISEM databases of input parameters at different resolutions and DEMs obtained from various sources. It evaluates the model sensitivity to different spatial representations of each DEM at three antecedent moisture conditions. A general discussion and conclusions are described in next Chapter.

Chapter 7 summarises a general discussion and conclusions on model performance on surface runoff and soil erosion at different resolutions of each DEM, and identifies the guidelines for spatial variability for catchment modelling. It also includes the recommendations for future work.

In addition to seven chapters, the thesis includes a comprehensive list of references and appendices for supporting the study.

At the end of the thesis, an optical disk is attached, which contains the key spatial data, 25 LISEM databases, a PCRaster script file, two batch files, a rainfall intensity file, spatio-temporal output files, AVI video files, a LISEM model and a PCRaster GIS. The description of the optical disk is given in Appendix F.

1.7 Study Area

1.7.1 The Eastern South Downs

The Eastern South Downs were chosen as the study area for generating the InSAR DEM, and land use and land cover map from remotely sensed data (Figure 1.3). They are located between 520 000 to 542 000 m easting and 101 000 to 114 000 m northing in the south east of England and encompass an area of 228.22 sq km. These are a range of east-west, low lying, rolling chalk hills, composed of a soft cretaceous limestone, draining towards the north and the south. These hills are bounded on northern side by steep slopes with characteristics of rolling chalk downland and dry valleys. The range of low rolling chalk hills is breached on the east by the river Ouse

and on the west by the river Adur. Most of the south-facing slope is cultivated for arable crops on slopes varying up to 50 per cent (Boardman, 2003). They rise up to 248 m above the mean sea level. Mean annual rainfall varies from 750 to 1000 mm with peak in autumn. The principal soils are thin, dark coloured and stony containing 60-80 per cent of silt. The stones in soils are either chalk or flint (Jarvis et al, 1984). In valley bottoms, superficial deposits of greater than 1 m depth can be found.

Rainfall is progressively less from west to east and from south to north because the predominant south westerly winds bring weather fronts from the Atlantic. The climate is favourable for a wide range of cropping, with a relatively long growing season. The Eastern South Downs remain frost free in most of winter and experience a few days of snowfalls in a normal year. January is usually the coldest month of year while July is normally the warmest month. The mean annual temperature is 9.8^0 C with a January mean of 3.9^0 C and a July mean of 16.3^0 C (Potts and Brownne, 1983).

1.7.2 Present and Future Problems

Before the Second World War, the Eastern South Downs were mainly grazed by sheep and cattle. Later on, agricultural mechanisation and guaranteed price policy to cereal growers brought more and more areas on steeper slopes under cereal cultivation. In late 1970s, the higher yielding winter cereals replaced spring cereals and the first serious flood occurred in winter 1976. In the 1980s, winter cereals were continued and grown in about 55 per cent of cultivated area in the Eastern South Downs (Boardman, 1990) and two major floods occurred in 1982 and 1987. In the 1990s, two more floods in 1991 and 1993 were experienced again even though cereals were on decline and more oilseeds and set-aside was introduced. Cropland and winter cereals have been in further decline in the Eastern South Downs due to implementation of set-aside and the environmentally sensitive area (ESA) schemes, which encouraged a return to grassland. A major autumn flood occurred in 2000 which caused serious damage to proximal properties. Increased flooding could also be a result of climate change in which more intense rainfalls are shifting towards autumn and early winter (Favis-Mortlock and Boardman, 1995)

Erosion causes depletion of soil on the site and flooding damage to proximal properties in autumn and early winter. The local flooding problem still persists although winter crop area has declined considerably. There is a need to understand the catchment hydrology and erosion dynamics in order to assess soil erosion and local flooding in future. This will help in mitigating local flooding problem through implementation of an effective conservation strategy. Therefore, a physically-based dynamic erosion model within a raster GIS is used for evaluating the effect of different spatial representations of input parameters derived from key spatial data on simulation of erosion and runoff for an extreme rainfall event.

1.7.3 Identification of a Catchment

For the purpose of this modelling study, an agricultural catchment of 10-50 sq km was required to utilise remotely sensed derived key spatial data effectively. The Eastern South Downs are composed of many small catchments less than 5 sq km. Moreover, it was difficult to locate a catchment of required size. The Woodingdean catchment was too small (approximately 1 sq km) to be used for the modelling purpose (Favis-mortlock and Boardman, 1997; Boardman, 2000). However, there was another catchment, which drains towards Brighton having a large area (more than 25 sq km) with the majority of the land under urban land use but, its drainage was also modified due to development of road and rail networks. Thus, this catchment too, was not suitable as per the requirement of the model. After a thorough survey, a small catchment of approximately 8 sq km area, located near Saltdean, was identified for this study. For the purpose of this study, it is referred to as the 'Saltdean catchment'. This catchment experienced a number of floods in the past with the most recent one in October 2000. It has drawn considerable attention from insurance companies and the local council from a flood modelling point of view. Thus, it was chosen as the study catchment for the modelling purpose. The drawback of this selection was that no previous study had been carried out on this catchment. Therefore, no catchment characteristics and validation dataset were available. The catchment characteristics were, therefore, derived from a synergistic use of remote sensing and GIS with a minimal field survey.

1.7.4 The Saltdean Catchment

The catchment is predominantly used for arable and grassland. It is located in the north of Saltdean village and lies between 536 000 to 540 000 m easting and 102 000 to 108 000 m northing (Figure 1.3). This catchment is of low rolling chalk hills with elevations ranging from 30 to 200 m above the mean sea level. The land uses of the catchment consist of 35 per cent arable, 59 per cent grassland, 5 per cent woodland and less than one percent built-up land. It has an average slope of 17 per cent. Mean annual rainfall is similar to that of the Eastern South Downs, ranging from 750 to 1000 mm with peak in autumn. It contains two major soil associations namely, Andover and Marlow. The Andover series soil has a single horizon layer with a depth of rarely more than 250 mm thick in the catchment.

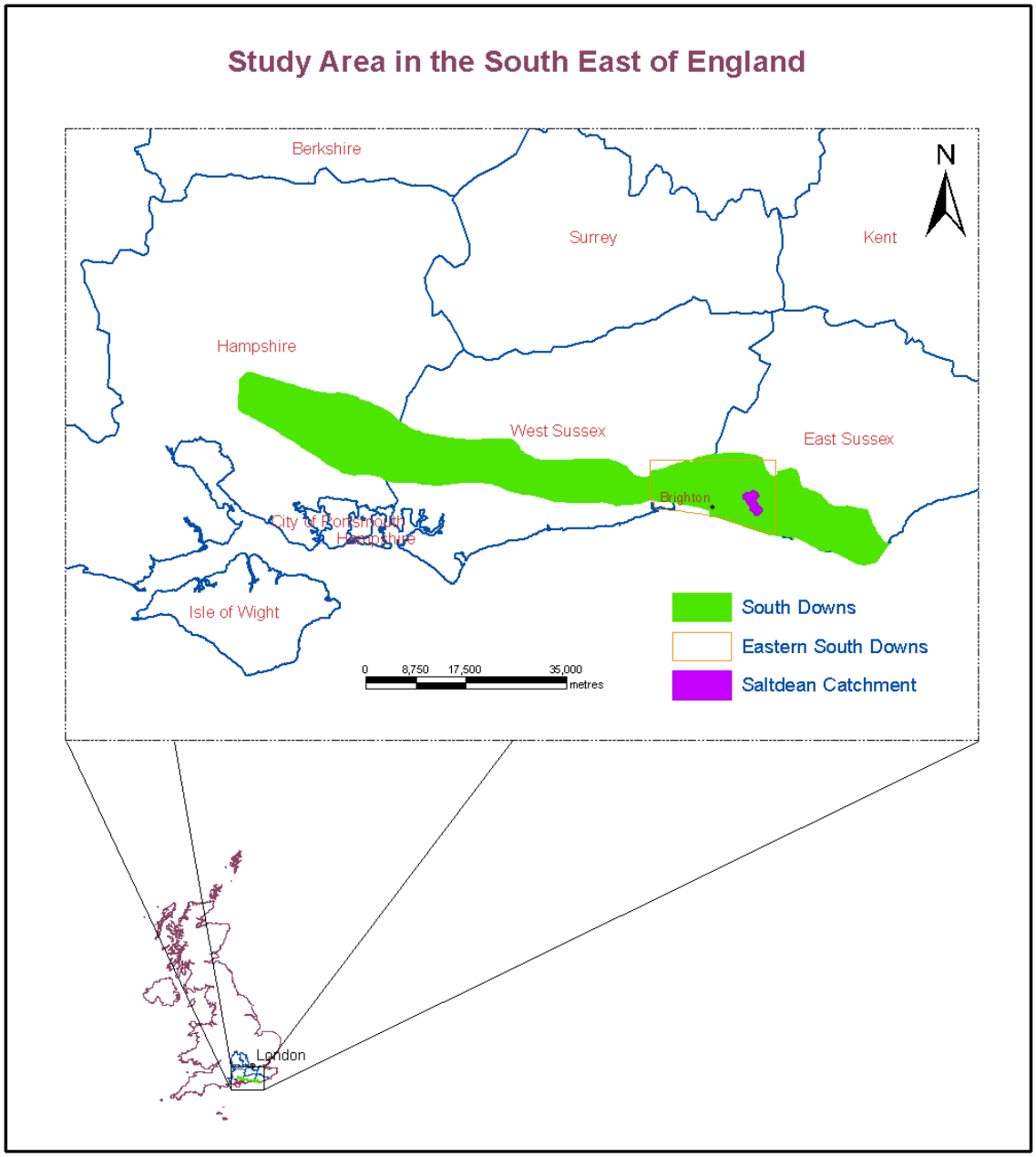

Figure 1.3: Map of the Eastern South Downs and the Saltdean catchment

2

Selection of a Dynamic Erosion Model within a GIS

The chapter presents criteria for the selection of an event-based erosion model within a GIS for distributed and dynamic modelling, a description of model theory, input parameter requirement and model outputs. The dynamic modelling capabilities of a GIS and a description of dynamic database structure are also included. After a review of models, LISEM in the PCRaster GIS was identified to be suitable for modelling within storm hydrology and erosion dynamics at catchment scale at a resolution. It integrates remotely sensed derived data for model parameterisation.

2.1 Introduction

Single event-based erosion models range from an empirically-based lumped to a physically-based distributed and dynamic one for the simulation of runoff and sediment dynamics at catchment scale. Application of physically-based distributed and dynamic models was constrained in the past by the requirement of a large number of spatial input parameters and variables, and huge computational resources. In the recent past, there has been an enormous increase in computational resources and availability of remote sensed data that facilitate to create a database of spatial input parameters and variables in a raster GIS environment for modelling (Müschen et al, 1999; Schultz, 1988). A GIS with a dynamic modelling language provides an ideal modelling environment for constructing dynamic models at catchment scale.

After a review of models and their embedding into a GIS environment, the LISEM model (Limburg Soil Erosion Model) (De Roo et al, 1996a & b) in PCRaster (a PC-based raster GIS) (Wesseling et al, 1996) was selected for the study because of its capability of integrating remotely sensed derived key spatial data for model parameterisation. Therefore, this model was to be used in the UK for evaluating effects of different spatial representations of a DEM and land use and land cover scenarios on runoff and erosion dynamics for an extreme rainfall event. This chapter deals with a review of hydrologic and erosion models, selection of a suitable model embedded into a GIS environment with its advantages and disadvantages as compared to other models, the theory of the LISEM Model, input parameter requirement and model outputs. It also looks at the functionality, capabilities and limitations of the PCRaster GIS with its dynamic database structure and integration approaches to models for dynamic and distributed modelling.

2.2 Review of Hydrologic and Erosion Models

Soil erosion by water in Britain and Europe occurs with a few heavy rainstorms in a year (Morgan et al, 1998), so an event-based model will be an appropriate for the simulation of runoff and erosion at catchment scale. Single event-based erosion models integrated into a GIS (Table 2.1 and Table 2.2) are grouped under two categories for the review:

- Grid-cell based models such as LISEM, EROSION-3D (Schmidt, 2000; Schmidt et al, 1999), EUROSEM in PCRaster (Van Dijck and Karssenberg, 2000), ANSWERS (Beasley & Huggins, 1981; Beasley et al, 1980), AGNPS (Young et al, 1989); and

- Elements or hydrologic response units (HRU)-based models such as EUROSEM (Morgan et al, 1998), KINEROS2 (Smith et al, 1995), WEPP (Flaganan and Nearing, 1995), GeoWEPP (Renschler, 2003)

The comparison of these models on the basis of formulation, spatial and temporal structure, scale of application, advantages and limitations are presented in Table 2.3.

Table 2.1: A list of hydrologic and erosion models

Model	Expanded form	References
LISEM	Limburg soil erosion model	De Roo et al, 1996a & b
EROSION-3D	Erosion from small catchment/ hill profile	Schmidt, 2000
EUROSEM	European soil erosion model	Morgan et al, 1998
ANSWERS	Areal nonpoint source watershed environment response simulation	Beasley et al, 1981 & 1980
AGNPS	Agricultural non point source	Young et al, 1989
KINEROS 2	Kinematic runoff and erosion simulation	Smith et al, 1999 & 1995
AVSWAT	ArcView based soil and water assessment tool	Di Luzio et al, 2004
CREAMS	Chemical, runoff and erosion from agricultural managed systems	Knisel, 1982
WEPP	Water erosion prediction program	Flaganan & Nearing, 1995
GEOWEPP	GIS interface of water erosion prediction program	Renschler, 2003

2.3 Selection of a Model

A single event-based erosion model needs to be selected on the basis of the following criteria such as process component, process formulation, spatial and temporal discretisation of a process, GIS integration and technical support. Every model contains a mixture of these criteria:

- ANSWERS, AGNPS, and CREAMS are the USLE-based empirical models while LISEM, EROSION-3D, EUROSEM, KINEROS2 and GEOWEPP are more physically-based models.
- LISEM, EROSION-3D, WEPP grid version, AGNPS and ANSWERS are based on grid-cell representation while GEOWEPP, KINEROS2, and EUROSEM are based on series of element representation.
- GeoWEPP and AVSWAT are static simulation models while LISEM, EUROSEM, AGNPS, and ANSWERS are dynamic models.

A grid-cell based model exploits remotely sensed derived spatial data whereas a dynamic model simulates runoff and erosion precisely from a storm event. LISEM is quite similar in the process description to EUROSEM, developed at Cranfield University at Silsoe, and KINEROS2 (Morgan et al, 1998), but it is written in the PCRaster GIS-based dynamic modelling language, which allows a greater flexibility for model process improvement at user end.

Table 2.2: Comparison of hydrologic and erosion models

Name	Formulation	Structure	Temporal	Scale	Application	Advantage/limitation
Grid-based						
LISEM	Physically-based	Distributed & dynamic	Single event	Small catchment (< 100 sq. km)	▪ To predict runoff, erosion and deposition for single event.	▪ The model has not been widely tested for forested and rural catchments
EROSION-3D	Physically-based	Distributed & dynamic	Single event	Small catchment (< 30 sq km)	▪ To calculate rainfall induced soil erosion and deposition.	▪ Channel processes are not well represented. ▪ It uses a time step of 1-15 min.
EUROSEM in PCRaster	Physically - based	Distributed & dynamic	Single event	Field/small catchment	▪ To predict erosion, deposition, and sediment transport and yield ▪ Applicable for agricultural and non-agricultural areas	▪ Outputs are over predicted ▪ Hydrology component is implemented only
ANSWERS	Empirically-based	Distributed & dynamic	Single event	Agricultural catchment	▪ To predict soil erosion and deposition for single event	▪ Applicable for agricultural catchment
AGNPS	Empirically-based	Distributed & dynamic	Single event	Watershed (up to 200 sq km)	▪ To simulate surface runoff, sediment and agricultural pollutants	▪ Total grid cells can be handled up to 1900 in the model.
Elements-based						
EUROSEM	Physically-based	Distributed & dynamic	Single event	Field/small catchment	▪ To predict erosion, deposition, and sediment transport and yield ▪ Applicable for agricultural and non-agricultural areas.	▪ Outputs are over predicted ▪ Landscape consists of a series of interlinked elements.
WEPP/ GeoWEPP	Physically-based	Distributed	Single event/ Continuous	Hill profile/ small watershed	▪ Can be applied for a range of land uses.	▪ Model can be applied to small catchment up to 2.5 sq. km.

Table 2.3: Criteria for the selection of an event-based erosion model

Major process	LISEM	EROSION-3D	ANSWERS	AGNPS	CREAMS	EUROSEM (PCRaster)	KINEROS2	GeoWEPP (event)
Infiltration	Holtan, Green & Ampt, SWATRE	Green & Ampt	Holtan	Holtan	Empirical equation	Smith & Parlange	Smith & Parlange	Green & Ampt
Hydrology	Hortonian/saturation excess	Hortonian flow	Hortonian	Hortonian	Hortonian	Hortonian	Hortonian	Hortonian
Detachment	Erosion-deposition theory	General theory	USLE	USLE	USLE	Erosion-deposition theory	Erosion-deposition theory	General theory
Transport	,,	,,	USLE	USLE	USLE	,,	,,	,,
Deposition	,,	,,	USLE	USLE	USLE	,,	,,	,,
Routing procedure	Kinematic with Manning's eq.	Lowest Neighbour	Manning's with stage-discharge	Kinematic wave eq.	Lumped routing	Kinematic wave eq.	Kinematic wave eq.	Kinematic wave eq.
Spatial structure	Grid-based	Grid-based	Grid-based	Grid-based	Lumped	Grid-based	Element-based	Element-based
GIS coupling	Within a GIS	Within a model	Loose to tight	Loose to tight	Loose to tight	Within a GIS	No	Tight
GIS package	PCRaster	ArcView	--	--	--	PCRaster	---	--
Input data	Many (24)	Moderate	Moderate	Moderate	Moderate	Many	Many	Many

The technical support is available for the LISEM model refinement and application. Therefore, LISEM model met the above stated requirements and was selected for the study (Table 2.3). Another advantage of the LISEM model is that it is developed for a European environment with a similar climate and site characteristics with respect to the South Downs (Boardman et al, 1996).

2.4 Limburg Soil Erosion Model (LISEM)

The LISEM model (LISEM, 2004; De Roo et al, 1996a & b) is suitable for catchments up to 100 sq. km. It is fully integrated to PCRaster, a PC-based raster GIS, and is written with the PCRaster dynamic modelling language with a current implementation of less than 200 lines of source code (De Roo et al, 1994). The model simulates rainfall, interception, surface storage in micro depressions, infiltration, vertical movement of water in the soil, overland flow, channel flow, detachment by rainfall, throughfall and leaf drainage, detachment by overland flow, transport capacity of the flow and deposition of soil particles within and from a catchment. It also models different types of surfaces such as crusted, compacted due to tractor tramline, small paved roads and grass strips within a grid cell.

LISEM is a powerful erosion model with a modular structure and consists of five modules:

(1) LISEM Basic, for simulating runoff and erosion for different type of soil surface inside a grid-cell,
(2) LISEM Wheeltracks, for simulating semi-permanent wheeltracks as a network of channels,
(3) LISEM Multiclass, for simulating erosion and deposition in six texture classes,
(4) LISEM Nutrients, for simulating nutrient losses (N and P) in solution and in suspension and,
(5) LISEM Gullies (EUROWISE), for simulating gully incision and formation.

Its current version is 2.158 build 19 September 2003 (LISEM, 2004). It requires a large number of spatial input parameters depending on the options chosen (Table 2.4). Twenty four spatial input parameters are essentially required to run a basic simulation.

Although it is a physically-based model, it still contains a few empirical equations, for an example, the transport capacity equation. It was originally developed for small agricultural catchments and it can be applied with care to small rural catchments containing built up and forest land cover. It can no longer be applied to medium and large catchments as catchment processes change with scale. A large amount of parameter requirement has limited its application in data poor catchments.

Table 2.4: List of input parameters required for a simulation with different options

S. No.	Categories	No of parameters required
1.	Catchment	5
2.	Landuse and vegetation	5
3.	Soil Surface	5
4.	Erosion related	4
5.	Green & Ampt - 1 layer	5
	Minimum:	24
6.	Channel	6
	Infiltration options:	
7.	Green and Ampt- 2 layers	5 (additional)
8.	Holtan empirical model	7
9.	SWATRE (Richard's equation)	A large number

2.5 Hydrologic and Erosion Process Modelling

The theory of the LISEM model is described in the literature by LISEM (2004), Jetten (2002), De Roo et al (1996 a & b), Morgan et al (1998a) and Smith et al (1995). The complete model theory is covered in various articles, manuals and books. An attempt was made to compile the complete theory from various sources in order to gain deeper understanding and knowledge behind each and every process. As there was no calibration dataset available for the study area, so it further helps to understand how a grid-cell size of input parameters influences model outputs, which is the main theme of this study.

The model simulates a number of surface hydrologic and erosion processes important for a single storm event (Table 2.5). A conceptual diagram of process descriptions and their interaction, and the parameter requirements of the LISEM model are presented in Figure 2.1. A process modelled by a variety of approaches and relevant

approaches is discussed in this Section with respect to the process description in the model. This model belongs to the EUROSEM-KINEROS model family because many processes in these models are common.

Table 2.5: Process description in the LISEM model

Process	Process modelling	Major parameters
Hydrological processes		
Rainfall	Single or multi raingauge time series data	Intensity-time pairs
Interception	Aston (1979)	Cover, LAI
Surface storage	Kamphorst et al (2000), Onstad (1984)	RR, Slope
Evapotranspiration	Not included	
Infiltration	Richards, one or two layer Green-Ampt and Holtan models	K-θ-h
Runoff	Hortonian & saturation excess overland flows	LDD, n, slope
Overland flow routing	Kinematic wave with Manning's equation	LDD, n, slope
Interflow	Not included	
Ground water flow	Not modelled	
Erosion processes		
Splash detachment by rainfall	Generalised erosion-deposition theory	Aggregate stability
Flow detachment	Generalised erosion-deposition theory	Soil cohesion
Transport capacity	Govers (1992 and 1990)	D50
Deposition	Govers (1992 and 1990)	Tc
Channel detachment and transport	Govers (1992 and 1990)	Channel cohesion

Dynamic and distributed erosion modelling is fundamentally based on numerical solutions of dynamic water and sediment mass balance equations over the surface of the catchment and over the time of the runoff. The dynamic water volume balance equation is expressed as:

$$\frac{\partial Q}{\partial x} + \frac{\partial A}{\partial t} = q \qquad \ldots \qquad \text{Eq. 2.1}$$

The sediment discharge used in the mass balance equation is defined as a product of the rate of runoff and sediment concentration in the flow at a given point in a given time. The dynamic sediment mass balance equation is expressed as:

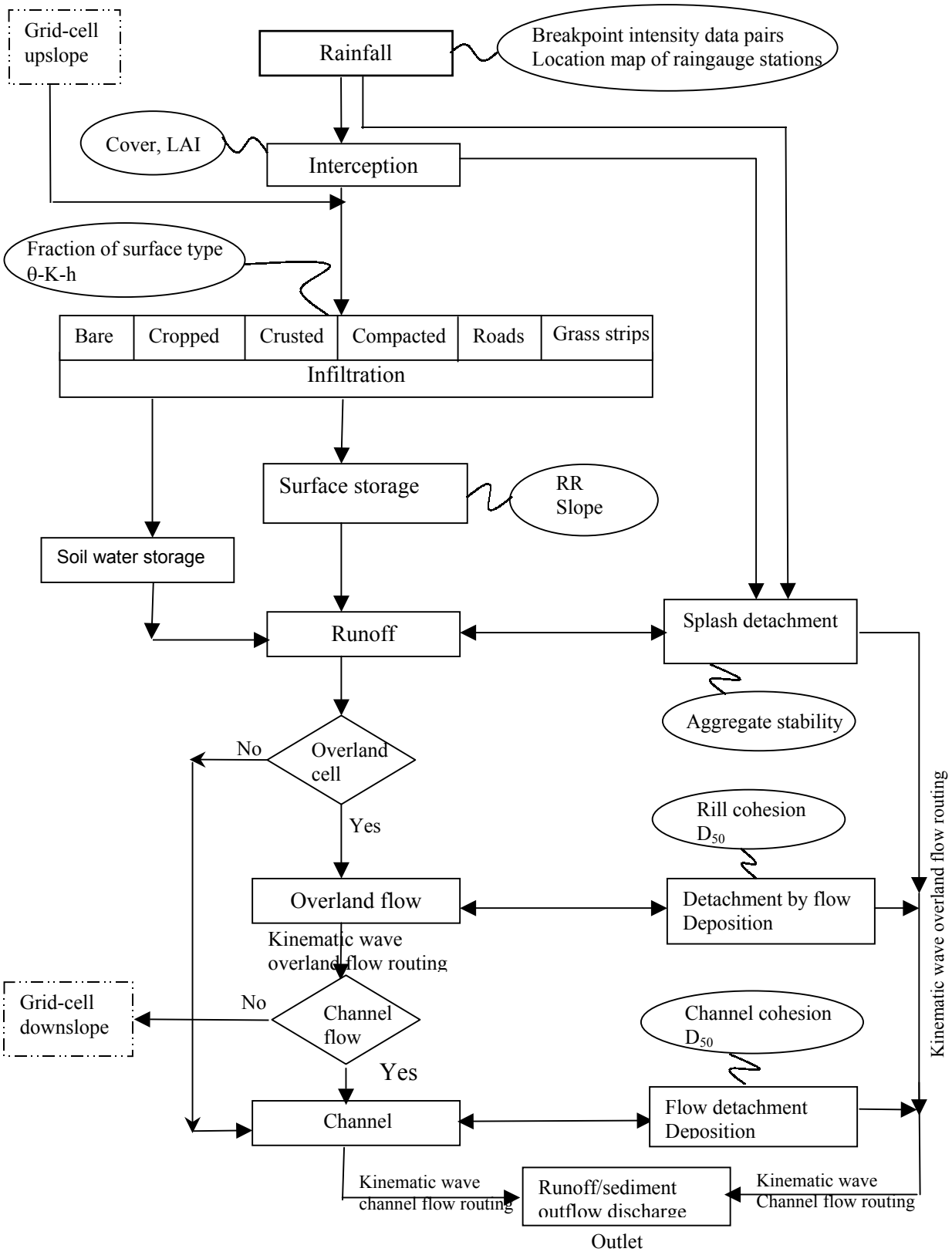

Figure 2.1: Conceptual diagram of the LISEM processes (adapted from De Roo et al, 1996a)

$$\frac{\partial(QC)}{\partial x} + \frac{\partial(AC)}{\partial t} = e(x,t) + q_s(x,t) \quad \ldots \quad \text{Eq. 2.2}$$

where Q(x, t) is the discharge ($m^3\ s^{-1}$), A(x, t) is the cross sectional area of flow (m^2), q is the infiltration surplus ($m^3\ s^{-1}m^{-1}$), C is the sediment concentration ($m^3\ m^{-3}$), e is the erosion or deposition rate per unit length of flow ($m^3\ s^{-1}m^{-1}$), q_s is the sediment inflow ($m^3\ s^{-1}m^{-1}$), dx is the horizontal cell size (m) and dt is the time step (s). The term, q in Equation 2.1 is a balance between rainfall rate minus interception and infiltration rate while the term, e in Equation 2.2 is a balance between erosion and deposition and is composed of two independent erosion processes: splash erosion by rain and net erosion by flow. For an overland flow, q_s is zero while for a channel flow, q_s is the lateral inflow of the sediment from the base of adjacent hillsides.

2.5.1 Rainfall

The spatial and temporal variability of a rainstorm is modelled in different ways in different models. In LISEM, the spatial distribution of a storm in a catchment can be derived from breakpoint rainfall intensity time series data from multiple raingauge stations using the Thiessen polygons or geomorphological analysis. The temporal distribution of a storm is determined from the recording interval of a raingauge. The model generates spatial distribution map of rainfall intensity for every time step from rainfall intensity time series file during the simulation of a storm and drives the processes and their interactions in the model. For the Saltdean catchment, uniform rainfall intensity over the catchment was assumed due to availability of rainfall data from a single raingauge station.

2.5.2 Interception

Interception is a fraction of rainfall retained by the canopy and later evaporated back to the atmosphere or absorbed within it. Crop and vegetation cover is the most important factor for interception modelling. A few approaches to model the interception loss have been developed. In the past, it was ignored in most of the erosion models such as CREAMS. In later approaches, it was considered as a minimum depth of rainfall required to fill interception store before rain is allowed to pass from the vegetation canopy to the ground in the model such as KINEROS. In the current approach, a more

dynamic modelling is adopted in which the rainfall is allowed to pass from the canopy to the ground at the same time as the interception store is being filled. This means that some transfer of water from the canopy will take place right from the start of the storm. This approach was adopted by Merriam (1973) and is used in the EUROSEM model. The depth of the interception store for a time step is modelled as a function of the cumulative rainfall from the start of a storm using an exponential relationship (Merriam, 1973).

In LISEM, a dynamic storage model is used to simulate the interception by crops and vegetation in terms of cumulative interception during a storm event expressed by an equation (Aston, 1979), which is a modified form of the Merriam's equation (Merriam, 1960):

$$S = c_p * S_{max}\left(1 - e^{-k\frac{P_{cum}}{S_{max}}}\right) \quad \ldots \quad \text{Eq. 2.3}$$

where S is the cumulative interception (mm), P_{cum} is the cumulative rainfall (mm), k is the correction factor for crop and vegetation density which is equal to 0.046*LAI, LAI is the leaf area index for crops and vegetation, Cp is the fraction of vegetation cover, and S_{max} is the canopy storage capacity (mm) estimated from the LAI (Von Hoyningen-Huene, 1981) as:

$$S_{max} = 0.935 + 0.498*LAI - 0.00575*LAI^2 \quad \ldots \quad \text{Eq. 2.4}$$

2.5.3 Infiltration and Soil Water Transport in Soils

Infiltration and vertical transport of water in soils can be modelled on the basis of an empirically, a semi-empirically, or a physically-based approach. In LISEM, two physically-based models, SWATRE (Belmans et al, 1983) and the Green and Ampt (Li et al, 1976) for one or two layers; and a semi empirically-based Holton model (Beasley and Hoggins, 1981; Holtan, 1961) are incorporated. The SWATRE model, a finite difference solution of the Richard's equation, simulates both infiltration excess and saturation excess overland flows for crusted, compacted and grass strip surfaces. Hence, a priori knowledge of runoff production mechanism in a catchment is not needed. Both

types of runoff production mechanisms can occur simultaneously in different areas of a catchment. The theory of the SWATRE model is given in the literature (Belsman et al, 1983; Jetten, 2002). An infiltration excess flow occurs in arable and grassland-based land uses while a saturation excess flow occurs in naturally vegetated and wild life recreation areas. SWATRE is a very data intensive model and can be used for a maximum of 20 soil horizons. It is applied when detailed soil properties data of a catchment are available.

The Green and Ampt model (Li et al, 1976) for one or two layers is a simpler approach to approximate the infiltration in homogeneous soils and simulates the Hortonian overland flow for crusted, compacted and grass strip surfaces. Its applicability is limited by the basic assumptions that the soil is homogeneous with depth; the saturation behind the front is uniform; the infiltration wetting front is perfectly sharp and the same everywhere in the horizons. When these assumptions are no longer valid, the Green and Ampt model should not be applied. The theory of the Green and Ampt model is described in the literature by Chow et al (1988). The Green and Ampt equations for the cumulative infiltration and infiltration rate for a single layer soil are expressed as:

$$F(t) - h\Delta\theta \ln\left(1 + \frac{F(t)}{h\Delta\theta}\right) = Kt \qquad \ldots \quad \text{Eq. 2.5}$$

$$f(t) = K\left(\frac{h\Delta\theta}{F(t)} + 1\right) \qquad \ldots \quad \text{Eq. 2.6}$$

Equation 2.5 can be solved for F (t) by either the method of successive substitution or Newton's iteration method for each time step. The value of F (t) is substituted in Equation 2.6 to obtain the infiltration rate. When the wetting front is in upper layer, a single layer Green and Ampt equations are used even for two layer soils.

When the wetting front enters the second layer, the two layer equations are applicable:

$$L2\frac{\Delta\theta_2}{K_2} + \frac{1}{K_1 K_2}\left[\Delta\theta_2 H_1 K_2 - \Delta\theta_2 K_1 (h_2 + H_1)\right] \ln\left[1 + \frac{L_2}{h_2 + H_1}\right] = t \qquad \ldots \quad \text{Eq. 2.7}$$

$$F = H_1\Delta\theta_1 + L_2\Delta\theta_2 \qquad \ldots \quad \text{Eq. 2.8}$$

$$f = \frac{K_1 K_2}{H_1 K_2 + L_2 K_1}(h_2 + H_1 + L_2) \quad \ldots \quad \text{Eq. 2.9}$$

where K_1, h_1, $\Delta\theta_1$ are the hydraulic conductivity, wetting front suction head and soil moisture storage capacity for the first layer, H_1 is the thickness of the upper layer. K_2, h_2, $\Delta\theta_2$ are the hydraulic conductivity, wetting front suction head and soil moisture storage capacity for lower layer, H_2 is the thickness of the upper layer and L2 is the distance of water front into the lower layer.

Equation 2.7 can be solved for L2 for each time step and then its value is substituted in Equations 2.8 and 2.9 to obtain the cumulative infiltration and infiltration rate respectively.

The Holton model is applicable when availability of soil properties data is minimal and simulates the Hortonian overland flow only. The infiltration sub model is selected according to the availability of soil data and intended purpose of the user. The requirement of soil data increases with least for the Holtan model (1961)/Overton model (1964) to intensive for the SWATRE model.

2.5.4 Surface Storage in Micro Depressions

Soil surface storage is a fraction of the net rainfall retained and detained on the soil surface irregularities before initiating overland flow after meeting the infiltration and or interception. The amount of surface storage is quantified by the surface roughness, which is estimated from surface micro topographic elevation data. The knowledge of surface storage modelling is extremely limited and hence it has been not considered in erosion models in the past. However, it is empirically modelled in both LISEM and EUROSEM to describe the different surfaces roughness produced by the tillage.

The random roughness is used as a parameter to quantify the soil surface roughness (Allmaras et al, 1966) and is determined from soil surface data measured by the profile pin meter with a digital camera. Other methods have also been used to measure it, such as the one metre long chain with 5 mm links, the laser profile meter and close range stereo photogrammetry.

Surface storage is estimated from the random roughness and slope in terms of maximum depression storage (MDS) determined from a variety of surface conditions and micro relief (Kamphorst et al, 2000). The surface depression storage was originally modelled by Onstad (1984) and is estimated in LISEM using an equation (Kamphorst et al, 2000):

$$MDS = 0.243RR + 0.010RR^2 + 0.012RR * S \quad \ldots \quad \text{Eq. 2.10}$$

where MDS is the maximum depression storage (mm), RR is the standard deviation of surface heights (cm) and S is the terrain slope (per cent).

The width of the overland flow is assumed to be linearly related to the fraction of ponded surface in the cell, which is related to the surface water depth and is expressed (Jetten and De Roo, 2001) as:

$$f_{pa} = 1 - e^{(-ah)} \quad \ldots \quad \text{Eq. 2.11}$$

where f_{pa} is the fraction of ponded area, h is the surface water depth (mm) and a is the empirical factor ranging from 0.04 to 2.8 and can be estimated as:

$$a = 1.406 * (10 * RR)^{-0.942} \quad \ldots \quad \text{Eq. 2.12}$$

The runoff before the water level reaches the maximum depression storage height is calculated on the basis of the MDS and the fraction of ponded area under an assumption of 10 per cent surface is ponded to start the runoff. Substituting this value and taking logarithm of Equation 2.11 becomes as:

$$h = \frac{\ln(0.9)}{-a} \quad \ldots \quad \text{Eq. 2.13}$$

where h is called the start depression storage (SDS). The runoff gradually increases nonlinearly when the water height is between the SDS and MDS. After the water height has passed the MDS, the runoff height increases linearly with the water height. If h is less than the SDS, no runoff (Q) is generated. If h is greater than the SDS, the runoff is estimated as:

$$Q = (h - SDS) * (1 - e^{\frac{(-h*(h-SDS))}{(MDS-SDS)}}) \quad \ldots \quad \text{Eq. 2.14}$$

2.5.5 Overland and Channel Flow and Its Routing

Overland flow starts when the net rainfall intensity exceeds the infiltration rate and surface depression storage of the soil. Two kinds of overland flows can occur in a rural catchment: the Hortonian and (or) saturation excess overland flow. The Hortonian overland flow occurs when rainfall intensity is higher than infiltration capacity of the soil and is dominant in arable, pasture and barren lands while the saturation excess flow occurs when the rainfall volume exceeds the moisture storage capacity of the soil and is dominant in naturally vegetated and forest lands. The channel flow occurs when overland flow concentrates in the defined rills and gullies. In the model, different types of surfaces within a grid cell such as road, crusted, compacted, ponded or dry can be simulated and the average water height is computed for each grid cell.

A four-point backward finite-difference solution of the kinematic wave together with the Manning's equation using the Newton-Raphson technique is used for routing of the distributed overland and channel flow over a drainage network in a catchment. The local drainage network is derived from a digital elevation model using the deterministic (D8) eight neighbour method. The kinematic wave method is based on equations of conservation of mass and momentum (Chow et al, 1988). The kinematic wave model assumes negligible inertial and pressure terms in the momentum equation and the wave motion is described by an equation of continuity:

$$\frac{\partial Q}{\partial x} + \frac{\partial A}{\partial t} = q \qquad \ldots \quad \text{Eq. 2.15}$$

Term q is the infiltration surplus, which is the resulting flux of rainfall, interception and infiltration. In order to deal with different types of surfaces, net rainfall and infiltration are first added to the water level in the cell. When there is still infiltration capacity left, this is added to the kinematic wave procedure. Thus, when water is routed over a grid cell that still has the capacity to infiltrate, infiltration takes place inside the kinematic wave routine. The equation of momentum for the kinematic wave is expressed as:

$$S_0 = S_f \qquad \ldots \quad \text{Eq. 2.16}$$

where S_0 is the gravity force and S_f is the friction force.

The equation of momentum can also be written in a curve rating form:

$$A = \alpha * Q^{\beta} \quad \ldots \quad \text{Eq. 2.17}$$

where α and β are the empirical constants.

Discharge by the Manning's equation per raster cell is expressed (Chow et al, 1988; Moore and Foster (1990) :

$$Q = \frac{A}{n} * R^{2/3} * S_0^{1/2} \quad \ldots \quad \text{Eq. 2.18}$$

The Manning's equation can be rearranged in the curve rating form with $S_0 = S_f$ and $R = A/P$:

$$A = \left(\frac{nP^{2/3}}{S_0^{1/2}} \right)^{3/5} Q^{3/5} \quad \ldots \quad \text{Eq. 2.19}$$

where A is wet cross section area (m^2), n is the Manning's roughness coefficient, P is the wet perimeter (m), S is the sine of the slope (fraction), R is the hydraulic radius (m) and Q is the discharge (m^3 /s).

Comparing Equations 2.19 with Equation 2.17, expressions for α and β are deduced as:

$$\alpha = \left(\frac{n^{2/3}}{S_0^{1/3} * P^{2/3}} \right)^{3/5} \quad \text{and} \quad \ldots \quad \text{Eq. 2.20}$$

$$\beta = 3/5 = 0.6$$

The alpha is constant for small rills and is the independent of slope and resistance (Govers, 1992 and 1990).

For a finite difference numerical solution for flow routing, Equation 2.15 is differentiated with respect to Q gives:

$$\frac{\partial A}{\partial Q} = \alpha\beta Q^{\beta-1} \quad \ldots \quad \text{Eq. 2.21}$$

Equation 2.21 is rearranged in terms of $\frac{\partial A}{\partial t}$ and is written as:

$$\frac{\partial A}{\partial t} = \alpha\beta Q^{\beta-1}\frac{\partial Q}{\partial t} \quad \ldots \quad \text{Eq. 2.22}$$

Substituting $\frac{\partial A}{\partial t}$ from Equation 2.22 to Equation 2.15 results in:

$$\frac{\partial Q}{\partial x} + \alpha\beta Q^{\beta-1}\frac{\partial Q}{\partial t} = q \quad \ldots \quad \text{Eq. 2.23}$$

Equation 2.23 is written in a linear finite difference form as:

$$\frac{Q_{x+1}^{t+1} - Q_x^{t+1}}{\Delta x} + \alpha\beta\left(\frac{Q_x^{t+1} + Q_{x+1}^{t}}{2}\right)^{\beta-1}\left(\frac{Q_{x+1}^{t+1} - Q_{x+1}^{t}}{\Delta t}\right) = \left(\frac{q_{x+1}^{t+1} + q_{x+1}^{t}}{2}\right) \quad \ldots \text{Eq. 2.24}$$

Equation 2.24 can be written in a simplified form of finite difference:

$$\frac{Q_{x+1}^{t+1} - Q_x^{t+1}}{\Delta x} + \alpha\beta\bar{Q}^{\beta-1}\frac{Q_{x+1}^{t+1} - Q_{x+1}^{t}}{\Delta t} = \bar{q} \quad \ldots \quad \text{Eq. 2.25}$$

where t is the beginning of a time step, t+1 is the next time step, x is the upstream side of grid cell, x+1 is the downstream side of grid cell, Q_{x+1}^{t+1} is the new discharge, Q_x^{t+1} is the new discharge at the upstream end of the grid cell (sum of all incoming water generated by the kinematic wave), Q_{x+1}^{t} is the discharge present in the grid cell, $\bar{Q} = (Q_x^{t+1} + Q_{x+1}^{t})/2$ is the diagonal average (in a space-time domain), $\bar{q} = \left(\frac{q_{x+1}^{t+1} - q_{x+1}^{t}}{2}\right)$ is the average infiltration surplus over the length of the grid cell.

The channel is located at the centre of the cell and a separate kinematic wave routing procedure is applied for it. Channel cells receive a part of the overland flow, depending on the velocity, thus the velocity in the channel is considered as an average velocity in the cell. The distance of the channel from the grid cell edge is equal to cell

width minus channel width, which is divided by two. A part of the water flows into the channel (F) is expressed using an equation:

$$F = V*dt / ((\text{grid-cell width} - \text{channel width}) /2) \quad \ldots \quad \text{Eq. 2.26}$$

2.5.6 Interflow

The infiltrated rainfall into the soil moves within the soil vertically and laterally. Interflow is the lateral flow through the surface layers to open channels. Interflow can occurs either in unsaturated or saturated flow conditions. Unsaturated interflow occurs when the lateral hydraulic conductivity is greater than the vertical hydraulic conductivity while saturated interflow occurs in situations where a thin soil overlies bedrock; layers of low hydraulic conductivity exist within the soil profile; and piping or artificial drainage occurs. Interflow has been proved to be of a minor importance for a single event simulation (Ritsema et al, 1996). Hence, it is not modelled in LISEM.

2.5.7 Soil Detachment by Raindrop Impact

The soil erosion by water comprises of three main processes: detachment, transport and deposition. Detachment modelling by rainfall and overland flow in LISEM is based on a generalised erosion-deposition theory (Morgan et al, 1998a; Smith et al, 1995) with an assumption that the transport capacity of the runoff reflects a balance between detachment and deposition and is expressed as:

$$e = D_s + D_f - D_p \quad \ldots \quad \text{Eq. 2.27}$$

where e is the amount of sediment in transport process (kg s^{-1}), D_s is the splash detachment (kg s^{-1}), D_f is the flow detachment (kg s^{-1}) and D_p is the deposition (kg s^{-1}).

The LISEM model incorporates splash detachment by rainfall, throughfall and leaf drainage as a function of their kinetic energy whilst most erosion models ignore the effect of leaf drips. Leaf drainage modelling enables the effects of different heights of crop and canopy covers on splash detachment. Splash detachment is modelled by an equation developed from splash tests:

$$D_s = \left[\frac{2.82}{A_s} * K_e * e^{(-1.48h)} + 2.96 \right] * P * A \quad \ldots \quad \text{Eq. 2.28}$$

where A_s is the soil aggregate stability in terms of the median number of drops to decrease the aggregate size by 50 per cent (number), K_e is the kinetic energy of rainfall, throughfall or leaf drainage (J m^{-2}), h is the depth of surface water layer (mm), P is the amount of rainfall in a time step (mm), A is the splash surface area over which the splash takes place (m^2).

The kinetic energy of the direct throughfall on reaching the ground surface is assumed to be the same as that of the natural rainfall. The kinetic energy of the natural rainfall (Ke_r) or throughfall (Ke_t) through the plant canopy is estimated as:

$$Ke_r = 8.95 + 8.44 * \log(I) \quad \ldots \quad \text{Eq. 2.29}$$

The kinetic energy of the leaf drainage (Ke_d) is estimated from an equation:

$$Ke_d = (15.8 * H^{0.5}) - 5.87 \quad \ldots \quad \text{Eq. 2.30}$$

where I is the rainfall intensity (mm h^{-1}) and H is the height of the plant or vegetation (m).

In the model, splash detachment area is estimated as the sum of all splash areas under and besides plants (rainfall, throughfall and leaf drainage) and on ponded and dry areas. The splash area for each condition is estimated separately and is summed up according to the conditions. Areas for splash detachment by rainfall and leaf drainage in ponded and dry areas in a cell are expressed as:

$A_{(Ds\_r\ ponded)}$ = (ponded area fraction)*(1- crop cover)*A and $Ke = Ke_r$ … Eq. 2.31

$A_{(Ds\_t\ ponded)}$ = (ponded area fraction)*(crop cover)*A and $Ke = Ke_d$ … Eq. 2.32

$A_{(Ds\_rdry)}$ = f*(1-ponded area fraction)*(1- crop cover)*A and $Ke = Ke_r$ … Eq. 2.33

$A_{(Ds\_tdry)}$ = f*(1-ponded area fraction)*(crop cover)*A and $Ke = Ke_d$ … Eq. 2.34

where f is the splash delivery fraction, which determines the amount of splashed soil transported from the dry part of the grid cell to the wet part of the grid cell through the air. Most splashes occur on the dry part of the grid cell and decrease exponentially with the water height.

2.5.8 Soil Detachment by Flow

Soil detachment by flow is modelled in LISEM using a generalised erosion-deposition theory (Morgan et al, 1998a; Smith et al, 1995) with an assumption that it is independent of the transport capacity of flow and is only a function of the flow energy exerted to detach. The detachment rate by flow is continually accompanied by the deposition rate equal to a product of w, C and V_s in which w is the width of flow (m), C is the sediment concentration in the flow (kg m^{-3}) and V_s is the settling velocity of the particles (m s^{-1}). Transport capacity of the flow (T_c) represents the sediment concentration at which the rate of erosion by the flow and accompanying rate of deposition are in balance. In this condition, the net rate of erosion is zero and detachment by flow (D_f) is equal to the deposition rate ($w*T_c*Vs$). A general equation for soil detachment by flow is expressed in terms of settling velocity and transport capacity as:

$$D_f = Y(T_c - C)V_s w * dx \quad \ldots \quad \text{Eq. 2.35}$$

where Tc is the transport capacity of the flow (kg m^{-3}), and Y is a flow detachment efficiency coefficient. Y accounts for the detachment limited by the cohesion of wet soil. Y is less than 1 for cohesive soils when C < Tc (detachment takes place). The coefficient, Y for cohesive soils is calculated as (Rauws and Govers, 1988):

$$Y = \frac{u_{min}}{u_c} = \frac{1}{(0.89 + 0.56Coh)} \quad \ldots \quad \text{Eq. 2.36}$$

where u_{min} and u_c are the minimum and critical shear velocities respectively (cm s^{-1}), and Coh is the cohesion of the saturated soil (kPa) and is the sum of bare soil cohesion and cohesion by plant roots. The model accounts for cohesion by plant roots as well.

Deposition takes place only when C is larger than Tc and is modelled using an exponential decay function (Equation 2.36) that simulates the effect of the settling of the

particles slows down when they reach the bottom of the water layer on the surface. Term, Y, then equals 1 as there is no effect of soil cohesion on deposition:

$$D_p = (T_c - C)(1 - e^{(dt*V_s/h)})h * w * dx \quad \ldots \quad \text{Eq. 2.37}$$

where h is the water depth (m), and h*w*dx is the volume of water in the grid cell.

2.5.9 Transport Capacity of Overland Flow

The transport capacity of overland flow is modelled in LISEM as a function of the unit stream power (Govers, 1992 and 1990):

$$Tc = \delta_s \, c \, (\omega - \omega_c)^{d} \quad \ldots \quad \text{Eq. 2.38}$$

where Tc is the volumetric transport capacity (kg m^{-3}), δ_s is the soil mass density (2650 kg m^{-3}), ω is the unit stream power (a product of flow velocity* slope) and ω_c is the critical unit stream power (0.4 cm/s) defined by Govers (1992 and 1990) for a fairly wide range of soils, c and d are the experimentally derived coefficients depending on the soil median texture (D_{50}). The transport capacity of the rill flow in the model can be estimated as:

$$Tc = 2650 \, c \, (V* S*100 - 0.4)^{d} \quad \ldots \quad \text{Eq. 2.39}$$

where V is the rill velocity (m/s), S is the slope of the bed (fraction), c and d are the experimentally derived coefficients depending on soil median particle size. The coefficients are estimated using equations valid for soil median particle size larger than 30 μm, which is based on work of Govers (1992 & 1990),

$$c = [(D_{50} + 5)/0.32]^{-0.6} \text{ and} \quad \ldots \quad \text{Eq. 2.40}$$

$$d = [(D_{50} + 5)/300]^{0.25} \quad \ldots \quad \text{Eq. 2.41}$$

The detachment by flow in the model is assumed to be the rill erosion. Currently, interrill transport capacity is not included in the model.

2.5.10 Sediment Routing

A backward finite difference scheme with the Newton-Raphson iteration is used to solve the dynamic sediment mass balance equation. For each time step, the grid cells are re-arranged in an order of flow beginning from the top of the branches of the

drainage network and progressing towards the outlet, using the sum of the discharges of the upstream grid cells at the end of the time step, as input for the downstream grid cell. Thus, the water is routed towards the outlet as a wave.

Suspended sediment is routed using the dynamic sediment mass balance equation and it is assumed that an explicit solution can be used without iterations:

$$\frac{\partial Q_s}{\partial x} + \frac{\partial (AC)}{\partial t} = e - d \qquad \ldots \quad \text{Eq. 2.42}$$

Second part of left hand of Equation 2.42 is differentiated with respect to time, gives:

$$\frac{\partial (AC)}{dt} = A\frac{\partial C}{\partial t} + C\frac{\partial A}{\partial t} \qquad \ldots \quad \text{Eq. 2.43}$$

Substituting value of A and $\frac{\partial A}{\partial t}$ from Equations 2.17 and 2.22 to Equation 2.43 gives:

$$\frac{\partial Q_s}{\partial x} + \alpha Q^{\beta} \frac{\partial C}{\partial t} + C\alpha\beta Q^{\beta-1} \frac{\partial Q}{\partial t} = e - d \qquad \ldots \quad \text{Eq. 2.44}$$

Equation 2.44 is written in a form of linear finite difference approximation:

$$\frac{Qs_{x+1}^{t+1} - Qs_x^{t+1}}{\Delta x} + \alpha \bar{Q}^{\beta} \frac{C_{x+1}^{t+1} - C_{x+1}^{t}}{\Delta t} + \bar{C}\alpha\beta\bar{Q}^{\beta-1} \frac{Q_{x+1}^{t+1} - Q_{x+1}^{t}}{\Delta t} = \bar{e} \quad \ldots \text{Eq. 2.45}$$

The average concentration can be calculated by the ratio of the average fluxes:

$$\bar{C} = \frac{Q_{s_x}^{t+1} + Q_{s_{x+1}}^{t}}{Q_x^{t+1} + Q_{x+1}^{t}} \qquad \ldots \quad \text{Eq. 2.46}$$

Substituting the value of C in Equation 2.45 is rewritten as:

$$Q_{s_{x+1}}^{t+1} = \frac{\bar{e}\,\Delta x\Delta t + \alpha \bar{Q}^{\beta} \Delta x \left(Qs_{x+1}^{t} \Big/ Q_{x+1}^{t} \right) + \Delta t Q_{s_x}^{t+1} - \bar{C}\,\alpha\beta\bar{Q}^{\beta-1} \Delta x \left(Q_{x+1}^{t+1} - Q_{x+1}^{t} \right)}{\Delta t + \alpha \bar{Q}^{\beta} \left(\Delta x \Big/ Q_{x+1}^{t+1} \right)} \quad \ldots \text{Eq. 2.47}$$

All the variables on right hand side of Equation 2.47 are known and it can be solved kinematically.

2.5.11 Channel Detachment and Deposition

Detachment, transport and deposition in channels are modelled in the same way as detachment, transport and deposition in rills, although, the unit stream power concept was originally developed for rill flow and it was later extended to the channel flow.

Hence, the same equations are used except rill parameters are replaced by channel parameters.

2.5.12 Flow Networks

Runoff and sediment routing in catchments with smaller slope is determined by agricultural practices. The LISEM model simulates routing for three independent drainage networks such as local drainage network, tillage network and wheel track based network. For each network, a separate kinematic wave with the Manning's equation is applied for routing the runoff and suspended sediment to the outlet.

2.5.13 Modelling Grass Strips

The model simulates grass strips as a type of surface. Different infiltration rates for different surface types including grass strips are applied inside a gridcell to estimate water height on each surface type. The average water height in a gridcell is calculated using surface weighted average. The overland flow from an average water height is routed to the outlet using a kinematic wave procedure. Generally, the water on the grass strip surface is completely infiltered. Surplus infiltration is then applied to the water on the other surfaces in the cell under an assumption that all the water within the grid-cell flow perpendicular to the strip. It is intercepted by the grass strips. Then, an average Manning's roughness coefficient for the grid cell is estimated as the surface weighted average of the Manning's n for the grass strip and other surfaces in the grid cell.

2.5.14 Quality Checks

Two quality checks are in-built in the model to avoid an incorrect calculation of soil detachment or deposition. The amount of detachment or deposition in a time step depends on the settling velocity. For a too large time step, it happens that all the sediments are already settled before the end of the time step. Therefore, the first quality check ensures that deposition can never be more than the amount of transport capacity surplus and is expressed as:

$$D_p = \max(\min(0, Tc - C), D_p) \quad \ldots \quad \text{Eq. 2.48}$$

A second quality check for the flow detachment ensures that the amount of detached soil cannot be more than the remaining carrying capacity of the flow and is expressed:

$$D_f = (Tc - C)\, Q\, dt \quad \ldots \quad \text{Eq. 2.49}$$

2.6 Selection of a GIS-based Dynamic Modelling Language

It is known that the LISEM model is written in the PCRaster dynamic modelling language. Therefore, PCRaster would be used to create the LISEM database of input parameters for the simulation study. PCRaster has a few limitations in terms of data exchange, data analysis, map composition and projection. Therefore, it would be better to review the other dynamic modelling languages available to code dynamic models.

A GIS for dynamic modelling must have modelling functionalities to describe the hydrologic and erosion processes in both space and time. It should also be capable of handling huge amounts of spatial data of catchment characteristics collected from various data sources including remotely sensed data. Therefore, there is a need for a GIS-based modelling language environment that is capable of constructing the physically-based dynamic erosion models.

After a review of modelling language in the GIS environment, it has been found that a GIS-based dynamic modelling language is incorporated into three GIS packages namely; PCRaster, GRASS (GRASS, 2004) and IDRISI (Clark Lab, 2004). The PCRaster dynamic modelling language has been widely used to construct dynamic erosion and environmental models such as LISEM (De Roo et al, 1996a), LISFLOOD (De Roo, et al, 2000), RHINEFLOW (Van Deursen, 1995), EUROSEM in PCRaster (Van Dijck, 2000; Van Dijck and Karssenberg, 2004). The GRASS GIS is gaining popularity while the IDRISI dynamic language has not been popular for constructing dynamic models. Therefore, the PCRaster GIS was chosen for dynamic erosion modelling. Its dynamic modelling language (Van Deursen, 1995) has enough functionality either to construct a new dynamic model or to improve the existing models written with it.

The LISEM model written in the PCRaster language is already available in the public domain, so there was no need to construct another new model, instead it was decided to use an existing model. The major advantages of an embedded model into a GIS are that the modeller can focus on the development and refinement of model

processes rather than programming the GIS database. The structure of the GIS-based modelling language is simple and straightforward so that the modellers no longer need to programme the database structure, display tools or optimising algorithms of the model.

2.7 PCRaster

PCRaster (Van Deursen, 1995; Wesseling et al, 1996) is a raster GIS-based modelling toolkit to code a dynamic model using its dynamic modelling language. It also includes cartographic, geostatistic and error propagation modelling functionalities. The PCRaster GIS is a powerful modelling tool either to construct an iterative complex dynamic model or to refine an existing model written in PCRaster. It includes functionality for data storage, manipulation and visualisation of spatio-temporal data in a raster format without data exchange between the model and GIS. It has a relatively open database and the architecture of the system permits the integration of environmental modelling functions with the GIS functions such as database maintenance and visualisation.

2.7.1 The PCRaster Dynamic Modelling Language

The PCRaster dynamic modelling language uses an iterative procedure for defining dynamic equations over a drainage network. It is an extension of the PCRaster spatial modelling language (Van Deursen, 1995; Wesseling et al, 1996) based on the map algebra (Tomlin, 1990) and the cartographic modelling language (Berry, 1993). The PCRaster language is a high level GIS scripting language and has more than 150 spatio-temporal operators drawn from the map algebra, cellular automata, hydrological routing and image filtering for the construction of both static and dynamic models (PCRaster, 1996). The PCRaster dynamic modelling script is composed of structured sequence of five sections to write a dynamic model (Figure 2.2) (PCRaster, 1996):

1. binding - it regulates the database management of the files in the program,
2. areamap – it defines the geographical attributes of the model area and the spatial resolution,
3. initial - defines the initial conditions for the model,

4. timer - regulates the duration and time slice of the model and,
5. dynamic - defines the operation of each time step in an iteration.

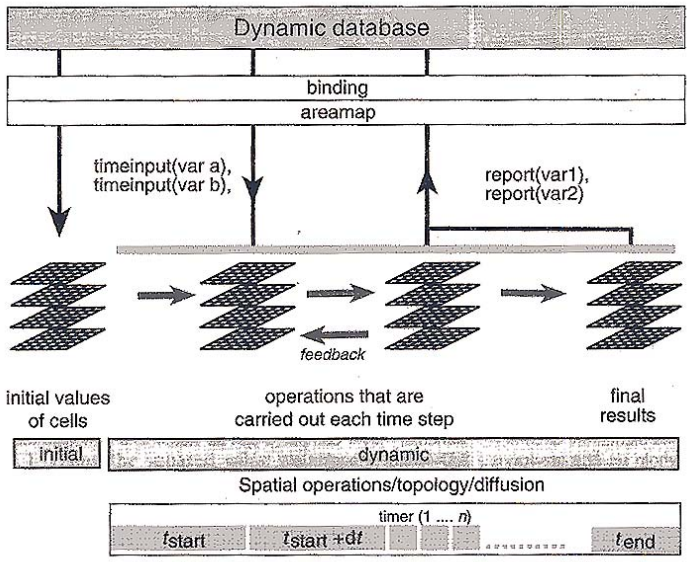

Figure 2.2: Structure of a dynamic model in PCRaster (reproduced from Burrough, 1998)

2.7.2 Software Platform and Characteristics

PCRaster (Van Deursen, 1995; Wesseling et al, 1996) is a free PC-based raster GIS program for dynamic environmental modelling and has been released in the Microsoft DOS and Windows environment. The UNIX version, in Linux, HP-UX and AIX platforms, has been tested but it is not made available in the public domain. The current release of the PCRaster GIS is the version 2.0, professional edition (30 October 2001). It has a modular structure and consists of six main modules:

- PCRCalc, a PCRaster calculator for functions and operations,
- Display, a 2D visualisation tool,
- Aguila, a 3D visualisation tool;
- Timeplot, a plotting tool for time series data;
- Data management tool for data conversion and data exchange, and
- Mapedit, a raster map editing tool.

In addition to six standard modules, the PCRaster package also includes two extra modules:

- GSTAT (Pebesma and Wesseling, 1998) for geostatistical modelling, kriging interpolation, conditional simulation and random field generation, and
- ADAM (Heuvelink, 1998) for estimation of error propagation in the GIS.

The minimum requirement for the PCRaster installation is the Microsoft Windows 98/NT or better with a minimum RAM memory of 64 MB and disk space of 50 MB. Recently, 'Nutshell', a shell-based window for PCRaster, has been introduced to facilitate the running of PCRaster modules and commands from a single window (LISEM, 2004). It is a user friendly window interface and can be used to create, edit and display the raster maps and time series data and at the same time, it can also create, edit and run the models.

2.7.3 Structure and Components of the Database

The PCRaster database holds four kinds of data:

- raster maps,
- point data,
- tables, for relationship between raster maps, and
- time-series, for representation of time varying attributes.

All these data contain six kinds of data type information, which describe the special properties of the entities modelled in a database. The application of each data type is described and is given in Table 2.6.

Raster maps are the most important data that enable the structured manipulation of raster spatial data. A PCRaster map, a binary file in the cross system format, contains three parts: a header, raster data and optional attributes (Wesseling, 1997). The header contains information necessary for geographic and raster data. Raster information contains both the location attributes and the data type of the map namely: number of rows and columns, the cell size, the origin of the map projection, the type of data, and the legend description. Optional attributes such as colour palettes and legends are

located at the end of the file. Tables, time series and point data column files are in the ASCII format with defined structures and can be analysed without a conversion. Two formats of tables, column and matrix format, are used in this database with column table by default while a matrix table is better to specify relations between two maps. The format of a time series file must match with the timer section of a dynamic model. Two types of format for time series data are used: time series with or without a header. The point data column files consist of first two columns for x and y coordinates and one or more columns for attribute data values. The column files should either be in a simplified Geo-EAS format or a plain column file format.

Table 2.6: Data representations in the PCRaster database and their applications (adapted from the PCRaster, 1996)

Data type	Description of attribute	Domain	Application
Boolean	Boolean	0 (false), 1 (true)	Catchment map
Nominal	Classified,	0 - 255, whole values	Land use and soil type maps
Ordinal	Classified, order	0 - 255, whole values	Classified elevation map
Scalar	Continuous, linear	-10^{37}-10^{37}, real values	DEM
Directional	Continuous, directional	0-2 π (rad)/ 0-360^0 (-1 for no direction), real	Slope map
LDD	Local drain direction to neighbour cell	1-9 (5 for sink)	Drainage network map

2.7.4 Data and Cell Representations

Data type and cell representations in PCRaster are not similar. Data type representation describes the data type checking mechanism while the cell representation determines the values of the cells stored and processed in the computer. The cell representations in PCRaster are single real or double real for scalar and directional data, and small integer or large integer for nominal and ordinal data. These are represented in the computer by REAL4 (single real), REAL8 (double real), UINT1 (small integer) and INT4 (large integer) (PCRaster, 1996).

2.7.5 Map Projection

Raster data are supported in a planar grid coordinate system in PCRaster. The location attributes of a raster map is defined by the projection, upper left x and y

coordinates, cell size, number of rows, number of columns and angle to position the map with respect to a real world coordinate system and the shape and resolution of the map. In projection, northing (Y-axis) decreasing and increasing from top to bottom are only supported. PCRaster does not support data projection and coordinate transformation.

2.7.6 Data Exchange

PCRaster is a raster GIS and does not support the creation of vector spatial data, so key vector spatial data are created outside PCRaster. The data management in terms of data import and export is limited and is not user friendly. Widely used GIS raster format data are not supported in PCRaster. Raster data from other GIS needs to be either in ASCII or column file format including ArcInfo GRID ASCII format to import to the PCRaster map format using an asc2map command. Similarly, the PCRaster maps are in the binary format, which needs to be converted to the ASCII or Column file format using a map2asc for import to other GIS package for map composition and further analysis. Other kinds of data in the PCRaster database are the ASCII formatted and can easily be created, analyzed and edited with other GIS packages.

2.7.7 Critical Assessment

The PCRaster dynamic modelling language is a powerful macro scripting language, which uses more than 150 spatio-temporal operators (Burrough, 1998) for constructing both static and dynamic models. A dynamic model written with the PCRaster GIS contains about 200 lines of source code as compared to thousands of line of code in an advanced computer programming language (Ungerer, 2000) but it takes much longer to run than advanced computer programming language-based models. The GIS-based language is easy to learn and implement for environmental modelling. Moreover, it is a freeware and operates in the MS-DOS environment. Nutshell, a shell window, has made PCRaster more user friendly by facilitating the running of PCRaster modules and commands from a single window. Provision for developing a new model in a short time and improving existing models makes it an even more attractive modelling environment. It has limited import functionality and does not support widely used raster GIS formats. It does not provide support for projection and coordinate transformation. Moreover, it needs a supporting GIS for digitisation, rasterisation and

coordinate transformation of key spatial data. Unfortunately, at the same time, most commercial GIS packages are still deficient of providing built-in dynamic modelling capabilities (Van Deursen, 1995; Peuquet, 1999).

2.8 Requirement of Input Parameters

All input parameters and variables of LISEM are required in the PCRaster GIS format except rainfall intensity data. The model requires a large number of spatial input parameters depending on the processes to be modelled. The spatial input parameters are grouped into six categories:

1. catchment parameters,
2. land use and vegetation parameters,
3. soil surface parameters,
4. infiltration parameters,
5. erosion related parameters, and
6. channel parameters

A minimum of 24 parameters are required for a simple simulation. The parameter requirements under various categories and options are described in Appendix A-1. Catchment parameters are derived from a digital elevation model and a raingauge location map. Land use and vegetation parameters are derived from a land use and land cover map with field observations on their parameters. Soil surface and erosion related parameters are generated from a soil map and a landuse and land cover map with field observations on their parameters. Infiltration parameters are derived from a soil map and its property database, and a landuse and land cover map with field observations. Channel parameters are generated from a digital elevation model with field observations on some parameters and a landuse and landcover map.

Generally, input parameters for the model either do not exist or are not available in full for a catchment. For planned events, these parameters can be measured but for a historic event simulation, synthetic techniques are resorted to estimate the representative parameter value. There are problems encountered with available input data in regard to their incompleteness, accuracy and inhomogeneity.

2.9 Model Outputs

The model generates a wide variety of output information to evaluate an erosion scenario in terms of total and time series outputs of the water and erosion balance variables, hyetograph, hydrograph and sedigraph from a catchment (Appendix A-2). The outputs are either in the PCRaster map format or CSV (comma separated value) ASCII format. The map format outputs can be displayed in both static and dynamic 2D and 3D environments. The CSV format hyetograph, hydrograph and sedigraph data can be displayed in Timeplot.

2.10 Sensitivity Analysis and Calibration

Sensitivity analysis examines the model sensitivity to input parameters where each individual input parameter is decreased and increased systematically to analyse its effect on model outputs while keeping other parameters unchanged. There are several approaches to perform the model sensitivity analysis. One at a time sensitivity analysis approach is preferred in this study. Generally, most of the variation in the outputs is caused by a small number of input parameters. The sensitivity analysis of the model is carried out for topographic parameters and the results are discussed in Chapter 6.

Calibration is carried out to adjust some input parameters to match the model behaviour to a set of measured data. In other words, it can be called as a restricted form of parameterisation of a model. A calibration strategy of the model can be carried out for different outputs. Total runoff from an event can be calibrated by changing the initial moisture content and saturated hydraulic conductivity. The peak runoff or shape of the hydrograph can be calibrated by changing the Manning's roughness coefficient. The correct erosion and soil loss from an event can be calibrated by changing the aggregate stability and cohesion of the soil. Due to non availability of measured dataset on runoff and erosion for the Saltdean catchment, no calibration was to be carried out.

2.11 Concluding Remarks

2.11.1 Discussion

A more physically-based distributed and dynamic model within a GIS environment, LISEM, has been selected for surface hydrologic and erosion dynamics

modelling for a storm at catchment scale on the basis of process formulation, process component, spatial and temporal representation, GIS integration and technical support. The model has an additional advantage of its development for a European climate and the similar catchment characteristics with reference to the Saltdean catchment (Boardman et al, 1996). The remotely sensed data derived products such as DEM and land use and land cover, and the National Soil Data can be used to create databases of input parameters of the catchment. The model is applied to simulate the runoff, erosion and deposition within and from the catchment for an extreme rainstorm event of 30 October 2000.

PCRaster is a public domain GIS and is used to create the LISEM databases for a simulation. Its dynamic modelling language has been widely used for constructing dynamic erosion and environmental models such as LISEM, LISFLOOD, RHINEFLOW and Celluna. It provides a powerful modelling environment, but it has limitations in terms of data exchange, projections, hardcopy outputs and user friendliness. It does not support widely used GIS formats and requires another GIS to create and convert vector data to a raster format with a suitable resolution and projection.

2.11.2 Conclusions

- The LISEM model written with the PCRaster dynamic modelling language is a useful tool for predicting runoff and erosion dynamics at catchment scale from an extreme real or a hypothetical rainstorm. It is also used to locate the sediment source and sink areas to adopt an effective conservation strategy.
- It integrates remotely sensed data and other spatial database for model parameterisation.
- It is used to evaluate the effect of different spatial representations of input parameters and key spatial data on model predictive capacity.

3

Rainstorm Identification and Infiltration Modelling

This chapter deals with non-remotely sensed data such as rainfall and soil data for some input parameter definitions, which involve procedures for identification of heavy rainstorms and extraction of infiltration parameters for a single layer Green and Ampt model. Fifteen storms were identified from daily rainfall data first and then locating the onset and ending of the storms from hourly rainfall data. A single storm was used for simulation study. Infiltration parameters were extracted from the 1:250000 scale National Soil Data using pedotransfer functions.

3.1 Introduction

A rainstorm event drives the hydrologic and erosion processes in a catchment. Infiltration is one of the major hydrological processes and is controlled by the rainfall rate before ponding and by the soil properties after the ponding occurs (Chow et al, 1988). An accurate estimation of infiltration is essential for physically-based erosion modelling. At the same time, a better understanding of spatial and temporal variability of a rainstorm at catchment scale is required to model these processes precisely. A few heavy rainstorms with their spatial and temporal distribution are, therefore, required to be identified to model the effect of DEM resolutions on hydrologic and erosion processes in a catchment using LISEM.

The LISEM model simulates infiltration and soil water transport in the soils. Soil hydraulic properties and infiltration parameters can be derived from available soil physical properties using pedotransfer functions (PTFs). These properties are known to vary in space and their measurement can be expensive and time consuming at catchment scale. Alternatively, available soil maps and a soil property database can be used to derive infiltration parameters for a single layer Green and Ampt model.

This chapter deals with non-remotely sensed data such as rainfall and soil data to describe methodologies for rainstorm identification and for estimating infiltration parameters from the 1:250 000 scale National Soil Map data. It also describes the rainstorm characteristics of autumn and early winter 2000 and advanced techniques of rainfall measurement.

3.2 Identification of Rainstorms

3.2.1 Rainfall Data Source

Ideally, rainfall data of autumn and early winter 2000 recorded at shorter time intervals is required to characterise the heavy rainstorms for modelling study. Rainfall data could be obtained from many sources: British Atmospheric Data Centre (BADC), Met Office, University of Sussex, Falmer and farmers' personal weather stations.

Fourteen meteorological stations identified from the BADC archives (Appendix B-1) were active during 2000 around the Saltdean catchment in the East and West Sussex but they were far from the study catchment. Therefore, they were not considered as a data source for storm identification. No weather station could be found in the catchment from any source. The University of Sussex weather station at Falmer was the nearest station from the study catchment and was selected as a source of the rainfall data of hourly, daily and monthly rainfall interval. Monthly rainfall data from the Saltdean and Newhaven weather stations were also obtained to assess the spatial variability of rainfall around the catchment. The description of rainfall data collected from three weather stations is described in Section 3.2.4.

3.2.2 Climate of the Eastern South Downs

The Eastern South Downs is a part of south Eastern England climatic region where a large percentage of rain falls in autumn and winter, arriving on south westerly winds accompanied by the fronts or cyclones associated with depressions. There is an orographic effect due to topography, resulting in heavy rains. Convective storms are active during spring and summer and bring heavy rainfall. North of the South Downs lies in a rain shadow area. Rainfall in the Eastern South Downs decreases progressively from west to east and from south to north. The mean annual rainfall of the Eastern South Downs varies from 750 to 1000 mm with the largest proportion being recorded in winter. Rainfall is becoming more intense in winter and less intense in summer with peak in autumn (Osborn et al, 2002; Mayes, 1997).

3.2.3 Spatio-Temporal Variability of Rainstorms

A distributed model requires a better spatio-temporal description of a rainstorm to simulate hydrologic and erosion process in a catchment. A rainstorm is measured at a finite number of points using rain gauges or pluviometers. Accuracy of spatial variability of rainstorms is dependent on the density of a raingauge network. A better spatial description of rainstorms can be achieved through a dense raingauge network, but such a network is expensive to keep operational. Spatial distribution of a rainstorm is generated from point rainfall data using spatial interpolators such as Thiessen polygons, geomorphological analysis, inverse distance weighting, splines and kriging. Applicability of these interpolation algorithms largely depend on the distribution of raingauges in a catchment and should be used carefully as spatial interpolators violate the physical aspect of a storm distribution in some cases. A few raingauges are required to map the spatial distribution of frontal or cyclonic storms while a denser raingauge network is required to map spatial distribution of convective and orographic storms.

Temporal distribution of a storm is recorded as the rainfall accumulations over time intervals of 1, 5, 15 and 30 minutes and hourly in automatic weather stations. A small catchment is more sensitive to a short temporal lumping of rainfall whereas a large catchment is sensitive to an hourly time intervals. Single event-based hydrologic and erosion models are more sensitive to small temporal resolution of rainfall depth and

intensities. Hence, a short temporal resolution is required for a single event-based modelling. The movement of a storm can possibly be tracked down by analysing several raingauge data simultaneously and is seldom required in distributed erosion models.

When there is no raingauge station in a study catchment, a weather Doppler radar can be used to provide a relatively accurate aerial estimates of spatial distribution of a rainstorm and ground estimates when adjusted with raingauge data (Collier, 1996). In an extreme case, when there is no raingauge and weather radar data available for a remote catchment, environmental satellite data such as Geostationary operational environmental satellite (GOES-1), METEOSAT (Meteorological satellites), NOAA (North Oceanic and Atmospheric Administration) and TRMM (Tropical rainfall measuring mission) can alternatively be used to provide rough estimates of rainfall amounts for a larger area (New et al, 2001; Levizzani et al, 2000).

3.2.4 Description of Raingauge Stations

The University of Sussex weather station was installed on the roof of Pevensey-1 building in the University Campus at Falmer, Brighton in May 1997. It continuously records temperature, humidity, barometric pressure, solar energy, rainfall, and wind speed and direction. The automatic weather station was configured to record all weather variables at an hourly interval since May 1997 (Appendix B-2). Hence, the rainfall data with less than an hour interval were not available (Chitty, 2002). Two other raingauges at Saltdean and Newhaven were also selected to collect monthly and yearly rainfall data. Table 3.1 presents the location coordinates of three weather stations and the kind of data collected.

Table 3.1: Periods of data collected along with the location of weather stations

Data description/ location	University of Sussex, Falmer	Saltdean	Newhaven
Hourly data	Sep-Dec 2000 (Select dates)	---	---
Daily	Jun 1997 – Feb 2002	---	---
Monthly data	1997-2003	1997-2003	1997-2003
Location:			
Latitude	50^0 51’ 52.8’’ N	50^0 47’ 45.6’’ N	50^0 47’ 39’’ N
Longitude	0^0 05’ 11.3’’ W	0^0 02’ 2.4’’ W	0^0 02’ 39’’ E
Altitude	77 m msl	Not available	Not Available

3.2.5 Identification of Rainstorms

It was necessary to identify a few major wet days from the analysis of daily rainfall data from 1998 to 2001 to locate the possible intense events as hourly data could not be supplied. This was done using the following rules, which state that the daily rainfall on a wet day must be more than 15 mm and should be preceded by one or two days of rainfall with a minimum of 5 mm. Using these rules, the possible periods for heavy rainstorm events were identified in autumn and early winter 2000 (Appendix B-3). Hourly rainfall depth and intensity data were then obtained for that specific wet period. Subsequently, the beginning and termination of rainstorm events were located exactly by the analysis of hourly rainfall intensity data. A rainstorm event was defined as the period of rain separated from preceding and succeeding rainfall periods by approximately 2 hours. This definition was based on the time of concentration (~1 hour) of the Saltdean catchment. Similar definitions of a storm based on catchment area have been reported in the literature (Huff, 1967; Vogel, 1986). Fifteen storm events were identified in autumn and early winter 2000 and their rainfall depth, duration, 1-hour maximum rainfall and maximum intensity were given in Table 3.2. The storm on 29-30 October recorded the maximum intensity of 11.4 mm/hour. Therefore, a 6-hour segment of this heavy storm (Figure 3.1) was used for simulation study due to the limitation of large storage space required for simulation results from a complete single storm.

3.2.6 Storm Characteristics of Autumn and Early Winter 2000

In autumn and early winter months of September, October November and December 2000, the storms were primarily the result of a continuous series of frontal depressions coming from the North Atlantic and resulted in the high rainfall on the Eastern South Downs. Autumn 2000 was the wettest autumn on record in the South Downs with a rainfall of 737.7 mm (DEFRA, 2001). The rainfall of October and November 2000 in the South Downs was 294 per cent higher than the regional average while the rainfall of four months (September-December 2000) was 233 per cent higher than the regional average. The regional average is used for calculating percentage of average due to lack of the station average. The estimated return periods for a two month and a four month rainfall were more than 200 years (DEFRA, 2001). Table 3.3 shows the rainfall accumulations and the percentage of average.

Table 3.2: The rainstorm events identified during autumn and early winter 2000

Storm No.	Date of storm	Depth (mm)	Duration (hours)	1-h max rainfall (mm)	Max intensity (mm/hr)
1.	1 Sept	26.4	3	13.5	9.7
2.	15 Sept	19.8	7	5.6	6.3
3.	19 Sept	13.2	3	7.4	2.5
4.	9 Oct	24.6	11	3.6	1.3
5.	10 Oct	9.2	4	4.6	1.3
6.	11 Oct	6.1	3	2.5	1.5
7.	11 Oct	86.7	17	12.4	10.2
8.	29 Oct	4.9	6	1.8	2.8
9.	29-30 Oct	40.1	25	6.3	11.4
10.	2 Nov	12.9	5	3.8	3.8
11.	5 Nov	38.1	11	5.8	1.5
12.	6 Dec	12.9	5	4.1	1.8
13.	1 Dec	22.5	11	4.6	1.0
14.	7 Dec	18.3	8	3.8	0.8
15.	12 Dec	15.5	7	5.1	12.2

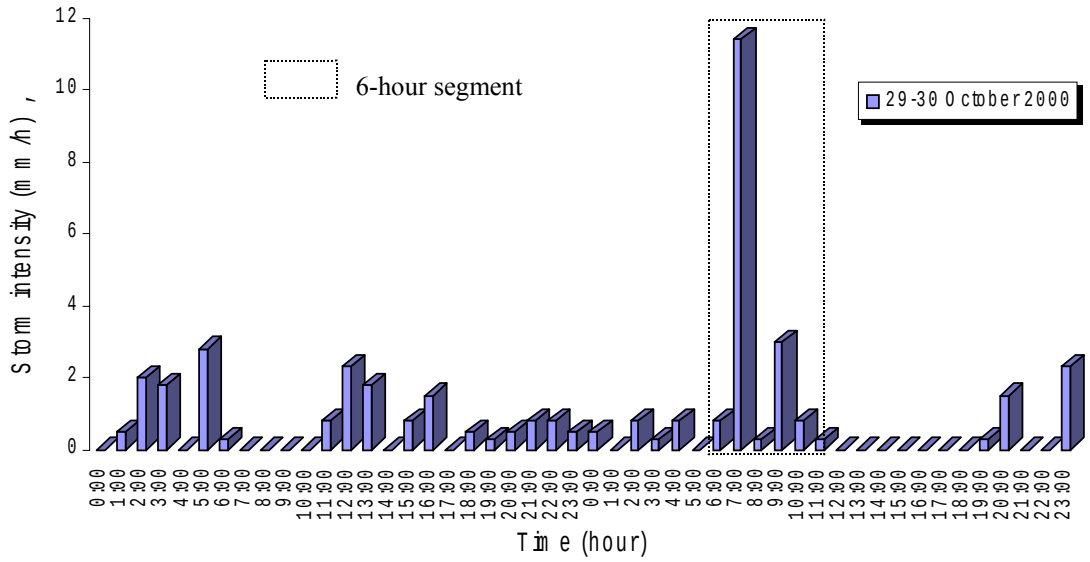

Figure 3.1: A 6-hour segment from the 29-30 October storm for modelling

The rainstorms of autumn and early winter 2000 were characterised by the rainfall intensity, pattern, duration, and frequency as well as the spatial and temporal distribution, and storm movement.

Table 3.3: Rainfall accumulations and their return period estimates (adapted from DEFRA, 2001)

Station/ region	October and November 2000				September- December, 2000			
	Rain (mm)	Average (1961-90)	% of average	Return period	Rain (mm)	Average (1961-90)	% of average	Return period
Falmer	485.7	165	294		794.3	316	251	
Saltdean	384.0	165	233		602.0	316	191	
Newhaven	584.5	165	354		816.8	316	258	
South Downs	484.7	165	296		737.7	316	233	
Southern England	402.0	165	244	> 200 years	634.0	316	201	> 200 years

Storm intensity and pattern

Heavy intense rainstorms last for a shorter period while low intense storms last for a longer duration. The rainfall intensity of fifteen major storms varied from 0.8 to 12.2 mm/h. The storm on 29-30 October lasted for nearly twenty five hours and produced 40.1 mm rainfall while the storm on 11-12 October resulted in 86.7 mm in seventeen hours. These storms are of a mixture of advanced, intermediate and delayed patterns. The delayed pattern storms resulted in heavy runoff and erosion in the catchment.

Storm duration

The duration of the storms varied from 3 to 25 hours. All the storms produced more or less heavy runoff and sediment outflow because their duration is longer than the time of concentration of the Saltdean catchment of around one hour.

Storm frequency

The frequencies of the rainstorms were assessed using the rainfall depth-duration-frequency (DDF) model reported in the Flood Estimation Handbook (FEH) (Faulkner, 1999). The return periods of observed storm events in the Eastern South

Downs were estimated from six parameters. These six parameters and the catchment descriptors of the University of Sussex weather station and the Saltdean catchment were extracted from the FEH CD-ROM (Bayliss,1999) (Appendix B-4). The return periods of the observed storms were calculated using the rainfall depth and its duration and is given in Table 3.4. It was found that there was no rainfall intensity-duration-frequency (IDF) model available for the South Downs. Hence, the DDF model was used for the return period analysis.

The return period of an observed storm event of any duration is estimated from the six DDF parameters. The Gumbel variate (y) is computed using following equations on the basis of storm duration:

For a storm duration less than 12 hours

$$y = \frac{\ln R - f - d_1 * \ln D}{c * \ln D + e} \quad \ldots \text{ Eq. 3.1}$$

For a storm duration between 12 and 48 hours

$$y = \frac{\ln R - f - d_1 * \ln 12 + d_2 * \ln 12 - \ln D}{c * \ln D + e} \quad \ldots \text{ Eq. 3.2}$$

where R is the rainfall depth (mm); D is the duration of a storm; and c, d_1, d_2, d_3, e and f are the DDF parameters.

The return period (T) of a storm is estimated from the Gumbel variate (y) using an equation:

$$T = \frac{1}{\left(1 - \frac{1}{e^{e^{-y}}}\right)} \quad \ldots \text{ Eq. 3.3}$$

Spatial distribution

Areal rainfall estimates are required for catchment scale distributed modelling. The areal estimate of a rainstorm is generated either using a spatial interpolator from multi point rainfall data in a catchment or using an areal reduction factor. A single raingauge station data was available in the catchment, so a uniform spatial distribution of rainfall was assumed. Alternatively, the point rainfall can be converted to the areal rainfall multiplying by an appropriate rainfall areal reduction factor (ARF). This method

is only applicable for rainfall depth, not for rainfall intensity. Hence, it was not used for converting the point rainfall into the areal rainfall.

Table 3.4: Return periods of the storms based on their depth and duration

Storm No	Date	Duration (hrs)	Rainfall (mm)	Return period (years)
1	01 Sep 2000	3	26.4	4.5
2	15 Sep	7	19.8	1.11
3	19 Sep	3	13.2	1.06
4	9 Oct	11	24.6	1.15
5	10 Oct	4	9.2	<1
6	11 Oct	3	6.1	<1
7	11-12 Oct	17	86.7	53
8	29 Oct	6	4.9	<1
9	29-30 Oct	25	40.1	1.8
10	02 Nov	5	12.9	1
11	05 Nov	11	38.1	3.4
12	06 Dec	5	12.9	1
13	01 Dec	11	22.5	1.06
14	07 Dec	8	18.3	1.02
15	12 Dec 2000	7	15.5	1

The areal rainfall is calculated from a point rainfall from an equation:

$$P_{areal} = R_D * ARF \qquad \ldots \quad \text{Eq. 3.4}$$

where P_{areal} is the areal rainfall in mm, ARF is the rainfall areal reduction factor and R_D is the point rainfall of duration, D and a return period, T.

The areal reduction factor (ARF) is expressed by an equation as quoted in the FEH Handbook.

$$ARF = 1 - b * D^{-a} \qquad \ldots \quad \text{Eq. 3.5}$$

where D is the duration in hours and a, and b are the ARF coefficients, which are the function of the area, A, in sq km and are expressed by equations given in Table 3.5.

Table 3.5: Equations for area reduction factor coefficients

A (sq km)	a	b
$A \leq 20$	$0.40-0.0208 \ln(4.6-\ln A)$	$0.0394 A^{0.354}$
$20 < A < 100$	$0.40-0.00382 \ln(4.6-\ln A)^2$	$0.0394 A^{0.354}$

Temporal distribution

The hourly rainfall intensity and depth data were used for the temporal analysis of storms. It was found that an hourly temporal resolution rainfall data was not sufficient for storm analysis. Some rainstorms of shorter duration might have gone unrecorded. The data for a historical event was only available at an hourly interval. Therefore, hourly data were used for modelling application.

Storm movement

The movement of a storm is possibly tracked down by analysing several raingauge data simultaneously. The storm movement towards a catchment outlet produces a heavy runoff and erosion. It was not possible to track down the storm due to the availability of a single raingauge data in the catchment. Moreover, it was not required in the LISEM model.

3.2.7 Analysis of Rainfall Pattern at Three Stations

The monthly rainfall distribution in autumn and early winter 2000 at Falmer, Saltdean and Newhaven is given in Figure 3.2. It was found that October 2000 was the wettest month at all three stations as the monthly rainfall occurred in October 2000 was higher than that of the other months at all three stations. Year 2000 was also an exceptionally wet year at all the stations as can be seen from Figure 3.3. There was no specific trend in annual rainfall among station data.

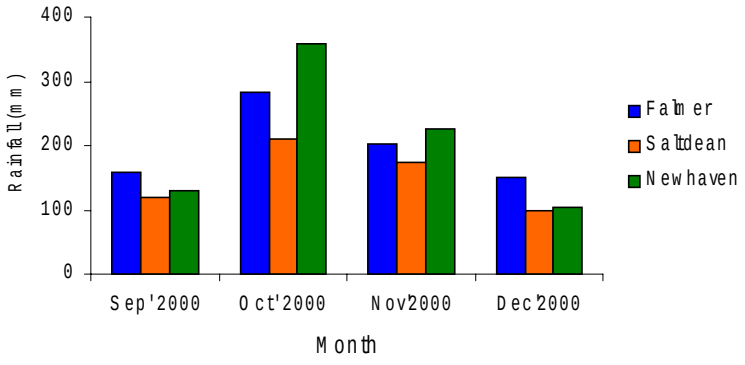

Figure 3.2: Distribution of monthly rainfall in autumn and early winter 2000 at three stations

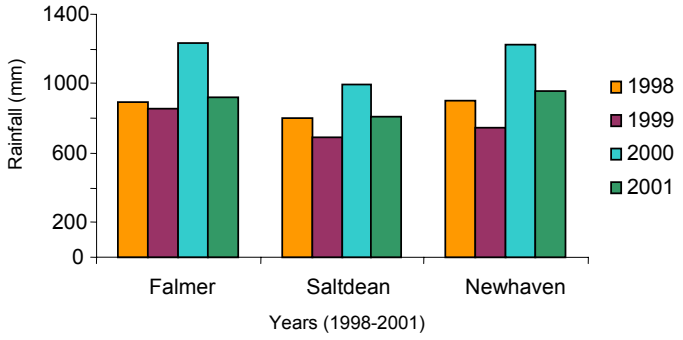

Figure 3.3: Distribution of annual rainfall at three stations

3.2.8 Weather Radar

The nearest weather Doppler radar from the study catchment is located at Chenies, some 100 km distant. It is C-band (5.6 cm) radar with a range of 250 km and is a part of the national weather radar network in the U. K. Radar completes a series of scans about the vertical axis at each of four elevation angles every five minutes and the precipitation products at resolutions of 1 km, 2 km and 5 km over the South Downs are produced. The radar aerial estimates are compared with raingauge estimates to convert the aerial estimates to the ground estimates. The radar data over a large river catchment is more useful than a small catchment. Moreover, radar derived products for October 2000 historical events on the Saltdean catchment were not available. Hence, they were not considered for the modelling.

3.2.9 Rainfall Input to the LISEM Model

The break point rainfall intensity data pairs of a storm are required to drive the LISEM model (Jetten, 2002). These break points pairs are obtained by dividing a storm into discrete time periods within which a nearly uniform intensity rainfall is recorded on the basis of rainfall graph slope. The break points are defined by the time of the start of each discrete period and nearly uniform rainfall intensity. It was not possible to extract break point intensity pair data exactly from available hourly data. It was, therefore, assumed that the same rainfall intensity continued a whole hour due to data limitation. This assumption could be valid for some of frontal storms and might not be valid for the storm considered for modelling study.

3.3 Infiltration Modelling

3.3.1 Soil Data Source

The National Soil Resources Institute (NSRI) is the national repository of soil information for England and Wales. Investigation of soil data at the NSRI revealed that soil data for the Eastern South Downs was only available at 1:250 000 scale (NSRI, 2003). Therefore, it was chosen for parameter estimation of infiltration and soil water transport sub model. The NATMAP vector data, a vector version of the 1:250 000 scale National Soil Map, was obtained from the NSRI in the ESRI Shape file format along with associated Profile and Horizon data. It was also revealed that even paper soil maps at larger scales such as 1:25 000, 1:50 000, 1:63 360 and 1:100 000 were not available for the study area (NSRI, 2003).

The NATMAP vector product is the most comprehensive national digital soil map available at a scale of 1:250 000 and is the product of a 'free soil survey' with an average of 2 to 3 soil observations per square kilometre (NSRI, 2004). It shows location of the 297 mapped soil associations, each of which contains three to five soil series. The map describes a wide range of soil conditions encountered across England and Wales. The Profile and Horizon data provide the detailed information of key soil physical and chemical properties of soil series identified in the soil map.

Soil property data supplied along with digital national soil map contained the Profile and Horizon data of each series. The Profile data contained information on a soil profile for each soil series while the Horizon data contained the properties of four separate soil horizons (topsoil, upper and lower subsoil, and substrate) for the profiles under four different land uses ranging from the arable to semi natural vegetation. These data were linked to the soil association polygons of a digital soil map to derive the thematic map and spatial parameters for infiltration and water transport sub models.

3.3.2 Soil Variability

Soils are spatially heterogeneous at catchment scale and their variability affects the measurements and predictions of soil properties. Soil variability is a result of many of soil formation processes and is mapped using a hierarchical system of soil classification. Soil series is the lowest category of the soil classification system and is used to map soil variability at catchment scale during detailed soil surveys. Soil series is characterised by the sequence of soil horizons present in a soil profile and the nature of substrate material from which the soil is developed. It thus forms a unit of soil characterisation for soil mapping purposes. Soil variability is mapped through a statistically sound sampling procedure from which soil maps are generated at local scale. The national scale soil map is generated by aggregating soil series to a soil association level. Therefore, soil variability needs to be mapped to derive representative parameters on infiltration and soil water transport at catchment scale for distributed modelling.

3.3.3 Soils and Geology of the Eastern South Downs

Soils of the Eastern South Downs comprise thirteen soil associations of which the Andover-1, Coombe 2 and Upton 1 are the three dominant soil associations covering about 80 per cent of the area (Table 3.6 and Figure 3.4). The soil association reflects the dominant soil series in a mapping unit but there are a few other soil series in it as well. Soils in the Eastern South Downs range from shallow to deep silty, deep silty to clay, deep loam to clay and wet deep clay (Avery, 1990). The dominant soil texture is silty loam, which is suitable for arable and grazing land uses due to the cool temperate oceanic climate. Rolling chalk downland has a thin soil at top and side slopes, and a deep soil in the stream terrace and valley.

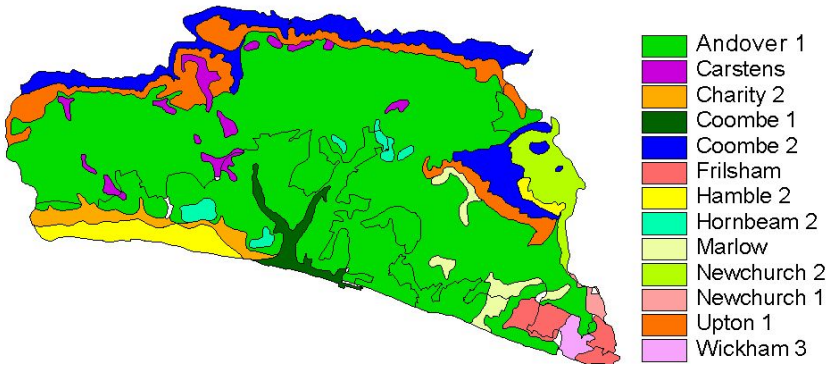

Figure 3.4: Soil associations in the Eastern South Downs

The low rolling hill range of the Eastern South Downs is composed of the calcareous chalk, which is a sedimentary and weakly consolidated soft limestone. The spatial distribution of chalk of the South Downs and South east England is presented in Figure 3.5. Lithologically, chalks are divided into three divisions; lower, middle and upper chalk. The lower chalk is least pure with 10-50 per cent clay and often grayish in colour. The middle chalk contains 5-10 per cent clay while the upper chalk contains less than 5 per cent clay and is the most pure. In the Sussex, middle and upper divisions are not distinguishable.

Table 3.6 : Description of the soil associations in the Eastern South Downs

Map unit	Name	Area (%)	Soil description	Geology
342a	Upton 1	7.64	Shallow silty over chalk	Chalk
U342a	Upton 1	0.26	Shallow silty over chalk	Chalk
343h	Andover 1	48.55	Shallow silty over chalk	Chalk
U343h	Andover 1	16.25	Shallow silty over chalk	Chalk
U511f	Coombe 1	1.81	Silty over chalk	Chalky drift and chalk
511g	Coombe 2	8.40	Silty over chalk	Chalky drift and chalk
U511g	Coombe 2	0.20	Silty over chalk	Chalky drift and chalk
571j	Frilsham	1.03	Loam over chalk	Drift over chalk
U571j	Frilsham	1.15	Loam over chalk	Drift over chalk
U571m	Charity 2	2.22	Deep silty to clay	Flinty and chalky drift over chalk
571z	Hamble 2	0.38	Deep silty	Aeolian silty drift
U571z	Hamble 2	2.76	Deep silty	Aeolian silty drift
581d	Carstens	2.00	Deep silty to clay	Plateau drift and clay with flints
U581d	Carstens	0.19	Deep silty to clay	Plateau drift and clay with flints
581e	Marlow	1.40	Deep loam to clay	Plateau and river terrace drift
U581e	Marlow	0.45	Deep loam to clay	Plateau and river terrace drift
582c	Hornbeam 2	0.40	Deep loam to clay	Plateau drift
U582c	Hornbeam 2	0.83	Deep loam to clay	Plateau drift
711g	Wickham 3	0.70	Seasonally wet loam to clayey over shale	Drift over Mesozoic and tertiary clay and loam
814b	Newchurch 1	0.37	Seasonally wet deep clay	Marine alluvium
814c	Newchurch 2	3.01	Seasonally wet deep clay	Marine alluvium

(Note: U in the map unit stands for soil in urban areas)

3.3.4 Soils of the Saltdean Catchment

Three soil associations are dominant in the Saltdean catchment namely; Andover-1, Marlow and Upton-1 (Figure 3.6). The urban Andover soil covered a small area under farm buildings in the catchment (Appendix B-5), so it was merged with Andover-1. Similarly, area under Upton-1 was also very small (0.05 percent) and it was, therefore, merged with Andover-1 because of similar soil characteristics. Two main soil associations namely, Andover-1 and Marlow (Table 3.7) and their description in (Appendix B-6) were considered for deriving infiltration parameters for modelling study. The Andover-1 soil association comprised five soil series with Andover as a dominant soil series while the Marlow soil association comprised four soil series with Marlow as a dominant soil series (Table 3.8). The Horizon data of the Andover and Marlow series for four land uses are given in Appendices B-7 (a & b).

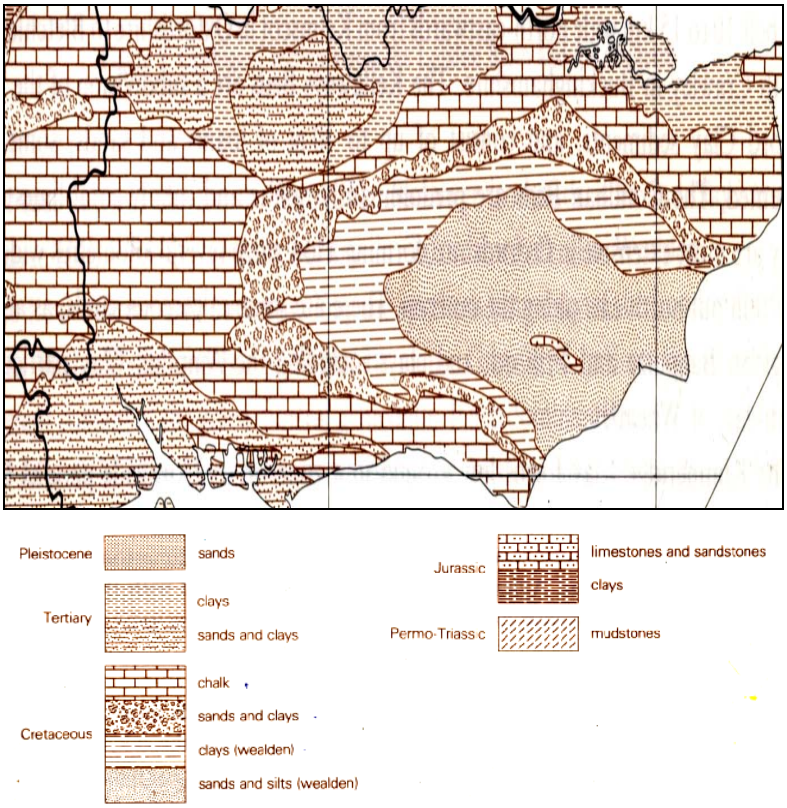

Figure 3.5: Geology of the Eastern South Downs (reproduced from Jarvis et al, 1984)

Figure 3.6: Soil associations in the Saltdean catchment

Table 3.7: Distribution of the dominant soil associations in the Saltdean catchment

Series	Area (ha)	Area (%)	Soil description	Geology
Andover 1	716.19	89.65	Shallow silty over chalk	Chalk
Marlow	82.70	10.35	Deep loam to clay	Plateau and river terrace drift
Total	: 798.89			

Table 3.8: Components of the soil associations in the Saltdean catchment

Map unit	Seq	Series	Series (%)	Series definition
0343h	1	Andover	55	Silty lithoskeletal chalk
0343h	2	Panholes	15	Medium silty material over lithoskeletal chalk
0343h	3	Coombe	10	Medium silty chalky drift
0343h	4	Upton	10	Loamy lithoskeletal chalk
0343h	5	Charity	10	Medium silty drift with siliceous stones
0581e	1	Marlow	45	Medium loamy over clayey drift with siliceous stones
0581e	2	Berkhamsted	10	Light loamy over clayey drift with siliceous stones
0581e	3	Hornbeam	10	Medium loamy over clayey drift with siliceous stones
0581e	4	Winchester	10	Clayey material over lithoskeletal chalk

(Note: Seq stands for sequence of soil series in a soil association)

3.3.5 Limitations of Soil Data

In the NATMAP soil map, each soil association polygon contains a dominant and a few subsidiary soil series. It was not possible to locate constituent soil series spatially in the polygons (Bradley, 2004), so it was assumed that each mapping polygon contains a dominant soil series only. Accordingly, the hydraulic properties and infiltration parameters were calculated for the dominant soil series of each polygon. In this way, soil variability in each polygon is almost lost. Although the soil association is not an appropriate mapping unit for catchment scale distributed modelling, detailed soil map with mapping unit at soil series level is, in fact, required for an optimal representation of soil variability at catchment scale. In the absence of a detailed soil map and corresponding properties, infiltration parameters were estimated on the basis of primary soil properties of the dominant soil series.

3.3.6 Description of Soil Properties Data

Soil mineral particle fractions, organic carbon and pH are calculated directly from individual analyses of different soil horizon samples taken from soil profiles during the field survey to characterise the soil series. The mineral particle size distribution is independent of land use and, therefore, the same particle fractions are used for all the four land uses. Both organic carbon and pH are dependent on land use within a soil series, so they are stratified into four land uses of each series.

Bulk density of a soil series varies with landuse, soil horizon and parent material. Bulk density data are estimated using pedotransfer functions and are stratified into 25 groupings on the basis of land use, soil horizon and parent material. The pedotransfer functions are empirical equations relating the bulk density to mineral soil particle fractions and organic carbon of the soil profile data. Each group is analysed statistically to derive the best possible pedotransfer functions for bulk density. These functions explain 77 per cent variations in bulk density with an overall standard deviation of 0.113 when compared with measured bulk densities data (Hollis et al, 1995).

3.3.7 Estimation of Soil Hydraulic Properties

Soil hydraulic properties are characterised by two relationships: the soil water retention (θ-h) curve and the hydraulic conductivity functions (K-θ/h). These are predicted using pedotransfer functions derived from a combination of sand, silt, clay, organic carbon and bulk density. Water retention and hydraulic conductivity values are predicted from a theoretical basis using both closed form equations of Van Genuchten and Hutson and Cass modification of Brooks-Corey. Initial estimation of soil water potential and moisture content curve for each horizon is made from the profile data using the Arya and Paris model (Arya and Paris, 1981). The Van Genuchten's equation is fitted to each curve to derive α and n parameters from sand, silt, clay, organic carbon and bulk density. Saturated hydraulic conductivity values are predicted from empirical curvilinear equations relating conductivity to air filled porosity at 5 kPa soil water potential (drainable pore space). These relationships are derived from a limited dataset of saturated hydraulic conductivity measurements. The hydraulic conductivity at 5 kPa is then estimated from a relationship between saturated hydraulic conductivity, unsaturated hydraulic conductivity and soil water content using closed form equations of Van Genuchten (1980).

Pedotransfer functions (PTFs)

Soil hydraulic properties and infiltration parameters can be estimated from available or cheaply measured soil data using pedotransfer functions (PTFs). PTFs are empirical equations mostly developed from soil databases of the temperate region and should be used with a great care for other climatic soils. PTFs rely on direct measurement methods for validation and thus can not exist without them (Wösten et al, 2001; Wösten et al, 1995).

Pedotransfer functions are of three kinds: point PTFs, parametric PTFs, and physico-empirical PTFs (McBratney et al, 2002). Parametric PTFs are preferred for predicting the water-retention curve and hydraulic conductivity characteristics. These can be predicted from soil properties either by the Van Genuchten and Mualem model or by the Brooks-Corey model. Five parameters: θr, θs, α, n, and Ks are required for the Van Genuchten and Mualem model to establish both soil water retention and soil

hydraulic conductivity relationships. The relationship between soil water content and water potential is expressed by an equation (Van Genuchten, 1980):

$$S_e = \left[1 + (\alpha h)^n\right]^{-m} \quad \ldots \quad \text{Eq. 3.6}$$

where S_e is the degree of saturation or relative water content and is expressed as:

$$S_e = \frac{\theta - \theta_r}{\theta_s - \theta_r} \quad \ldots \quad \text{Eq. 3.7}$$

Equation 3.7 can be rewritten after substituting S_e from Equation 3.8:

$$\theta(h) = \theta_r + \frac{\theta_s - \theta_r}{(1 + (\alpha h)^n)^m} \quad \ldots \quad \text{Eq. 3.8}$$

where θ_r and θ_s are the residual and saturated water content, α is the scaling parameter, n and m are the curve shape parameters (m=1-1/n) and h is the soil water potential.

Relationships between hydraulic conductivity and soil water content or water potential are expressed by equations (Mualem, 1976).

$$K(S_e) = K_s * S_e^{\ell}\left[1 - \left(1 - S_e^{1/m}\right)^m\right]^2 \quad \text{and} \quad \ldots \quad \text{Eq. 3.9}$$

$$K(h) = K_s \frac{\left\{1 - (\alpha h)^{mn}\left(1 + (\alpha h)^n\right)^{-m}\right\}^2}{\left(1 + (\alpha h)^n\right)^{m\ell}} \quad \ldots \quad \text{Eq. 3.10}$$

where Ks is the saturated hydraulic conductivity and ℓ is the empirical parameter describing pore tortuosity (usually 0.5).

Water-retention and hydraulic conductivity characteristics can also be predicted from soil physical properties using equations (Brooks-Corey, 1964):

$$\theta(h) = \begin{cases} \theta_s & \text{If } h \geq h_b \\ \theta_r + (\theta_s - \theta_r)\left(\dfrac{h_b}{h}\right)^{\lambda} & \text{If } h < h_b \end{cases} \quad \ldots \quad \text{Eq. 3.11}$$

If $h \geq h_b$

$$K(S_e) = \begin{cases} K_s \\ K_s * S_e^{2/\lambda+3} \end{cases} \qquad \text{If } h < h_b \qquad \ldots \qquad \text{Eq. 3.12}$$

where h_b is the bubbling pressure or air entry potential (cm), h is the wetting front suction head, and λ is the pore size distribution index.

3.3.8 Estimation of Infiltration Parameters

Infiltration and vertical transport of water in the soils can be simulated by three models in LISEM: Holton (Beasley and Hoggins, 1982), Green and Ampt (Li et al, 1976) for one or two layers, and SWATRE (Belmans et al, 1983; Feddes et al, 1978). The Holtan and Green-Ampt models simulate the Hortonian overland flow only. The SWATRE model simulates both the Hortonian and saturation excess overland flows. Different surfaces such as crusted, compacted and grass strip can also be simulated in both the SWATRE and Green and Ampt models. The selection of a model is done on the basis of availability of soil data and the user understanding on catchment characteristics and processes. Input data requirement increases from least for the Holtan model to intensive for the SWATRE model.

The Holton model is a semi-empirical method and requires seven parameters to simulate the infiltration process, which are described in the LISEM Manual (Jetten, 2002). These seven parameters can be derived from the 1:250 000 scale soil data. Being an empirical model, it may not be an appropriate choice for simulating the infiltration process for the Saltdean catchment.

The SWATRE model is a finite difference numerical solution of the Richards's equation and can be set up for a maximum of 20 soil horizons. It requires a series of maps and tables of soil profiles and soil hydraulic properties that describe the profile of each land use and land cover with K-θ-h values for each horizon (Jetten, 2002). In other words, the SWATRE model requires a large number of parameters and some of which can be measured from the laboratory experiments for each land use such as K-θ-h relationships. It was not possible to derive the precise range of K-θ-h for each horizon and land use from available soil data. Therefore, it was not used for modelling infiltration of a historic storm event. It would be more appropriate to choose a

physically-based model, which requires medium level of data requirement and simulates infiltration more or less reasonably. The Green and Ampt model met this requirement and was, therefore, selected for the Saltdean catchment with its parameters being derived from the 1:250 000 scale soil map and its soil properties data.

Single layer Green and Ampt model

The Green and Ampt model is a physically-based approach, computationally efficient and easy to derive its parameters from soil and land use information (Chow et al, 1988). It assumes the homogeneous soil profile and soil moisture distribution. Infiltration process can be modelled as a saturation wetting front crossing the soil profile vertically. The soil moisture above the wetting front is at saturation and the soil moisture below the wetting front is equal to the initial soil moisture. The model can also simulate the infiltration for a soil depth limited by impermeable subsoil and different types of surfaces such as, crusted, compacted and grass strips.

Application of a single layer Green and Ampt model requires the estimation of its parameters: hydraulic conductivity, K; effective porosity, ϕ_e; and wetting front suction head, h; initial volumetric soil moisture content, θ_i; and soil depth (d) (Jetten, 2002). First three parameters can be estimated from soil properties using pedotransfer functions. Initial moisture content before a storm can either be measured or assumed. Soil depth can be taken from the soil profile data. The Green and Ampt parameters can be estimated either by the Brooks-Corey model or by the Van Genuchten model. The Brooks-Corey model was used for computing the Green and Ampt parameters.

The effective porosity (ϕ_e) of a horizon in a soil series is calculated as:

$$\phi_e = \phi_{total} - \theta_r \quad \ldots \quad \text{Eq. 3.13}$$

where θ_r is the residual moisture content and ϕ_{total} is the total porosity which is calculated using an equation:

$$\phi_{total} = 1 - \frac{BD}{PD} \quad \ldots \quad \text{Eq. 3.14}$$

where BD is the bulk density and PD is the particle density.

The wetting front suction head is estimated using the Brooks and Corey soil water retention parameters (Rawls et al, 1983):

$$h = \frac{2\lambda + 3}{2\lambda + 2}\left(\frac{h_b}{2}\right) \quad \ldots \quad \text{Eq. 3.15}$$

where h_b is the bubbling pressure (cm) and λ is the pore size distribution index and these are computed using pedotransfer functions (Jarvis et al, 1997):

$$\log h_b = 0.4104 + 0.002684*sand + 0.006354*silt + 0.17766*BD + 0.00013855*clay^2 \quad \ldots \quad \text{Eq. 3.16}$$

$$\log \lambda = -0.475662 + 0.005165*sand + 0.002066*silt - 0.023327*clay - 0.040628*BD + 0.6824*OC - 0.000136162*sand^2 - 0.0000954716*silt^2 + 0.000298891*clay^2 - 0.0637*BD^2 - 3.1679*OC^2 + 0.0000010388*sand^3 + 0.0000010299*silt^3 - 0.0000013251*clay^3 \quad \ldots \quad \text{Eq. 3.17}$$

where sand, silt and clay contents are in per cent; the bulk density is in g cm^{-1} and OC is the organic carbon in g g^{-1}.

Saturated hydraulic conductivity, Ks (cm/h) is estimated from the effective porosity, bubbling or air entry pressure and pore size distribution index (Rawls et al, 1983) as:

$$K_s = 21 * \frac{(\theta_e / h_b)^2 \lambda^2}{(\lambda + 1)(\lambda + 2)} * 3600 \quad \ldots \quad \text{Eq. 3.18}$$

Parameter estimation for the Saltdean catchment

The Saltdean catchment contains two dominant soil series such as Andover and Marlow as described in Section 3.3.4. The Andover series consists of three horizons. The soil properties are available for the first horizon only as other two horizons contain the rubble and rock. The Marlow series contains four soil horizons. The soil properties are available for all the horizons with four land uses each. Due to constraint of horizon soil properties in the Andover series, a single layer Green-Ampt model was selected for both series. Soil primary properties of the first horizon of the Andover and Marlow series each (Table 3.9) were required for the estimation of hydraulic properties and infiltration parameters. Ten hydraulic properties were predicted from the soil primary

properties using pedotransfer functions (Hollis, 2004) (Appendices B-8a and b) and were compared against the available hydraulic properties. As can be seen from Table 3.10, both available and predicted values have a very high correlation and reasonable variability in most parameters.

Table 3.9: Soil primary properties of first horizon of the Saltdean catchment

S. No.	Properties	Unit	Andover	Marlow
1.	Layer depth	cm	25	25
2.	Sand (60-2000 μm)	per cent	22	41
3.	Silt (2-60 μm)	per cent	56	37
4.	Clay (< 2μm)	per cent	22	22
5.	Organic carbon	per cent	3.8	2.2

The bubbling pressure and pore size distribution index for four land uses of each soil series were estimated using Equations 3.16 and 3.17. The effective porosity, wetting front suction head and saturated hydraulic conductivity were then predicted for four land uses of both soil series using Equations 3.13, 3.15 and 3.18. The wetting front suction heads and saturated hydraulic conductivities for four land uses in each series varied from 7.434 to 7.991 and from 4.833 to 6.979 respectively (Table 3.11). Moreover, the predicted values need to be calibrated as they are at the higher end of parameter range. Therefore, a single value for effective porosity, wetting front suction head and saturated hydraulic conductivity for each series based on arable land use was used to make calibration easier. Furthermore, validation of the model was not involved in the study. Therefore, in this approach, it was considered acceptable to use a single set of value for both series for infiltration modelling from a storm of high intensity, which makes small variations in infiltration relatively unimportant.

Table 3.10: Comparison between available and predicted parameters for the first horizon

S. No.	Parameter	Andover Series		Marlow Series	
		Available	Predicted	Available	Predicted
1.	Bulk density, g/cm^2	1.12	1.12	1.28	1.28
2.	Particle density, g/cm^2	2.59	2.59	2.61	2.61
3.	Total pore space volume, %	56.7	56.7	51.0	51.1
4.	Water content at 5 kPa, %	43.6	43.2	37.9	37.7
5.	Water content at 10 kPa, %	39.3	41.0	34.0	35.7
6.	Water content at 40 kPa, %	31.4	35.65	27.0	31.2
7.	Water content at 200 kPa, %	24.5	26.96	21.0	23.8
8.	Water content at 1500 kPa, %	18.9	17.7	16.3	16.8
9.	Saturated K, cm/day	115.6	126.5	116.0	120.3
10.	Saturated water content, %	47.44	50.7	37.8	39.9
11.	Residual water content, %	8.75	7.9	7.0	6.6
12.	Van Genuchten Alpha	0.042	--	0.055	--
13.	Van Genuchten N	1.243	--	1.250	--
14.	Van Genuchten M	0.195	--	0.200	--

Table 3.11: Infiltration parameters for four land uses of each soil series

Infiltration parameter	Effective porosity	Wetting front suction head	Saturated hydraulic conductivity
Andover series			
Arable	0.480	8.532	4.817
Ley grass	0.462	9.145	4.454
Permanent grass	0.523	8.220	6.688
Woodland and other vegetation	0.534	7.978	7.658
Marlow series			
Arable	0.440	7.844	4.833
Ley grass	0.447	7.991	5.538
Permanent grass	0.468	7.826	5.600
Woodland and other vegetation	0.497	7.434	6.979

Available saturated hydraulic conductivity values for both soils were used as there was a large variation between available and predicted values. Antecedent soil moisture condition for a historic storm could not be established so it was assumed for three possible levels for simulation such as low, medium and high. The depth of soil

layer was taken from soil properties data. In this way, all the parameters for single layer Green and Ampt model were derived for each series (Table 3.12).

Table 3.12: Green and Ampt parameters for the Andover and Marlow series

Parameter	Andover series	Marlow series	Unit
Brooks-Corey parameters			
Bubbling pressure, h_b	12.400	11.220	cm
Pore size distribution index, λ	0.124	0.113	
Green and Ampt parameters			
Effective porosity, □e	0.48	0.44	cm^3/cm^3
Wetting front suction head, h	8.533	7.844	cm
Saturated hydraulic conductivity	4.817	4.833	cm/hr
Ksat (predicted from soil properties)	3.327	2.792	cm/hr
Depth of the first soil layer	25.00	25.00	cm
Antecedent soil moisture levels			cm^3/cm^3
High (assumed)	0.46	0.44	Fraction
Medium (assumed)	0.24	0.22	,,
Low (assumed)	0.08	0.07	,,

Hydraulic conductivity for the Green and Ampt model is one half of the saturated hydraulic conductivity predicted from the soil data (Bouwler, 1966). Therefore, the saturated hydraulic conductivity and water front suction head were to be calibrated to get reasonable outputs from a model.

3.4 Concluding Remarks

3.4.1 Discussion

A methodology is used to identify heavy wet periods from daily rainfall data to obtain hourly data for the specific periods. Subsequently, fifteen storms were identified from hourly rainfall in autumn and early winter 2000. The storm on 11-12 October 2000 has a return period of 53 years while all other storms have return periods less than 5 years. A 6-hour single storm from 30 October 2000 would be used for modelling study to optimise the computer storage requirement. The spatial and temporal resolutions of rainstorm data were coarse for the catchment. Storms were the result from frontal depressions which last for at least a couple of hours. Therefore, a single raingauge data

has provided a spatially representative rainfall data of the storms over the catchment. An hour temporal resolution was too coarse for analysing the temporal variability of a storm. Short duration storms might have gone unrecorded. Hourly data were more or less representative for frontal storms and, therefore, were suitable for modelling study.

Infiltration and water transport in the soils is a major hydrologic process controlling runoff and associated soil erosion. The soil map at a scale of 1:250 000 was only available data for the Eastern South Downs and the Saltdean catchment. Although, it was not the best soil data for catchment scale modelling, but it was used for estimation of the Green and Ampt infiltration parameters and soil hydraulic properties using pedotransfer functions. The soil was mapped at soil associations, which comprise of a dominant and a few other soil series of similar origin. It was not possible by any means to locate each constituent soil series spatially in a soil association polygon (Bradley, 2004), therefore, it was assumed that each mapping polygon contained the dominant soil series only. A single layer infiltration model was chosen because the Andover series contains a single horizon soil properties data. These limitations result in unrealistic parameter values, which ultimately affect the prediction capability.

3.4.2 Conclusions

- Fifteen rain storms were identified from daily rainfall data using rules to target the specific heavy wet periods to obtain hourly rainfall data for a better description of a storm. A 6-hour storm of 30 October 2000 would be used for the simulation study. Hourly data was reasonably representative for describing spatial and temporal distribution of the 30 October 2000 frontal storm.

- Infiltration parameters for a single layer Green and Ampt model were estimated from the national soil map at a scale of 1:250 000 using pedotransfer functions.

4

Land Use and Land Cover Mapping

This chapter treats a hybrid classification methodology for SPOT-1 multispectral data for mapping of land use and land cover for a historic storm event. An overall classification accuracy of 90 per cent was achieved which reflects reliable land use and land cover information suitable for the modelling study.

4.1 Introduction

Land use and land cover are key spatial data derived from remotely sensing and is necessary for distributed erosion modelling. They are used for deriving model spatial input parameters by reclassifying the land use and land cover thematic map to produce parameter maps. Performance of an event-based distributed model largely depends on reliable information obtained on land use and land cover with its spatial and temporal variations in a catchment because it is highly dynamic in nature and changes with seasonal and climatic variations.

The Eastern South Downs have been transformed from a grazing landscape to an arable landscape with more winter cereal crops in last fifty years of the 20th Century. This led to severe soil erosion and degradation in fields and flooding in near by residential areas during the winter season (Boardman, 2003). Landscape conservation and enhancement schemes viz. Set-aside, Environmentally Sensitive Areas (ESA) monitoring, Countryside Stewardship and Area of Outstanding Natural Beauty (AONB)

are in operation to safeguard and conserve the chalk landscape from degradation and to mitigate local flooding (Countryside Agency, 2001; DEFRA, 2003). Land use and land cover of the Eastern South Downs was mapped three times using visual interpretation of 1:10 000 scale aerial photographs (ADAS, 1996a). Another source is the Land Cover Map 2000 (Fuller et al, 2002), which provides broad land cover classes. The available information does not meet the requirement for distributed modelling of the storm event that occurred on 30 October 2000. The required information needs to be close to the rainstorm event for obtaining reliable modelling results. Therefore, a remote sensing approach needs to be employed to obtain this information close to the storm.

A quick and reliable method is required for mapping the spatial distribution of land use and land cover close to the storm event from remotely sensed data. The format of classification results and information required for the modelling needs to be compatible for ingesting a thematic map directly to the model to derive model parameters. This chapter is dedicated to exploring for a quick and reliable procedure for mapping of land use and land cover of the Eastern South Downs.

4.2 Remote Sensing Approach

Reliable and timely land use and land cover information is necessary at catchment scale for distributed modelling study. Conventional mapping approaches alone are time consuming and expensive. Remote sensing can be exploited to provide timely information, but it requires some form of ground data as a check to make it reliable. Satellite remote sensing with a limited field work has been successfully used for mapping a range of land use and land cover classes at a variety of spatial and temporal scales (Schultz, 1988). It is a cost effective alternative and major source of timely and reliable information for environmental distributed modelling, because of repeated observations in relatively short period and synoptic multispectral coverage. Multispectral classification techniques for land use and land cover mapping have been proved to be promising as a key spatial input data to several erosion modelling studies.

Erosion models based on land use and land cover have been modified to directly ingest thematic data derived from multispectral classification to identify land use and

land cover classes in a catchment (Davis et al, 1991; Engman and Gurney, 1991).

4.3 Land Use and Land Cover Status

The Eastern South Downs was selected as the study site for land use and land cover mapping (Figure 4.1). Land use and land cover of the Eastern South Downs was first mapped extensively in 1987 and later revised in 1991 and 1995 using visual interpretation of aerial photographs with some limited ground checking under the Environmentally Sensitive Areas (ESAs) monitoring programme. These surveys indicated that areas under arable, grassland and dense scrub and woodland were about 53, 22 and 18 percent respectively with 91 per cent classification accuracy for classes (ADAS, 1996a). The change in land cover was remapped by comparison of aerial photographs under revised ESAs and results of land cover of various surveys are given in Table 4.1.

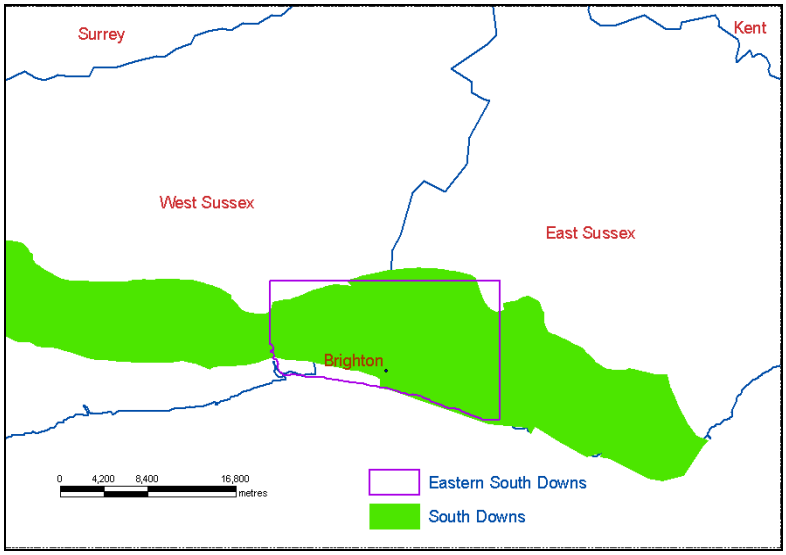

Figure 4.1: Location map of the Eastern South Downs study area

4.4 Hierarchical Classification Scheme

Land use and land cover mapping attempts should be accompanied by a suitable classification scheme for use at a desired scale, for a designated area and within the capability of information gathering techniques being used (Anderson et al, 1976). Land use and land cover are conceptually different. The former is related to man's activity on

land while the latter describes the spatial distribution of actual land cover, mainly variations in vegetation. A hierarchical classification scheme provides a better framework for organising and categorising the information to be extracted at several levels from an image (Jensen, 2000).

Table 4.1: Land use and land cover changes in the Eastern South Downs (adapted from ADAS, 1996a)

Land use and cover	Area in per cent		
	1987	1991	1995
Arable	53.57	53.15	44.92
Grassland	22.22	21.61	29.69
Dense scrub and woodland	17.88	18.40	18.36
Non-agricultural land	6.03	6.54	6.72
Open water	0.30	0.30	0.31

A suitable hierarchical classification scheme for the Eastern South Downs was worked out on the basis of a few classification schemes such as the South Downs Environmentally Sensitive Areas Landscape Monitoring (ADAS, 1996a & b), Monitoring Land cover Changes in National Parks of England and Wales (Taylor et al, 1991 a & b), USGS Land Use and Land Cover Classification System for Use with Remote Sensor Data (Anderson et al, 1976) and Land cover Classification in Countryside Survey 2000 under the UK Biodiversity Action Plan (Fuller et al, 2002). A land use and land cover classification scheme (Table 4.2) was proposed and used for mapping of land use and land cover of the study area. The definition of classes of the scheme is given in Appendix C-1.

Table 4.2: Hierarchical classification scheme for the Eastern South Downs

Level-1	Class	Level-2	Sub class with cover description
1	Arable land		
		10	Bare soil
		11	Harvested field with stubbles
		12	Set-aside or fallow
		18	Ley grass
		19	Horticulture and vegetables
2	Grassland		
		20	Semi-improved grassland- good cover
		21	Semi-improved grassland - poor cover
		22	Natural or hill grazing - good
		23	Natural or hill grazing - poor
		24	Improved grassland - good
		25	Improved grassland - poor
3	Scrub and woodland		
		30	Hedges
		31	Gorse scrub - open
		32	Gorse scrub - dense
		33	Open woodland
		34	Dense woodland (plantation)
		35	Dense mixed woodland
4	Built-up land		
		40	Buildings and farmsteads
		41	Villages
		42	Urban area
		43	Roads
5	Water body		
		50	Inland water
		51	Sea water

4.5 Image Preprocessing

4.5.1 Availability and Description of Remotely Sensed Data

The optical images of the study area can be selected from a number of high resolution satellite sensors (Flügel and Müschen, 2000; Jacobsen, 1998; Aplin et al, 1997). Cloud persistence is a major problem in the UK to select images just before and after a storm event. Another factor is the cost of imagery, which sometimes is a budgetary constraint. The SPOT images have a better spatial resolution and geometric integrity than the Landsat images but they have a lower spectral resolution. So a trade off between spectral and spatial resolutions was made. Therefore, the SPOT images were selected for the identification of land use and land cover of the study area.

Description of the SPOT satellites

The SPOT (Satellite Pour l'Observation de la Terre) satellite is the French earth observing satellite system and consists of five satellites that operate from a sun-synchronous, near polar orbit, 832 km above the earth. At present, three satellites are in operation: SPOT-2 (since 1990), SPOT-4 (since 1998) and the recently launched SPOT-5 (since 2002). SPOT-1 was active till 2002 while SPOT-3 was in orbit between 1993 and 1996. They are inclined 98.7 degrees, cross the equator at 10:30 AM local time and have an orbital cycle of 26 days (SPOT Image, 2004; Brachet, 1986). The characteristics of the SPOT satellite sensors are compared (Appendix C-2).

The SPOT-1 images are collected in visible and near-infrared bands from the High Resolution Visible (HRV) sensors. The SPOT-1 satellite carries two HRVs with the capability of scanning in either a multispectral mode or a panchromatic mode. The multispectral mode captures images in three spectral bands: 0.50- 0.59, 0.61- 0.68 and 0.79- 0.89 μm. These bands are co-registered and have a ground resolution of 20 m. The panchromatic mode collects images in the spectral range 0.51- 0.73 μm at a 10 m ground resolution. Each nominal scene covers an area of 60 km by 60 km. The viewing angle of each HRV sensor can be adjusted to collect images up to 27 degrees right or left of satellite nadir. This cross-track pointing capability allows the same point on the earth to be viewed from several different orbits and thus, enables the acquisition of stereoscopic imagery.

Applications of SPOT data

The SPOT multispectral imagery has widely been used for land use and land cover mapping. The SPOT image applications with their respective discipline are discussed in the literature (Brachet, 1986). The SPOT bands have also been applied to many applications since the launch of the SPOT-1 HRV sensor. However, SPOT-1 had only three band multispectral data. The principal applications of the SPOT bands are described (Table 4.3).

Table 4.3: Applications of the SPOT spectral bands (adapted from Lillesand and Kiefer, 1999).

Band	Wavelength (μm)	Principal applications
Pan	0.51-0.73	Fine geometrical detail mapping for precision farming, cadastral and cartographic mapping, DEM generation
XS1	0.50-.59	Vegetation discrimination, vigour assessment, cultural feature identification iron content in rocks and soils
XS2	0.61-.68	Plant species differentiation, cultural feature identification
XS3	0.79-.89	Vegetation type discrimination, vigour assessment, biomass survey, water body delineation, soil moisture discrimination
Xi4	1.58-1.75	Plant and soil moisture content indicator, snow differentiation from cloud

4.5.2 Selection of SPOT Images

Images of around 29-30 October 2000 storm event and June 2000 were thoroughly browsed in the SIRIUS online catalogue. Unfortunately, no image with new SPOT sensors for the period of interest was found due to the persistence of cloud cover (Appendix C-3). A winter scene of 26 October 2000 and a summer scene of 18 June 2000 (Table 4.4) were selected for this study. The winter scene selected was the one after ploughing and drilling to highlight tilled land and after the first frost when deciduous vegetation showed clear sign of winter senescence. The summer scene was intended to cover the main growing season of arable crops and semi-natural vegetation (Fuller et al, 1998). Before ordering data, quicklook images of selected scenes were checked for presence of cloud cover particularly over the area of interest.

Table 4.4: General information of the selected scenes

GRS	Date	Satellite	Sensor ID	Cloud cover	Image quality	Comment
033/247	26 Oct' 2000	SPOT-1	HRV-1, XS	10 %	Excellent	Study area cloud free
033/247	18 June' 2000	SPOT-1	HRV-1, XS	Nil	Excellent	

The selected scenes were obtained with a level-1B preprocessing (Appendix C-4) from the Spot Image, Toulouse under the ISIS (Incitation à l'utilisation Scientifique des Images SPOT) programme (CNES and Spot Image, 2000). The scene acquisition parameters of both images are given in Appendix C-5. These images were supplied as

the standard scene in a CEOS structure with a CAP format (Appendix C-6) on an optical disk. The scenes were imported to the ERDAS Imagine version 8.6 for further processing.

4.5.3 Geometric Correction

The study area was small as compared to a full scene size and was identified in the central part of the scene using distinct ground features. A subset larger than the study area would be a better choice in order to utilise disk storage space efficiently and to improve data processing. Therefore, the subset image of 1400 pixels by 700 pixels was extracted from the 26 October scene. Similarly, the same area was also extracted from the 16 June image and both images were then used for geometric correction.

Geometric correction is the process of transforming an image to conform to a standard projection and coordinate system, to be integrated with other key spatial data in a GIS (Williams, 1995). Satellite images usually contain significant geometric distortions, which need to be corrected in two steps, systematic correction and local correction. A systematic correction is usually applied at a ground station using a parametric sensor model while image warping for local correction is applied to system corrected images using a polynomial transform equation based on sufficient and well distributed ground control points over a study area collected from various sources. Local geometric correction involves locating the ground control points, computing the transformation matrix and then creating an output file with a new projection by resampling (ERDAS, 2002).

The images obtained with the Level-1B geometric format were already geometrically corrected for systematic errors associated with sensor operation, and earth motion and curvature (Richards and Xia, 1999). The study area image of 26 October was geometrically corrected to the British National Grid coordinate system using a first order polynomial transformation with 31 ground control points (GCPs) well distributed all over the area (Appendix C-7(a)). The reference GCPs were collected from 1:25 000 scale Ordnance Survey Pathfinder series map, published in 1991. This map is based on the Transverse Mercator projection, Airy spheroid, Ordnance Survey Great Britain 1936 datum and mean sea level vertical datum at Newlyn. The RMS error for the

transformation was within an acceptable limit, less than a pixel (0.67 pixels). The input image was resampled to a 20 m output image using the cubic convolution technique. This rectified image was used for further processing.

An 18 June image subset was co-registered to a 26 October rectified image as reference image using a first order polynomial transformation with 26 GCPs well distributed over the image. The RMS error for the transformation was 0.40 pixel (Appendix C-7 (b)) and output image was obtained with 20 m pixel size using the cubic convolution resampling. An 18 June image was used for visual interpretation of major land use and land cover classes, which were used to check the classes with a 26 October image in case of confusion as there was a large time gap between the field survey and the time of image acquisition. It was not used at all for digital classification.

4.5.4 Delineation of the Study Area

The geometrically corrected sub set image of 26 October 2000 was used in conjunction with a 1:50 000 scale Ordnance Survey Landranger map of the South Downs (sheet number 198, second series) with 10 m contour intervals, published in April 2000, to delineate the Eastern South Downs study area. The study area was delineated by an easting grid line of 542 000 m on the east, by the river Adur on the west, by northing grid line of 114 000 m on the north and by sea on the south.

4.5.5 Evaluation of Multispectral Data

The univariate statistics, and variance-covariance and correlation matrices of the study area image delineated from the 26 October 2000 image were computed to assess the relationship between bands. Table 4.5 shows that the first band, XS1 and second band, XS2 are highly correlated with each other while second and third bands, and third and first bands are poorly correlated. Therefore, there is some redundancy of information in the image. The false colour composite image of the study area delineated from 26 October 2000 image is displayed in Figure 4.2.

Table 4.5: Statistics properties of the study area image (26 October 2000)

Parameter/band	Univariate statistics		
	XS1	XS2	XS3
Minimum	29	7	8
Maximum	235	112	150
Mean	47.83	25.18	56.62
Standard deviation	7.42	6.53	18.37
Median	47	24	54
Mode	46	22	44
Variance co-variance matrix			
XS1	55.00		
XS2	45.11	42.68	
XS3	23.99	-0.98	337.35
Correlation matrix			
XS1	1.000		
XS2	0.931	1.000	
XS3	0.176	-0.008	1.000

4.5.6 Image Enhancement

Image enhancement techniques are applied to increase the general sharpness and separability of the data. These are in-built within most digital image processing software and include contrast manipulation, grey level slicing, spatial filtering, band ratioing and principal component analysis (Jensen, 1996). Linear, Gaussian, histogram equalisation, standard deviations, gamma etc are a few of contrast enhancement functions. The standard deviation enhancement was applied to both images to improve their interpretability.

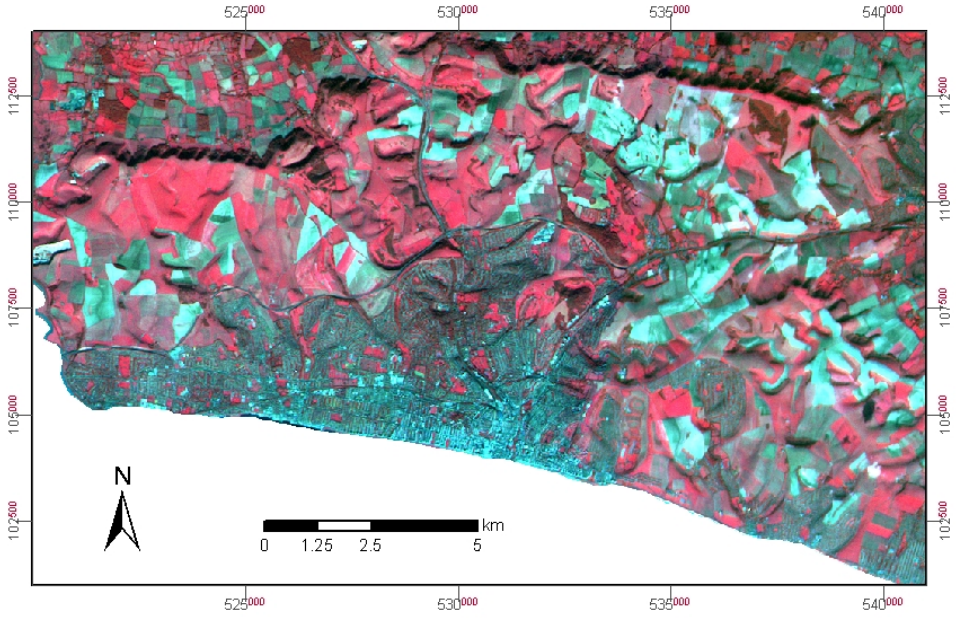

Figure 4.2: False colour composite of the Eastern South Down study area (26 Oct 2000)

4.6 Ground Data Survey Strategy

4.6.1 Need for Ground Data

Ground data collection is an integral part of supervised classification and involves field survey to record land use and land cover information and conditions of an area of interest. The field survey is planned to collect the ground data information for:

- extracting training signatures for supervised classifier (Taylor et al, 1997; Campbell, 1999),
- assessing the accuracy of supervised classification of remotely sensed data (Congalton and Green, 1999; Congalton, 1991),
- verification of land use and cover classes generated by unsupervised classification (Campbell, 1999), and
- identification of empirical relationships between biophysical parameters and satellite observation (Colombo et al, 2003; Carlson, and Ripley, 1997).

4.6.2 Integrated Survey Approach

Area estimates by sampling with ground survey are unbiased, but they suffer from high sampling errors. Similarly, area estimates by image classification have no sampling error, but they usually suffer from misclassification (biased). These two techniques are complementary with each other and are, therefore, combined to obtain the improved estimates, which are more accurate than either of the two approaches used (Figure 4.3). This approach was not used as there was a large time lag of two and a half years between ground survey and image acquisition. Therefore, estimates from ground survey could not be treated as very reliable.

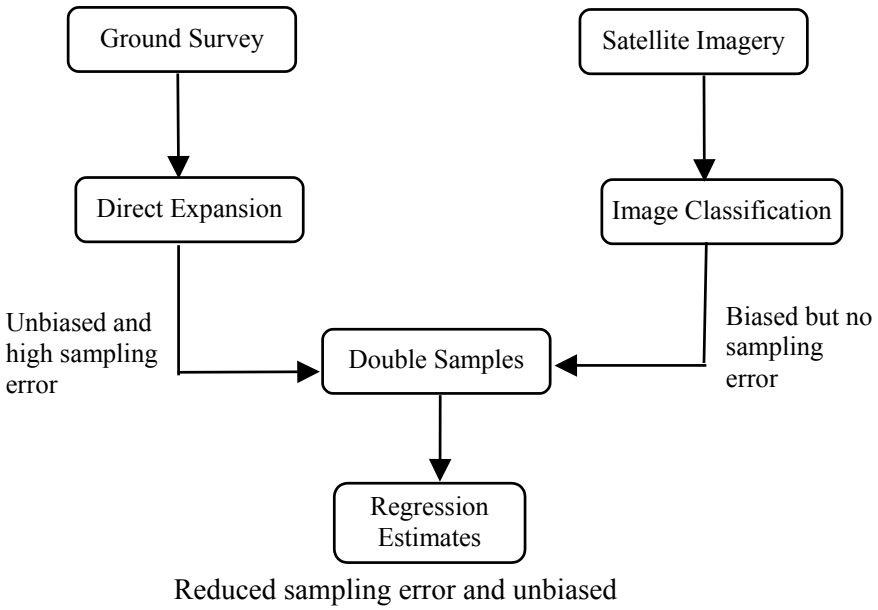

Figure 4.3: Flow diagram of an integrated survey methodology

4.6.3 Sampling Framework

Ground data is necessary in some forms for most of remotely sensed data for earth resources studies and is collected through a statistically sound sampling survey design scheme. Several sampling design schemes have been suggested for ground data collection for supervised image classification (Taylor et al, 1997; Taylor and Eva, 1992). Every sampling scheme has its own inherent merits and demerits.

An area frame methodology (Taylor and Eva, 1992) was employed for ground sampling. The study area was divided into 6 x 4 blocks of segments with each block of

4 x 4 segments of 1 km x 1 km each. A segment sampling area frame of 1 km x 1 km was selected because the same grid markings were available in the Ordnance Survey maps. An unaligned systematic random sample design of segments was chosen from blocks within the study area. No stratification was done in the sample design for the Eastern South Downs because there was no basis for doing so. A random sampling procedure was adopted which led to the selection of 14 segments highlighted in Appendix C-8(a). Out of fourteen segments, three segments fell in urban areas. No survey work was carried out as these samples were masked out separately by visual interpretation. Eleven segments were finally selected for the field survey. The layout of selected sample segments in the study area is given in Figure 4.4. The nominal sample size was 4.82 per cent. The coordinates of top left corner of each segment selected for field survey is given in Appendix C-8(b).

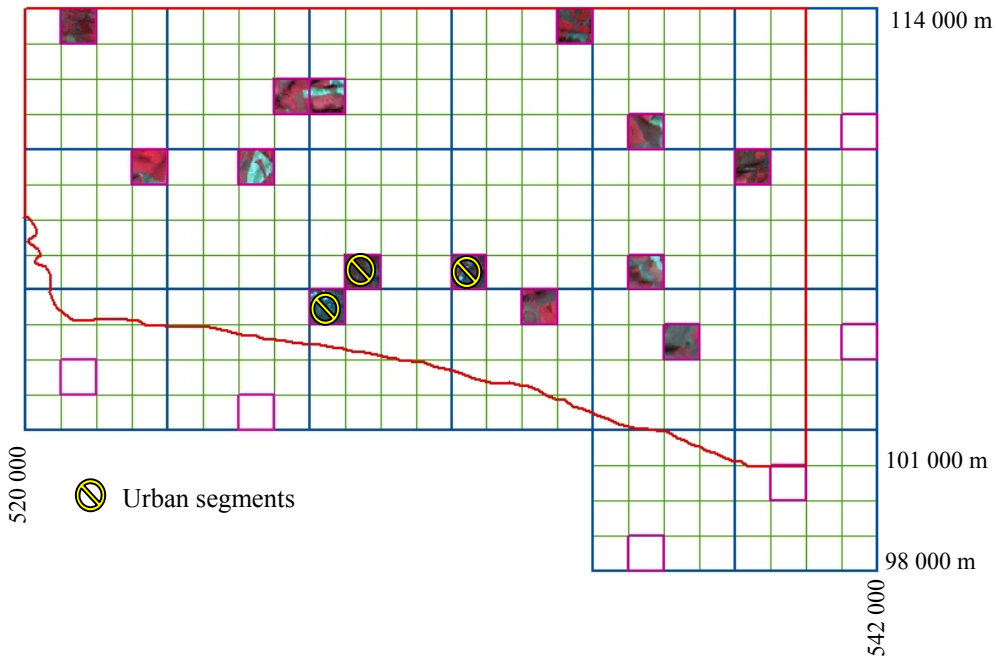

Figure 4.4: Layout of ground sample segments in the study area

4.6.4 Field Survey Essentials

Image segments and map overlays

Eleven image segments of 1 km by 1 km each of the study area were extracted from a false colour composite (FCC) image of 26 October using boundary coordinates of sample segments. An image segment normally consisted of 50 pixels x 50 pixels of 20 m resolution. A buffer boundary of 200 m around an image segment was kept to make recognition of large and continuous ground features easily and comparable with adjoining image segments. All the image segments were produced at 1:10 000 scale for ground data collection. An image segment with the buffer is shown in Figure 4.5, left.

In addition to the image segment of each survey site, a transparent map overlay of each sample segment (Figure 4.5, right) was produced at 1:10 000 scale from the Ordnance Survey maps available in the University Map Archive. The map overlay was used as an aid to compare land use and land cover information in the field with an image segment. Two map overlays were produced from 1:10 000 scale topographical maps, published in 1991 and remaining nine were produced from 1:25 000 scale Pathfinder second series maps, published in 1991, by the enlargement of the scale because 1:10 000 scale maps were not available for all the segments in the Map Archive.

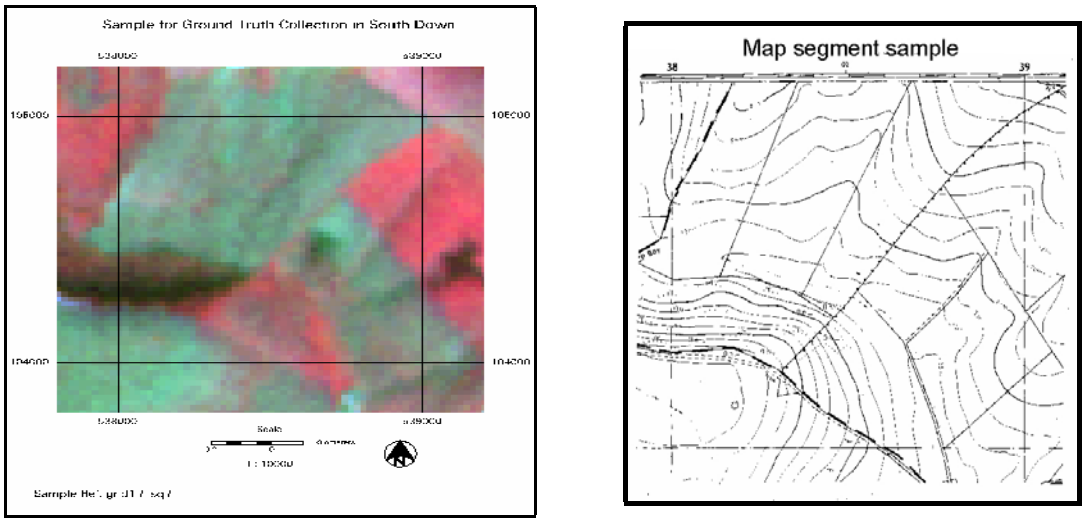

Figure 4.5: Image segment (left) and map segment (right) produced for the segment no. 11 at 1:10 000 scale

Field documentation and maps

A field survey form was worked out and used to record field data corresponding to field parcels on an image segment. A transparent sheet was overlaid on a map overlay and an image segment to draw field parcel boundaries by a permanent marker pen and record the land use and land cover of the parcels with all other details in a survey form. An appropriate class definition of land use and land cover under a classification scheme was also required during the field survey.

Maps and GPS instrument for navigation

The Ordnance Survey Pathfinder maps at 1:25 000 scale and a Landranger second series map at 1:50 000 scale along with a Garmin GPS-12 handset were used for navigating and locating ground sample segments in the study area. The handset was also used for locating real time position within and outside a segment.

4.6.5 Field Survey

The field survey was carried out by visiting each sample segment to produce an accurate spatial map of land use and land cover information of all the field parcels existed within a segment. The field work was conducted during April - July 2003 to make a full use of summer weather. In the field survey, individual parcels of each land use and land cover in each sample segment were identified and drawn on a transparent overlay sheet from a 1:10 000 scale image segment with the aid of a 1:10 000 scale map overlay.

A Garmin GPS-12 Personal Navigator handset was used for navigation to locate ground segments in the study area. The Pathfinder and Landranger series maps were also used for route planning and for quick access to sample segments. The topographical maps at 1:10 000 scale were used to locate field boundary in a segment. A survey form of each segment was completed (Appendix C-9) corresponding to a ground segment and a map overlay. All efforts were made to record the detailed information of field parcels at the time of survey to enable to make an appropriate judgment for possible land use and land cover at the time of a storm event.

4.6.6 Problems Experienced in the Field Survey

A number of problems associated with the field survey were experienced in the Eastern South Downs. Problems, which are important from survey accuracy point of view, are as follows:

- Drawing of small and irregular shaped field parcels on a transparent overlay was time consuming and less accurate in spatial extent.
- Many new features were found in the segments due to development taken place and were not seen on the map overlays produced from the old topographical and Pathfinder maps.
- Some new access paths to two segments were made, but they were not available on the maps, which led to confusion and it took a long time to access the segments through a long walk.
- Location coordinates of a point displayed in the Garmin GPS-12 Personal Navigator handset were not accurate enough to locate field/parcel boundary exactly and sometimes, the handset was not able to lock with the GPS satellite network.
- A segment could not be accessed as there was no public footpath or bridleway. Access through a private path was declined on request, so field survey was completed from a distance which made some field work less accurate.
- A few fields in two segments were fenced with 'live electric fences' and were out of bounds, so the field survey was completed from a distance.
- During a segment survey, I was surrounded by a cattle herd. Thank God, they were friendly.

4.7 Processing of Ground Data

4.7.1 Digitisation of Ground Segments

Digitisation can be accomplished either in on-screen mode or table mode (Cohen, 1995) and the latter is more accurate than the former. With the development of an optical intelligence mouse and improved GIS software, on-screen digitisation is now

widely accepted within GIS community. A transparent overlay with drawn field parcels of each surveyed segment was scanned at an appropriate resolution using a UMAX's Mirage II series flatbed desktop scanner. It was then georeferenced to the British National Grid projection using a first order polynomial transformation with four corners as control points in ArcGIS. The field parcels were subsequently digitised (Figure 4.6) in on-screen mode in ArcGIS and their associated attributes were entered. The perimeter and area of each parcel polygon in a segment were calculated. Similarly, ten other overlays were scanned, georeferenced and digitised and their attributes were entered. Care was taken to keep the error at the minimum level possible during scanning, georeferencing and digitisation. The average error of digitisation of all the segments was found to be 0.8 pixel. The RMS error of digitisation of each segment is given in Appendix C-10.

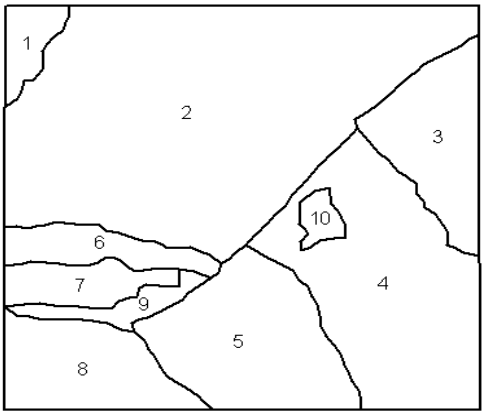

Figure 4.6: Digitised parcels of the segment no.11 at a 1:10 000 scale

(The number in parcels refers to parcel serial number used in the survey form given in Appendix C-9)

4.7.2 Creation of a Segment Database

All the digitised segments and their attribute database were merged to create a single vector mosaic of all segments (Figure 4.7). The vector mosaic was linked to an image mosaic for collection of training sites and accuracy assessment of supervised classification.

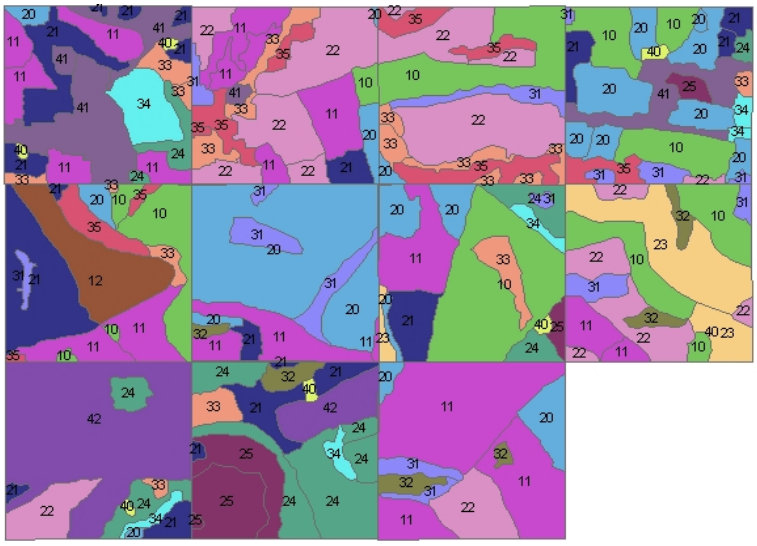

Figure 4.7: A GIS database of field parcels from all the ground segments

(The number in the parcels refers to level 2 classes in the classification scheme Table 4.2)

4.7.3 Direct Area Expansion and Results

Area estimation by direct expansion approach is a method of quantifying proportions of land use and land cover classes in a study area through a statistically sound sampling strategy. The estimates were aimed to provide unbiased class proportions, not area coverage. However, these proportions provided a priori weightings which were later used in supervised classification (ERDAS, 2002). The classes used in ground surveys for grassland, woodland and built-up land were merged to make them compatible with the classes extracted from the image. The hill grazing, semi-improved and improved grassland; open and dense woodland and a single built-up class were finally created and are given in Appendix C-11. Random selection of 1 km by 1 km sample segments provided unbiased proportions of the distribution of land use and land cover in each segment. Hence, the results of direct expansion represented reasonable proportions of each land use and cover class in the Eastern South Downs and are given in Table 4.6. The accuracy of each class estimate at 95 per cent confidence interval was calculated while ignoring the correction factor (Appendix C-12).

The theory of direct expansion estimates is given in the literature by Taylor et al (1996). The estimate of a proportion of area covered by the class c and its variance are given by:

$$\bar{y}_c = \frac{1}{n}\sum_{i=1}^{n} y_i \quad \text{and} \qquad \ldots \quad \text{Eq. 4.1}$$

$$\mathrm{Var}(\bar{y}_c) = \left(1 - \frac{n}{N}\right)\frac{1}{n(n-1)}\sum_{i=1}^{n}(y_i - \bar{y}_c)^2 \qquad \ldots \quad \text{Eq. 4.2}$$

where y_i is the proportion of segment i covered by the class c, N is the number of segments in a study area and n is the number of segments selected for sampling.

When a sample fraction (n/N) is less than 5 per cent, the correction factor, (1-(n/N)), for a finite population is omitted from Equation 4.3 (Cochran, 1977).

The estimate of class estimates and its variance are expressed as:

$$\hat{Z}_c = D * \bar{y}_c \qquad \text{and} \qquad \ldots \quad \text{Eq. 4.3}$$

$$\mathrm{Var}(\hat{Z}_c) = D^2 * \mathrm{Var}(\bar{y}_c) \qquad \ldots \quad \text{Eq. 4.4}$$

where D is the area of study.

The accuracy of a class estimate (Accuracy) at 95 per cent confidence interval is calculated by an equation:

$$\text{Accuracy} = \hat{Z}_c \pm 1.96 * \sqrt{\mathrm{Var}(\hat{Z}_c)} \qquad \ldots \quad \text{Eq. 4.5}$$

Table 4.6: Estimates of class proportions from the ground survey in all the segments and the study area

Segment No	Arable 10	Arable 11	Arable 12	Rough grazing	Improved grass	Semi-improved grass	Open woodland	Dense woodland	Built-up land
1.	0.0000	0.2235	0.0000	0.0000	0.0571	0.2186	0.0581	0.1120	0.3307
2.	0.0261	0.2574	0.0000	0.4337	0.0000	0.0763	0.1083	0.0854	0.0127
3.	0.2568	0.0000	0.0000	0.4200	0.0000	0.0136	0.1574	0.1522	0.0000
4.	0.2600	0.0000	0.0000	0.0094	0.0399	0.3940	0.0608	0.0733	0.1626
5.	0.1923	0.1659	0.2301	0.0000	0.0000	0.2965	0.0360	0.0791	0.0000
6.	0.0000	0.1619	0.0000	0.0000	0.0000	0.7225	0.1043	0.0112	0.0000
7.	0.4345	0.1465	0.0000	0.0208	0.1209	0.1885	0.0622	0.0203	0.0063
8.	0.2512	0.0899	0.0000	0.5497	0.0000	0.0000	0.0585	0.0462	0.0045
9.	0.0000	0.0000	0.0000	0.0971	0.0902	0.0505	0.0095	0.0191	0.7337
10.	0.0000	0.0000	0.0000	0.0000	0.6420	0.1235	0.0458	0.0580	0.1307
11.	0.0000	0.6868	0.0000	0.1203	0.0000	0.0978	0.0535	0.0417	0.0000
Mean	0.1292	0.1575	0.0209	0.1501	0.0864	0.1983	0.0686	0.0635	0.1256
Sum		Arable:	0.3075	Grassland :	0.4348	Woodland :	0.1321	Built-up land :	0.1256

4.8 Multispectral Image Classification

4.8.1 Overview

Multispectral classification is the procedure of sorting all pixels in an image into a finite number of land use and land cover classes or themes based on digital numbers (DNs), which are measures of the surface reflectance. A classification technique uses the spectral pattern present within data as a basis for an automated classification. Proposed classes of a classification scheme rarely form distinct groups of clusters.

4.8.2 Classification Methodology

Two main procedures of digital image classification are widely used viz., unsupervised and supervised classification (Lillesand and Kiefer, 1999). There is no single right approach to attain optimal results of a classification. Therefore, a hybrid classification, a combination of both unsupervised and supervised classification (Figure 4.8) was used in this study.

4.8.3 Unsupervised Classification

Unsupervised classification is the clustering procedure of defining, identifying, labelling and mapping of natural groupings or clusters within multispectral data without a prior knowledge of existing classes (Campbell, 2002). Clustering procedures employ K-means clustering viz. an ISODATA (Iterative self organising data analysis) technique, (Lillesand et al, 2003) or RGB clustering (ERDAS, 2002) for unsupervised classification. Advantages, disadvantages and limitations of unsupervised clustering are discussed in detail in the literature (Campbell, 2002; ERDAS, 2002; Richards and Jia 1999; Mather, 1999).

Unsupervised classification methodology used for this study was based on a hybrid and hierarchical classification approach (Figure 4.8). The number of classes in a classification was based on a subjective judgement.

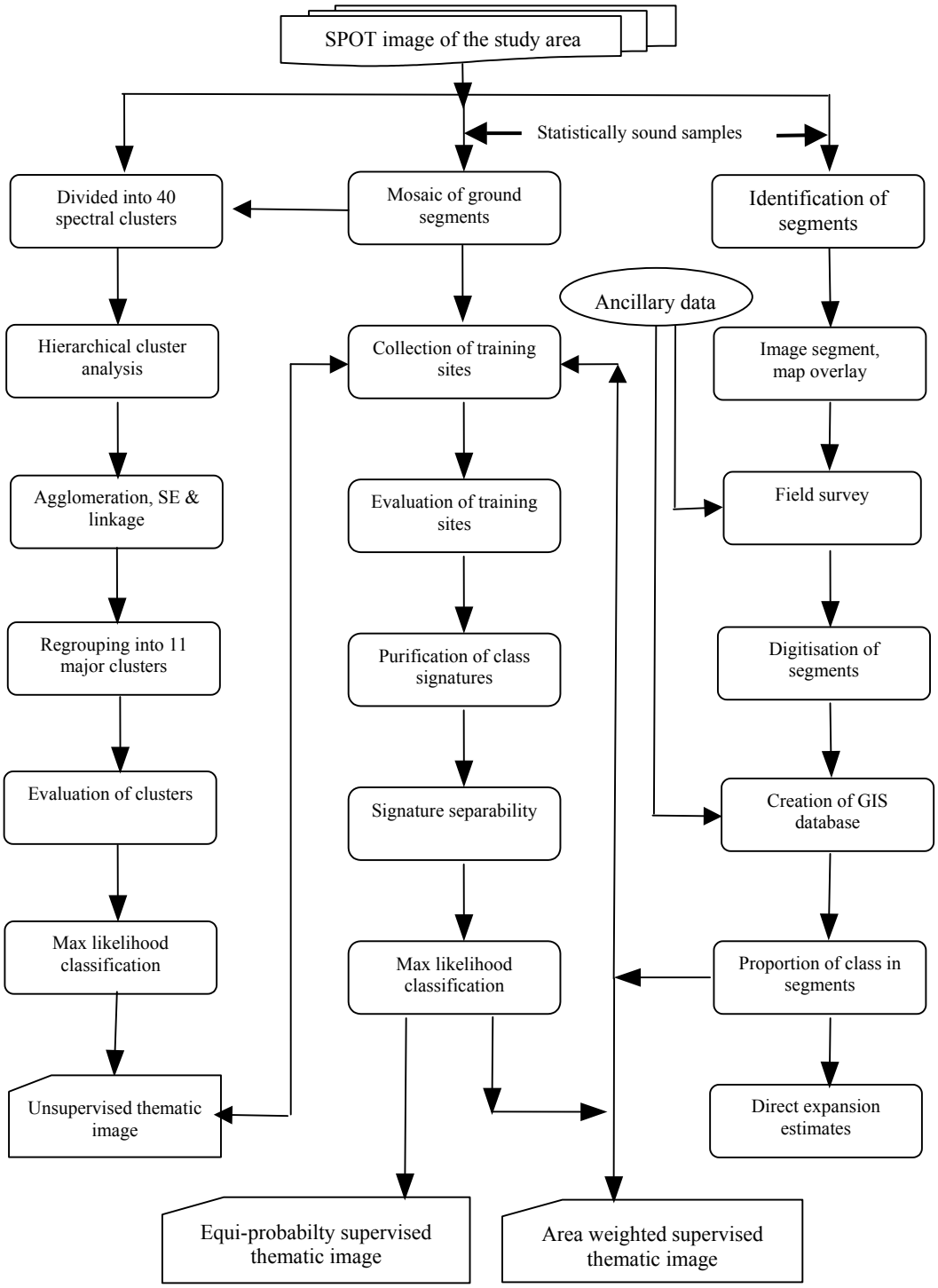

Figure 4.8: Flow diagram of a hybrid image classification

The ISODATA method, based on a minimum spectral distance to form clusters, was used to sort 26 October mosaic image pixels into 40 spectral clusters. The means and standard deviations of forty clusters were extracted for a hierarchical clustering analysis (Appendix C-13).

4.8.4 Agglomerative Hierarchical Cluster Analysis

Hierarchical clustering methods are employed to obtain a greater insight into the overall structure of clusters or groups of clusters in multispectral space. There are two approaches of performing a hierarchical analysis; agglomeratively or divisively. The agglomerative method with Euclidean distance and the Ward's method of cluster linkage is a preferred method. It begins with each cluster, joining two most similar, and then repeatedly joining new clusters together until all clusters are joined in a tree structure. The Ward's method is based on minimizing the within-cluster sum of squares. The between-groups method is also similar to the Ward's method.

In the past, a hierarchical clustering analysis was usually carried out outside an image processing through a statistical package. It has recently been introduced in the ERDAS Imagine 8.6 through a 'class grouping tool' and is performed within an image processing system. The means and standard deviations of 40 clusters were used for the cluster analysis. Two hierarchical cluster analyses, first with a squared euclidean distance and the Ward's method of linkage and between linkage; and second with a euclidean distance and average linkage were carried out to regroup the 40 clusters into 11 groups using the class grouping tool (Appendix C-14). A dendogram was generated for describing each linkage between clusters. The sub clusters of major 11 group clusters were merged and finally major group clusters were generated. The ISODATA based unsupervised classification was again used to classify the image into 11 clusters on the basis of major group cluster properties (Figure 4.9). Cluster regrouping using between linkage and squared euclidean distance was found to be the most suitable for this study.

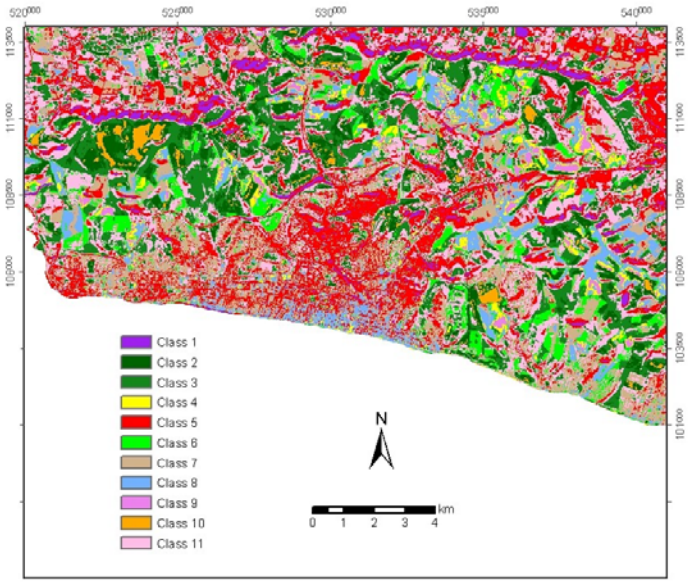

Figure 4.9: Unsupervised classification of the image with 11 classes

4.8.5 Mosaicking of Segment Imagettes

A mosaic of eleven ground segments from 26 October image (Figure 4.10) was created by extracting survey segments from the study area image using a FILQUILT program written in Turbo C++ (Thomas, 1984). The mosaic was further used for unsupervised classification, agglomerative hierarchical cluster analysis, training of a classifier for supervised classification and also in assessing the accuracy of classification (Taylor and Eva, 1992).

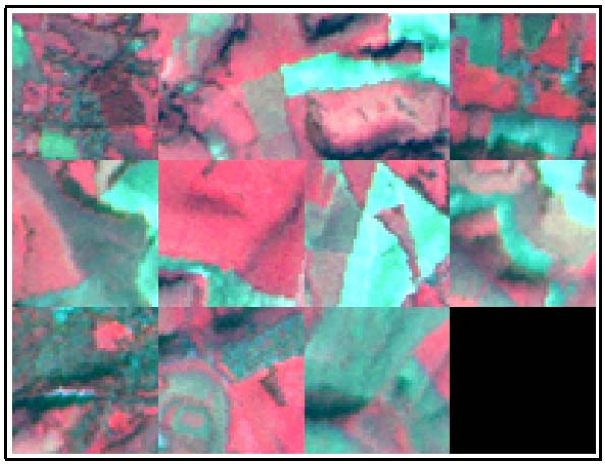

Figure 4.10: Image mosaic of 11 ground segments selected for field survey

The FILQUILT, a DOS program, requires two inputs and an output information viz., an input image file in the LAN format, an ASCII coordinate file of ground segments with header information and an output 'quilt' file in the LAN format to create a mosaic image of segments from an image file. The FILQUILT program creates a mosaic image using map co-ordinates given in the coordinate file.

4.8.6 Spectral Signatures for Supervised Classification

Supervised classification is the process of using samples of known identity to classify pixels of unknown identity in an image (Campbell, 2002). Advantages, disadvantages and limitations of supervised classification are found in detail in the literature (Campbell, 2002; ERDAS, 2002; Richards and Jia 1999; Mather, 1999).

Spectral signatures of classes can be obtained either from analyst chosen or from geostatistically chosen training sets (Chen and Stow, 2002; Shine and Wakefield, 1999) to collect representative training data from the ground segments. The former was used for this study as the time of field survey and image acquisition was different. The number of training sites chosen was proportional to the class proportion derived from the ground sample survey. Training parcels were randomly selected from the image mosaic of 26 October. It was carried out carefully to choose the spatially independent training datasets from almost all of the ground sample segments for all eleven classes. A total of 198 training sites for eleven classes was selected and used for the supervised classification (Table 4.7). Out of eleven classes, five arable, three grassland and two woodland classes and a single built-up class were finally used for collection of training sites for classification. The mean and standard deviation values of pixels for each band for all the classes are presented in Table 4.8.

Table 4.7: Training dataset of 11 classes for supervised classification

Class	Training sites	No. of pixels
Arable 2	12	106
Arable 3	13	117
Arable 4	23	207
Arable 5	16	144
Arable fallow	9	81
Hill grassland	27	495
Improved grassland	34	306
Semi-improved grassland	30	270
Open woodland	18	90
Dense woodland	16	80
Built-up land		65
Total :	198	1961

Table 4.8: Statistical properties of signatures of 11 classes

Class	Name of class	Band 1		Band 2		Band 3	
		Mean	Std Dev	Mean	Std Dev	Mean	Std Dev
1	Arable 2	73.09	4.30	50.49	3.50	64.28	3.96
2	Arable 3	57.61	3.20	36.77	2.83	47.30	4.41
3	Arable 4	51.77	1.83	29.66	2.03	54.37	4.85
4	Arable 5	49.19	1.67	28.29	1.92	41.23	3.70
5	Arable fallow/set-aside	44.07	1.74	22.74	1.19	48.52	5.58
6	Hill grassland	45.13	2.98	22.21	2.64	66.46	6.32
7	Improved grassland	47.35	2.01	21.94	1.96	97.13	6.85
8	Semi-improved grassland	48.06	3.59	24.52	3.98	78.75	4.95
9	Open woodland and scrub	38.90	1.93	19.29	1.70	40.14	6.34
10	Dense woodland and scrub	35.46	1.47	16.60	1.62	23.41	3.80
11	Built-up land	51.49	3.33	27.63	2.19	47.46	4.72

(Arable 2 and Arable 3 are basically parts of bare fields and Arable 3 and Arable 4 are parts of harvested fields)

4.8.7 Spectral Homogeneity and Separability

The spectral uniformity of training datasets was checked by the unimodal frequency distribution in each spectral band. Bimodal signatures should either be discarded or further purified using the ISODATA clustering. The spectral homogeneity

was also verified by overlaying signatures on unsupervised classified map. This helped in minimising spectral confusion emanating from mixed pixels in a training dataset. All pure signatures were merged together to produce a class signature for classification.

The class signatures were evaluated for spectral separability by two methods such as scatterplot and divergence distance. Scatterplots of signatures were viewed in two dimensional feature spaces by displaying two bands at a time using ellipses. The overlapping of signature ellipses was checked to minimise the signature confusion. Signature divergence, a statistical measure in multispectral space, was calculated to analyse all the signatures for class separability. The transformed divergence (TD) and the Jeffries Matusita (JM) distance methods were used (ERDAS, 2002; Swain and Davis, 1978). The transformed divergence has a range from 0 to 2000 while the Jeffries Matusita distance has a range from 0 to 1414. The upper limit reflects the total separability and lower limit reflects total confusion in both methods. The TD and JM distances were calculated for 11 class signatures. The average and minimum separability of all the classes by both methods is given in Table 4.9. The each class wise separability for both methods is given in Appendix C-15. Spectral confusion between bare soil class and urban class was strongly evident. The polygons of spectrally confused classes were separated and purified. Therefore, in this way, all the signature files were purified and then used for classification.

Table 4.9: Signature separability of 11 classes

Parameter	Transformed Divergence distance	Jefferies-Matusita distance
Average separability	1893.03	1358.94
Minimum separability	1082.75	1082.75

4.8.8 Classification Decision Rule and Training

A variety of parametric decision rules are used in digital image processing (Campbell, 2002; ERDAS, 2002). The decision boundary for each class was generated during decision rule training. The Gaussian and Bayesian maximum likelihood decision rules were used initially to classify the mosaic image and then the study area image. The Gaussian decision rule is based on an assumption of equal probabilities of all classes

while the Bayesian decision rule is based on priori probability weight factors of classes. Both rules compare the variance and covariance of training class signatures with a candidate pixel to assign a particular class according to a decision rule. The assumption of normality in training class signatures is adhered in the maximum likelihood classifier (Lillesand et al, 2003; ERDAS, 2002).

4.8.9 Classification Results

The Gaussian classifier with equal probabilities and the Bayesian classifier with area weight probabilities, derived from direct area expansion, were used to produce equal weighted and area weighted classified images. The mosaic image of 26 October 2000 was initially classified for 11 classes by the Gaussian classifier (Figure 4.11). In case of the Bayesian classifier, direct area estimates were available for nine classes, not for all the eleven classes. Arable 2 and Arable 3 classes were the parts of the bare soil fields while Arable 4 and Arable 5 classes were parts of the harvested field. Hence, direct area estimates of both bare soil and harvested field were split up equally and shared by two clusters of each class. The image mosaic was classified for 11 classes with area weight probabilities (Figure 4.12) and both results are compared in Table 4.10. Both classified image were verified with the original image. Both classifications were found to be equally acceptable and then, the study area image was classified with area weighted training data set. Figure 4.13 shows the area weighted probability classified image with 11 classes.

Table 4.10: Comparison of area of each class in both equal and area weight classified mosaics

Class	Area under each class (per cent)	
	Equal weight classified image	Area weight classified image
Arable 2	4.33	4.31
Arable 3	4.19	4.09
Arable 4	8.61	7.20
Arable 5	5.29	4.97
Arable set aside	9.10	5.17
Hill grassland	20.47	22.60
Improved grassland	12.34	10.89
Semi-improved grassland	18.37	20.83
Open woodland and scrub	11.15	11.48
Dense woodland and scrub	1.89	1.87
Built-up land	4.27	6.59

4.8.10 NDVI-based Image Classification

Normalised difference vegetation index (NDVI) is the most commonly used vegetation index, which normalises external effects of sun angle and viewing angle, atmospheric effects, and internal effects of shadowing, soil and amount of plant material. It can be directly related to the biophysical parameters, such as percent green vegetation cover, leaf area index, vegetation density, amount of green leaf biomass, and fraction of absorbed photosynthetically active radiation (fAPAR). Its value ranges from -1 to 1 with:

- negative values for clouds, snow, water, bare soil, rocks and shadows,
- near zero values for rock, dry soil, senesced vegetation and other non-vegetated surfaces, and
- positive values for vegetated surfaces.

NDVI of an image is computed on a pixel by pixel basis using an expression:

$$NDVI = (NIR - Red)/ (NIR + Red) \quad \text{…Eq. 4.6}$$

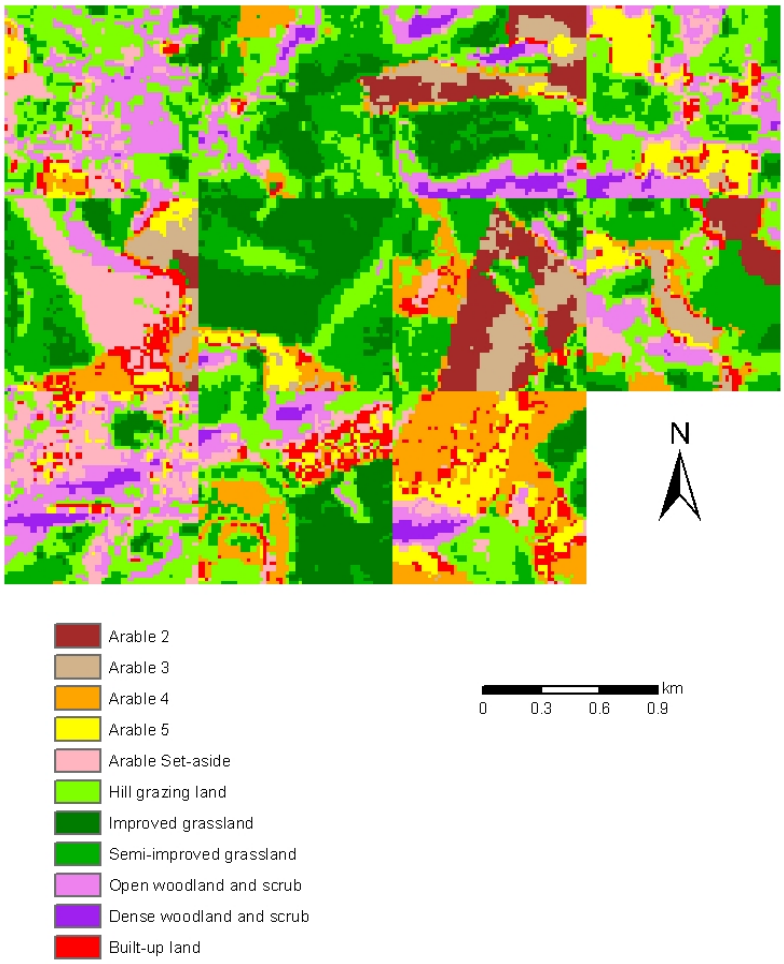

Figure 4.11: Equal weighted supervised classification of the image mosaic with 11 classes

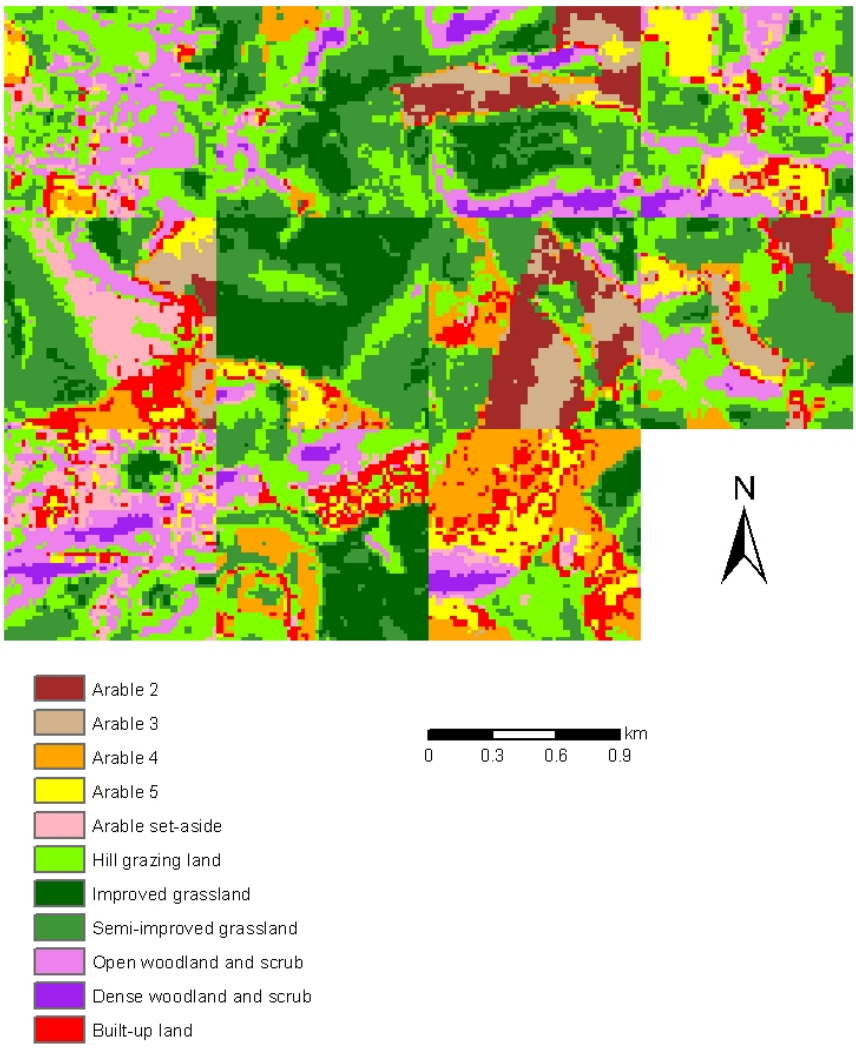

Figure 4.12: Area weight supervised classification of the image mosaic with 11 classes

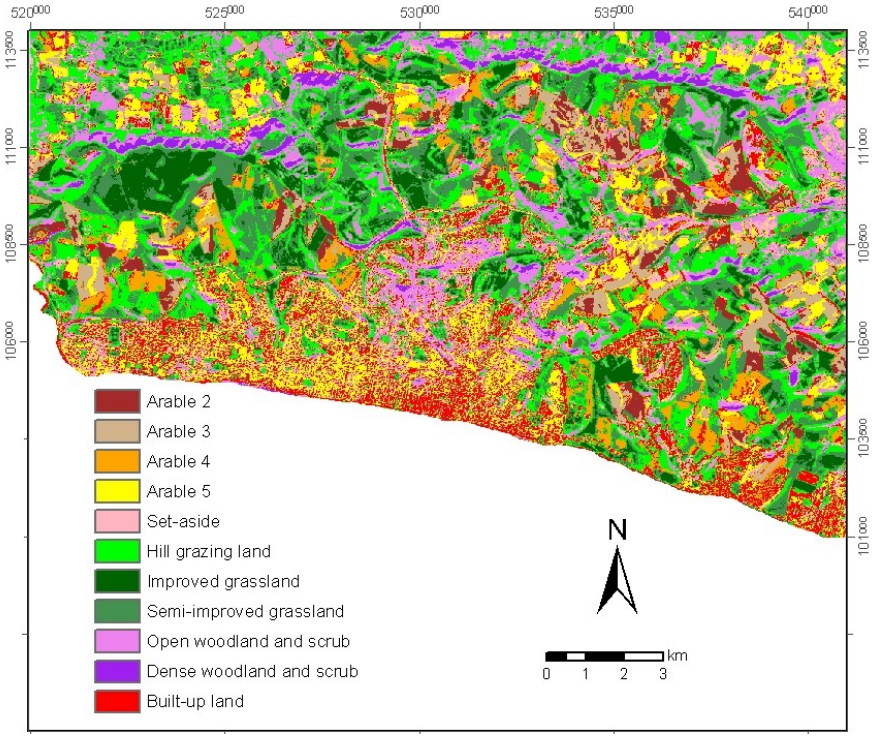

Figure 4.13: Area weighted supervised classification of the study area with 11 classes

The NDVI was used to infer information on major classes based green ground cover to differentiate the major land use and land cover and to help to improve the accuracy of supervised classification. Another aspect was to establish a direct relationship with NDVI to extract the percent ground cover and leaf area index required for modelling, which was also explored in this study. The NDVI derived land use and land cover map could also be used as alternative to supervised classification based land use and land cover map for quick assessment of the classes.

Raw DN-based NDVI classification

NDVI not only varies with the spectral and spatial characteristics of a sensor but also with the radiometric processing applied to an image data (Guyot and Gu, 1994). NDVI can be computed from digital signal levels, top of atmospheric radiance, top of atmospheric reflectance or atmospherically corrected surface reflectance. NDVI also

depends on image product characteristics such as numerical representation in binary form for data storage and display purposes (Teillet et al, 1997)

The NDVI image was computed from the digital numbers of the image mosaic of 26 October. It can be seen from the statistical properties given in Table 4.11 that NDVI values range from -0.081 to 0.727 with a mean of 0.384.

Table 4.11: Statistical properties of NDVI image

Image	Minimum	Maximum	Mean	SD	Median	Mode
26 Oct	-0.081	0.727	0.384	0.192	0.417	-0.012

Both unsupervised classification procedure and density slicing were applied to classify the NDVI image to six clusters or classes. The density slicing was based on the histogram analysis of the image while the unsupervised clustering was based on the ISODATA procedure (Figure 4.14). It was noticed that density slicing has a better control in classification than unsupervised procedure. The range of NDVI values for each class for unsupervised clustering and density slicing is given in Table 4.12. Both procedures show that the range of each class is not same in both classifications.

Table 4.12: Class statistics of unsupervised and density sliced clusters of NDVI image

Class	Name	Unsupervised clusters	Density sliced clusters
Class 1	Bare soil	-0.081- 0.200	≤ 0.0
Class 2	Harvested field	0.204 - 0.318	0 - 0.20
Class 3	Set-aside	0.319 - 0.413	0.20 - 0.33
Class 4	Poor vegetation cover	0.413 - 0.496	0.33 - 0.50
Class 5	Medium vegetation cover	0.500 - 0.583	0.50 - 0.60
Class 6	Good vegetation cover	0.584 - 0.727	> 0.60

Calibration of the SPOT image

NDVI values vary significantly and are functions of sensor calibration, atmospheric conditions, directional surface reflectance effects and terrain relief. The SPOT image of 26 October was calibrated to the reflectance at top of atmosphere (ρ_0) (Appendix C-16) using an equation (Guyot, and Gu, 1994; Henry, and Dinguirard, 1997).

$$\rho_0 = \frac{\pi * DN_k * d^2}{A_k * E_{sun} * Cos(SZ)} \quad \text{... Eq. 4.7}$$

where ρ_0 is the exoatmospheric reflectance at the satellite (0-1), A_k is the absolute calibration gain in $W^{-1}m^2$ sr μm, DN_k is the digital number for the band k, d^2 is the square of the Earth-Sun distance in astronomical units (~149.6 x 10^6 km), E_{sun} is the mean solar exoatmospheric irradiance in W m^{-2} μm^{-1}, and SZ is the sun zenith angle in radians at time of scene acquisition.

Atmospherically corrected surface reflectance could not be computed due to non availability of enough weather data at the time of image acquisition to model the atmospheric condition. Moreover, it was beyond the scope of this study.

NDVI classification based on apparent reflectance

26 October image was calibrated to the apparent reflectance and the NDVI image was then computed. The statistical properties of the apparent reflectance and NDVI are given in Table 4.13 and Table 4.14. The mean of DN-based NDVI image is slightly lower than the mean from apparent reflectance. This did not result in significance difference in classification whether used DNs or apparent reflectance values.

Table 4.13: Statistical properties of apparent reflectance of 26 October image

	Reflectance at top of atmosphere		
Band	XS1 (G)	XS2(R)	XS3 (IR)
Minimum	0.095	0.056	0.060
Maximum	0.262	0.270	0.561
Mean	0.141	0.107	0.294
Standard deviation	0.022	0.030	0.085
Median	0.139	0.098	0.283
Mode	0.136	0.094	0.234

Table 4.14: Statistical properties of apparent NDVI image

Image	Minimum	Maximum	Mean	SD	Median	Mode
26 Oct	-0.042	0.745	0.449	0.156	0.471	0.366

Both unsupervised classification procedure and density slicing were carried out to classify the apparent NDVI image to six classes. Unsupervised class and density slicing statistics are given in Table 4.15.

Table 4.15: Statistical properties of unsupervised classes of apparent NDVI image

Class	Unsupervised clusters	Density sliced clusters
Class 1	0.042 - 0.234	≤ 0.0
Class 2	0.237- 0.352	0 - 0.20
Class 3	0.352 - 0.444	0.20 - 0.33
Class 4	0.445 - 0.525	0.33 - 0.50
Class 5	0.529 - 0.608	0.50 - 0.60
Class 6	0.608 - 0.744	> 0.60

4.8.11 Band Ratio-based Image Classification

A common problem with remotely sensed images is the effect of varying illumination caused by topography. Relief causes some slopes to be illuminated more than others, thus surfaces with homogeneous reflectance properties show varying digital numbers across a scene. A band ratio image can be obtained by ratios of band 1 by band 2, band 2 by band 3 and band 1 by band 3 to minimise the topographic contribution in the image.

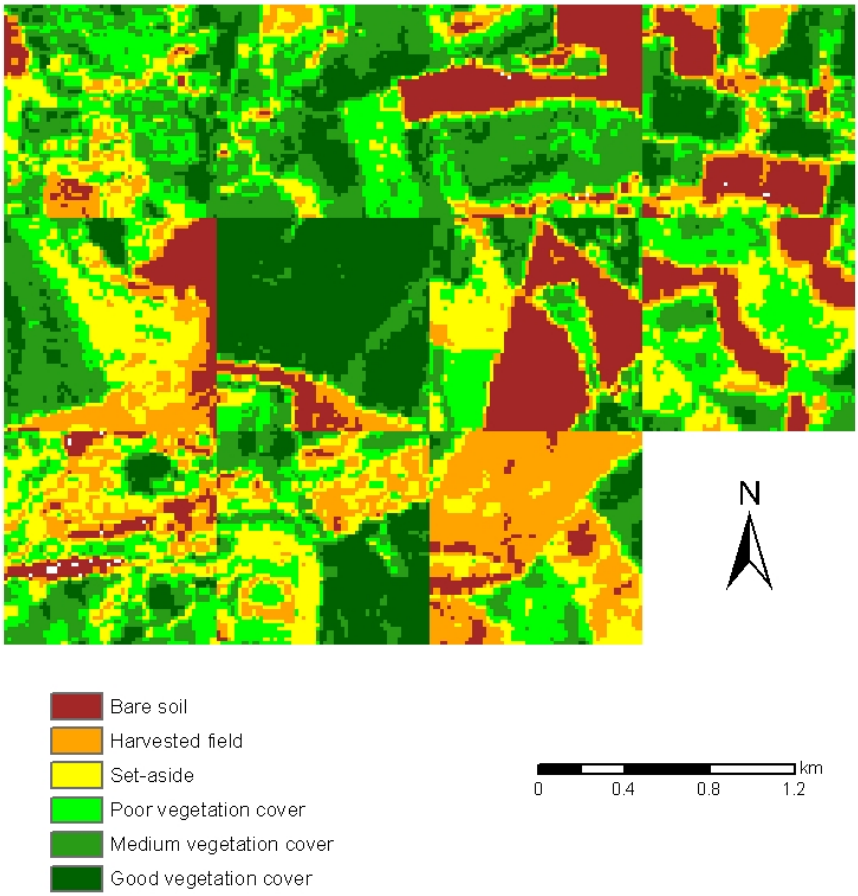

Figure 4.14: Unsupervised classification of the NDVI image with six classes

A ratio image (B1/B2; B2/B3 and B1/B3) of the image mosaic was computed to reduce the illumination effect by topography. The image was stretched to 8 bits and then was classified to six classes based on an unsupervised clustering (Figure 4.15). The area under each class derived from the band ratio image is compared with six classes derived from unsupervised classification of DN-based NDVI and apparent NDVI images (Table 4.16). It was found that first four classes are over predicted in ratio images as compared to both other images. There was not significance difference in area of each class derived from DN-based and apparent NDVI images. In the DN-based image, 20 pixels were turned into no data values during computing NDVI image.

Table 4.16: Area of each class derived from unsupervised classification of DN-based NDVI, apparent NDVI and band ratio images

Class	Area under each class (per cent)		
	DN-based NDVI	Apparent NDVI	Ratio image
Unclassified	0.07	0.00	0.00
Bare soil	13.13	12.71	15.99
Harvested field	13.80	14.14	20.07
Set-aside	16.70	16.82	19.99
Poor vegetation cover	19.36	19.39	15.89
Medium vegetation cover	20.21	20.05	9.90
Good vegetation cover	16.73	16.89	18.15

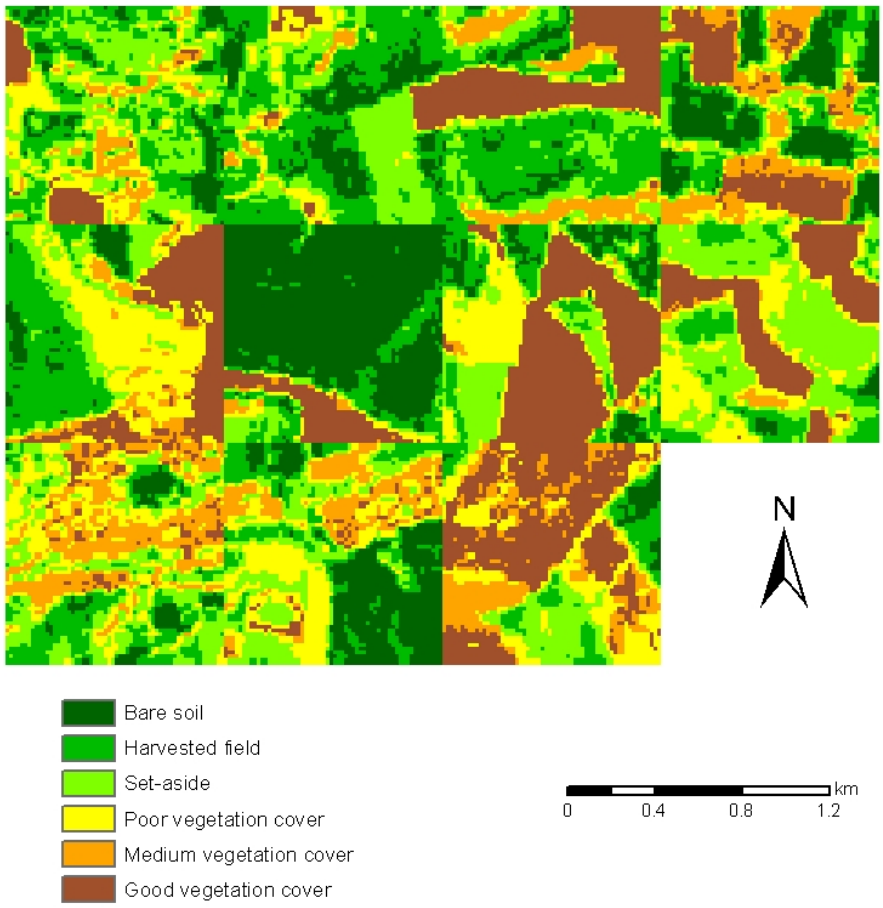

Figure 4.15: Unsupervised classified band ratio image of six classes

4.9 Assessment of Classification Accuracy

In the context of thematic classifications of remotely sensed data, accuracy refers to the degree of correctness of a classification in comparison to the ground data (Foody, 2002; Campbell, 2002). Accuracy assessment measures are widely used to quantify the error in classifications. Accuracy assessment in land use and vegetation mapping studies is reviewed in the literature by Foody (2002) and Congalton (1991). More than 250 reference pixels on a classified image are required to be randomly selected to estimate the mean accuracy of a class within plus or minus five per cent (Congalton, 1991).

4.9.1 Confusion Matrix

A confusion matrix (Congalton, 1991) is a basis to describe both classification accuracy and errors and is used to derive accuracy assessment statistics. It also helps in refining classification in case of an interclass confusion. Accuracy measures such as errors of omission and commission, user and producer's accuracies and the Kappa coefficient (Congalton and Green, 1999) are derived from the confusion matrix to assess the overall accuracy of classification. Confusion matrix and accuracy measures of 26 October image were calculated. The confusion matrix in Table 4.17 shows that the overall classification accuracy, producer's accuracy and user's accuracy are 89.9, 60-100 and 59-100 per cent respectively. The higher accuracy was achieved in the bare soil class and least accuracy in the built-up area.

4.9.2 Kappa Statistics

Kappa statistics is a standard measure of classification accuracy. It compensates for a chance agreement between the classified data and reference data (Congalton et al, 1983; Rosenfield and Fitzpatrick-Lins, 1986; Hudson and Ramm, 1987; Congalton, 1991) and is based on the maximum likelihood theory. Landis and Koch (1987) have defined the agreement criteria for Kappa coefficient to assess a classification. The agreement is poor when KHAT is less than 0.4, good when KHAT is in between 0.4 and 0.75 and excellent when KHAT is greater than 0.75. The kappa coefficient of agreement

of 26 October scene is found to be 0.88. It can be concluded that there is good agreement between mapped and observed classes. The thematic image represents reliable information on land use and land cover. Therefore, it is suitable for modelling study.

The variance of Kappa statistics and its application for testing of significance difference between two confusion matrices are discussed in the literature (Congalton and Green, 1999; Hudson and Ramm, 1987).

The formulation of Kappa statistics is expressed as:

$$\hat{k} = \frac{N\sum_{i=1}^{r} x_{ii} - \sum_{i=1}^{r} x_{i+} x_{+i}}{N^2 - \sum_{i=1}^{r} x_{i+} x_{+i}} \quad \text{… Eq. 4.8}$$

where + represents the summation of row index.
For a computation purpose, Equation 4.9 is used to calculate the Kappa coefficient, KHAT ($\hat{k}$);

$$\hat{k} = \frac{\theta_1 - \theta_2}{1 - \theta_2} \quad \text{… Eq. 4.9}$$

where θ_1 is the proportion of units which agree, and θ_2 is the proportion of units for expected chance agreement. θ_1 and θ_2 are computed using Equations 4.10 and 4.11:

$$\theta_1 = \frac{\sum_{i=1}^{r} x_{ii}}{N} \quad \text{and} \quad \text{… Eq. 4.10}$$

$$\theta_2 = \frac{\sum_{i=1}^{r} x_{i+} x_{+i}}{N^2} \quad \text{… Eq. 4.11}$$

where x_{ij} is the number of counts in the ij^{th} cell of the confusion matrix, N is the total number of counts in the confusion matrix, x_{i+} is the marginal total of row I and x_{+i} is the marginal total of column i.

Table 4.17: Confusion matrix for 11 class based classification (26 October 2000)

Class	1	2	3	4	5	6	7	8	9	10	11	Total	User's accuracy
1	106											106	100.0
2		114		1							1	116	98.28
3			180	2		4					13	199	90.45
4		2	3	132							9	146	90.41
5			2	1	72	8			5		2	90	80.00
6			1			210		15	3		1	230	91.30
7							292	14				306	95.42
8			2			30	14	241				287	83.97
9					6				78	3		87	89.66
10									4	77		81	95.06
11		1	14	9	3						39	66	59.09
Total	106	117	202	145	81	252	306	270	90	80	65	1714	
Producer's accuracy	100.0	97.44	89.11	91.03	88.89	83.33	95.42	89.26	86.67	96.25	60.00	Overall accuracy	= 89.9
												KHAT	= 0.88

Name of the classes:

1	Arable 2	2	Arable 3
3	Arable 4	4	Arable 5
5	Set aside/fallow	6	Hill grazing grassland
7	Improved grassland	8	Semi-improved grassland
9	Open woodland and scrub	10	Dense woodland and scrub
11	Built-up land		

4.10 Reclassification and Post Processing

Classification error is caused by the interaction of numerous factors including landscape and its illumination characteristics, sensor resolution, spectral overlap, preprocessing, image enhancement and classification procedures (Campbell, 2002). The overall accuracy and Kappa coefficient of agreement of the classification with 11 classes was reasonably good. Therefore, the 11 class area weighted classified image was reclassified into 9 major classes by combining the Arable 2 and Arable 4 into the bare soil and Arable 4 and 5 into the harvested field on the basis of similar characteristics for hydrologic and erosion modelling. The resultant reclassified image is presented in Figure 4.16. The major urban area was not separated digitally. Therefore, it was manually separated and added to the image after classification.

The overall accuracy of reclassified image was recalculated. It was found that the user and producer accuracies range from 52.87 to 97.94 and 67.90 to 97.76 per cent respectively. The overall accuracy and Kappa coefficient of agreement remained the same (Table 4.18). The area estimates by sampling and image classification were compared in Table 4.19. It was found that estimates from both methods were not compared as such because of a large time lag between survey time and acquisition time. There was strong evidence between bare soil and built-up land. Even after reclassification, a few scattered pixel patches different from neighbouring pixels were present in the reclassified image, so a majority filter of 3x3 window was, therefore, applied to minimize noisiness in the thematic image. The disadvantage of filtering was that it increased the minimum mapping unit substantially. The filtering and resampling of 9 class based land use and land cover to five resolution datasets were discussed in Section 6.3.2 to derive input parameters for modelling study.

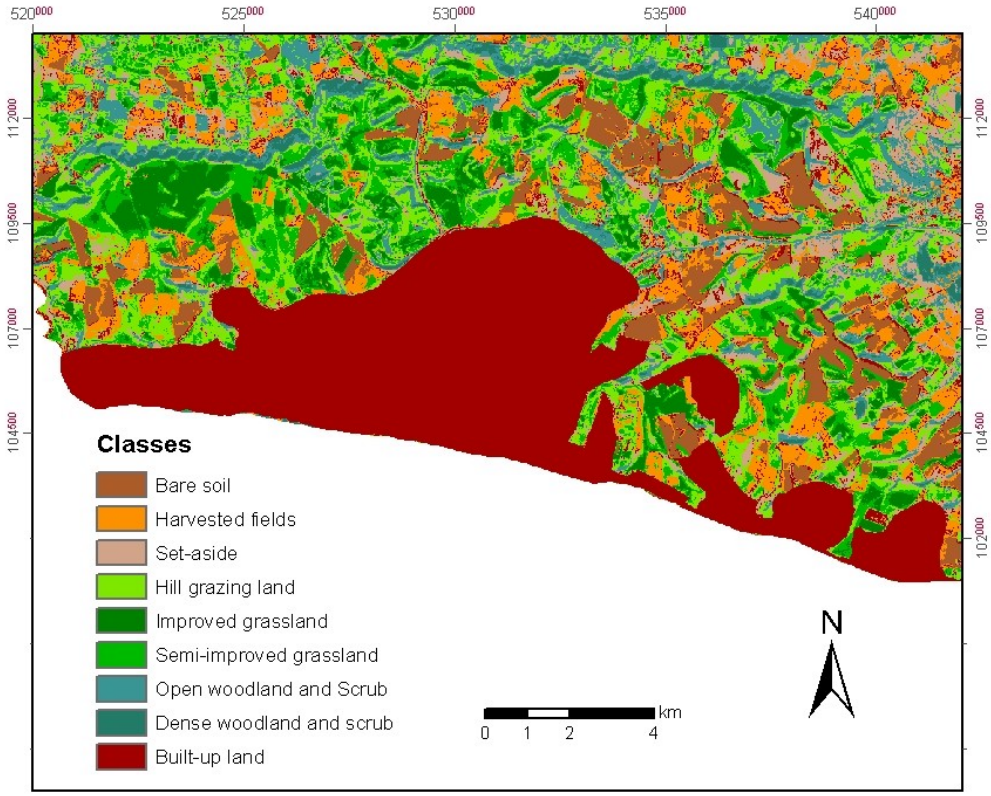

Figure 4.16: Area weighted supervised classified image with 9 classes

Table 4.18: Confusion matrix for the reclassified image with 9 classes

Class	1	2	3	4	5	6	7	8	9	Total	User's accuracy
1	218	3	3						1	225	96.89
2	4	309							16	329	93.92
3			55	1			4		1	61	90.16
4		1	5	217	9		3		1	236	91.95
5		2		34	255	21				312	81.73
6					6	285				291	97.94
7			9				79	3		91	86.81
8							4	77		81	95.06
9	1	31	9						46	87	52.87
Total	223	346	81	252	270	306	90	80	65	1713	
Producer's accuracy	97.76	89.31	67.90	86.11	94.44	93.14	87.78	96.25	70.77	Overall accuracy	= 89.9
										KHAT	= 0.88

Name of Classes:

1 Bare soil
2 Harvested field with stubbles
3 Set aside/ fallow
4 Rough grazing land
5 Semi-improved grassland
6 Improved grassland
7 Open woodland and scrub
8 Dense woodland and scrub, and
9 Built-up land

Table 4.19: Comparison of area estimates by sampling and image classification

Class	Area by direct estimate (ha)	Area by image classification (ha)
For the study area		
Bare soil	2948.1	1736.5
Harvested field with stubbles	3593.4	2530.4
Set aside/ fallow	477.4	1684.2
Rough grazing land	3425.3	2560.4
Semi-improved grassland	4526.6	3819.6
Improved grassland	1971.2	1495.7
Open woodland and scrub	1565.2	2039.6
Dense woodland and scrub	1449.5	495.2
Built-up land	2865.7	6559.6
Sum :	22822.4	22921.1
For segment mosaic only		
Bare soil	142.1	96.1
Harvested field with stubbles	173.2	137.6
Set aside/ fallow	23.0	100.7
Rough grazing land	165.1	231.2
Semi-improved grassland	218.2	201.3
Improved grassland	95.0	135.7
Open woodland and scrub	75.4	122.1
Dense woodland and scrub	69.9	20.8
Built-up land	138.1	54.5
Sum :	1100	1100

4.11 Concluding Remarks

4.11.1 Discussion

Remote sensing approach

The usefulness of remote sensing for land use and land cover mapping using multispectral classification is established and is evident in this study. The hierarchical classification scheme was compatible with the land use map required by LISEM so that it can be directly ingested to a LISEM database using PCRaster for deriving distributed input parameters. Although the SPOT-1 HRV sensor was beyond its life expectancy but it has captured the excellent quality of images, which were comparable with other earth resource satellites. SPOT-1 has three bands only, which was a limitation as compared to other sensors. The remote sensing approach for mapping should not be viewed in terms of absolute quantified value of land use and land cover classes rather than a representative value of classes in the study area.

Delineation of the study area

The study area was delineated from a 1:50 000 scale Landranger map. The water body was intentionally not included in the study area to avoid spectral confusion between sea water, urban area and bare soil during classification

Field documentations and navigation

Essential field survey documents with a well defined classification scheme help to complete the segment survey quickly. With the preparation of a false colour composite image, image segments and map overlays, the interpretation of segment parcels took less time as compared to locating the boundaries of segments using the maps and a GPS. Twelve year old maps led to confusion in a few segments due to either presence or absence of some field features such as boundary hedges, new buildings and roads.

GPS was found to be a useful equipment for successful ground data collection particularly with twelve year old maps. The Garmin GPS-12 Personal Navigator handset without real time code correction was used and thus, resulted in less accurate

coordinates. It was found that accuracy degradation was more than what was reported in the equipment manual (15 m). In a few cases particularly in valleys, the accuracy was further degraded. The real-time code corrected GPS equipment would be ideal for locating ground segment parcels more accurately and quickly.

Ground segment sampling

Large discrepancy between the direct area and classification estimates resulted due to some extent by possible spectral confusion between information classes, which was further compounded by the large time lag between the field survey and the time of image acquisition. This emphasises the importance of timely field survey. This discrepancy could be reduced to some extent by choosing a larger sampling fraction.

Field problems

Significant problems were experienced in the field due to small scattered patches of buildings, scrubs, trees and hedge lines. The smaller patches less than a pixel size (400 sq m) were not considered. Access to a few segments was the problem due to absence of public paths or bridleways and the field survey was completed from a distance which made some segment survey less reliable. The larger time lag further added the problems during the in field survey.

Image classification

A few significant problems were experienced during the classification due to spectral confusion caused by bare fields, buildings, urban features and sea water; and grasslands in valleys and slopes. The supervised classification assumes that images are composed of spectrally homogeneous and separable classes. It was not really true in this study. A smaller variability within each class was introduced to improve the supervised classification. Therefore, a hybrid classification was found to be an appropriate solution to identify the land use and land cover and achieved an overall accuracy of 90 per cent.

Classes for modelling

The erosion model mostly relies on land use and land cover spatial data for deriving its distributed parameters. Some input parameters could be derived by reclassifying this key spatial data. Biophysical parameters such as per cent ground cover, and LAI could not be related to NDVI because of absence of field observations in this study. Land use and land cover map could be reclassified by establishing a direct relationship between classes and parameters collected either through field observations or estimation. There was a problem of different resolutions between key spatial data. Therefore, they were resampled to the resolution of the thematic map.

4.11.2 Conclusions

- A statistically sound sampling scheme with a timely field survey is a prerequisite for reliable image classification for modelling.
- The Garmin GPS-12 handset is not accurate enough for locating the boundaries of ground segments. Therefore, a real-time code corrected differential GPS should preferably be used for collecting location specific data. Some of the maps used in the survey were approximately 12 years old and were not very useful, so it emphasises the need and importance of updated maps in survey and classification.
- The SPOT-1 HRV sensor, although working beyond of its expected life, captured good quality images, which were found to be suitable for image classification
- A large time lag between the image acquisition and field survey reduced drastically the reliability of ground data for supervised classification. It suggests the role of timely survey for modelling.
- Signature of each land use and land cover class was not very distinct as it was assumed in the classification scheme. The problem was more aggravated due to a large survey time lag, so a hybrid approach of image classification was found to be an appropriate solution.

- The overall accuracy and Kappa coefficient of classification was found to be satisfactory and therefore, the image was reclassified for modelling study.
- Bare soils, urban areas and seashore water could not be separated digitally due to strong spectral confusion. They were manually masked before classification and added to the thematic map after classification.
- Spectral vegetation indices and band ratioing were also used in conjunction with image classification procedures to verify possible land use and land cover at the time of image acquisition to improve the classification accuracy

5

Generation and Quality Assessment of InSAR DEMs

This chapter reviews the elevation mapping technologies in terms of their capabilities and limitations. Spaceborne radar interferometry was identified and used for the generation of high resolution and quality DEMs from an ERS-1 and ERS-2 SAR raw data pair. Their quality was assessed against reference data. It was found that they are suitable for distributed modelling.

5.1 Introduction

Topographic data is represented digitally by several forms of data models in a computer. The digital elevation model (DEM) is one of the data models required for distributed hydrologic and erosion modelling at catchment scale for extracting drainage networks and topographic parameters (Moore et al, 1991). It is often not readily available at an adequate resolution and quality at catchment scale. Topography can be modelled digitally from elevation data collected from a variety of sources.

Elevation data collection by ground survey is expensive and time consuming at catchment scale while topographic data is available worldwide at coarse resolutions particularly in the developing countries. They can be applied at regional scale. Moreover, they are not regularly updated. At the same time, remotely sensed mapping technology has proved to be a timely and cost effective alternative for generation of high resolution and quality DEMs at catchment scale. These technology have an

advantage of potentially taking measurements from anywhere on the terrain, thus avoiding the spatial interpolation problems of contours (Wise, 2000). Satellite images can be obtained for an area of interest at a specific time unlike airborne data. Availability of optical data is constrained by the persistence of cloud cover in the developing countries, particularly in tropical regions. About 10 per cent of annually acquired data in Europe are only useable for topographic mapping due to cloud cover (Hanssen, 2001).

Synthetic aperture radar (SAR) has all weather and day-night capability to collect data for elevation mapping. SAR interferometry has been applied worldwide and has been successfully used in a few projects for generating high resolution and quality DEMs such as Landmap (Landmap, 2003), Shuttle Radar Topography Mission (SRTM) (USGS, 2003) and NEXTMap Britain (Mackay, 2002). These interferometric SAR (InSAR) DEMs can further be used for the parameterisation of a distributed model. Therefore, spaceborne radar interferometry was selected for this study to explore its potential to generate quality DEMs for developing countries for distributed modelling. For this study, an ERS-1 and ERS-2 tandem SAR raw pair was selected to derive InSAR DEMs of the Eastern South Downs, which would be further used to investigate the effect of different resolutions on model predictive capacity.

This chapter is dedicated to exploring the use of radar interferometry for extracting high resolution and quality DEMs suitable for distributed modelling for developing countries, in particular, and developed countries, in general. It also deals with the generation of a validation DEM data using digital photogrammetry. Elevation mapping technologies with respect to spaceborne radar interferometry is also reviewed in terms of their capabilities and limitations.

5.2 Elevation Data and Models

The bare-earth terrain data is required for distributed hydrologic and erosion modelling. Elevation data can either be from the first reflective surface or bare-earth surface, which is largely a technology specific issue. In case of first reflective surface, elevation data needs to be corrected to obtain bare earth terrain surface to meet one of the requirements of modelling.

There are three elevation data models used for the digital terrain representations (Maune, 2001; Moore et al, 1991; Weibel and Heller, 1991): DEM, TIN (Triangular irregular networks) and contour. The DEM data model is used in the LISEM erosion model. DEMs are of two kinds: DSM and DTM. A digital surface model (DSM) refers to the first reflective or highest elevation of the ground acquired from the space whereas a digital terrain model (DTM) refers to the elevation information of the ground or water surface. DEMs are simple two-dimensional regularly spaced raster grids and can be produced by the interpolation of contours, profiles, breaklines and mass points collected from various sources described below. DEMs can miss important ground features such as stream, steep banks and other similar features due to the inherent limitation of having uniform grid-cell spacing. However, DEMs are computationally efficient for handling of large georeferenced spatial data due to simple topological data structure.

TIN and contour-based data models are not directly used in the LISEM model, but they can be converted to the DEM data model for their application into the erosion model. A TIN, the variable resolution data model, is based on irregularly spaced points, lines and triangles interpreted as mass points and breaklines. It can be produced from contours, profiles and mass points with a topology. It has major advantages over DEMs in terms of efficient storage of elevation information in the high relief and low relief terrains, thus avoiding a problem of data redundancy in the low relief terrain. It also uses soft and hard breaklines to define smooth and interrupted surface. Soft breaklines maintain constant z-values along a linear feature while hard breaklines define interruptions in a smooth surface. Hard breaklines are used to represent stream centrelines, top and bottom of stream banks, ridgelines, road crowns, seawall, road embankments and other artificial features.

The contour-based data model is least preferred for distributed modelling due to complex data structure. It is represented in the form of lines or polygons of equal elevation and is produced from profiles and mass points. Profiles are the cross sections produced from the ground survey, stereo photogrammetry and LiDAR. Mass points are the irregularly spaced point cloud produced from photogrammetric auto image correlation, radargrammetry, InSAR and LiDAR.

5.3 Characteristics of a DEM

The main characteristics of a DEM are resolution, quality and usability (Maune, 2001), which are discussed below.

Resolution and quality

Resolution of a DEM refers to horizontal and vertical resolutions while quality of a DEM refers to horizontal and vertical accuracies. The horizontal resolution is defined by the horizontal grid spacing and the vertical resolution by the data type. Integer data type can store the whole numbers while float data type can store smaller quantity than integer data type. Float data type can represent smaller variation in topography than integer data type, but it results in large file sizes. The horizontal and vertical accuracies are assessed by standard procedures under National Standard for Spatial Data Accuracy (NSSDA), (FGDC, 1998), which are discussed in Section 5.6. Horizontal accuracy of a DEM is difficult to assess and can be performed by co-registering it with an image or a DEM of higher resolution to make linear features clearly visible. A poor horizontal accuracy may result in a poor vertical accuracy, so it should be corrected to improve the vertical accuracy. Resolution and quality determine the actual data requirements of distributed modelling

Usability

Usability addresses the issues of compatibility with other georeferenced spatial data. The parameters for usability of a DEM with other georeferenced spatial data are georeferencing information, file format, data type representation and metadata. The georeferencing parameters such as ellipsoid, horizontal and vertical datums, and coordinate system and projection are different for spatial data obtained from the various sources such as Ordnance Survey topographic maps, ASTER DEM and GPS survey (Table 5.1). The GPS positional coordinates are in geographic coordinates referenced to WGS 84. The ASTER DEM coordinates are in UTM referenced to WGS 84 whereas data supplied from the Ordnance Survey are in the British National Grid coordinates. These data should either be converted to planar coordinates preferably or to geographic coordinates with suitable datums to make them compatible with each other for

overlaying and further analysis. Ellipsoid heights from GPS survey should be converted to orthometric heights above the mean sea level using either local or global Geoid models such as National Geoid Model, 2002 (OSGM02) or Global Equipotential Gravitational Model 1996 (EGM96) as orthometric heights are required for distributed modelling. File format should be compatible with image processing and GIS software for quick import. A metadata file contains information about data and its processing history. An FGDC-compliant metadata is usually better with a DEM (FGDC, 1998).

Table 5.1: Georeferencing parameters of spatial data used in the UK

Ellipsoid	Horizontal datum	Vertical datum	Coordinate system and projection
Airy	OSGB1936	OS Datum Newlyn	British National Grid, Transverse Mercator projection
WGS84	WGS84	WGS84 (EGM96) Geoid	Planar coordinates, UTM projection (zone 29, 30 and 31)
WGS84	WGS84	WGS84 Ellipsoid	Geographic
WGS84	WGS84	WGS84 (EGM96) Geoid	Geographic

5.4 Review of Elevation Mapping Technologies

5.4.1 Introduction

DEM data sources are grouped into three categories for the review namely, cartographic, ground survey and remotely sensed data. There have been an enormous change in cartographic data capture technology, ground survey and remotely sensed mapping technologies. New digital elevation collection technologies include differential GPS, laser total station, digital aerial stereo photography, image stereo grammetry, radar stereogrammetry, radar interferometry, radar altimetry and laser altimetry. These technologies have increased the acquisition speed and improved the horizontal and vertical accuracies as well as coverage and reduced the cost. In the light of these developments, DEM technologies are reviewed in terms of the type of technology, accuracy, comparative performance, cost effectiveness and limitations.

5.4.2 Cartographic Data

Cartographic data at various scales are available worldwide. It is a standard method of generating digital elevation data for large areas and remains as the main

source of elevation data at coarser resolutions in the developing countries. On the contrary, good quality cartographic data are available at 1:10 000 scale in the UK such as Land-Form profile data at 10 m grid-cell spacing (Ordnance Survey, 2004). This scale and resolution data are not at all available in the developing counties. The hypsographic contours, spot heights and hydrographic features are digitised from cartographic data to create cartometric DEMs using a suitable interpolation method. Higher resolution of interpolation DEMs gives a better terrain representation and vertical accuracy (Gao, 1997). The quality of cartometric DEMs also depends on the map scale and contour interval as well as quality of original source data. Even during the cartographic production, small scale features contained in the original measurements are often filtered out and result in elevation data of a lower quality. The limitation of this data source is that these data are not updated regularly and contains spatial interpolation errors (Wise, 2000). Cartometric DEMs at coarser resolutions and lower accuracy are still being applied at regional scale. Therefore, they can not be a preferred data source for distributed modelling at catchment scale.

5.4.3 Ground Surveys

Elevation data collected from ground surveys are the most accurate because the surveys are statistically designed to draw the most accurate information from an area of interest. Surveying and subsequently interpolation result in high resolution and accurate DEMs. Advanced methods of ground survey such as differential GPS and laser total station can be used. A laser total station can capture roughly 1000 DEM points per day while DGPS can collect approximately 2000 DEM points in an hour (Barret et al, 2000). Therefore DGPS survey is faster than total station based survey. Differential GPS survey with survey grade equipment in a static mode results in a better accuracy than in a kinematic mode. Both survey accuracies degrade further with a longer baseline length. The horizontal accuracy is in the order of tens of centimetres and sub metre for static and kinematic survey respectively with a shorter baseline of a few kilometres (Barret et al, 2000). The vertical accuracy is one and half times of the horizontal accuracy due to influence of tropospheric conditions. Surveys are time consuming and not economically feasible at catchment scale. Therefore, they can not be used for this study.

5.4.4 Digital Photogrammetry

Remotely sensed mapping technology employs a variety of sensors and methodologies to generate elevation data. Airborne elevation data result in a better accuracy and resolution while spaceborne elevation data achieve larger ground coverage in a relatively short span of time, though a lower resolution and accuracy. These methods have the advantage of collecting measurements potentially from anywhere on the terrain, thus avoiding the spatial interpolation problems. Mapping technologies described here include digital stereo photogrammetry, radargrammetry, radar altimetry, radar interferometry and LiDAR altimetry. Each technology is reviewed for both aerial and space platforms in terms of DEM resolution, quality, and limitations.

Digital photogrammetry (also referred to as stereogrammetry for satellite images is a standard approach for generating DEMs from stereo pairs of aerial photographs and satellite imageries. Its theory is discussed in Section 5.8 and in the literature by Li et al (2002), Wolf and Dewitt (2000), Mikhail et al (2001), ERDAS (2002), and PCI Geomatics (2003). The performance of a stereogrammetry technique depends on several factors including base to height ratio of a pair, the flying height of an aircraft, and image texture. Image matching is a crucial step in an automated stereo processing, but it fails in image area covered with the cloud, shadow, snow and glacier, and having poor texture, geometric distortion and featureless area. Therefore, these factors influence the accuracy of elevation measurements and limit the usability of both air and satellite derived DEMs. A considerable post processing in terms of filling, filtering and interpolation is required to make them usable for distributed modelling.

DEMs are derived from high resolution sensor data such as SPOT Pan, IRS Pan, ASTER VNIR, Landsat 7 ETM+ Pan and MOMS; very high resolution sensor data such as SPOT-5, IRS-P5, IKONOS-II, QuickBird and EROS-A; and mixed sensor data as well. As can be seen from Table 5.2, accuracies of along-track stereo pairs are better than that of adjacent-track stereo pairs. The adjacent-track stereo data are acquired from two adjacent-track images with an overlapped area as Landsat did not have sensor steering capability. Across-track and along-track stereo data are stereo images acquired by steering the viewing angle of the sensor in the same track and from different tracks respectively. Along-track stereo data are better for achieving high image correlation by

avoiding the atmosphere disturbance. The mixed sensor stereo pairs resulted in lower accuracies than both individual accuracies. The achieved accuracy varies considerably with the image quality, base to height ratio and nature of terrain (Sasowsky et al, 1992).

Table 5.2: Vertical accuracies of stereo DEMs extracted from VNIR scanners (adapted from Toutin, 2001 and 2002)

Stereo-Pairs	Spatial Resolution (m)	Vertical accuracy (m)		
		Adjacent-track	Across-track	Along-track
IKONOS	1		1.5-2	
SPOT Pan	10		5-15	
MOMS-2P	18			10-30
IRS-1C/D	5.6		10-30	
ASTER	30		15	12.5
MOMS-2	13.5			5-15
JERS OPS	20			20-40
Landsat TM	30	45-70		
Landsat Pan	15	92		
Mixed sensors				
SPOT/ERS	10 /30		20-30	
SPOT/Landsat	10 /30		35-50	

5.4.5 Radargrammetry

The principles and methods of digital photogrammetry extended to satellite radar stereo images to extract the elevation information are known as radargrammetry (Leberl, 1990). Synthetic aperture radar (SAR) has been used for elevation mapping of cloud-covered regions and of high altitude areas. The radargrammetric processing is discussed in the literature by Leberl (1998 and 1990) and Mercer (1995). Airborne stereo SAR technology such as STAR-1 was used for topographic mapping and the vertical and horizontal accuracies achieved at 50 m grid-cell spacing were 15 - 25 m and 10 -15 m RMS respectively (Mercer, 1995). Satellite stereo SAR images from RADARSAT-1, ERS-1, ERS-2, ENVISAT, JERS and mixed-sensor such as ERS-SAR and SPOT-Pan (Toutin, 2000b) have been used for DEM generation (Toutin, 2000a). The achievable DEM accuracy from RADARSAT-1 data is around 12 m for the fine mode and 20 m for the standard mode independently of the method used (Toutin,

2000a). The achieved vertical accuracy from RADARSAT stereo pairs is 10-15 m (within 68 per cent) for moderate terrain (Mercer et al, 1998). The type of relief influences the DEM accuracy and, therefore, it is assessed for different relief types. The vertical accuracies achieved from different sensors with opposite side and same-side stereo-pairs for various terrain types are presented in Table 5.3. The same-side and opposite-side stereo pairs are acquired from same side and opposite side of the scene centre respectively.

Table 5.3: Vertical accuracies of radargrammetric DEMs derived from various sensors (adapted from Toutin and Gray, 2000).

Satellite	Band-polarisation	Resolution (m)	Relief type	Vertical accuracy (m)	
				Same-side	Opposite-side
Airborne					
STAR-1	X- band	10	Medium	2-4	
Almaz	S-HH	Fine: 7-9	Low	8-10	20
		15	High	30-50	
Spaceborne					
RADARSAT	C-HH	Standard: 20-29	Medium	15-20	40
		Wide: 20-40	High	25-30	
ERS-1/2	C-VV	24	Medium	20	20
		24	High	45	
SIR - B	L-HH	40	Medium	25	
		40	High	60	36
JERS	L-VV	18	High	75	
SIR-A	L-HH	25	High	100	

5.4.6 Radar Altimetry

Spaceborne radar altimeters deployed on ERS-1, ERS-2, SRTM and ENVISAT have been designed to measure the ground surface, surface height over ocean, ice surface, bathymetry and marine geoid characteristics. Altimeters provide accurate elevation measurements regardless of weather conditions over ocean, and relatively flat and lower slope ground surface, but they are prone to errors over steep sloped and rugged terrain due to a relatively large footprint. Spaceborne altimeters have large footprint up to 21 km and the resulting point measurement after correction represents the average height within a first pulse limited footprint. New RA-2 altimeter on

ENVISAT is used to generate terrain models. ENVISAT radar altimetry has been proved to be a useful tool for tracking river and inland lake water levels (ESA, 2003).

5.4.7 Radar Interferometry

Radar interferometry from both air and space platforms is an operational technology that has been used worldwide for topographic mapping. Interferometric synthetic aperture radar is generally termed as InSAR or sometimes IfSAR or ISAR in the literature. Interferometric data pairs can be collected from an aircraft in a single pass and from space either in a single pass or repeat passes to generate the high resolution DEMs. Airborne InSAR technologies such as STAR-3i, Aero Commander (AeS-1) and TOPSAR have been successfully used for the regional and national topographic mapping projects such as NEXTMap Britain (Mackay, 2002) while spaceborne InSAR technologies have been used for national and global topographic mapping projects such as Landmap (Muller et al, 2000) and SRTM global DEM (USGS, 2003; Balmer, 1999).

Airborne radar interferometry produces higher resolution and quality DEMs (1- 5 m grid-cell spacing with vertical accuracy of 10 cm - 3 m RMSE). The InSAR data pairs and derived DEMs are not available worldwide. At the same time, spaceborne radar interferometry produces high resolution DEMs with 15- 25 m grid-cell spacing and accuracy of 10-20 m vertical RMSE and the datasets are available worldwide. This is the most cost effective for large-area applications and produces the resolution and accuracy of DEMs suitable for distributed erosion modelling at catchment scale. Therefore, this technology was selected for this study to create high resolution and quality DEMs and to investigate the influence of various resolutions of InSAR DEM on predictive capacity of the LISEM model. The vertical accuracy from InSAR relies on a baseline length and its orientation measurement error, phase measurement, unwrapping errors, temporal decorrelation and geometric distortions. The vertical accuracies achieved from both airborne and spaceborne derived InSAR DEMs are given in Table 5.4. The theory and processing of SAR interferometry is described in Section 5.8.

Table 5.4: Vertical accuracies of InSAR DEMs from various sensors (adapted from Toutin and Gray, 2000)

Satellite	Grid-cell spacing (m)	Swath (km)	Vertical accuracy (m)
Airborne sensors			
TOPSAR	5-10		1-3
STAR-3i	5-10	4-10	2-3
AeS-1	5-10	3-8	< 3
Space sensors			
ERS 1/2	25	100	3-20
RADARSAT-1			
Fine mode	7-9		3-10
Standard mode	20-29	50-300	10-20
JERS	18	75	10-20
SRTM	30	80	20

5.4.8 LiDAR Altimetry

Airborne laser altimeter is an active sensor and can be preferred over aerial photography for data acquisition at night, in low sunlight or in inclement weather conditions. It penetrates through gaps in vegetation and urban areas to measure ground points to create both surface and terrain models. The vertical accuracy generally varies from 10-20 cm at 68 per cent with 2 m grid-cell spacing for terrain models. The sub metre accuracy is achieved for DSMs in urban and forest environments (Mercer, 2001). The LiDAR theory and processing is discussed in the literature by Wehr and Lohr (1999), Axelsson (1999), and Mercer (2001). The laser scanning system consists of a differential GPS receiver, an inertial navigation system and a scanning system with a laser rangefinder. It collects multiple pulse reflections in a narrow swath with a ground spot size varying from decimetre to two metres in diameter. It is time consuming for regional or catchment scale mapping. Spaceborne laser altimeter provides less accurate measurements than airborne altimeter but more accurate measurements as compared to spaceborne radar altimeter. With a footprint of 70 m by 170 m sampling spacing along track, the Geosciences laser altimeter system (GLAS) on ICESAT provided accurate and dense measurements over the Antarctic (Schutz, 2001).

5.5 Comparison of Mapping Technologies

Availability of DEMs with a requisite resolution and quality continues to be a major area of concern for distributed modelling. Cartometric DEMs in the developing countries are available at coarse resolutions and reasonable quality and can be applied for regional scale modelling. A high resolution DEM with 20-30 m grid-cell spacing with a reasonable vertical accuracy in the order of metres is required for modelling. Therefore, cartometric DEMs can not be preferred for modelling study. Two emerging remotely sensed mapping technologies such as radar interferometry and LiDAR have potentials to improve the DEM quality and coverage (Maune, 2001). Radar interferometry yields vertical accuracies and resolutions of DEMs comparable with optical stereo DEMs. Airborne radar interferometry produces higher resolution and accuracy DEMs than spaceborne InSAR technology, but the dataset is available only from satellite platform for the developing countries. LIDAR is appropriate for more detailed delineation of ground features in urban or forested environments. Airborne stereo radar technology has been phased out due to lower resolution compared to airborne InSAR. Spaceborne stereo radar is still in operation and produces much lower resolution and vertical accuracy as compared to spaceborne InSAR. Interferometric SAR DEM is the cost effective for large-area applications. Moreover, InSAR from both air and spaceborne has been successfully used in a few research and commercial applications such as Landmap, SRTM, and NEXTMap Britain. InSAR DEM generation is also less cumbersome and expensive than the optical stereo and radargrammetric DEM generation.

Advanced mapping technologies such as InSAR, LiDAR, optical stereo and radar stereo produce superior quality DEMs, but they too contain errors which are technology specific and vary from low to severe in some of the cases (Toutin and Gray, 2000; Endreny et al, 2000; Kervyn, 2001; Leberl, 1990). Remotely sensed derived DEMs, in fact, contain elevation data from first reflective surface, which requires a considerable post processing to obtain a bare earth surface required for modelling study. Cost of a DEM per square km increases with higher resolution and vertical accuracy, and varies from technology to technology. As can be seen from Figure 5.1, InSAR DEM has better vertical accuracy and lower cost than optical stereo and radar stereo DEMs.

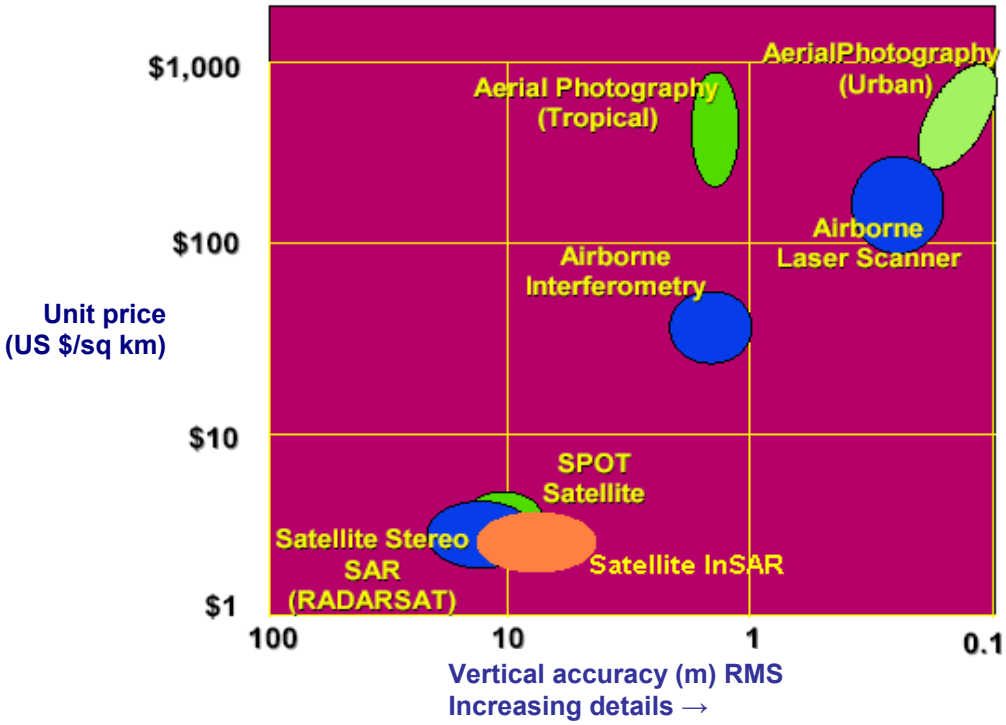

Figure 5.1: Comparison of DEM unit price from various mapping technologies (adapted from Mercer et al, 1998)

5.6 DEM Quality Assessment Procedure

The quality of a DEM should be assessed before deriving the input parameters of a distributed model. It can be assessed at two stages: firstly at engineering analysis and quality control during acquisition and production processes, and secondly at an independent DEM assessment against reference data. The former is used for quality assessment of derived InSAR DEMs and the procedure is described below in terms of most suitable quality measures, descriptors, criteria and reference data.

Quality assessment measures

The quality of a DEM is assessed mostly on the basis of its height values against height values of the corresponding points from reference data. Ackermann (1996) defined a more detailed quality measure using the first two derivatives of height: slope (slope gradient and slope aspect) and convexity (profile and plan convexity). These derivatives are more sensitive to change than the height accuracy.

Quality descriptors

A few descriptors are used for DEM quality assessment namely, standard error, root mean square error (RMSE), histogram analysis, vertical difference and fractal dimension estimator. A quality descriptor is chosen on the basis of availability of reference data. An RMS error is used for checkpoint reference data while the vertical difference and histogram analysis descriptors are used for reference DEM data.

Quality criteria

The horizontal and vertical accuracies of a DEM are assessed using an independent statistically sound testing methodology under the NSSDA (National standard for spatial data accuracy) (FGDC, 1998) described below. The NSSDA methodology is applied to estimate the horizontal and vertical accuracies of georeferenced maps and digital spatial data derived from aerial photography, satellite remotely sensed data and ground survey sources (FGDC, 1998). The horizontal and vertical accuracies at 95 per cent confidence level is tested at ground scale against an independent source of higher accuracy with a minimum of 20 check points well defined and distributed over an area of interest (FGDC, 1998). The criteria for horizontal and vertical accuracies are used on the basis of either normal or non-normal distribution of random error.

For normally distributed case

The horizontal accuracy is assessed in terms of radial (also referred to as circular accuracy) at 95 per cent confidence level ($Accuracy_r$). Radial accuracy is the radius of a circle of uncertainty within which 95 per cent of points are located. It is estimated using Equations 5.1 and 5.2 for two cases, depending on x and y direction errors and assuming that systematic errors are eliminated as best as possible and random errors are normally distributed.

When $RMSE_x$ is equal to $RMSE_y$, the circular accuracy is expressed:

$$Accuracy_r = 1.7308 * RMSE_r \quad \ldots \quad \text{(Eq. 5.1)}$$

where $RMSE_r$ is the radial root mean square error and is calculated by:

$$RMSE_r = RMSE_x^2 + RMSE_y^2$$

When $RMSE_x$ is not equal to $RMSE_y$ and then the circular accuracy is given:

$$Accuracy_r \approx 2.4477 * 0.5 * (RMSE_x + RMSE_y) \quad \ldots \quad \text{(Eq. 5.2)}$$

The vertical accuracy ($Accuracy_z$) is assessed in terms of vertical RMSE ($RMSE_z$) at 95 per cent confidence level and is defined as the linear uncertainty within which 95 per cent of points fall. It is given by Equation 5.3 assuming that systematic errors are eliminated as best as possible and the vertical random error is normally distributed:

$$\text{Accuracy}_z = 1.9600 * \text{RMSE}_z \quad \ldots \quad \text{(Eq. 5.3)}$$

For non normal distributed case

When errors are not normally distributed, the 95th percentile method is used (Daniel and Tennant, 2001). An RMSE procedure is not applicable in such cases. The 95th percentile indicates that 95 per cent of errors are of equal or lesser value and 5 per cent of errors are of larger value.

Reference data

Three kinds of reference data namely: check points, a DEM and a drainage network can be used for quality assessment. First reference data source is the most common and widely used for DEM quality assessment (FGDC, 1998; USGS, 1997). A minimum of twenty independent check points is required and collected from the various sources The descending order of preference for accepting check points is ground control points (GCPs), aero-triangulated test points, spot heights, or contour points from maps with appropriate contour intervals (USGS, 1997).

Another approach of quality assessment is based on an error free reference DEM since it provides the possibility of comparing both DEMs on every grid-cell basis. The reference DEM should be at least one order better than the DEM to be evaluated statistically (USGS, 1997). DEM sources such as aerial photogrammetric DEM, stereo optical DEM, InSAR DEM, LiDAR DEM, and even cartometric DEM can be used for the purpose.

The error free reference DEM assumption is rarely valid. The errors in both DEMs are compared and they may not exhibit a true representation of error distribution. A comparison of the drainage networks is another alternative to a reference DEM for quality assessment. The reference drainage network can either be produced by digitisation of an appropriate scale topographic map or extracted from a DEM using a drainage extraction algorithm based on a single or multiple flows. Both networks are compared on the basis of stream orders.

5.7 Off the Shelf Public Domain DEM Data

DEM data of the Eastern South Downs are available from both commercial and public domain sources. The Landmap DEM was the only public domain source available in the beginning of the study. Later on, the ASTER DEM and SRTM DEM were made available in the public domain. Table 5.5 lists the 'off the shelf DEMs' of the study area obtained from the public domain. In the developing world, researchers either rely on public domain DEMs or cartometric DEMs, which can be generated at their end. Therefore, it is a reason to look at the quality of public domain DEMs. The commercial domain 'off the self DEMs' are also reviewed for the study area. It might be available soon in the developing world. The commercial DEMs are created from various sources such as contours, optical stereogrammetry, airborne radar interferometry, LiDAR and mixed sources are given in Appendix D-1. Three public domain DEMs (Table 5.5), namely Landmap, ASTER and SRTM-3, were used in this study to investigate the influence of their resolutions on model predictive capacity. The selection of a DEM should be based on its resolution and quality, which must be consistent with the scale and physical processes in a model.

The Landmap DEM version 2.0 (Landmap, 2003), is a 25 m multipass InSAR DEM derived from ERS tandem SAR data and is an improved version of original version 1.0, which included some erroneous SAR strips. These strips are later detected and reprocessed to remove the errors (Landmap 2003). The ASTER DEM (USGS, 2004) is a 30 m relative DEM generated from an along-track stereo pair of ASTER Level 1A images acquired on 9 December 2002, which include bands 3N (nadir) and 3B (aft-viewing) from the VNIR in the spectral range of 0.78 to 0.86 μm. This Relative ASTER DEM is generated without ground control points (GCPs) and can be used to

derive absolute slope gradient and slope aspect accurate up to 5 degrees over a horizontal distance of over 100 metres and meets map accuracy standards for scales from 1:50 000 to 1:250 000 (USGS, 2004). The SRTM-3 is a three arc second unedited DEM generated from C-band single pass interferometry with data acquired during the SRTM project (USGS, 2003). This DEM is produced by 3x3 averaging of one arc second DEM data which contain ground clutter and water body artefacts. These errors are reduced by this averaging by a factor of three approximately. This is also available with 75 m postings in the British National grid coordinates from Landmap (Landmap, 2003).

Table 5.5: Public domain digital elevation data of the Eastern South Downs

DEM data	Grid Spacing (m)	Extent of each tile (km x km)	Vertical accuracy (m) (RMSE)	Technique	DEM Source
Landmap DEM	25	100 x 100 or user defined	Not available	InSAR	Landmap
SRTM DEM	3''	1^0 x 1^0	< 16	InSAR	USGS/ Landmap
ASTER DEM	30	~60 x 60	10-30 (relative height)	Optical stereo	USGS

5.8 Generation of InSAR DEMs for Modelling

5.8.1 Introduction

Radar (radio detection and ranging) operates in the microwave range from a metre to a few millimetres in wavelength. There are two basic radar systems namely; real-aperture radar and synthetic aperture radar and both differ principally by the method used to achieve a better azimuth resolution (resolution in the direction of travel). Real aperture radar produces a narrow angular beamwidth while synthetic aperture radar (SAR) employs a small antenna and synthesises a relatively broad beam using the Doppler principle and synthetic aperture data processing techniques to improve the azimuth resolution (Sabins, 1997). The SAR processor is based on a two-dimensional reference function and received signals. The SAR processing involves an accurate modelling of the SAR response to a point target and a continuous field of targets (Kramer, 2002). The SAR systems and SAR data processing is discussed in the literature by Curlander and McDonough (1991).

Radar interferometry is a technique for extracting the three-dimensional information of the Earth's surface by exploiting the phase content of complex radar signals obtained either from multiple passes with a single antenna or in a single pass with two antennae. Three methods can be employed to acquire SAR data for interferometry namely; along-track, across-track and repeat-track (repeat-pass) observation methods. First method is applicable to airborne SAR systems for earth deformation and displacement studies while second method is suited to both airborne and spaceborne SAR systems with dual antennae for topographic mapping application. Last method is applicable for the spaceborne SAR system with a single antenna for mapping application. A single pass interferometry requires two antennae separated by a baseline distance to obtain a scene pair in a single flight, for example, SRTM and NEXTMap Britain projects. Similarly, repeat-pass interferometry requires a single antenna to obtain a scene pair in repeat orbits (Figure 5.2) and the precise location of the satellite during acquisition (Gens and van Genderen, 1996). The generation of InSAR DEMs from SAR raw data pairs involves SAR processing and InSAR processing, which are discussed here.

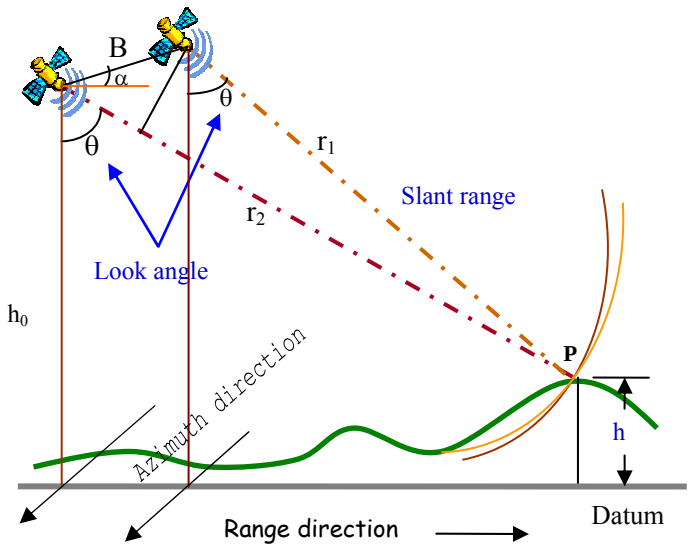

Figure 5.2: InSAR geometry of repeat pass observations

5.8.2 Review of SAR Interferometry

SAR interferometry has successfully been applied for topographic mapping (Zebker and Goldstein, 1986; Goldstein et al, 1988; Gabriel and Goldstein, 1988), thematic mapping (Ichoku et al, 1998; Askne and Hagberg, 1993) and atmospheric delay mapping studies (Hanssen, 2001) while differential SAR interferometry has successfully been demonstrated for earth deformation monitoring (Massonnet et al, 1993, Zebker, 2000) and recently for estimation of erosion and deposition by the water (Smith, 2001; Smith et al, 2000).

Radar interferometry was begun with the observation of the surface of the Venus and the Moon. Graham in 1974 theoretically introduced the synthetic aperture radar (SAR) interferometric technique with a side looking airborne and spaceborne geometry for topographic mapping of the Earth. First airborne SAR interferometer for topographic mapping was successfully applied by Zebker and Goldstein (1986), but a better vertical accuracy could not be achieved due to lack of aircraft roll data. The first application of spaceborne repeat pass SAR interferometry for earth topography became possible with data acquired during 100 day long SEASAT mission in 1978 and subsequently its results were published (Gabriel et al, 1989). Gabriel and Goldstein (1988) adapted the repeat pass interferometric technique to cross orbits data acquired in October 1984 from SIR-B in a repeat orbit for an area in Canada. Li and Goldstein (1990) studied the effects of multibaselines ranging from 60 to 1000 m on phase errors and topographic heights and showed that the larger baseline length increases phase errors and sensitivity of heights.

Since the launch of ERS-1 satellite with C-band SAR in July 1991 by the European Space Agency (ESA), the research was mostly concentrated on potentials and limitations of SAR interferometry. After the launch of ERS-2 in 1995 and simultaneously operation in a tandem mission mode with a 24 hour time difference, the applications of spaceborne SAR interferometry were greatly expanded worldwide with availability of InSAR datasets. The assessment of DEMs from ERS tandem data appeared most promising (Duchossois and Martin, 1995). Recent studies of Zebker et al (1994) and Rufino et al (1998) showed that the achievable accuracy for DEM generation is about 10 m and 5 m respectively in favourable situations. DEMs of

Finland from ERS tandem mission using 35 image pairs of ascending and descending pass showed an elevation accuracy of about 10 m (Herland, 1997). Zebker et al (1997) also mentioned that the atmospheric effect might deteriorate DEM accuracy as much as 100 m at unfavourable baseline.

With the launch of JERS-1 in 1992, L-band repeat pass interferometry was applied for topographic mapping due to its vegetation penetration capability and lower sensitivity to temporal change. The vertical accuracies (RMSE) of 22 m (Werner et al, 2000), 6-16 m (Dammert and Wegmüller, 1999) and 27.7 m (Tokunaga, 1997) have been reported for InSAR DEMs derived from JERS-1 SAR data. The orbital accuracy of JERS-1 was not as precise as required for interferometry, so data were not extensively exploited despite its potentials. SAR data of three bands (X, C and L) were collected from SIR-C /X-SAR, flown on the space shuttle Endeavour on two missions in 1994. The InSAR DEMs were generated from L-band data (Sun and Ranson, 1997; Lanari et al, 1996) with a vertical accuracy of 16.14 m (Chao et al, 1999). Since the launch of RADARSAT in 1995, large amounts of InSAR data pairs were made available with various look angles and swaths. Due to imprecise orbit parameters, its full interferometric potential could not be exploited.

Two major problems of temporal decorrelation and atmospheric effect were experienced in repeat pass interferometry for DEM generation. This experience culminated in the Shuttle Radar Topographic Mission (SRTM) in early 2002 with a single pass interferometry from space (Farr and Kobrick, 2000; Balmer, 1999). It mapped the globe with C and X-bands and 30 m global DEMs have been generated from the SRTM SAR data (Farr and Kobrick, 2000). Recently, SRTM-3 DEMs with three arc second grid-cell spacing have been released to the scientific community without accuracy assessment (USGS, 2003). In March 2002, the ESA launched the ENVISAT with an advanced SAR system to continue ERS SAR data and to provide improved capability on different spatial resolutions, incidence angles, swath and polarisations for SAR interferometry (ESA, 2004).

5.8.3 Selection of SAR Data

SAR raw or single look complex data pairs can be obtained from a number of spaceborne imaging radar systems (Appendix D-2). A few parameters need to be optimised for selecting a quality InSAR pair:

- terrain characteristics,
- radar band,
- baseline,
- temporal decorrelation, and
- orbital accuracy

The terrain is characterised by slopes and landcover types, which act as a guide for selecting an optimal pair. There is an optimal baseline range for each radar band. For steep slopes, shorter baseline data pairs are selected for best results while for lower slopes, longer baseline data pairs are preferred for successful DEM generation. Larger wavelength (L-band) radar can allow longer baseline, which has higher sensitivity to height and also results in a higher DEM accuracy, but there is an upper limit of baseline for a particular band. Increase of baseline decreases the phase coherence, a critical parameter for interferometry. The optimal perpendicular baseline for ERS system is 50-300 m for topographic mapping (ESA, 2004). The upper baseline limit has an acceptable coherence loss but it is not preferred for high quality DEM generation.

Temporal decorrelation is related to the loss of phase coherence due to a time difference between two acquisitions and depends on the nature of target and its backscattering properties variation over time. Agricultural and grassland have stable backscatters for a short time interval as compared to the forest cover. Large temporal difference results in a significant coherence loss, which may not allow generation of high quality DEMs. An optimal pair with least possible temporal difference for a given situation should be selected from different spaceborne SAR sensors (Table 5.6). It should be shorter time difference possible for agricultural and grassland catchments. The best pairs can be obtained from ERS tandem data pairs, which were acquired with 24 hours time difference. Orbit errors directly affect the position and height accuracy of a DEM and are translated into position and height shifts during phase to height conversion and geocoding steps. Therefore, it is essential to select a sensor platform

with precise orbit control and maintenance. Orbital accuracy of ERS and ENVISAT are better than that of Radarsat-1 and JERS-1.

Table 5.6: Temporal difference for the acquisition of a pair from satellite SAR sensors

InSAR Pair	Band	Repeat pass temporal difference (days)
ERS-1 / ERS-1	C	3, 35 or multiple of 35 (3 days-during Ice phases)
ERS-1 / ERS-2	C	1 day (Tandem mission)
ERS-2 / ERS-2	C	35 or its multiple (Multidisciplinary phase)
ENVISAT / ENVISAT	C	35 or its multiple (4 days with antenna steering)
JERS-1 / JERS-1	L	44 or its multiple
RADARSAT / RADARSAT for standard and fine mode	C	24 or its multiple

A suitable SAR raw data pair of the Eastern South Downs from the ERS tandem mission archive (Table 5.7) was selected using both an online EOLI (Earthnet online interactive) browser and an offline multi mission DESCW (Display earth remote sensing swath coverage for windows) catalogue browser based on baseline and other information of the pairs. The pair of quicklook images was also checked for data quality and atmospheric perturbations. Selected dataset was obtained under the European Research Club from the Eurimage, Italy via Infoterra.

Table 5.7: Scene parameters of a SAR raw data pair of the Eastern South Downs

Mission	Date	Orbit no	_|_ Baseline	Δ Day	Other information
ERS-1	13 March 1997	29598	--	--	Track: 051, Frame: 2583,
ERS-2	14 March 1997	9925	145 m	1	Descending path

5.8.4 Selection of SAR and InSAR Processors

Numerous commercial and research packages (also called processors) have been developed to generate digital elevation models (DEMs) from SAR raw or SLC data. A processor system with a precision phase preserving focussing and interferometric processing was the preferred choice assuring the smooth import and analysis of input data for interferometric analysis. Two processors viz. PulSAR/ InSAR Toolkit from the Phoenix System on the Linux platform, and SARscape and SARscape DEM from the

SARMAP on the Windows platform were used in this study. InSAR processing consists of a standard processing chain of various steps with various options at each step to solve a constraint. Most of the processors have inherent advantages and limitations, as they are not available in all the operating platforms and do not support all the SAR sensors, data formats, and processing and archive facilities (PAFs) (Gens, 1999). The processors are compared from their capability point of view (Appendix D-3).

Both SAR and interferometric processing involve complicated tasks requiring a lot of user interactions for obtaining the best results. The optimal processing procedures for each task and of a complete chain were discussed on the basis of various processing steps and available software functionalities in the following sections.

5.8.5 SAR Data Focussing

SAR data focusing or processing involves:

- range focusing,
- range migration compensation, and
- azimuth focusing

The range focusing is performed by matched filtering of a returned radar signal with a replica of the transmitted signal. The range migration translates the radar return from a target in successive pulses that it falls within one column of dataset. For ERS-1 and ERS-2 system, the maximum translation is less than one range bin (Curlander and McDonough, 1991). The azimuth focusing is carried out by correlating the returns from a target within successive pulses of the radar with a theoretical chirp function defined according to the expected frequency shift and phase of the return from that target as it passes through the radar antenna. All the above three steps are performed on patches of data at least corresponding to the size of the radar footprint of 1200 pulses for ERS-1 and ERS-2 (Curlander and McDonough, 1991).

A SAR raw data pair was supplied in the CEOS SAR format on two optical disks (Appendix D-4). A single scene SAR data contained four files namely, volume directory, leader, data and null volume directory. Both leader and data files were mainly used to extract the processing parameters and to ingest SAR data for each scene to the SAR processing system. In the study, two precision phase preserving digital processors such as range-Doppler (Zebker et al, 1994; Smith, 1991) and Omega-k in frequency

domain (Cafforio et al, 1991; Balmer, 1992) were used to focus raw data to single look complex (SLC) images (Figure 5.3). The image quality was checked for an optimal focusing (Appendix D-5). The images were then multilooked with a single look in the range and five looks in the azimuth direction to reduce the speckle noise and to view pixels in a square shape (Figure 5.4, left). The phase of a single SLC image (Figure 5.4, right) was found to be completely random in the most image areas and has not been used for an application. The range-Doppler processor has been widely used in the most commercial software and in the ESA PAFs' SAR processors (Table 5.8). A few new digital SAR processors have been developed (Hanssen, 2001), but they are not widely used.

SAR SLC images obtained from the ESA PAFs are not optimally focussed for a specific interferometric application such as topographic mapping but they are reasonable processed images for the most applications. SAR processing at user end could be optimally customised for the best resolution, focus, speckle reduction factors, and many other image parameters which result in a better image quality for interferometry (Lightstone, 1996). Many other interferometric applications can also be benefited from such customised SAR processing at user end.

Table 5.8: SAR processors used at the ESA PAFs and in software

PAF/Software	SAR Processor name	Algorithm used
PulSAR/InSAR Toolkit	PulSAR	Range-Doppler
SARscape	SARscape	ω-k frequency domain
Gamma SAR	Modular SAR Processor	Range-Doppler
EarthView	Advanced Precision Processor	Range-Doppler Chirp scaling (optional)
Vexcel's InSAR	FOCUS	Range-Doppler
I-PAF	VMP 6.8	Range-Doppler
UK-PAF	VMP 6.8	Range-Doppler
D-PAF	VMP 6.8	Range-Doppler
EECF, Italy	VMP 6.8	Range-Doppler

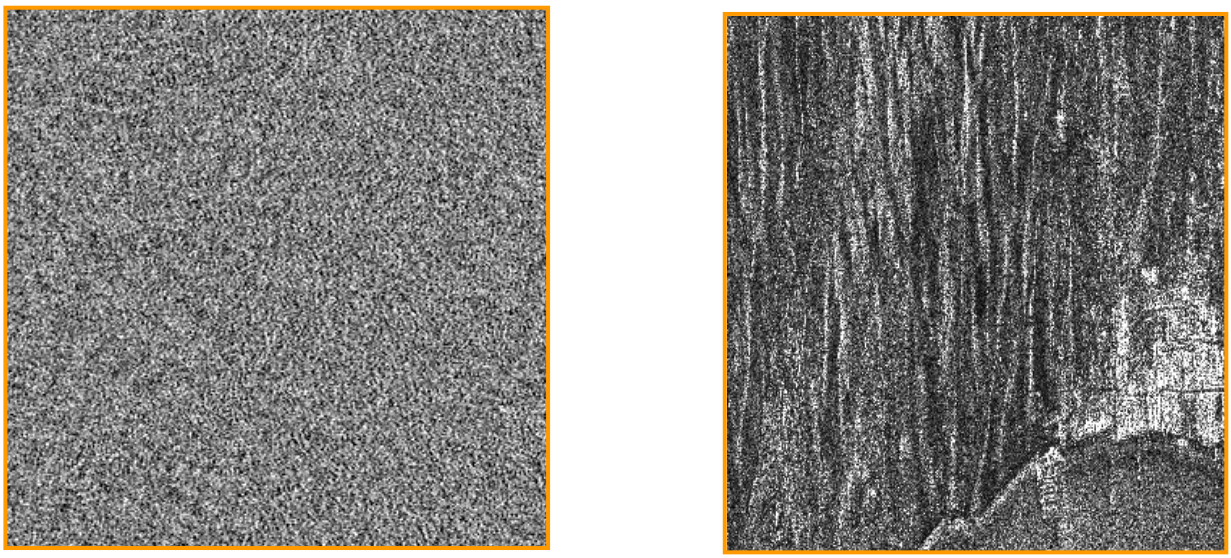

Figure 5.3: SAR raw data (left) and SAR single look complex image (right) of the Eastern South Downs

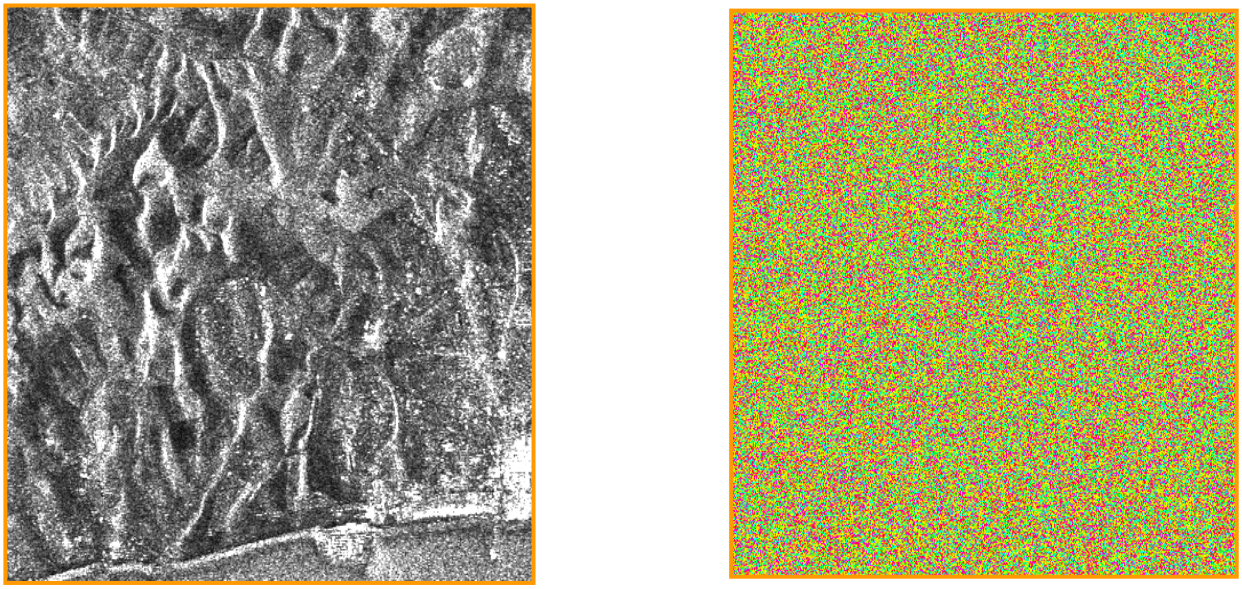

Figure 5.4: Multilooked SAR intensity image (left) and phase image (right) of the Eastern South Downs

After focusing, interferometric SAR processing involves the following steps. The conceptual diagram of InSAR processing is given in Figure 5.5:

- SLC sub scene generation,
- precise baseline estimation,
- precise co-registration of two complex images,
- generation of interferograms,
- multilooking, filtering and coherence computation,
- phase unwrapping, and
- phase to height conversion and geocoding

5.8.6 Creation of a Sub Scene Pair

A full scene of ERS data covers an area of approximately 100 km x 100 km. The study area is relatively small, so a pair of sub scenes was extracted after focussing to minimize the disk storage requirement and to improve the speed of InSAR processing.

If a SAR SLC image pair is used for InSAR processing, both images must be imported to extract the processing parameters before creating a pair of sub scenes.

5.8.7 Estimation of Precise Baselines

The parallel and perpendicular baselines were estimated on the basis of restituted orbital parameters supplied along with raw SAR data. The perpendicular baseline is a quality parameter to assess the suitability of a dataset for an InSAR DEM generation. The perpendicular and critical baseline lengths of the data pair were 145.55 m and 907.15 m. The perpendicular baseline lies within the optimal baseline range for the ERS system (50-300 m). It can be concluded that the selected pair is suitable for topographic mapping.

Increase of a perpendicular baseline between two SAR images results in the phase decorrelation. The critical baseline is the maximum allowable baseline of a data pair with an acceptable phase decorrelation. Data pairs with more than a critical baseline are completely decorrelated and, thus, are not useful for DEM generation. The critical baseline of a data pair is expressed:

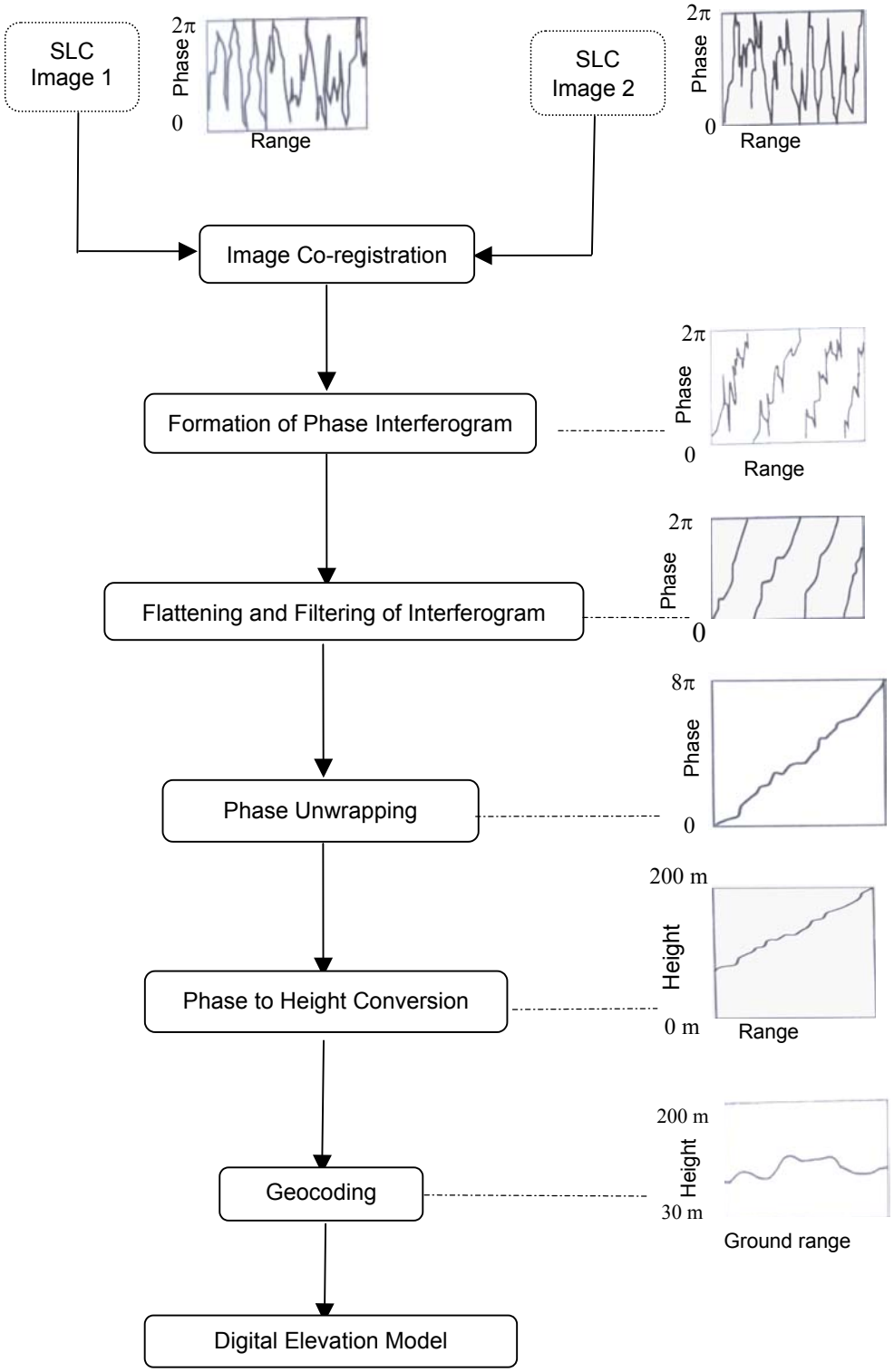

Figure 5.5: Conceptual diagram of InSAR processing

$$B_{\perp(\text{critical})} = \frac{\lambda * W * r * \tan(\theta - \alpha)}{c} \quad \ldots \quad \text{(Eq. 5.4)}$$

where W is the bandwidth of a SAR system, r is the slant range from sensor to target, θ is the angle of look, α is the local terrain slope in range direction and c is the velocity of light.

5.8.8 Precise Co-registration

Co-registration is the crucial step of InSAR processing and involves alignment of a slave image with a master image and resampling of amplitude and phase values of a slave image. It was carried out in two steps namely; coarse and fine registration. Coarse co-registration of the master and the slave images was performed from orbital state vectors, the moments and the centre of the image. An accuracy of 2 pixels in range direction and 10 pixels in azimuth direction was achieved. The fine registration based on phase information in InSAR Toolkit and fringe detection in SARscape DEM was performed. The range and azimuth offsets shifts between the SAR image pair were found to be 8.046 pixels and -33.952 pixels respectively. The fine co-registration was performed with an accuracy of 1/1000th of a pixel. Poor co-registration with a very small offset results in a drastic loss of coherence. The precision of co-registration must be better than half a pixel to minimise the loss of coherence.

5.8.9 Formation of Interferograms

Spectral range filtering was applied to minimise the decorrelation due to a non overlapping range spectra. Similarly, common Doppler bandwidth filtering was applied to the registered images to minimise the decorrelation due to a partial overlap of the azimuth spectra. The interferogram (Figure 5.6, left) was then generated by multiplying the complex value of the slave image to complex conjugate value of the master image (Equation 5.9). The quality of fringes shows the high level of phase correlation in the interferogram. The assumption of an identical object phase in both SAR images is only valid for ERS tandem datasets.

After focusing, the phase of a SAR image has two components namely: a deterministic geometric phase due to the distance between sensor and object; and a random phase component contributed by object phase and thermal noise (Equation 5.7). Random phase component is the coherent sum of the signals from the randomly arranged elemental scatters within the cell to the centre of the cell. This component, although random from a resolution element to a resolution element, remains the same if the viewing geometry is nearly identical and if the relative position of the elemental scatterers within a cell remains the same. The thermal noise is the same for images acquired in repeat pass observations due to the single antenna and depends on its magnitude relative to the desired signal. It is different for transmitting and receiving antennae used in single pass interferometry. The phase of a SAR image is the sum of a deterministic phase, an object phase and a thermal phase and is expressed as (Balmer, 1997):

$$\phi = \phi_{\text{det}} + \phi_{obj} + \phi_{ther} \qquad \ldots \qquad \text{(Eq. 5.5)}$$

The deterministic phase of an image pixel is directly proportional to the slant range and is expressed:

$$\phi_{\text{det}} = -\frac{\omega * \text{p}}{\text{c}} \text{r} \qquad \ldots \qquad \text{(Eq. 5.6)}$$

where p is acquisition mode factor and is equal to1 for a single pass interferometry and 2 for repeat pass interferometry, ω is the angular frequency, r is the slant range distance and c is the speed of light. Hence, the phase of a pixel in a master image and a slave image is given as:

$$\phi_1 = \frac{2\omega}{c} r_1 + \phi_{obj} + \phi_{ther} \qquad \text{and} \qquad \ldots \qquad \text{(Eq. 5.7)}$$

$$\phi_2 = \frac{2\omega}{\text{c}} \text{r}_2 + \phi_{\text{obj}} + \phi_{\text{ther}} \qquad \ldots \qquad \text{(Eq. 5.8)}$$

The interferometric phase difference is computed as a hermitian product of Equations 5.7 and 5.8 and is given as:

$$s_2 * s_1^* = \rho_1 * \rho_2 e^{i(\phi 2 - \phi 1)} \qquad \ldots \qquad \text{(Eq. 5.9)}$$

The phase difference of a pixel between two images is expressed assuming random phase component between two acquisitions remains same:

$$\phi_2 - \phi_1 = \Delta\phi_{21} = \frac{2\omega}{c}(r_2 - r_1) = \frac{2\omega}{c}\Delta r_{21} \qquad \ldots \qquad \text{(Eq. 5.10)}$$

The phase difference between two images Δr_{21} can be estimated to a sub wavelength precision of C-band (5.66 cm) of the ERS SAR sensor.

5.8.10 Multilook Processing

Multilook processing reduces speckles in an image and can be applied either during image focussing or after. During image formation, a full synthetic aperture beam is arranged into a number of independent or overlapping sub apertures and these apertures are then combined via an averaging to form a multilook image whereas pixels of a full resolution image are combined to average either in range or in azimuth or both directions to produce a multilook image.

Speckle noise in an interferogram is reduced by multilooking. The phase noise reduction in an interferogram improves the accuracy of phase unwrapping (Goldstein et al, 1988), which leads to a better height accuracy. Multilook processing after generation of an interferogram is the best option to filter out the phase noise and to preserve the fringe pattern of the interferogram as well (Huang and van Genderen, 1996). The interferogram was multilooked with a single look in range direction and five looks in azimuth direction, and the resultant pixel size of a multilooked interferogram is given in Table 5.9.

Table 5.9: Effect of multilooking on pixel sizes of the interferogram

Parameter	Pixel size (m)
Resolution in range in slant range	7.904
Ground resolution in azimuth	3.972
No of looks in range	1
No of looks in azimuth	5
Ground resolution in range	20.231 m
Ground resolution in azimuth	19.959 m
Final ground resolution pixel size	25.0 m

The multilook phase and intensity images are computed from a single look complex image:

$$g_{phase} = \frac{1}{m_a * m_r} \sum_{y=1}^{m_a} \sum_{x=1}^{m_r} \tan^{-1}\left(\frac{Q_{(x,y)}}{I_{(x,y)}}\right) \quad \ldots \quad \text{(Eq. 5.11)}$$

$$g_{intensity} = \sqrt{\frac{1}{m_a * m_r} \sum_{y=1}^{ma} \sum_{x=1}^{mr} I^2_{(x,y)} + Q^2_{(x,y)}} \quad \ldots \quad \text{(Eq. 5.12)}$$

where m_r and m_a are the number of looks in range and azimuth, I is the real component of a complex SAR image at location (x, y) and Q is the imaginary component of a complex SAR image at location (x, y).

5.8.11 Removal of Flat Earth Phase and Phase Filtering

A derived interferogram comprises the phase components attributed by the flat terrain, topography and a form of noise. The phase due to the flat terrain appears in the form of periodic fringe pattern over range, which needs to be removed to obtain the topography directly. Two methods are used for interferogram flattening: the ellipsoidal flattening and the terrain flattening. The ellipsoidal flattening is achieved using either orbital data or interferogram fringes. The terrain flattening is performed using a coarse resolution DEM.

The flat earth phase component in SARscape DEM was removed from the interferogram using Equation 5.13 based on the orbital parameters and an ellipsoidal model of the earth's surface. The resultant flattened interferogram is given in Figure 5.6 (right).

$$\phi_{fe} = \frac{2\omega B \cos(\theta - \alpha)}{cr \tan\theta} \Delta r_{df} \quad \ldots \quad \text{(Eq. 5.13)}$$

where ϕ_{fe} is the phase contributed by the flat earth, B is the baseline distance, α is the local slope angle and Δr_{df} is the range difference between two acquisitions.

The fringes were not sharp and very clear in the interferogram and phase noise was present in the flattened complex interferogram. The interferogram was filtered

using an adaptive filter to improve the phase coherence for a trouble free unwrapping and improving the height accuracy. The flattened and filtered interferogram is presented in Figure 5.7 (left). In InSAR Toolkit, the terrain flattening was performed using a 1 km coarse GTOPO30 DEM.

5.8.12 Interferometric Coherence

Interferometric coherence is a measure of phase correlation and its absolute value varies between 0 and 1 with a lower limit reflecting complete phase decorrelation and an upper limit, a full phase correlation. The interferometric coherence (Figure 5.7, right) was calculated from a flattened and filtered interferogram before phase unwrapping to assess the phase noise. The coherence value varied from 0.0003 to 0.9286 with a mean of 0.617 and a standard deviation of 0.219. The coherence statistics reflected a low level of noise in the interferogram, which is suitable for a smooth phase unwrapping. At the same time, effort was made in processing to minimise the coherence loss during interferogram generation.

The noise in an interferogram emanating from various sources may be a system noise, a decorrelation noise and a processor noise. The system noise could not be avoided, but it is quite small as compared to sensed signals. The decorrelation noise resulted from the baseline and temporal decorrelation. The processor noise emanates during focussing and co-registration and is brought under control using an optimisation strategy. The temporal decorrelation decreases the coherence by changing of conditions between two acquisitions such as the scattering geometry within the resolution cell, the physical properties of the scattering mechanisms and the behaviour of the propagation medium. Interferometric coherence depends on several factors before phase unwrapping such as; system noise, terrain decorrelation, baseline decorrelation, temporal decorrelation, low quality SAR focussing, and insufficient co-registration. Phase coherence is the product of all the above factors and is given in Equation 5.14:

$$\gamma = \gamma_{temporal} * \gamma_{baseline} * \gamma_{thermal} * \gamma_{focusing} * \gamma_{co-reg} \quad \ldots \quad \text{(Eq. 5.14)}$$

If the phase noise in an interferogram is high, some fringes are completely lost and result in errors in the DEM. The sources of phase noise are described in the literature by Zebker at al (1994) and Huang et al (1996).

Interferometric coherence is defined as the normalised complex cross section of two interferometric SAR signals, s1 and s2 shown in Equation 5.15. The SNR (signal to noise ratio) can also be expressed in terms of the interferometric coherence:

$$\gamma = \frac{\left|\left\langle s_1 s_2^* \right\rangle\right|}{\sqrt{\left\langle \left|s_1 s_1^*\right| \right\rangle \left\langle \left|s_2 s_2^*\right| \right\rangle}} \qquad \ldots \quad \text{(Eq. 5.15)}$$

$$\text{SNR} = \frac{\gamma}{1-\gamma} \qquad \ldots \quad \text{(Eq. 5.16)}$$

where γ is the interferometric coherence, asterisk (*) is the complex conjugate operator and angular brackets are the statistical expectation, realized by a spatial averaging within a defined rectangular filter, a product of complex signal s_1 and complex conjugate of signal s_2 for a SAR pair.

5.8.13 Phase Unwrapping

After removal of flat earth phase and phase filtering, the phase in an interferogram is wrapped into intervals of 2π modulus and is directly related to the physical qualities of the surface topography. In order to reconstruct a surface topography, the phase is unwrapped by a phase unwrapping procedure for solving the integer ambiguities. A number of phase unwrapping algorithms based on local and global approaches have been developed (Gens, 2003). A thorough description on phase unwrapping is found in the literature reviewed (Gens, 2003; Ghiglia and Pritt, 1998).

The interferogram (Figure 5.7, left) was unwrapped using a classical branch cut unwrapper (Goldstein, 1988) and a minimum cost flow (MCF) network unwrapper (Costantini, 1996) in InSAR Toolkit and using a region growing unwrapper (Xu and Cumming, 1999) in SARscape DEM. The unwrapped phase interferogram is given in Figure 5.8.

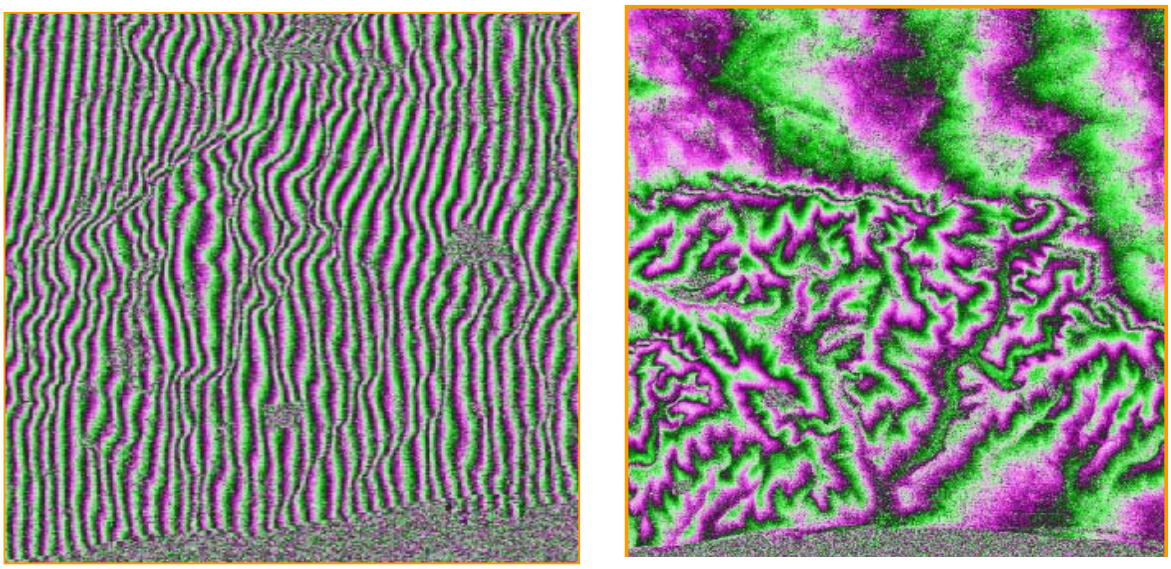

Figure 5.6: Phase interferogram before (left) and after removal of flat earth phase (right)

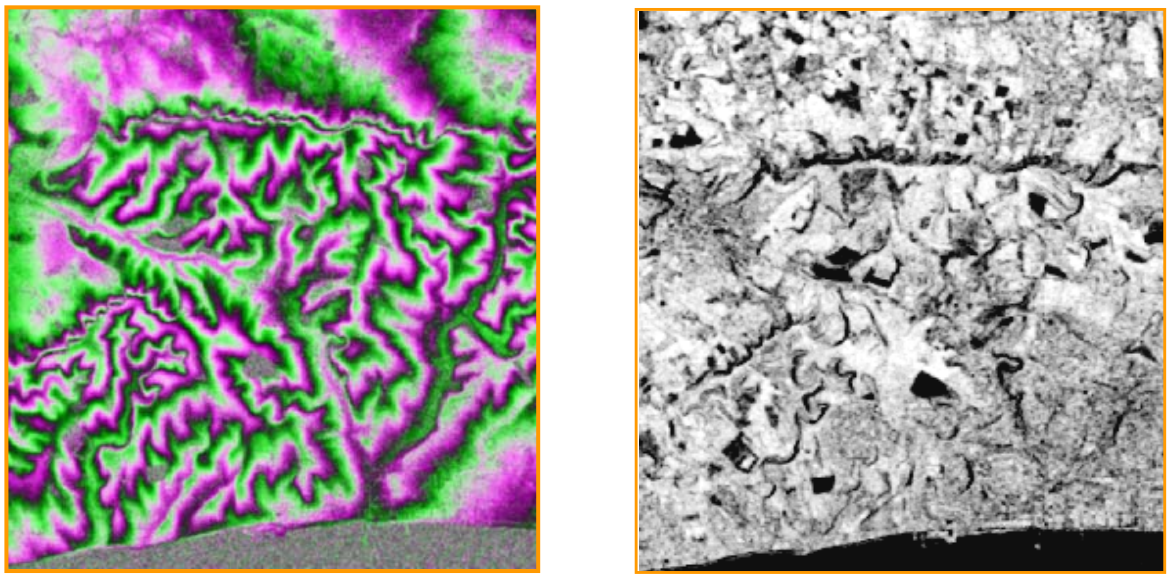

Figure 5.7: Filtered and flattened interferogram (left) and interferometric coherence image (right)

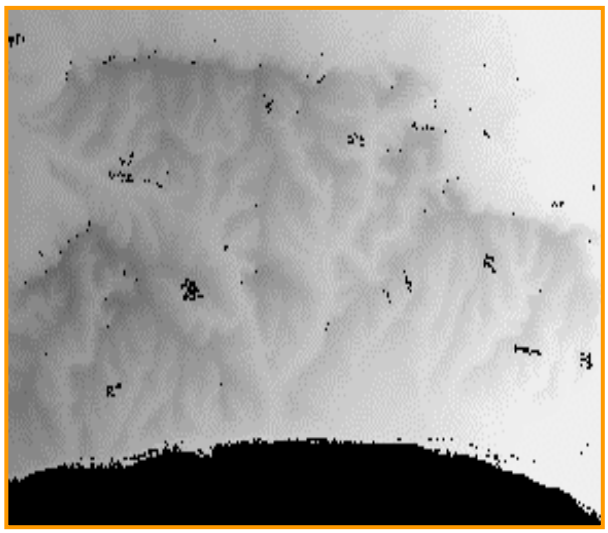

Figure 5.8: Unwrapped interferometric phase image

The phase in a flattened and filtered interferogram is unwrapped in an integer multiple of 2 л and is given by Equation 5.17. Phase unwrapping algorithms attempt to estimate the correct value of N for every pixel while considering unwrapping error propagation in the image:

$$\phi_{unwrap} = \phi_{wrap} + 2\pi * N \qquad \ldots \qquad \text{(Eq. 5.17)}$$

The phase unwrapping is a two dimensional problem and is solved with local and global approaches. The classical branch cut algorithm (Goldstein, 1988) is a local approach based on the path following method. It relies on branch cuts between all detected residues preventing any integration path from crossing these cuts. These residues are either balanced by a residue of opposite polarity or by a branch cut connected to the image border. The sum of the branch cut lengths are minimised in this approach. It is computationally very efficient with a little memory requirement, but it has a poor performance in areas of low coherence and with densely placed branch cuts. The suggestions to improve the performance of this algorithm by different preprocessing steps are discussed in the literature by Ghiglia and Pritt (1998) and Goldstein and Werner (1998).

The minimum cost flow (MCF) unwrapping algorithm (Costantini, 1996) is based on a classical branch cut method using a minimum cost flow networks for solving the unwrapping problem. Phase difference of neighbouring pixels with an error of integer

multiple of 2π leads to formulating the phase unwrapping problem as a global minimization problem with integer variables: the weighted deviation between the estimated and the unknown discrete derivatives of the unwrapped phase is minimized subject to the constraint that the two functions must differ by integer multiples of 2. The propagation of errors is prevented with this constraint and the resultant unwrapped phase is identical to the original wrapped phase when rewrapped. The minimization problem with integer variables is usually solved efficiently using the network structure strategies.

The region-growing algorithm (Xu and Cumming, 1999) begins unwrapping pixels of high coherence and proceeds along dynamic paths to pixels of high unwrapping confidence. Difficult areas of low coherence are later approached from a number of directions to unwrap. Thus, the algorithm is able to correct unwrapping errors to a certain extent and minimise their error propagation into a whole image.

5.8.14 Orbit Geometry and Baseline Refinement

Precision orbital state vectors of the satellite position and velocity supplied along with an ERS data pair have small errors of the order of tens of centimetres (ESA, 2004; Massonnet et al, 1993), which are not accurate enough to allow a rigorous transformation from the interferometric phase to the topographic height. The small orbit errors are translated into horizontal and vertical shifts in a resultant DEM. In order to minimise errors in orbit state vectors, a viewing geometry and baseline refinement procedure is used to calibrate the phase to height transformation. Viewing geometry and baseline are refined using a few GCPs well distributed in the image.

The ERS data pair was supplied with restituted orbital vector data due to telemetry failure during the pair acquisition (Smith, 2003). It contained larger errors than tens of centimetres error of precision orbital data. Therefore, viewing geometry optimization was used using GCPs. In SARscape DEM, the baseline refinement was achieved using 13 GCPs collected during a DGPS survey in the study area discussed below. The horizontal and vertical shift adjustment was incorporated to correct orbit error during geocoding in InSAR Toolkit.

GPS data processing

13 GCPs for orbital geometry refinement were collected during a differential GPS survey conducted with Trimble Pathfinder Pro-XRS GPS equipment with optimal settings (Appendix D-6). The Trimble Pathfinder Pro-XRS GPS is a mapping grade receiver and provides 10-30 cm accuracy with a carrier phase differential correction, but its accuracy degrades with an increase of baseline distance between a base station and a rover unit. The GPS data were logged for minimum 10 minute at a 15 second interval, a compatible logging interval with the Ordnance Survey London Active Station, at each point. The data were first real time code corrected with radio beacon of the UK Marine differential GPS service (MDGPS) located at North Foreland. The code phase corrected data were recorded during the survey. These code corrected positions are approximately 5 m accurate and the height accuracy is around two and half times lower than the horizontal accuracy. The data were post processed against the London Active Station to improve both horizontal and vertical accuracies. Trimble GPS Office Pathfinder version 3.00 software was used to determine the precise position and height coordinates of control points in WGS 84 reference by applying differential correction evolved from GPS code pseudo range and carrier phase measurements to minimise satellite ephemeris and atmosphere refraction errors. The precise height determination was possible with a single GPS receiver data when post processed for a differential correction against an OS active station within a baseline distance of 100 km (Penna et al, 2002) because the OS active station was 73 km from farther most point in the study area.

The RINEX data from the London Active Station for a longer duration than the survey period was downloaded from the National GPS network website. Control point data was post processed for code and carrier phase processing in which the code phase data was first differentially corrected and then carrier phase data was corrected for a high precision. The test points with shorter baselines were carrier phase corrected and yielded a fixed ambiguity position solution accurate to 60 cm in position and 1.50 m in height at 68 per cent of time while for longer baselines, lesser accuracy solution from code phase post processing was possible to compute due to a greater noise in carrier phase signal and yielded a float ambiguity position good to 1.2 m in position and 2.5 m in height at 68 per cent of the time (Appendix D-7). For longer baselines, it was

difficult to resolve the carrier phase ambiguities within GPS position computation due to the ionospheric and tropospheric refraction effects. Main (2000) also reported that the horizontal and vertical accuracies achieved with Trimble Pro XRS GPS are 0.2 m and 0.6 m for carrier phase post processing (with a base station set up within a few km) and 0.7 m and 1.5 m for real time code differential correction.

5.8.15 Phase to Height Conversion

The interferogram pattern is a function of both viewing geometry and surface topography. The surface topography is inferred from an interferogram, if the viewing geometry is accurately known. The topographic height is derived from an unwrapped interferometric phase based on a viewing geometry determined by means of orbital parameters using an equation:

$$\Delta\Delta\phi = \frac{2\omega BCos(\theta - \alpha)}{cr \sin\theta}\Delta z \qquad \ldots \qquad \text{(Eq. 5.18)}$$

The unwrapped phase was transformed to the height relative to the lowest point on the basis of orbital parameters in InSAR toolkit while in SARscape DEM, the orbital geometry and baseline were refined using 13 GCPs and then the phase was converted to the height relative to the lowest point based on the refined orbit parameters.

5.8.16 Geocoding

Geocoding is the transformation of the height interferogram from radar coordinates to a geographic coordinate system using range-Doppler approach in which the slant range is converted to the ground range and the azimuth direction is rotated to the north direction by resampling. Two methods are used to carry out geocoding namely; forward geocoding and backward geocoding. Forward geocoding (also referred to as ellipsoid geocoding) is applicable when no input DEM is used and is applied to transform the radar image directly to map geometry based on current or refined orbit parameters using a few well-distributed GCPs (Small et al, 1996). The backward geocoding (also referred to as terrain geocoding) is applied when a coarse DEM is used.

The forward geocoding was used in SARscape DEM and the resultant DEM was projected to geographic coordinates with the WGS84 ellipsoid at 1 arc second postings

and with heights above the mean sea level (Figure 5.9. left). The backward geocoding was performed in PulSAR/InSAR Toolkit using a 1 km coarse GTOPO30 DEM to project the DEM to geographic coordinates with WGS 84 ellipsoid at 1 arc second grid-cell spacing and with heights above the mean sea level (Figure 5.9, right).

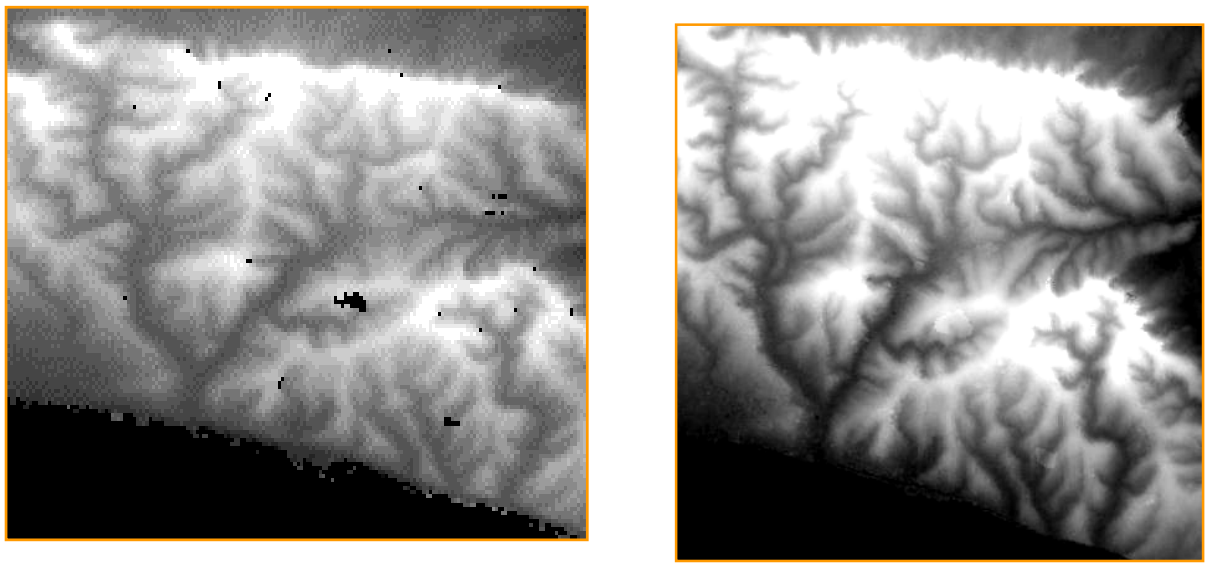

Figure 5.9: Geocoded InSAR DEMs derived from SARscape (left) and from PulSAR/InSAR Toolkit (right)

Backward geocoding

Backward geocoding is used to transforms from map geometry back to radar geometry and is a much faster than forward geocoding. Range and Doppler equations relate the position in the radar image to geodetic positions on the earth's surface as:

$$(s_x - p_x)^2 + (s_y - p_y)^2 + (s_z - p_z)^2 = r_s^2 \quad \ldots \quad \text{(Eq. .5.19)}$$

$$\frac{2}{\lambda} x \frac{s - p}{|s - p|} * (v_p - v_s) = f_{ref} \quad \ldots \quad \text{(Eq. 5.20)}$$

where s_x, s_y and s_z are the spacecraft position vectors at point S, v_s is the spacecraft velocity vector, p_x, p_y, and p_z are the position vectors at a DEM position P corresponding to spacecraft position S; v_p is the velocity vector of a DEM point, λ is the radar wavelength, r_s is the slant range and f_{ref} is the Doppler frequency of reference image.

The position P is iterated along a model of the spacecraft's orbit until the Doppler equation is satisfied. This provides the spacecraft position vector S and then the range equation is used to solve for the local slant range r_s.

Forward geocoding

Forward geocoding proceeds from radar geometry to map geometry. The extracted output pixels are located irregularly in space and, hence, an interpolation is applied to extract regularly spaced data. The interferometric height maps are geocoded to a map projection through solutions of the Range, Doppler and Ellipsoid datum equations.

Range equation (Equation 5.19), Doppler equation (Equation 5.20) and Datum equation based on three parameter datum shift transformation (Equation 5.21) are used to locate the position in the radar image to geodetic position on the earth's surface. The datum equation is given as:

$$\frac{(p_x - x_0)^2}{(a+h)^2} + \frac{(p_y - y_0)^2}{(a+h)^2} + \frac{(p_z - z_0)^2}{(b+h)^2} = 1 \qquad \ldots \qquad \text{(Eq. 5.21)}$$

where h is the height obtained from phase to height conversion, a and b are the semi major and semi minor axes of local earth ellipsoid respectively. In the geocoding, a, b and h are known, x, y and z coordinates of a point P (p_x, p_y and p_z) are computed by solving Equations 5.19, 5.20 and 5.21.

5.8.17 Post Processing

Visual inspection of a DEM in 3D display is used as a means of preliminary quality check to identify the mistakes or systematic errors. Both of these can be corrected by DEM editing. DEMs derived from remotely sensed data usually contain either systematic or random or both. The random error can be reduced to some extent by editing, but it can not be completely eliminated.

The InSAR DEMs are digital surface models, which contain first reflective elevation of surface in woodlands, scrublands and built-up areas. These also contain errors in forms of holes, spikes and failure values. Three methods of DEM editing are used to improve InSAR DEM quality derived from a single pair dataset namely,

filtering, filling and interpolation. Spikes are removed using mean filters. Small holes are filled using interpolation and large holes are edited and then interpolated to fill it. The derived DEMs of the Eastern South Downs from SARscape were edited to remove a few spikes and to smooth the surface of water bodies. The DEM from PulSAR /InSAR Toolkit were free from holes and failure values. It contains a few spikes and top of canopies and buildings.

5.8.18 Error Sources in SAR Data and InSAR DEMs

Technically, SAR Interferometry is a sound mapping technology for extracting a DEM in all weather conditions. It is influenced by the atmospheric perturbation between pair acquisitions. The factors influencing the accuracy of SAR data and their derived DEMs are listed in Table 5.10.

5.8.19 Strategies for Improving Accuracy with a Single Pair

The basic requirements for a repeat pass interferometry from ERS-1 and ERS-2 data pairs are stable terrain backscatter, similar atmospheric conditions, stable viewing geometry between two acquisitions, and a phase preserving SAR focussing. The accuracy of an InSAR DEM depends on the factors such as orbit accuracy, phase accuracy, atmospheric disturbance, processing error propagation, temporal decorrelation and phase height ambiguity discussed below.

Orbital accuracy

Current satellite navigation and tracking technology does not allow determining the orbital vectors precisely. Orbital errors result in horizontal and vertical shift in an entire DEM as well as height distortions. These are more evident and significant with increasing swath width. The orbital errors of ERS satellites are in the order of tens of centimetres and introduce systematic elevation errors ranging from metres to tens of metres. The orbit errors are reduced by an optimisation approach to refine the baseline and orbital geometry using the flat areas of known elevation, ground control points or seashores. The orbit geometry and baseline were refined with 13 GCPs collected using a differential GPS survey.

Table 5.10: Error sources in SAR data and derived InSAR DEMs (adapted from Gens and van Genderen, 1996)

Major element	Factors
Satellite System	• incidence angle • spatial resolution • internal clock drift • approximate focusing • image misregistration • system noise
Orbit	• determination of accuracy (precise range and range rate equipment) • baseline (coherence, geometric decorrelation) • repeat phase (temporal decorrelation) • non-parallel orbits (range mis-registrations)
Signal	• frequency • polarization (backscattering behaviour) • bandwidth (averaging) • noise/speckle
Topography	• phase difference (volume scattering) • direction of slope (angle of phase gradient) • surface characteristics (e.g. frozen soil)
Weather conditions	• wind (backscattering behaviour) • snow coverage (decorrelation)
Atmosphere	• Repeat pass SAR interferometry is not independent of clouds.

Phase accuracy

Phase noise originates at different stages of a DEM generation from acquisition, telemetry link, SAR focussing to InSAR processing. Phase noise (Zebker et al, 1994; Huang et al, 1996) is mainly caused by radar thermal noise, quantisation noise, speckle noise, defocussing, baseline and temporal decorrelation, registration noise, unwrapping error, processing artefacts, resampling and interpolation noise. The high phase noise can lead to loss of some fringes completely in the interferogram.

Phase noise is added by a large perpendicular baseline and is expressed in terms of height error using Equation 5.22, which was found to be 10.53 m for the selected data pair:

$$\Delta z = \frac{\lambda}{4\pi}\frac{R}{B} * \mathrm{Sin}\theta * \Delta\Delta\phi_{12} \quad \ldots \quad \text{(Eq. 5.22)}$$

Image co-registration is a crucial step in the entire InSAR processing chain. An insufficient co-registration between two images causes a drastic loss of coherence. It must be precise enough to achieve high phase coherence and must be more than half a pixel. If phase noise has crept in co-registration stage due to insufficient registration, it should be corrected before generating interferogram.

The geometric distortions in radar images depend on the characteristics of the sensor looking geometry and terrain type. The distortions in radar images result in forms of layover, shadow and foreshortening. Layover is caused by slopes steeper than the sensor incidence angle while shadow is caused by slopes less than sensor incidence angle. SAR images from ERS-1 and ERS-2 satellites contain almost no shadows due to 23 degree of incidence angle for earth observation (Eineder and Holzner, 2000), but they contain large amount of layover and foreshortening for mountainous region (Figure 5.10). A catchment with a moderate topography (average slope of 17 per cent) was selected to minimise these errors. The radiometric distortion was also lower for moderate relief catchment.

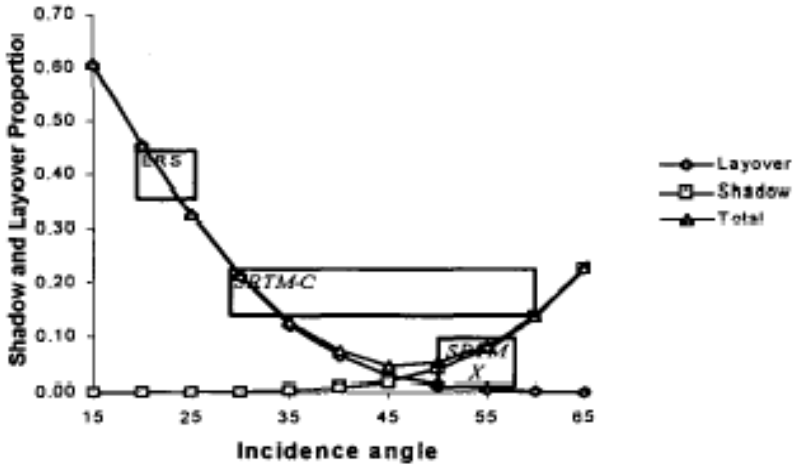

Figure 5.10: Layover and shadow proportions in the ERS and SRTM images and box showing range of that sensor (reproduced from Eineder and Holzner, 2000).

Atmospheric effects

Repeat pass interferometry relies on similar atmospheric conditions between two acquisitions, which are rarely met. Hence, atmospheric perturbation has become a major problem in images acquired in repeat pass observations particularly in the UK. It is

mainly due to the spatio-temporal variations of atmospheric water vapour in the ionosphere and troposphere. It generally affects the low frequency phase. Two methods can be used to minimise this effect. The first method is based on use of a larger baseline data pair to mitigate atmospheric perturbation, but the interferogram so derived is noisy and difficult to unwrap. The second method is based on the use of a coarse DEM available from public domains such as 1 km GTOPO30 DEM with an optimal baseline single data pair. This was applied in this study. The phase due to topography of a coarse DEM was subtracted from an interferogram and the residual interferogram was filtered to remove the low frequency atmospheric phase and to preserve the high frequency phase information. The filtered interferogram was unwrapped and the external topographic phase was then added back to the unwrapped phase. It helped in unwrapping phase in the low coherence areas. The influence of the ionosphere is still a subject of research. Hence, it was assumed to be a constant in both images, which cancelled out during interferogram formation.

Temporal decorrelation

Temporal decorrelation is a major problem in repeat pass acquisitions of InSAR data pair using a single SAR antenna because of the few weeks time difference between repeat pass acquisitions such as ERS-1, ERS-2, ENVISAT, Radarsat-1, JERS-1 etc (Table 5.6). This decorrelation was minimised during the dedicated tandem mission mode operation of ERS-1 and ERS-2 during 1995-96 to create valuable InSAR data pairs worldwide with a 24-hour time difference between acquisitions. A data pair from multidisciplinary mission with 24 hour was selected to minimise the temporal decorrelation and hence, led to generation of a quality DEM.

Processing error propagation

The phase errors are introduced at various stages of InSAR DEM generation and are identified using control parameters at that stage and needs to be minimised using an effective alternative strategy before proceeding to the next stage.

Broadly, phase noise in the derived interferogram is the summation of topographic phase, earth curvature error, orbital error, ionosphere and troposphere delay, and phase noise due to processing. Any source of phase noise results in decorrelation and is

characterised independently by the coherence. The level of noise in the interferogram is assessed by the coherence value and is filtered out using adaptive complex filters.

Height sensitivity and ambiguity

The height ambiguity (Massonnet and Rabaute, 1993) is a function of radar wavelength, satellite altitude, incidence angle and perpendicular baseline and represents a specific elevation interval for each fringe cycle of 2 π for all fringes across the interferogram. The height sensitivity is a function of phase ambiguity and is expressed for a repeat pass InSAR data pair:

$$\Delta z = \frac{z_{2\pi}}{2\pi} * \Delta\Delta\phi_{12} = \frac{\lambda}{4\pi}\frac{R}{B} * \mathrm{Sin}\theta * \Delta\Delta\phi_{12} \qquad \ldots \qquad \text{(Eq. 5.23)}$$

where Δ_Z is the corresponding height sensitivity, $z_{2\pi}$ is the height ambiguity, B is the perpendicular baseline, θ is the look angle and $\Delta\Delta\phi_{12}$ is the phase error in the interferogram.

The height ambiguity for each fringe is calculated:

$$Z_{2\pi} = \frac{\lambda}{2}\frac{R}{B} * \mathrm{Sin}\theta \qquad \ldots \qquad \text{(Eq. 5.24)}$$

where $z_{2\pi}$ is the height ambiguity in metres for each fringe cycle of 2π.

The height ambiguity per degree of each fringe is calculated by Equation 5.25

$$Z_{2\pi} = \frac{\lambda}{4\pi}\frac{R}{B} * \mathrm{Sin}\theta \qquad \ldots \qquad \text{(Eq. 5.25)}$$

For selected data set, the height ambiguity for fringe cycle of 2π and per degree are 66.55 m and 0.185 m respectively.

5.9 Generation of Validation DEM Data

5.9.1 Introduction

Digital photogrammetry was chosen to extract a reference DEM of a smaller area in the Eastern South Downs from 1:25 000 colour aerial stereo photographs for rigorous quality assessment of InSAR DEMs because it provides an independent DEM data set of a higher order accuracy, which is required for quality assessment of 25 m InSAR DEMs. Digital photogrammetry is the process based on digital stereo image analysis to extract digital elevation models and digital orthophotos (ERDAS, 2002). It is applied to stereo pairs collected by standard film and digital cameras and optical and SAR sensors from aerial and satellite platforms.

Photogrammetry has passed through the phases of plane table photogrammetry, analogue photogrammetry and analytical photogrammetry, and it is now in the phase of digital photogrammetry (Konecny, 2002). Digital photogrammetry is also referred to as softcopy photogrammetry. Its major application has been for the extraction of digital elevation information and orthophotos for integrating with other geo referenced spatial data in a GIS. Manual and automated digital photogrammetry both are used to extract elevation information from stereo photographs and images. The processing of digital photogrammetry and its quality assessment are discussed here.

Digital photogrammetry is performed by two broad ways for generating a DEM. The first way is based on original images and triangulation results for a DEM extraction and is used in the ERDAS Imagine OrthoBase Pro8.6 (ERDAS, 2002) while the second way relies on an epipolar stereo pair for DEM extraction and is used in the Geomatica OrthoEngine 9.1 (PCI Geomatics, 2003). The processing chain of DEM generation is different in both packages. In OrthoBase Pro, mass points in an area of relief change and good tonal contrast are generated to create a TIN model which is later converted to a raster DEM. This gives poor results in the area of small relief and poor tonal variation. On the other hand, Geomatica OrthoEngine generates regular mass points at specified grid-cell spacing across the photo stereo overlap and, subsequently, a DEM is generated. Geomatica OrthoEngine was preferred for this study and was chosen for

extracting a DEM from 1:25 000 scale colour aerial stereo photographs of the Saltdean catchment as compared to the Imagine OrthoBase Pro.

The photogrammetric processing chain (Figure 5.11) involves a number of processing steps to generate a DEM using an aerial stereo-image pair:

- acquiring and scanning of a stereo photograph or diapositive film pair,
- collecting precise GCPs from DGPS ground survey,
- setting up stereo-model,
- image matching, and
- extracting elevation parallaxes and heights

The theory of digital photogrammetric processing is discussed in the literature by Wolf and Dewitt (2000), Mikhail et al (2000), ERDAS (2002), and PCI Geomatics (2003).

5.9.2 Scanning of Aerial Stereo Pairs

Two pairs of stereo colour diapositive films were obtained from Infoterra and were scanned at an appropriate resolution of 20 μm (0.50 m ground equivalent pixel size) through a UMAX desktop flatbed scanner (Table 5.11). Colour films are usually scanned between 20 to 40 μm (Kasser, 2002; ERDAS, 2002). The digitised photographs were stored in a TIFF format with a storage space of about 370 MB each and were used to set up a photogrammetric project for elevation extraction. The scanning resolution was kept high to identify small features in an image and to locate ground control points precisely.

Although desktop scanners lack the image details and geometric accuracy but they are appropriate for the validation of 25 m InSAR DEM. It is known that a photogrammetric scanner produces high image quality and excellent position accuracy of 4 μm or less and was not a requirement for this study. Therefore, it was considered appropriate to use the desktop scanner for film scanning.

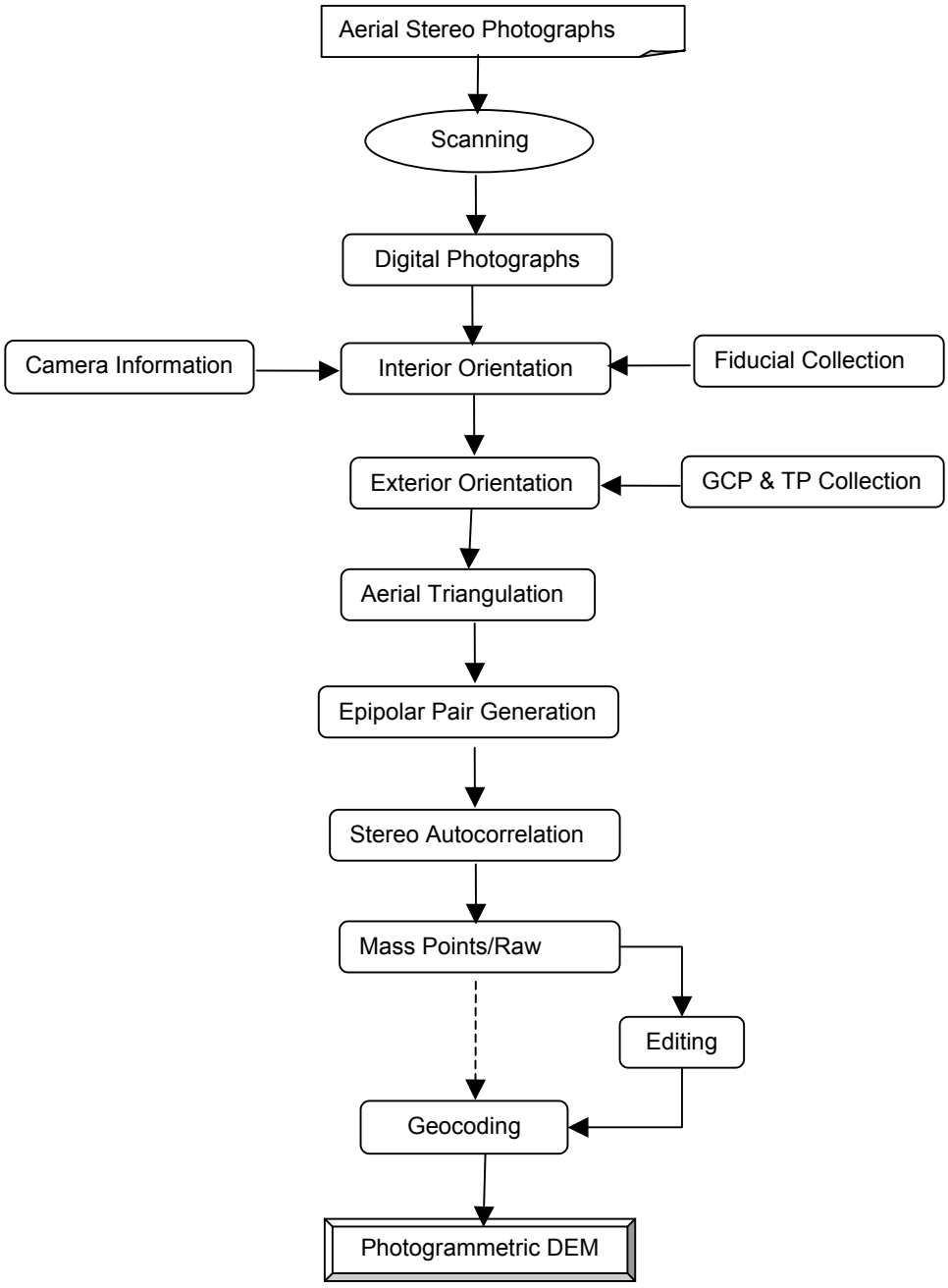

Figure 5.11: Digital photogrammetric processing chain

Table 5.11: Details of aerial photography for the Saltdean catchment and scanning specifications

Description of photographic project	
Name of photography project	East/West Sussex
Type of photography:	Colour
Date of photography	10 July 1991
Mission and flight line ID No:	43 and 91
Photo ID Number:	265, 264 and 263
Average photograph scale	1:25 000
Aircraft flying height	3805 m
Agency conducted survey	NRSC (Now, Infoterra)
Camera make and series	Leica, 15UAG 1072
Focal length	152.199 mm
Date of calibration	1 February 1991
Scanner	UMAX Mirage II Series A3 colour flatbed
	700 x 1400 dpi and 9800 dpi (interpolated)
Scanning resolution	20 μm (0.5 m ground equivalent)

5.9.3 Collection of GCPs for Exterior Orientation

Digital photogrammetry requires very precise measurements of interior and exterior orientations of a photograph pair. Precise GCPs are required for estimating the exterior orientation. Theoretically, three GCPs are required for estimating the exterior orientation for a pair of images (ERDAS, 2002). Twelve GCPs well distributed in an image area were used to increase the accuracy of an exterior orientation. These GCPs (Table 5.12) were obtained through a DGPS survey. The GCP data were post processed against the Ordnance Survey London Active Station discussed in Section 5.8.14. The GCP coordinates were carrier phase corrected and yielded a fixed ambiguity solution accurate to 60 cm RMSE in position and 1.50 m RMSE in vertical at 68 per cent. The GCPs were in the geographic coordinates with WGS 84 reference and were transformed to the British National Grid using the National Grid Transformation (OSTN02) (Figure 5.12), which provides better than 1 m transformation accuracy (Ordnance Survey, 2004). Similarly, the ellipsoid height were converted to the orthometric heights above the mean sea level referenced to the ODN datum using the National Geoid Model

(OSGM02) (Ordnance Survey, 2004) (Figure 5.13). The GCP coordinates in the British National Grid were used for estimating the exterior orientations. However, achieved horizontal and vertical accuracies of GCPs were adequate for exterior orientation. In addition to control points, two 1:10 000 scale topographic maps were also used for collection of validation data.

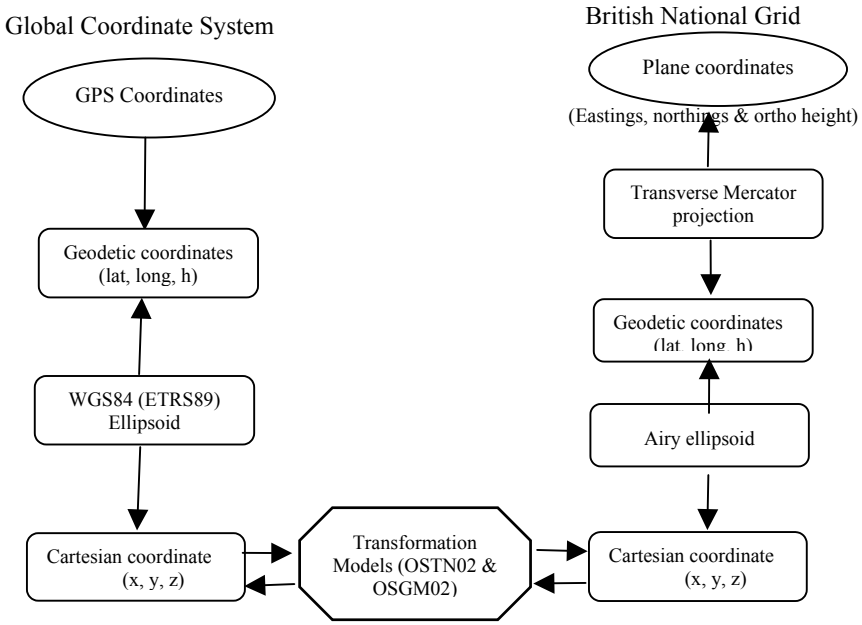

Figure 5.12: 3D coordinate transformation from WGS 84 coordinates to the British National Grid coordinates.

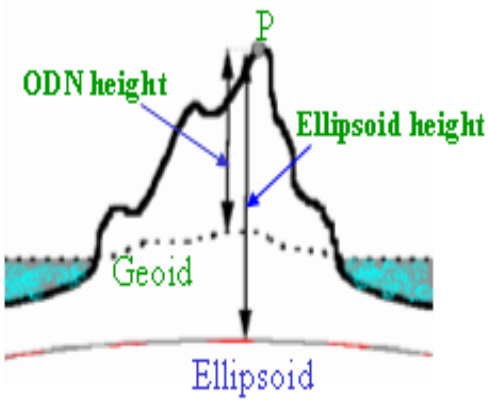

Figure 5.13: Transformation of ellipsoid heights to orthometric heights above mean sea level (reproduced from Ordnance Survey, 2002)

Table 5.12: GCPs for aerial photogrammetry

S. No.	Point type	Easting (m)	Northing (m)	Height (m)
1	GCP	535196.4	106077.4	154.8
2	GCP	535817.2	104098.4	76.1
3	GCP	538572.1	103267.9	28.3
4	GCP	540366.7	105809.9	115.2
5	GCP	539100.9	108428.7	30.6
6	GCP	536743.1	107377.2	177.2
7	GCP	536845.0	102829.5	31.9
8	GCP	539775.3	103655.1	124.7
9	CP	539849.6	103689.1	120.4
10	CP	540756.3	105673.1	85.0
11	CP	535622.1	106280.9	162.1
12	CP	537784.2	105017.8	76.1

(Note: CP stands for control point)

5.9.4 Computation of an Aerial Triangulation Model

A photogrammetric project in Geomatica OrthoEngine was set up for DEM generation. The camera calibration parameters (Appendix D-8) were specified from the camera calibration report to correct the distortions in the photographs due to the curvature of the lens, the focal length and the perspective effects. The projection information and scale of photographs were also specified in the project. The interior orientation was computed from calibration parameters and manual collection of camera fiducial marks located at each corner in the images. The exterior orientation parameters (X, Y, Z, ω, ϕ, κ) were estimated from the GCPs and tie points collected in the images. The location of GCPs in each image was identified and their coordinates were manually entered. Image tie points can either be collected manually or automated. The automatic collection procedure did not produce reliable results, so manual tie point collection was used and 10 tie points well distributed in the study area were collected. Addition of more tie points increases the accuracy of the triangulation, which was not possible to obtain from GCPs alone. A bundle block adjustment triangulation model was used to establish a rigorous mathematical relationship between the camera, the images and the ground using GCPs and tie points. The residual errors were used as the quality

parameters to determine the best possible solution for a triangulation model and reflected the overall quality of the triangulation model. Four check points were also introduced to provide an independent accuracy assessment of the triangulation model.

5.9.5 Image Matching and DEM Extraction

After an aerial triangulation model was established, the epipolar stereo pairs were produced to eliminate the y-parallax as well as to increase the speed of an image matching process. The epipolar images are a stereo pair reprojected such that both left and right images have a common orientation and matching feature appears along a common x-axis. An image matching process extracts matching pixels in an epipolar stereo pair. The aerial geometry from computed triangulation model is then used to calculate x, y, and z positions. There are three image matching approaches namely; area, feature or hierarchical-based matching. The hierarchical matching was used in this study as it is quick and reliable and minimises the number of mismatches.

Two epipolar DEMs were extracted using the hierarchical matching in the overlap area between epipolar pairs at 15 m with defined options (Appendix D-9) as there was more failure area at lower pixel spacing. Two DEMs derived from a left epipolar and a right epipolar pairs are given in Figure 5.14. It can be seen that these DEMs contained large areas at edges with clutter and holes. The mosaic of both DEMs was also created (Figure 5.15). It is also clearly seen that clutters and holes are the main feature at edges. The large clutter and holes at edges made this DEM not suitable as a reference DEM. The derived DEMs contained poorly correlated areas and artefacts, which need to be corrected either before or after the geocoding. The matching correlation was used for quality assessment of image matching. The vector points were generated from an epipolar DEM for 3D editing. The resultant DEMs could not be edited at edges due to software glitch. Therefore, it was decided to use mass points as reference data for quality assessment of the InSAR DEM because the derived photogrammetric DEM contained clutters at its edges and holes and DEM editing was very time consuming process so that it could be avoided by using mass points. After a close inspection of mass points, it was found that they too contained spikes, so it was further decided not to use the mass points for quality assessment of InSAR DEMs.

5.9.6 Post Processing and Error Sources

The quality of the derived photogrammetric DEM was assessed qualitatively in perspective view or 3D display. This has revealed many obvious serious anomalies in the DEM surface such as spikes, holes, and clutter at edges shown in Figure 5.15. The clutter in the DEM could not be edited in 3D editing environment as it was a time consuming exercise. Therefore, it was considered to use the mass points as the reference data to avoid 3D-DEM editing.

The quality of mass points was assessed in perspective view and it was found that they too contained spikes and holes. In other words, the quality of the derived DEM was so poor, so it was not appropriate to conduct its quality assessment. This DEM could not be further used for quality assessment of InSAR DEMs because of poor quality. The derived DEM accuracy depends on a number of factors (Smith and Smith, 1997) such as the scale and quality of the photographs, scanning resolution and quality, image matching control parameters, the quality of the aerial triangulation solution, DEM point spacing and terrain characteristics. The quality of ground control points also contributes to the DEM accuracy.

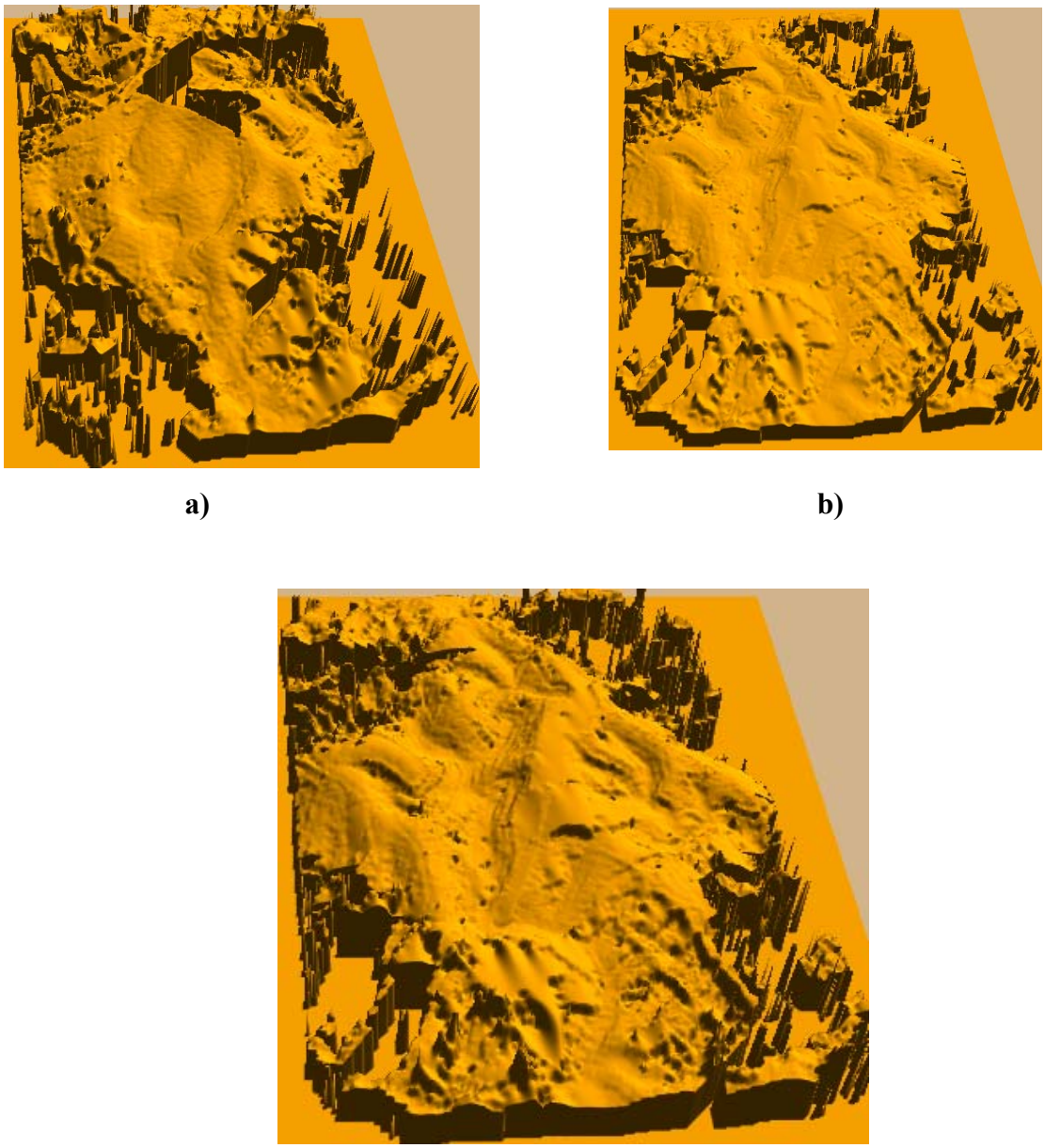

Figure 5.14: Photogrammetric DEMs of the Saltdean catchment extracted from a) left photograph pair, b) right photograph pair and c) a mosaic showing clutter at edges and holes in low tonal area with 100% level of details

5.10 Quality Assessment of InSAR DEMs

5.10.1 Introduction

The quality of an InSAR DEM depends on SAR system characteristics, terrain characteristics and processing strategy. Once the SAR system and terrain parameters were defined for a particular sensor and study area, the DEM accuracy can be assured and improved using an optimal processing chain with enough quality control parameters during a production process. The quality of InSAR DEMs can also be assessed independently against reference data of higher quality, irrespective of quality control in acquisition and production processes. Quality of InSAR DEMs was assessed by analysing statistical parameters and against reference checks points, a DEM and a drainage network and is discussed below.

5.10.2 Statistical Properties of InSAR DEMs

The InSAR DEMs were generated from an ERS-1 and ERS -2 tandem SAR raw data using the PulSAR/InSAR Toolkit and SARscape software with a different processing chain adopted with different algorithm chosen at different processing steps given in Figure 5.16 and Table 5.13. Basically, phase unwrapping is a crucial step in InSAR processing. Three unwrapping algorithms: a classical branch cut, a minimum cost flow network and a region growing were used to reconstruct DEMs. The statistical parameters of derived DEMs were first compared to evaluate their quality. The coordinate systems of derived InSAR DEMs are in the geographic coordinates with WGS 84 ellipsoid and datum and heights referenced to the mean sea level (Table 5.14).

Table 5.13: Coordinate systems and projections of InSAR and other DEMs

DEM	Coordinates/ projection	Horizontal datum	Vertical datum
1'' Pulsar DEM	Geographic	WGS 84	WGS 84 Geoid
1'' SARscape DEM	Geographic	WGS 84	WGS 84 Geoid
Off the Self DEMs			
25 m Landmap DEM	National Grid	OSGB36 (Airy)	MSL (OSGM02)
30 m ASTER DEM	UTM	WGS 84	Relative height
3'' SRTM DEM	Geographic	WGS 84	WGS 84 Geoid (EGM96)

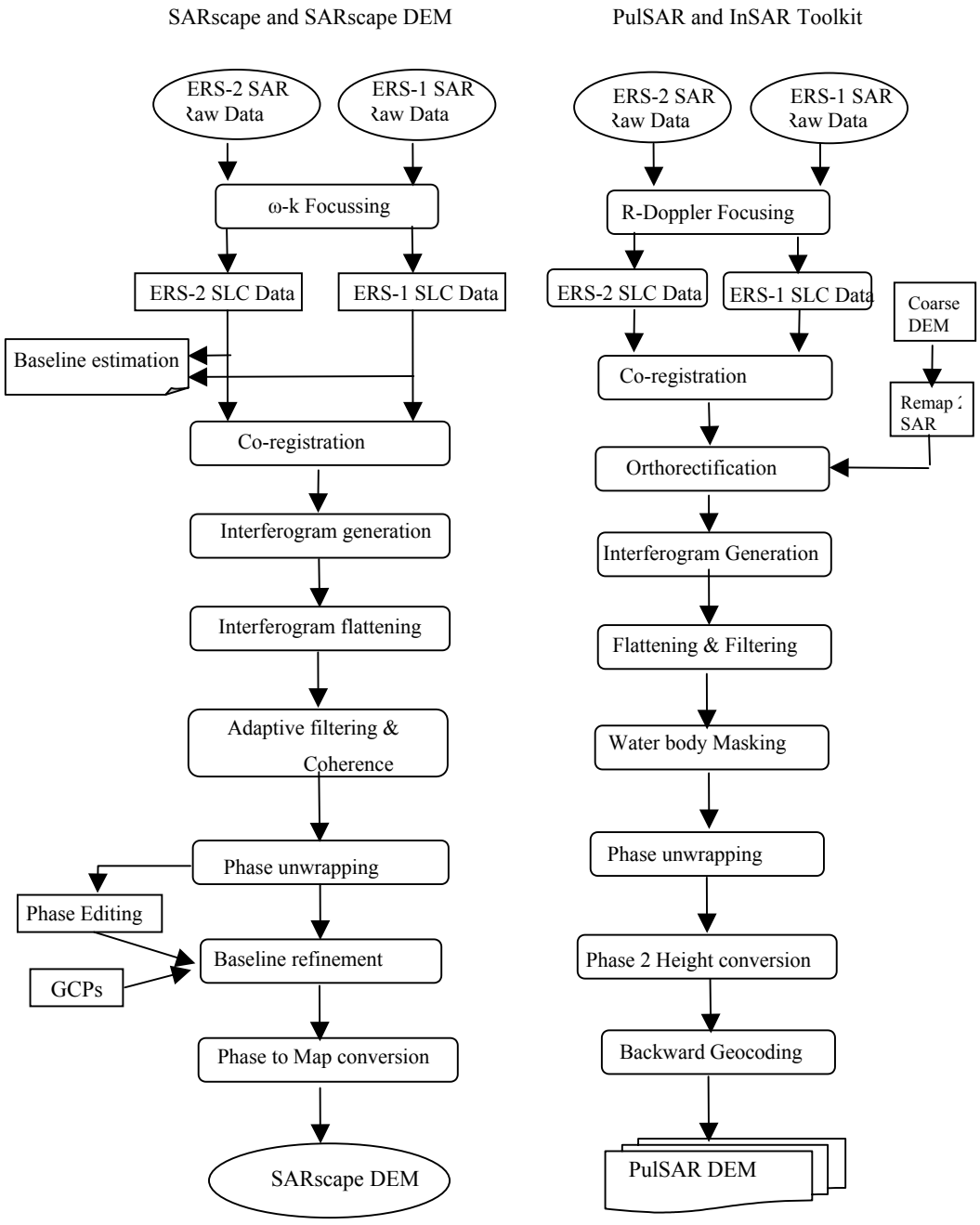

Figure 5.15: Comparison of SAR and InSAR processing chain in both SARscape and PulSAR/InSAR Toolkit packages

Table 5.14: Comparison of two InSAR processors

Processing step	SARscape & SARscape DEM	PulSAR & InSAR Toolkit
Similar Processing Step		
Baseline estimation	Orbit data	Orbit data
Coarse registration	Amplitude cross correlation	Orbital information
Fine registration	fringe visibility criterion	Coherence approach
Range filtering	Spectral shift filtering	Spectral shift filtering
Azimuth filtering	Common Doppler bandwidth	Common interferometric bandwidth
Interferogram generation	Hermitian product	Hermitian product
Filtering	Adaptive	Spatial smooth filtering
Coherence generation	Yes	Yes
Waterbodies masking	Yes (By Phase editing)	Yes
Phase to height conversion	Range-Doppler & ellipsoid equation	Range-Doppler equations
Different processing step		
Focussing	Ω-k in frequency domain	Range-Doppler
External DEM input	Not fully operational	1 km GTOPODEM
Baseline refinement	GCPs based	DEM based
Flattening	Ellipsoid flattening DEM flattening (No good result)	Terrain flattening (Phase detrending)
Phase unwrapping	Region growing unwrapper	• Standard unwrapper • MCFU unwrapper
Geocoding	Forward geocoding	Backward geocoding

As can be seen from Table 5.15, the DEM derived with MC-CT (minimum cost flow networks unwrapper with cartometric DEM as input) case has lower mean and higher standard deviation than the DEM derived with MC-GT (minimum cost flow networks unwrapper with GTOPO30 DEM as input). DEM derived with BC-CT (branch cut unwrapper with cartometric DEM as input) has lower mean and higher standard deviation than that of BC-GT (branch cut with GTOPO30 DEM as input) case. In other words, DEM derived with MC-CT appeared to be better than all other DEMs, but DEM derived with BC-GT is not poorer than that with MC-CT. The DEMs derived with PulSAR/InSAR Toolkit is better than that with the SARscape DEM. Rescaled SARscape DEM has heights ranging from 48-131 m which is lower than the actual ground height range and the PulSAR DEM. It appeared visually satisfactory, but statistically, it contained a large height shift. Even float SARscape DEM appeared visually satisfactory, but there is large height shift which is assessed and discussed later.

Table 5.15: Statistical Properties of InSAR DEMs using different unwrappers and input DEMs

Unwrapper/DEM Parameter	Data type	Min	Max	Mean	Std Dev	Median	Mode	Case
GTOPO30 as input DEM								
Branch cut (BC)	2 byte	-24	347	43.80	46.20	33	0	BC-GT
Minimum cost flow (MCF) networks	2 byte	-12	326	43.65	45.41	35	0	MC-GT
250 m cartometric DEM as input DEM								
Branch cut (BC)	2 byte	-12	318	42.55	47.46	28	0	BC-CT
Minimum cost flow (MCF) networks	2 byte	-19	319	42.38	47.58	28	0	MC-CT
SARscape DEM with GCPs								
Region growing (Rescaled)	1 byte	48	131	85.54	12.29	84	84	RG-RS
Region growing (RG)	Float	0	631	376.98	136.84	399.7	0	RG-FT

(GT stands for GTOPO30 DEM; CT for coarse Cartometric DEM; RS for rescaled to one byte; FT for float data type)

5.10.3 Quality Assessment against Reference Check Points

Twenty two reference check points were collected during a differential GPS survey to assess the accuracy of InSAR DEMs. The post processing of GPS data against the OS London GPS Active Station is discussed in Section 5.9.14. The accuracy of 22 check points during differential GPS survey was assessed (Appendix D-7). The heights in the InSAR DEMs were referenced to orthometric heights above the mean sea level (WGS84 Geoid) while the heights in check points were referenced to WGS 84 ellipsoid heights. Therefore, the GPS heights were transformed to orthometric heights above the mean sea level using the Global Equipotential Gravity Model (EGM96) (Limoine et al, 1998). The distribution of reference points in the Eastern South Downs is presented in Figure 5.17. The height values corresponding to the locations of 22 check points were extracted from an InSAR DEM and are tabulated against height value of the corresponding reference check points. First assessment was performed on the unfiltered InSAR DEMs and resulted in large RMS errors of 20.3 m due to spikes and holes, vegetation canopy and building tops. The accuracy assessment was also performed on off the shelf DEM data and RMS errors are presented in Table 5.16.

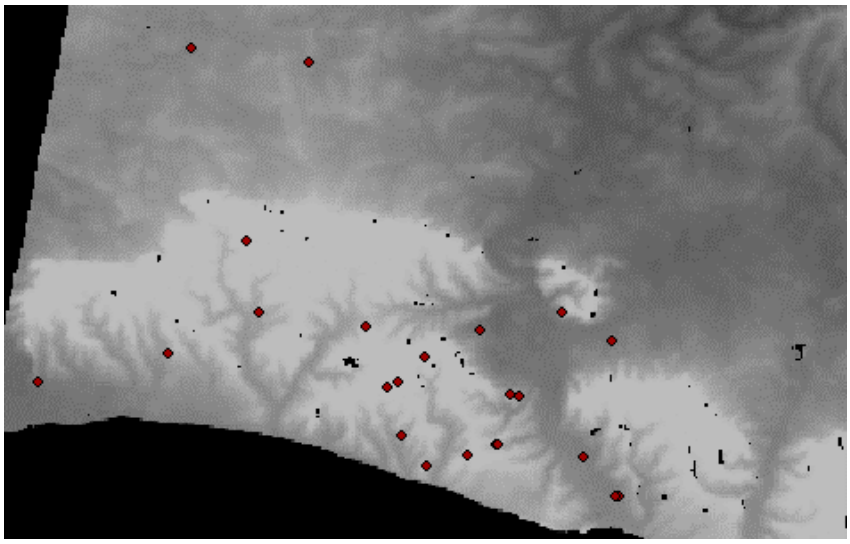

Figure 5.16: Spatial distribution of check points for quality assessment

Table 5.16: Quality assessment of derived InSAR and public domain DEMs

DEM	Data type	RMS Error (m)
Pulsar Raw DEM	2 byte integer	20.30 (12.8*)
SARscape Raw DEM	1 byte integer	35.79
Public domain DEMs		
Landmap DEM	2 byte integer	6.17
ASTER DEM	Float	5.94
SRTM DEM	2 byte integer	3.59

(* shows the recalculated RMSE after exclusion of four points close to obstructions)

When four check points were excluded from the accuracy assessment due to closeness to the buildings, tree canopy and electric power line, the RMS error was reduced to 12.8 m. Raw or unfiltered InSAR DEMs contained spikes and holes, vegetation canopy and building tops can be filtered with a 3x3 low pass filters to remove the spikes and holes. It was deliberately chosen to use raw DEM for the modelling to compare results with the Landmap DEM.

5.10.4 Quality Assessment against a Reference Drainage Network

The drainage network derived from the PulSAR DEM (Figure 5.18a) was assessed against the reference drainage network drawn and digitised from the 1:10 000 scale Ordnance Survey topographic maps. The PulSAR DEM was first conditioned to remove sinks using a standard flooding approach described by Jenson and Domingue (1988). Later, a drainage network was extracted from the conditioned InSAR DEM using a deterministic eight neighbours (D8) method on the basis of single flow (O'Callaghan and Mark, 1984) using Arc Hydro Tools. The stream ordering (Strahler, 1964) was assigned to both networks and length of each order was computed for both networks. The stream lengths of different stream orders were compared (Table 5.17). The first order stream length derived from the PulSAR DEM is poorly related to the reference drainage network while the second order stream length is better related between PulSAR DEM and the reference drainage network. The drainage networks from SARscape DEM (Figure 5.18b) and public domain DEMs (Figure 5.19, a, b, and c) were also derived and were compared against PulSAR DEM visually. The drainage network derived from SARscape is quite similar to that from PulSAR DEM. Other three public domain DEMs produced the drainage network of lower quality.

Table 5.17: Quality assessment of DEM on the basis of stream order lengths

Stream order	No of streams and total length (m)				Change (%)
	1:10 000 map		PulSAR DEM		
1	20	13898.07	4	2568.50	-81.52
2	9	3066.16	2	3263.48	6.44
3	9	5074.09	5	6728.43	32.60

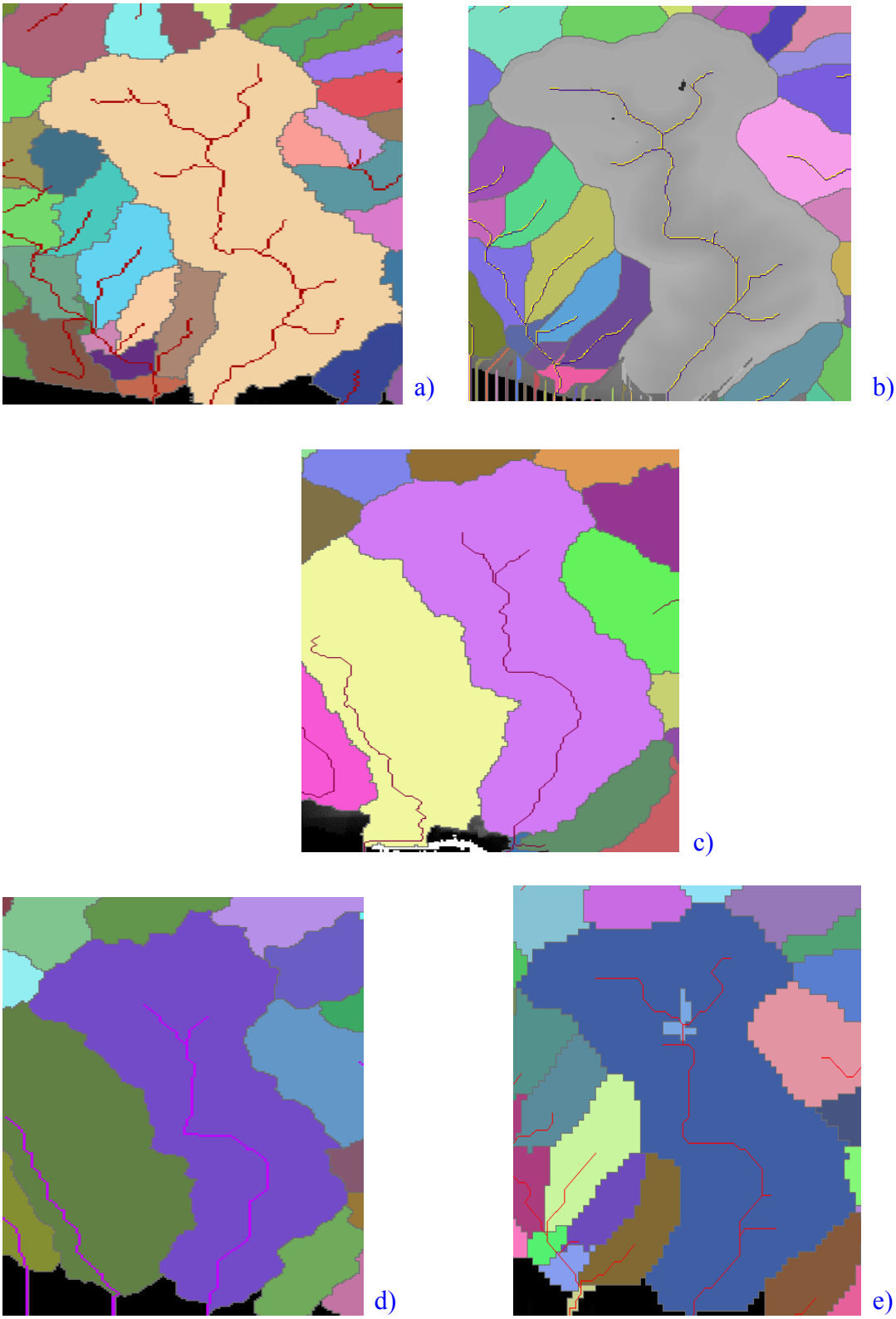

Figure 5.17: Drainage networks derived from a) a SARscape DEM, b) a PulSAR DEM, c) a 25 m Landmap DEM version 2, d) a 30 m ASTER DEM, and e) a 75 m SRTM-3 DEM

5.11 Concluding Remarks

5.11.1 Discussion

In this chapter, elevation data collection technologies were reviewed with reference to spaceborne SAR interferometry, which was explored to generate high resolution and quality DEMs for distributed modelling at catchment scale in the context of developing countries. The procedures and standards of quality assessment of a DEM were also discussed. The InSAR DEM quality was assessed using reference check points and a drainage network. Finally, strategies for deriving a high quality DEM from a single SAR pair are also discussed here.

Topographic mapping technologies

Cartometric DEMs are available at coarse resolution in developing countries and are the main source of elevation data because of non-availability of adequate quality DEMs derived from advanced technology. They are not produced to provide heights of the high density and accuracy required for distributed modelling (Shortridge, 2001). GPS and laser total station ground survey have operational constraints at catchment scale mapping. Remotely sensed topographic mapping technologies are cost effective and timely for catchment scale mapping. This is evident from this study that InSAR DEM was derived quickly from an ERS tandem data pair. Quality InSAR DEMs can be generated for developing countries and are used for distributed modelling.

Selection of an optimal SAR data pair

One of major problems in radar interferometry is how to select an optimal baseline data pair. The key parameters for selecting a quality InSAR pair: terrain type, radar band, baseline distance, temporal decorrelation and orbital accuracy are discussed. The optimal perpendicular baseline for ERS system is 50-300 m for topographic mapping (ESA, 2004). Considering key parameters, a suitable raw SAR data pair with 145 m baseline for the Eastern South Downs study area was selected from the ERS tandem mission archive.

Selection of SAR and InSAR Processors

Five processors such as SARToolbox, Imagine IFSAR DEM, EarthView InSAR, SARscape, PulSAR/InSAR Toolkit and ASF InSAR were tested in this study. These processors were evaluated for their capabilities on sensor and data format support, platform, processing facility and user friendliness. The SAR processor combined with an interferometric SAR processing should be preferred for customised raw data focussing, smooth import and analysis of input data for interferometric analysis. PulSAR/InSAR Toolkit and SARscape include both SAR and InSAR processing and were used for DEM generation.

InSAR DEM generation

Both SAR and InSAR processing involves a standard processing chain with a lot of inputs for an optimal result. The optimal processing parameters at each step within software functionalities were achieved to obtain the best results. InSAR DEMs were derived from an ERS tandem raw data using two selected processors. Some functionality in SARscape did not work satisfactorily as the software was not fully operational while PulSAR/InSAR Toolkit was an operational processor. PulSAR/InSAR Toolkit produced a better quality DEM than SARscape. This could be caused by different SAR and InSAR processing algorithms available in software. The quality of an InSAR DEM was optimised using the best processing strategy. InSAR DEM generation is less cumbersome and expensive than the optical stereo and radargrammetric DEM generation. A high accuracy could not be achieved for this pair discussed in following section. The derived DEM appears suitable for catchment scale distributed modelling.

InSAR DEM Quality assessment

Firstly, the quality of InSAR DEMs was assessed independently against 22 check points of higher quality collected from a DGPS survey. The accuracy of the raw DEM was found to be 20.3 m RMSE. This large RMS error was a result of non availability of precision orbital data because of satellite telemetry failure during the pair acquisition.

Secondly, a photogrammetric DEM was derived from 1:25 000 scale aerial photographs. It was found that derived DEM was of poor quality because of spikes,

holes and large clutter at edges. The quality of mass points was also poor. They too contained similar problems, which made mass points unsuitable to be used as reference data. Therefore, this validation DEM could not be used. The reason for this problem was that the Sussex photography project was not intended for topographic mapping.

A third assessment was performed against a reference drainage network. First order stream length has a poor correlation extracted from InSAR DEM and a reference network. Second and third order stream lengths have a good correlation. It indicates that a 25 m InSAR DEM is less suitable for the extraction of first order stream, but it is more suitable for the extraction of second and third order stream. In other words, InSAR DEMs are more appropriate for the extraction of a drainage network at 1:25 000 or smaller scale.

Suitability of InSAR DEM for Modelling

The main characteristics of a DEM for distributed modelling are resolution and quality. The horizontal and vertical resolutions of an InSAR DEM are 25 m and 1 m respectively. The vertical resolution is consistent with resolvable power of the InSAR technology. InSAR DEM generally provides the vertical accuracy on the order of metres, which is appropriate for catchment modelling. In this study, achieved vertical accuracy was on the order of tens of metres, which was caused by satellite telemetry failure during pair acquisition. This error was a systematic error, which was minimised during computation of slope gradient and aspect parameters for the model. Therefore, this systematic error did not affect the modelling results. Therefore, the InSAR DEM meets the modelling requirement despite a large vertical error.

5.11.2 Conclusions

- Elevation data collection technologies were reviewed with respect to radar interferometry. It was found that DEMs derived from advanced technology are not error free and contain some form of errors in some respect.

- SAR Interferometry has potential for catchment scale mapping in all weather conditions and provides the vertical accuracy on the order of metres. The DEM derived provided the vertical accuracy on the order of tens of metres despite

imprecise orbital data of a selected data pair. It has also shown potential for deriving quality DEMs for developing countries to meet the demand of the DEM for distributed modelling.

- The strategies for selecting an optimal single SAR data pair and a suitable SAR and InSAR processors are shown to be practicable. Five processors were tested in this study and two of them were found to be useful for generation of InSAR DEMs.

- InSAR DEM generation was found to be less cumbersome and expensive than optical stereo and radargrammetric DEM generation.

- The error reduction strategies have shown to improve the DEM accuracy for a single SAR data pair affected by orbital errors and atmospheric perturbations.

- The quality of InSAR DEMs was assessed against reference check points and the accuracy was found to be 20 m (RMSE) for unfiltered DEMs. The accuracy improved to 12.8 m after exclusion of four points, which were close to obstructions.

- A photogrammetric DEM derived from 1:25 000 scale aerial photograph pairs was found to be of poor quality due to clutter at edges and holes in low tonal areas.

- The drainage network derived from an InSAR DEM was assessed independently against a reference drainage network. It was found out that the InSAR DEM is poor for delineating the first order stream and is better for second and third order streams. The results indicate that InSAR DEMs are more appropriate for the extraction of a drainage network at 1:25 000 or smaller scale.

6

Analyses of Modelling Results

This chapter deals with the creation of twenty-five LISEM databases of input parameters at five spatial representations from five DEMs and other key spatial data. These databases were tested for model sensitivity to five resolutions of each DEM at three antecedent soil moisture conditions from a 6-hour storm. It was found that predicted runoff and soil loss decreased at coarser resolutions for each DEM dataset.

6.1 Introduction

Distributed modelling incorporates the spatial variability of input parameters and variables of catchment characteristics into the model response. Spatial variability of parameters can be obtained by choosing an appropriate spatial scale in terms of grid-cell resolution. A grid-cell resolution affects the routing of surface runoff and sediment movement across the catchment. It also affects the model response in terms of spatial distribution of runoff and sediment, and shapes of hydrograph and sedigraph observed at an outlet. Antecedent soil moisture condition is another factor which influences the model response is also considered in modelling. In this study, effects of different resolutions on surface hydrologic and erosion processes at three antecedent moisture conditions are, therefore, investigated from a 6-hour storm.

For this study, key spatial data of the Eastern South Downs: five DEMs from various sources namely, three interferometric SAR DEMs, a cartometric DEM and an optical stereo DEM; a land use and land cover map; and a soil map were resampled into

five resolution datasets; 20, 40, 60, 80 and 100 m. Twenty-five datasets of the Saltdean catchment were extracted at five resolutions each for five DEMs and were brought into PCRaster to create twenty-five LISEM databases of catchment characteristics. These databases were tested in the LISEM version 2.03 for model performance evaluation and sensitivity analysis at three moisture conditions such as low, medium and high for a storm on 30 October 2000. This chapter reports extraction of twenty-five datasets of the catchment, creation of 25 LISEM databases of input parameters and testing performance evaluation and their sensitivity to model outputs. It also includes the error propagation in dynamic and distributed modelling.

6.2 Selection of a Model Version

A LISEM model version 2.03 was selected for this study because it was developed for slope ranges of the Saltdean catchment. The slope in most of the catchment (98.8 per cent) is below 50 per cent (Appendix E-1). This version resulted in same catchment area and cumulative rainfalls from a single resolution dataset derived from five DEM datasets unlike current versions discussed below. The disadvantage of this model was that it did not include a surplus infiltration procedure to the kinematic wave, which resulted in slightly less infiltration and, hence, a little more runoff. As this study was mainly concerned with the effects of different spatial representations on surface hydrologic and erosion processes, so it was considered appropriate to use the model for this study.

Current LISEM versions namely, 2.158 and 2.154 have been modified for very steep terrain catchments of China with slopes ranging from 50 to 250 per cent (Jetten, 2004; Hessel et al, 2003; LISEM, 2004). The slope has been added to modify new grid-cell length in the direction of flow, which is equal to the grid-cell length divided by cosine of its slope instead of actual grid-cell length. This affected many calculations in the model and resulted in different cumulative rainfalls and catchment areas from a single resolution dataset derived from five DEM datasets (Appendix E-2). Therefore, the current version could not be used.

6.3 Key Spatial Data of the Saltdean Catchment

A small agricultural catchment of approximately 800 hectares was selected from the Eastern South Downs for modelling storm surface runoff and erosion dynamics. Key spatial data of the Eastern South Downs derived from various sources were first resampled into five resolutions namely, 20, 40, 60, 80 and 100 m using sampling schemes discussed in the later part of this Section. Then, key spatial data of the Saltdean catchment were extracted. A raingauge map is required to represent spatial variability of a rainstorm in the catchment through multiple raingauge stations. Table 6.1 shows the key spatial data source and their five resampled spatial representations. The extraction of each key spatial data of the catchment is discussed in next sections.

Table 6.1: Key spatial data and their five spatial representations for modelling

Key spatial data	Data source	Spatial representations
DEMs	1'' PulSAR DEM	20, 40, 60, 80, and 100 m
,,	Cartometric DEM from 1:25 000 scale	20, 40, 60, 80, and 100 m
,,	25 m Landmap DEM	20, 40, 60, 80, and 100 m
,,	3 arc SRTM-3 DEM	20, 40, 60, 80, and 100 m
,,	30 m ASTER DEM	20, 40, 60, 80, and 100 m
Land use and land cover	20 m SPOT-1 XS data	20, 40, 60, 80, and 100 m
Soils	NATMAP Vector 1:250 000 scale	20, 40, 60, 80, and 100 m
Raingauge location	University of Sussex	Single point raingauge data

6.3.1 Digital Elevation Models

Firstly, a few InSAR DEMs of the Eastern South Downs with 1" grid-cell spacing were generated by radar interferometry from an ERS-1 and ERS-2 SAR raw tandem pair. The best of them was used for modelling. The methodology of generating InSAR DEMs and their quality assessment was discussed in Chapter 5.

Secondly, cartometric DEMs of the Saltdean area at five grid-cell sizes: 20, 40, 60, 80 and 100 m were generated using a nonlinear interpolation method from 849 points collected manually from a 1:25 000 scale Pathfinder map. Thirdly, three public

domains DEMs namely, two interferometric SAR DEMs such as 25 m Landmap DEM version 2.0 (Landmap, 2003) and 3" SRTM-3 DEM (USGS, 2003), and an optical stereo DEM such as 30 m ASTER DEM with relative heights (USGS, 2004) were obtained. The description of public domain DEMs was discussed in Section 5.7.

All five DEMs were in different coordinates, ellipsoids and datums (Table 6.2). The PulSAR DEM was projected to the British National Grid coordinates at five grid-cell sizes using a national coordinate transformation, OSTN02 and cubic convolution resampling method. Similarly, SRTM and ASTER DEMs were suitably projected to the British National Grid coordinates at five grid-cell sizes. The Cartometric and Landmap DEMs were already in the British National Grid. Therefore, they were used as such. DEMs of the Saltdean catchment at each resolution were extracted from five resampled DEMs using a catchment area mask digitised from the 1:10 000 scale topographic maps. These DEMs were imported to PCRaster for generation of LISEM databases discussed in the next sections.

Table 6.2: Projection of five DEMs to the British National Grid

DEM	Coordinates/ projection	Horizontal datum	Vertical datum	Reprojected to
1'' Pulsar DEM	Geographic	WGS 84	WGS 84 Geoid	National Grid (OSTN02)
20 m Cartometric DEM	National Grid	OSGB36 (Airy)	Mean sea level	Not reprojected
25 m Landmap DEM	National Grid	OSGB36 (Airy)	Mean sea level	Not reprojected
3''Raw SRTM DEM	Geographic	WGS 84	WGS 84 Geoid	National Grid (OSTN02)
30 m ASTER DEM	UTM	WGS 84	Relative height	National Grid

The choice of an appropriate DEM grid-cell resolution is one of the key problems in distributed modelling in a GIS. Maidment (1996) suggested using one thousand-million rule as a guide. The grid-cell resolution of a DEM for the Saltdean catchment was worked out to be approximately 10 m as per rule, but there was a constraint in data availability as the original resolutions of SPOT-1 multispectral data

and InSAR DEM were 20 m and 25 m respectively, so a 20 m grid-cell resolution was chosen as it matched with resolution of SPOT XS-1 data, thus avoiding resampling. The minimum catchment area to be delineated using a DEM was worked out to be 40 hectares, which is lower than the area of the selected catchment. Therefore, it satisfies the rule.

6.3.2 Land Use and Land Cover Data

The land use and land cover map of the Saltdean catchment was extracted from the land use and land cover of the Eastern South Downs derived from digital classification of SPOT multispectral data of 26 October 2000, described in Chapter 4. Area weight classified image of nine classes was filtered four times using a 3x3 majority filter to remove the unrelated scattered pixel patches and to smooth the thematic image. The smoothed classified image was used to extract the land use and land cover map of the catchment at 20 m resolution. The smoothed thematic image was further resampled using a nearest neighbour method to extract 40, 60, 80 and 100 m resolution maps of the catchment to derive land use dependent model parameters. Table 6.3 shows the distribution of each land use and land cover class in the catchment at 20 m resolution.

Table 6.3: Area of land use and land cover class of the Saltdean catchment

S. No.	Description of class	Id	Area (ha)	Per cent
1.	Bare soil - ploughed/sown field	1	114.04	14.06
2.	Harvested field	2	150.24	18.52
3.	Set-aside	3	21.64	2.67
4.	Hill grassland	4	213.16	26.28
5.	Semi-improved grassland	5	198.56	24.48
6.	Improved grassland	6	64.6	7.96
7.	Open wood and scrub land	7	40.08	4.94
8.	Dense wood and scrub land	8	2.48	0.31
9.	Built-up land	9	6.36	0.78

6.3.3 Soil Data

The soil map of the Eastern South Downs at a 1: 250 000 scale was rasterised to five grid-cell resolutions (Table 6.1) on the basis of dominant soil series, discussed in

Section 3.2. The soil map of the catchment at each resolution was then extracted. The small fractions of Upton-1 and unsurveyed Andover associations were merged into the Andover-1 association discussed in Section 3.4.3. Two dominant soil series were finally used in the soil map of the catchment, which were used to assign the infiltration parameter values to obtain infiltration parameter maps at five resolutions.

6.3.4 Distribution of Rainfall Intensity in the Catchment

Spatial distribution of the rainfall in a catchment can be computed from a location map of multiple raingauge stations using either the Thiessen polygon or geomorphological analysis technique. A single raingauge station data was available for the catchment from the University of Sussex, Falmer, Brighton which is approximately 2.5 km from the northwest of catchment top boundary (Figure 6.1), described in Chapter 3. Therefore, the distribution of rainfall intensity over the catchment was assumed to be uniform, which is valid for a frontal storm considered for simulation. A rain zone map was created from a raingauge station map using a 'spreadzone' command. A breakpoint rainfall intensity data file was created in the ASCII format with a defined structure from hourly rainfall intensity data to drive the model (Appendix E-3). The breakpoint rainfall intensity data are discussed in Section 3.2.9.

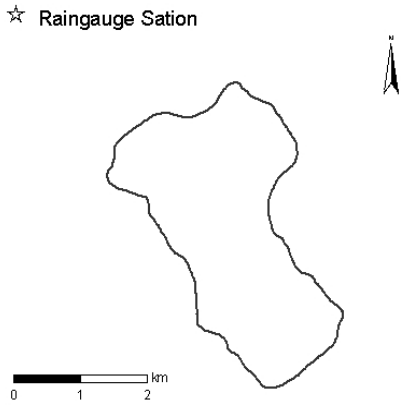

Figure 6.1: Location of the raingauge station with reference to the catchment

6.4 Creation of LISEM Databases

Three key spatial data such as a DEM, a land use and land cover map, and a soil map at 20 m grid-cell resolution were first converted into the ArcInfo Grid ASCII

format for importing to PCRaster as its import functionality is very limited. These key spatial datasets were imported into PCRaster using an 'asc2map' command (Appendix E-4). In addition to three key datasets in the PCRaster map format, crop, soil and surface parameter values were required to create a LISEM database of input parameters. Most of these parameters were estimated for possible field conditions observed and assumed in the catchment for a storm on 30 October 2000 in combination with the guidelines of parameters given in the LISEM and EUROSEM Manuals (Jetten, 2002; De Roo et al, 1995; Morgan et al, 1998) and similar catchment datasets. The characteristics of the Saltdean catchment are quite similar to that of the Catsop catchment, South Limburg for which the model was originally developed, and Ganspoel catchment where the model was applied (Boardman et al, 2000). It has also similarity with flood prone region in France as well. These parameters are estimated and discussed in the following sections. Similarly, four other resolution key spatial datasets were imported into PCRaster to create LISEM databases at five resolutions each from five DEMs.

6.4.1 Topographic Parameters

A DEM itself was not used in the model and its derived topographic parameters such as slope gradient, local drainage direction (aspect), catchment area and outlet of the catchment were used. These were derived from a DEM using the PCRaster commands (Appendix E-5). The slope gradient used in the model was the sine of the slope, not the tangent and its value lies between zero and one. The calculated slope gradients of each resolution datasets were well in agreement with the defined limit.

6.4.2 Micro-topographic Parameter

Micro-topographic parameter such as random roughness for a storm of 30 October 2000 was not available. In that case, it was estimated for assumed field conditions with the guidelines in the LISEM and EUROSEM Manuals (Jetten, 2002; Morgan et al, 1998) and relevant random roughness data from similar catchments in the Limburg, Waremme and Ganspoel. Random roughness value (Table 6.4) was taken for same land use and nearly same time period from the Catsop, Waremme, and Ganspoel

catchment datasets (LISEM, 2004). Similarly, other parameters for a historical event were also estimated from relevant data of other catchments and standard tables.

6.4.3 Crop and Vegetation Parameters

Crop and vegetation parameters such as soil cover, crop height and leaf area index (Table 6.4) were estimated for similar land use classes from the Manuals and other catchment datasets. Leaf area index for each crop and vegetation at same time period in the catchment were estimated from leaf area index data of crop and vegetation for whole crop growth period given in the ANSWERS Manual (Dillaha, 2004; Beasley and Huggins, 1981). Soil cover and crop height values were estimated for similar conditions in the catchment from relevant catchment datasets.

6.4.4 Soil Erosion Parameters

Soil erosion parameters such as soil aggregate stability, soil cohesion, additional cohesion by plant roots and soil median texture (Table 6.4) were estimated for possible field conditions from a combination of parameter standard table and the Catsop and Ganspoel catchment datasets (LISEM, 2004). Crop parameters for October month were estimated from the Catsop catchment dataset for same month assuming that arable land were either sown or fallow with nearly no soil cover. In the Manuals, erosion parameter tables for winter-wheat, forest, orchards, grassland and bare soils were given indicating input values for a particular land use.

6.4.5 Soil Surface Cover Parameters

Soil surface cover such as crust cover, wheel-track cover, grass strips, stone cover and road cover were not possible to estimate from land use and land cover map derived from remote sensing. Therefore, it was assumed that none of them existed in the catchment. Hence, all cover parameters were set to zero (Table 6.4). The maps of zero parameter values were created as they were required for running the model.

6.4.6 Channel Parameters

The local drainage direction (aspect) and slope gradient of the main channel were derived from a DEM. Channel width and its cross section shape was measured

during the field survey. The Manning's roughness and cohesion of the channel were estimated from a combination of parameter standard table and similar catchment datasets (Table 6.4).

Table 6.4: Crop, soil and erosion parameter table for the Saltdean catchment

Landuse	*Units*	PER	CH	LAI	RR	N	AGGRSTAB	COH
	0	1	2	3	4	5	6	7
Bare field	1	0.000	0.030	0.000	0.970	0.120	-1.000	3.000
Harvested field	2	0.150	0.150	0.390	0.970	0.140	10.000	3.000
Set-aside	3	0.500	0.050	0.450	0.970	0.140	10.000	3.000
Hill grassland	4	0.950	0.100	1.860	0.700	0.227	-1.000	3.000
Semi-improved grassland	5	0.950	0.100	1.860	0.700	0.227	-1.000	3.000
Improved grassland	6	0.950	0.100	1.860	0.700	0.227	-1.000	3.000
Open woodland and scrub	7	0.950	5.000	1.860	1.360	0.300	-1.000	3.000
Dense woodland and scrub	8	0.950	5.000	1.860	1.360	0.300	-1.000	3.000
Built-up land	9	0.000	0.000	0.000	0.500	0.010	200.00	9999

Units	COHADD	D50	ROADWIDT	GRASSWID	CRUSTFRC	COMPFRC	STONEFRC
0	8	9	10	11	12	13	14
1	0.100	30.00	0.00	0.00	0.00	0.00	0.00
2	0.600	30.00	0.00	0.00	0.00	0.00	0.00
3	0.600	30.00	0.00	0.00	0.00	0.00	0.00
4	3.320	30.00	0.00	0.00	0.00	0.00	0.00
5	3.320	30.00	0.00	0.00	0.00	0.00	0.00
6	3.320	30.00	0.00	0.00	0.00	0.00	0.00
7	2.800	30.00	0.00	0.00	0.00	0.00	0.00
8	2.800	30.00	0.00	0.00	0.00	0.00	0.00
9	9999	30.00	0.00	0.00	0.00	0.00	0.00

6.4.7 Hydraulic Parameter

The Manning's roughness (n) for overland and channel flow was estimated for each land use and land cover from the standard table and similar catchment datasets.

The Manning's n for channel flow was estimated for the channel condition and cross section observed during the field survey (Table 6.4).

6.4.8 Infiltration Parameters

A single layer Green and Ampt model was chosen for simulating the infiltration process in the catchment. Its parameters such as hydraulic conductivity, average suction head at wetting front, effective porosity, antecedent moisture content and soil depth were estimated from soil property dataset of the NATMAP data. Antecedent soil moisture content (AMC) was assumed to be uniform for a soil series in the catchment and was considered for three possible conditions. Low, medium and high AMCs were assumed as 0.07 and 0.08; 0.22 and 0.24; and 0.44 and 0.46 for the Marlow and the Andover series respectively for an extreme event on 30 October. The calculated values of saturated hydraulic conductivity and corresponding suction head at the wetting front (Table 6.5) were higher because the effective hydraulic conductivity used for an unsaturated flow is not saturated hydraulic conductivity and is approximately half the corresponding value for a saturated flow (Rawls, 1983). Moreover, a PTF used for calculating saturated hydraulic conductivity was correlated with measured saturated values which did not reflect hydraulic conductivity during a rain storm. Therefore, these values were calibrated in the model on the basis of runoff coefficient and total amount of erosion in the catchment and were finally set to 2.408 mm h^{-1} and 4.266 cm and 2.416 mm h^{-1} and 3.922 cm for the Andover series and Marlow series respectively for the catchment (Table 6.5), except for built-up land where the parameter value was set to zero. These assumptions simplified both the spatial and temporal variations to a large extent. Nevertheless, this approach was considered to be acceptable given the very high intensity of the storm event making small variations in infiltration being relatively unimportant and the fact that surface conditions on arable fields were with nearly no soil cover and fine seedbed during October 2000. The limit of each parameter value (Table 6.6) provides a cross check on calculated parameter value.

Table 6.5: Calculated and calibrated parameters for a single layer Green and Ampt model

Soil series	Unit	Ksat1	Psi1	Thetas1	Thetai1	Soildep1
	0	15	16	17	18	19
Calculated values						
Andover	3	4.817	42.666	0.48	0.24	250.0
Marlow	8	4.833	39.218	0.44	0.22	250.0
Calibrated values						
Andover	3	2.408	4.266	0.48	0.24	250.0
Marlow	8	2.416	3.922	0.44	0.22	250.0

Table 6.6: Limits of Green and Ampt parameters for the Saltdean catchment (adapted from Chow et al, 1988)

Soil Class	Porosity	Effective porosity	Wetting front suction head, cm	Ksat (cm/h)
Silt loam	0.501	0.486	16.68	0.65
	(0.420-0.582)	(0.394-0.578)	(2.92-95.39)	

(The number in parentheses below each parameter is one sigma of the parameter value given)

6.4.9 Creation of LISEM Databases

Crop and vegetation, soil and erosion parameters for each land use and land cover class were estimated and tabulated with a defined structure to create each parameter map by reclassifying the land use and land cover map (Table 6.4). Similarly, infiltration parameters for dominant soil series were estimated and tabulated in a defined structure table (Table 6.5). After having imported key spatial datasets of various grid-cell resolutions into the PCRaster GIS, these data were used to derive individual input parameter map using a PCRaster command. Or alternatively, a PCRaster script was written for creating a LISEM database of input parameters from key spatial datasets and two parameter tables (Appendix E-5). This script was run at the PCRaster prompt by a single command and a LISEM database of 30 input parameters was created in a single operation. Another PCRaster script batch file was written for quick displaying of rainfall time series data, key spatial dataset and input parameters category wise from a single batch command at the PCRaster prompt (Appendix E-6). A total of twenty-five

LISEM databases of 30 parameters each were created which include 750 maps for testing their sensitivity in the LISEM version 2.03 at three antecedent moisture conditions. It was not possible to include all the maps created in this chapter but a LISEM database of 30 parameter maps of the Saltdean catchment are presented in Figures 6.2 through 6.7.

6.5 Effects of Resolution of DEM Derivatives

DEM datasets of the catchment at five spatial representations were studied to assess the effects of grid-cell size on four DEM derivatives such as catchment area, slope gradient, drainage and channel lengths. The grid-cell resolution and grid-cell size are inversely correlated. In other words, increased grid-cell resolution corresponds to a decrease in the grid-cell size and vice versa. The effects of resolution on DEM derivatives are discussed below.

6.5.1 Catchment Area

The catchment area derived from the PulSAR DEM increased by 8.86 per cent as the grid-cell size was increased from 20 to 100 m (Figure 6.8). The similar trend was observed at all five resolutions for all DEMs except there was a little change at 80 m resolution in the ASTER DEM caused by exclusion of two boundary pixels, and at 100 m resolution in the Landmap, SRTM and ASTER DEMs caused by inclusion of two to three boundary pixels. The catchment area increased by approximately 9 per cent as the grid-cell size was increased from 20 to 100 m (Appendix E-7).

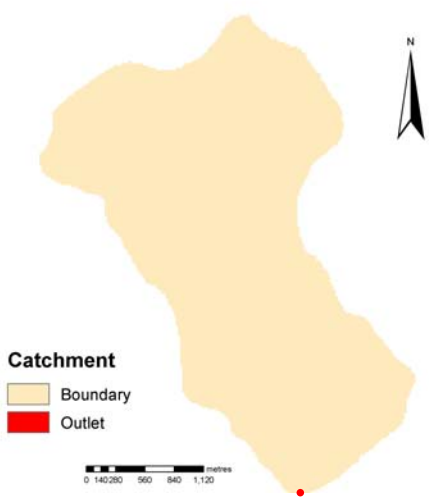

a)

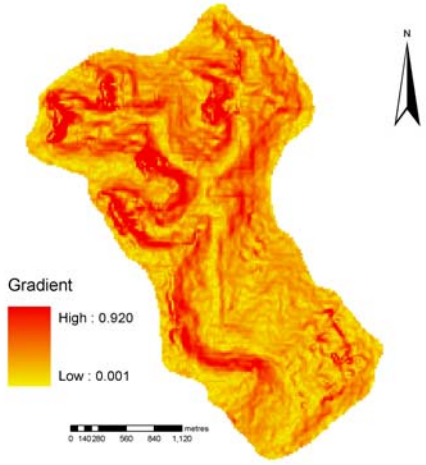

b)

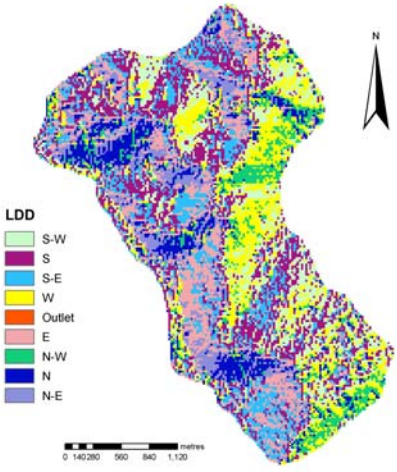

c)

d)

Figure 6.2: Catchment parameter maps; a) catchment boundary and outlet, b) slope gradient, c) local drainage direction (LDD), and d) spatial distribution of a rain storm

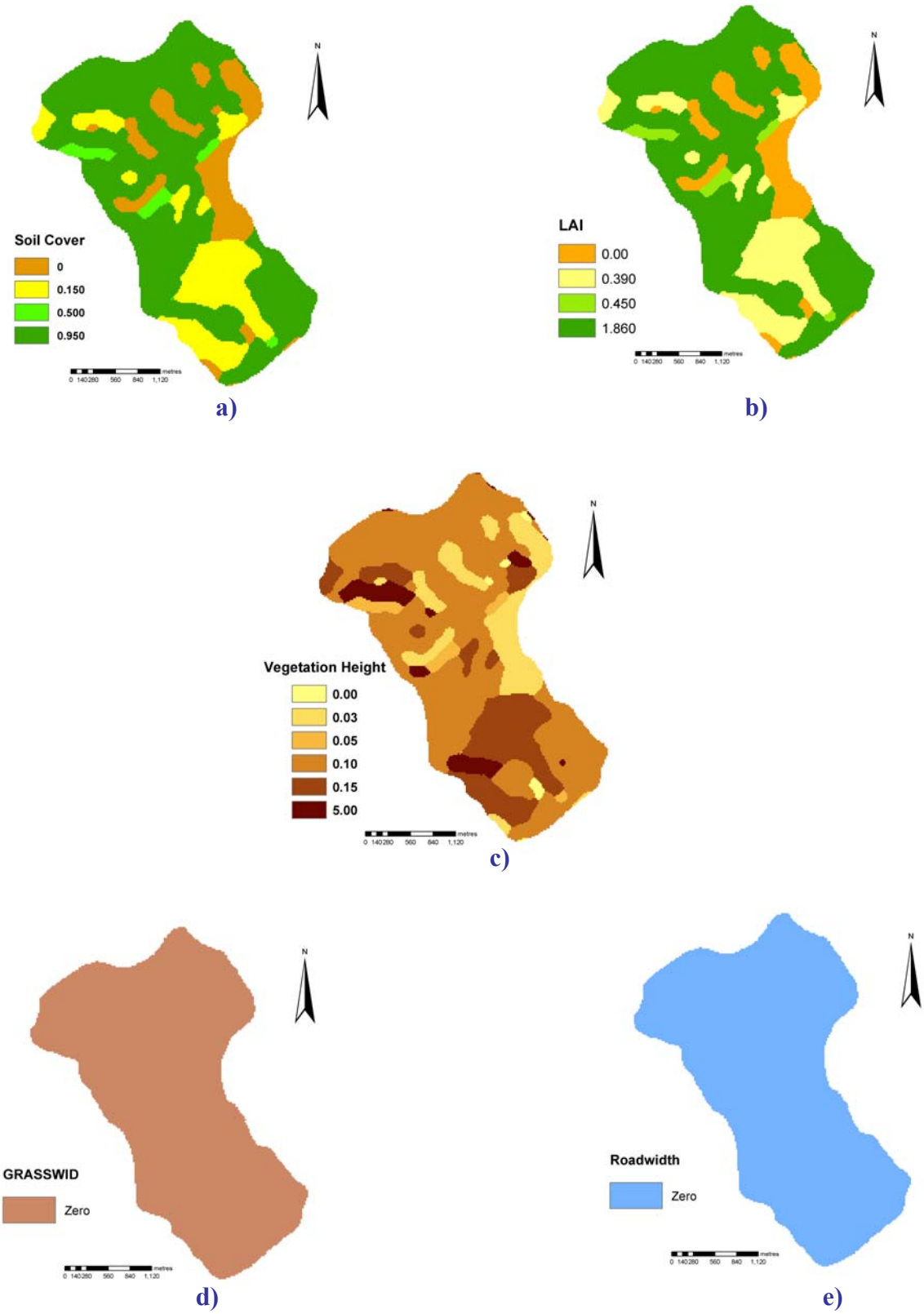

Figure 6.3: Land use and vegetation parameter maps; a) soil cover, b) leaf area index (LAI), c) crop and vegetation height, d) grass width (GRASSWID), and e) road width

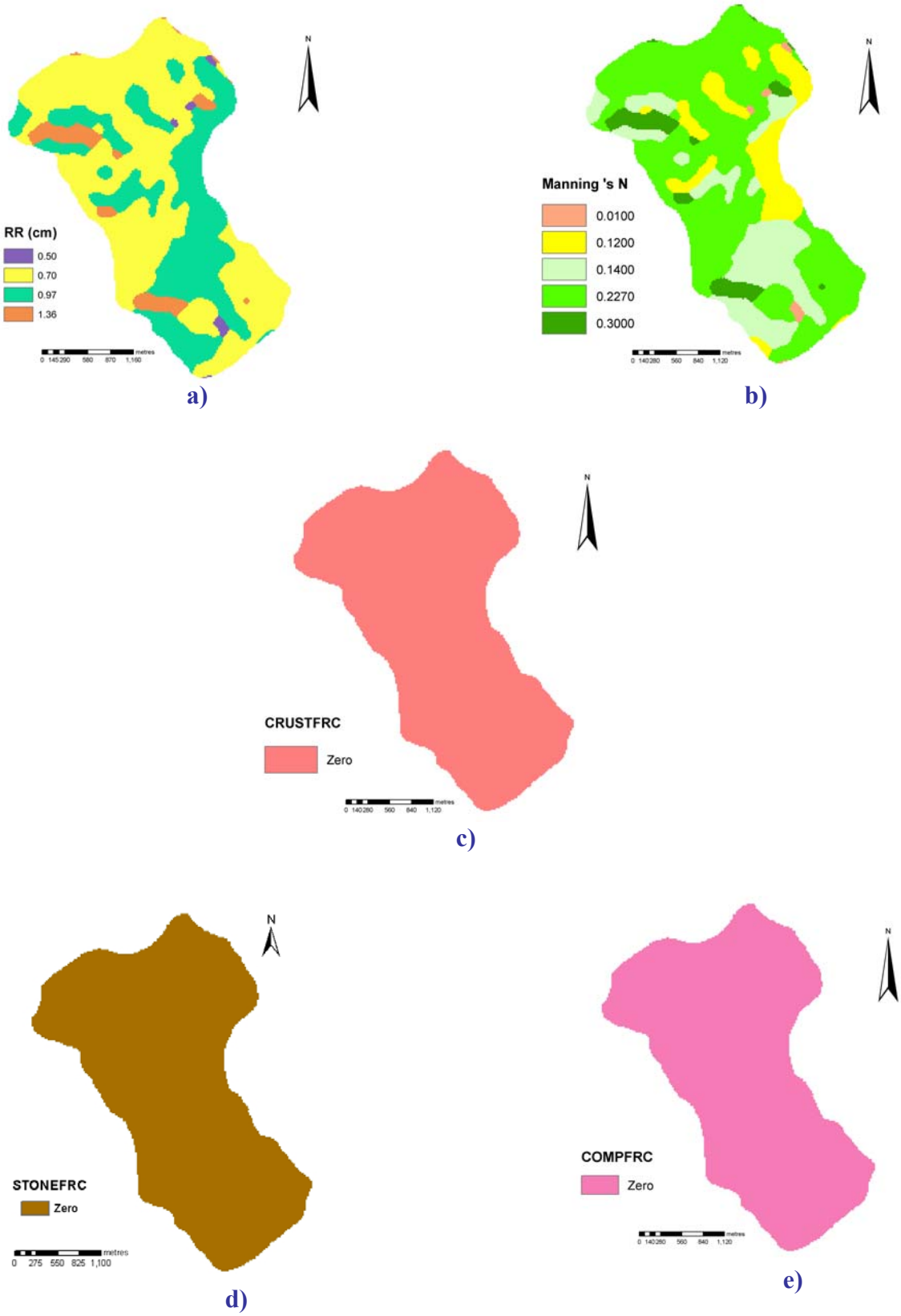

Figure 6.4: Soil surface parameter maps; a) random roughness, b) Manning's roughness, c) crusted surface, d) stone covered surface, and e) compacted surface

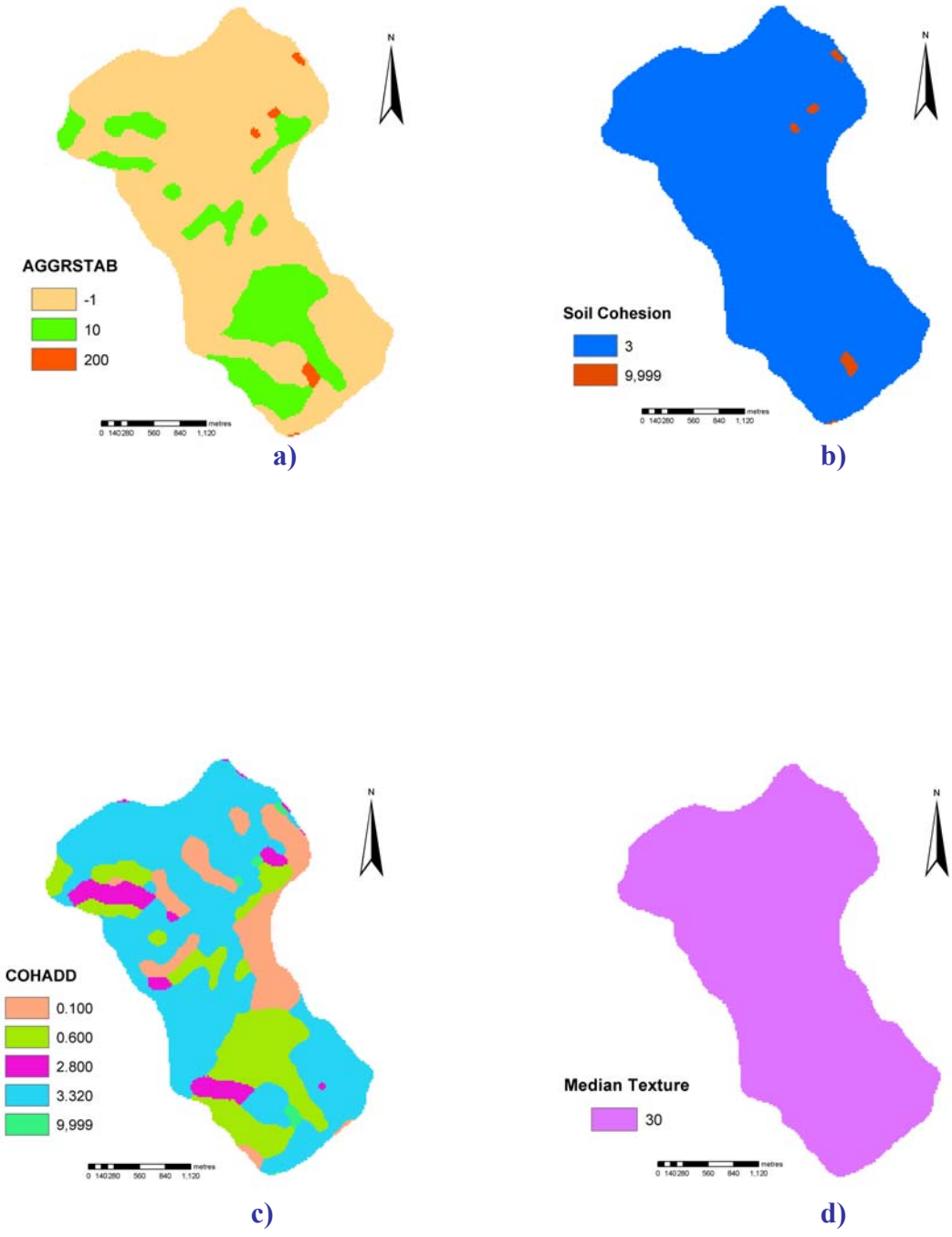

Figure 6.5: Erosion and deposition parameter maps; a) soil aggregate stability (AGGRSTAB), b) soil cohesion, c) additional cohesion by plant roots (COHADD), and d) soil median texture (D50)

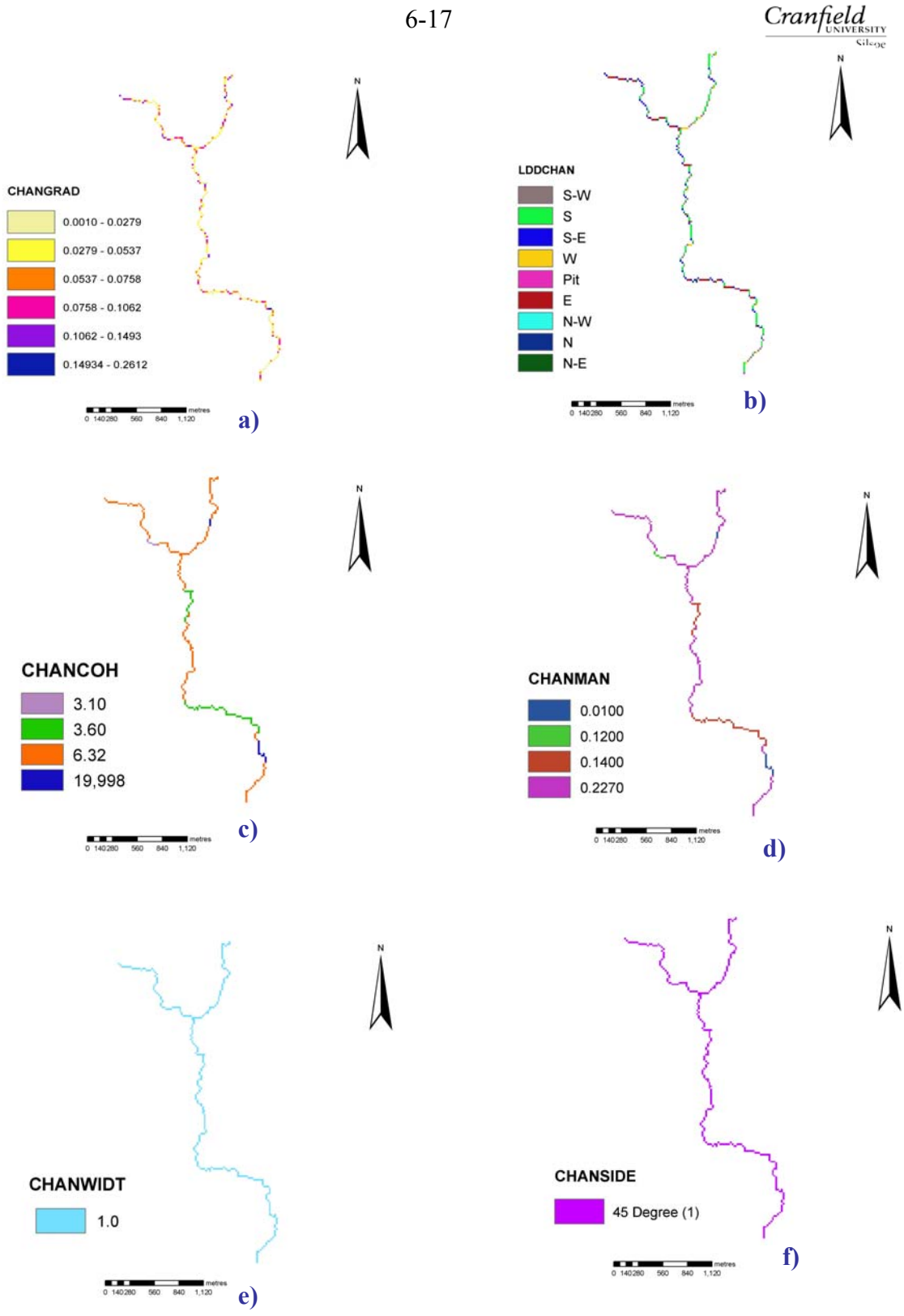

Figures 6.6 Channel parameter maps; a) channel gradient (CHANGRAD), b) LDD of the channel (LDDCHAN), c) channel cohesion (CHANCOH), d) Manning's N of the channel (CHANMAN), e) channel width (CHANWIDT), and f) channel side slope (CHANSIDE)

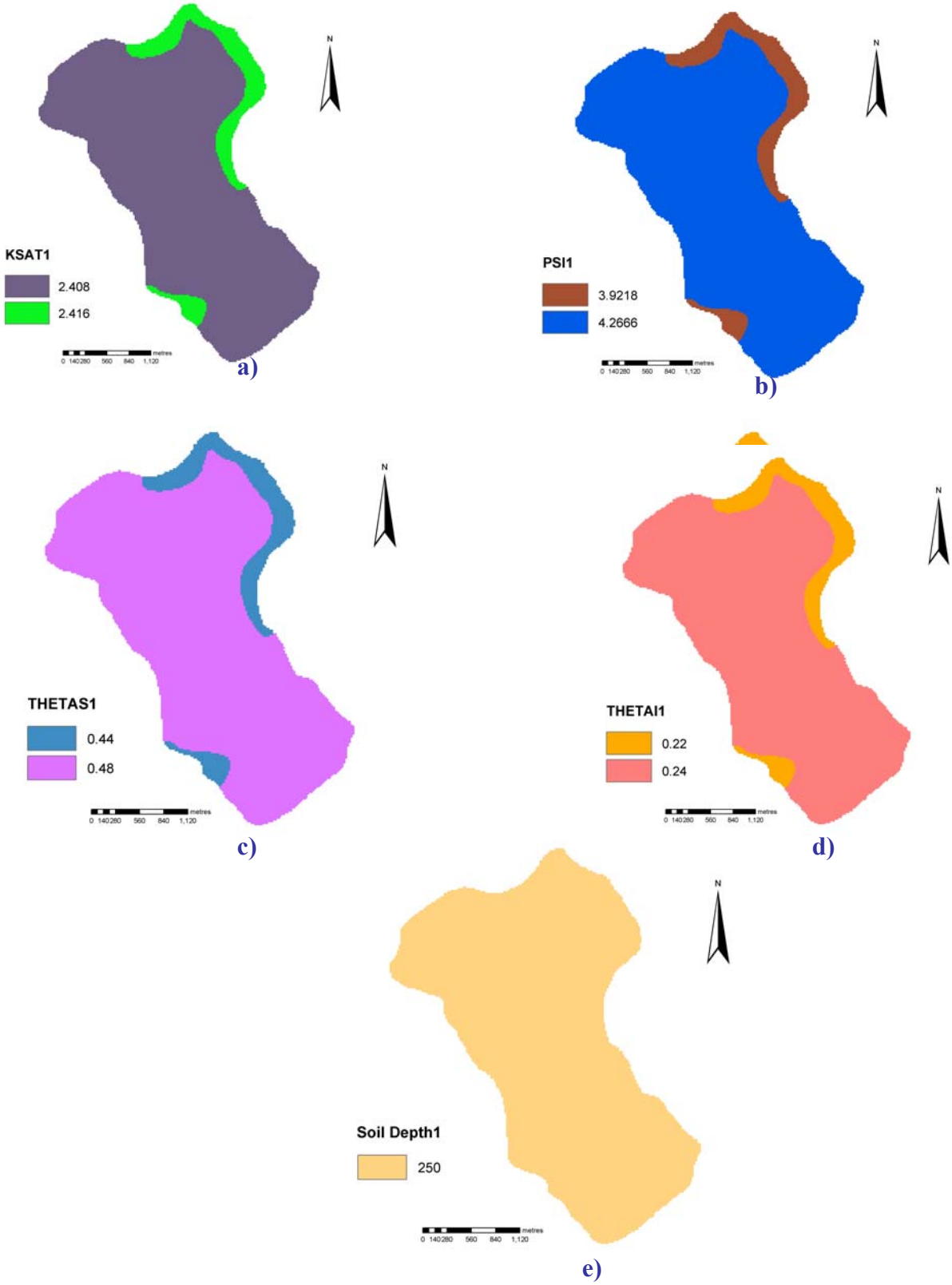

Figures 6.7: Infiltration parameter maps; a) saturated hydraulic conductivity (KSAT1), b) water front suction head (PSI1), c) moisture content at saturation (THETAS1), d) antecedent moisture content (THETAI1), and e) soil depth (SOILDEP1)

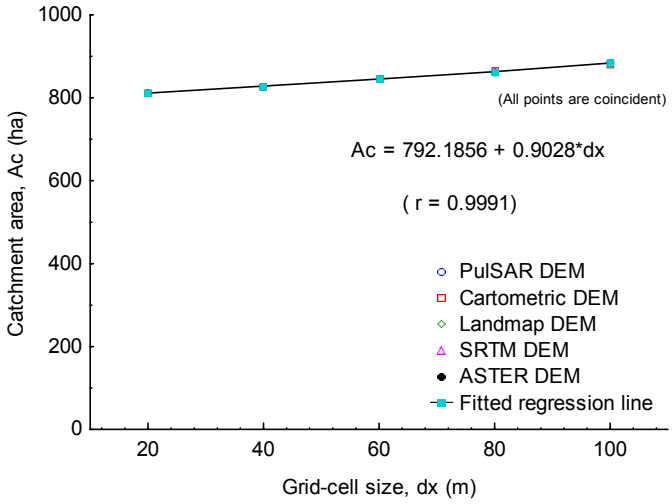

Figure 6.8: Effect of grid-cell size on catchment area

6.5.2 Slope Gradient

The slope gradient used in the LISEM model is the sine of the slope in the direction of local drainage direction. This was used to assess the effect of an aggregation scheme on various sources of DEMs. The mean slope gradient was the highest for the PulSAR DEM because of no smoothing applied and the lowest for the SRTM DEM because of higher level of smoothing (Figure 6.9; Appendix E-8). The mean slope gradient of the Landmap, Cartometric and ASTER DEMs lie between the PulSAR DEM and SRTM DEM due to different level of smoothing applied during their production. The mean slope gradient of the PulSAR DEM was flattened by 28 per cent as the grid-cell size was increased (Figure 6.10; Appendix E-9). The same trend is reported by Vieux (2000). It was caused by cutting of hills and filling of valleys at lower resolutions by sampling. A similar trend was also observed with four other DEMs.

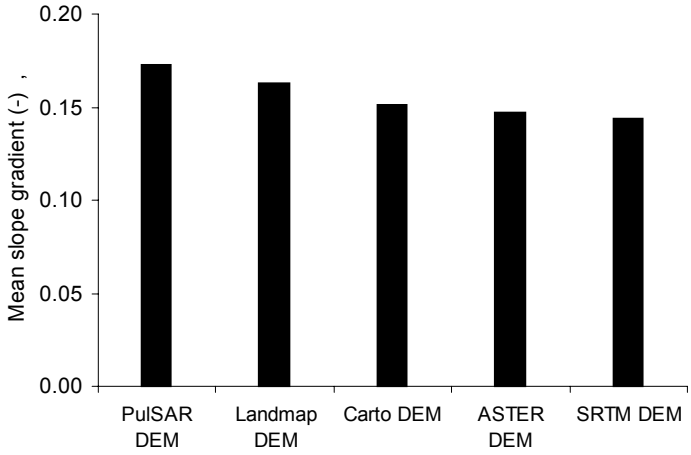

Figure 6.9: Comparison of mean slope gradients among all five DEMs

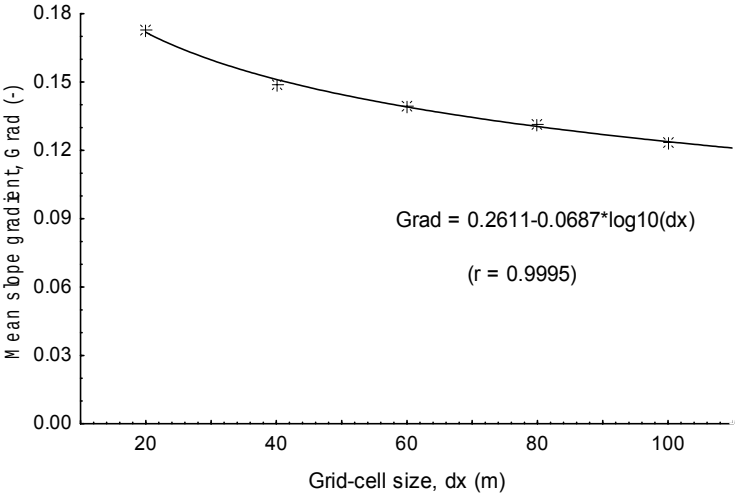

Figure 6.10: Effect of grid-cell size on mean slope gradient (PulSAR DEM)

6.5.3 Drainage Network

A distributed model requires a drainage network to route the water and sediment movement from the upstream to an outlet. The total length of drainage is the sum of overland and channel flows. The total drainage length of the PulSAR DEM dataset decreased by 78.9 per cent as the grid-cell size was increased from 20 to 100 m (Figure 6.11 (upper); Appendix E-10). Coarser grid-cell resolutions short circuited the drainage streams by cutting of hills and filling of valleys, causing an overall shortening of the drainage network. Similarly, channel length shortened by 13.41 per cent for resolution changing from 20 to 100 m. (Figure 6.11 (lower)). The drainage and channel length

shortening and slope flattening have profound effects on distributed simulation of runoff and erosion processes.

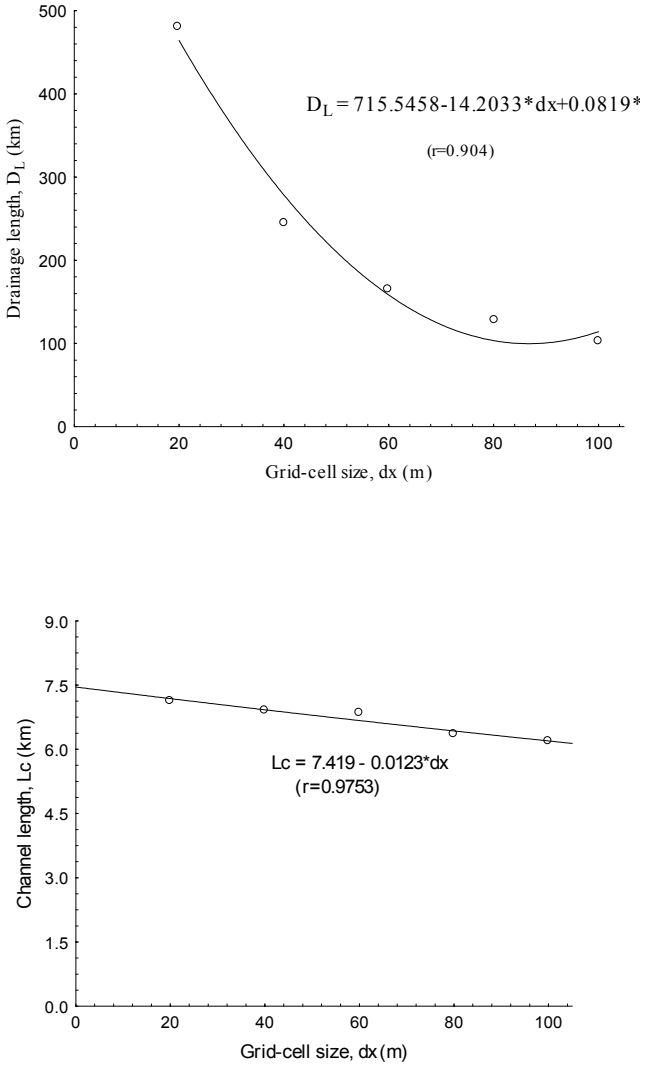

Figure 6.11: Effect of grid-cell size on drainage length (upper) and channel length (lower) (PulSAR DEM)

6.6 Effects of Resolution on Hydrologic and Erosion Processes

Twenty-five LISEM databases were tested to investigate the effects of resolution on hydrologic and erosion processes using LISEM version 2.03 at three antecedent soil moisture levels for a 6-hour storm of 30 October 2000. The model was run seventy-five times to process all datasets. The results of the effects of resolution on hydrologic and erosion processes from a storm are discussed below.

6.6.1 Selection of a Time Step

First and the most important thing in a dynamic simulation study was to choose an appropriate time step. The time step in the model was studied by varying it from 10 to 60 seconds with every increase of 10 seconds for the 20 m resolution PulSAR dataset at a medium antecedent moisture condition. It was found that the runoff coefficient decreased by 0.1 per cent as the time step was increased from 10 to 60 s (Figure 6.12). This was caused by the lower accuracy of the kinematic wave solution at larger time steps. A smaller time step resulted in a greater accuracy of the kinematic wave solution. Both either a smaller or a larger time step causes instability in numerical solution. Therefore, a 30 second time step was chosen for the 20 m resolution datasets and it was kept constant for testing all datasets. This time step also lies within a range of 0.2 - 2 times of the grid-cell size as recommended by the model developer to avoid instability in the algorithm (Jetten, 2002).

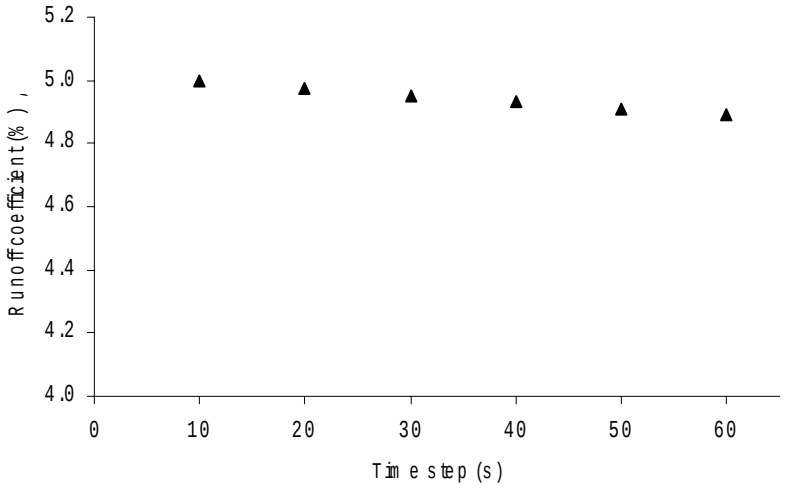

Figure 6.12: Effect of simulation time-step on runoff coefficient at medium AMC

6.6.2 Interception

A dynamic storage model (Aston, 1979) was used to compute the interception by crops and vegetation during the storm event. As can be seen from Figure 6.13, the interception remained unchanged (0.03 per cent) for all DEM datasets as the grid-cell size was increased. This trend was observed at all three antecedent moisture conditions. The change in the interception was insignificant and it was caused by the rounding

errors, which decreased at larger resolutions involving smaller number of grid-cells. There was a slight decrease at 40 m resolution in all the DEM datasets (Appendix E-11). This could be caused by the instability in the model algorithm.

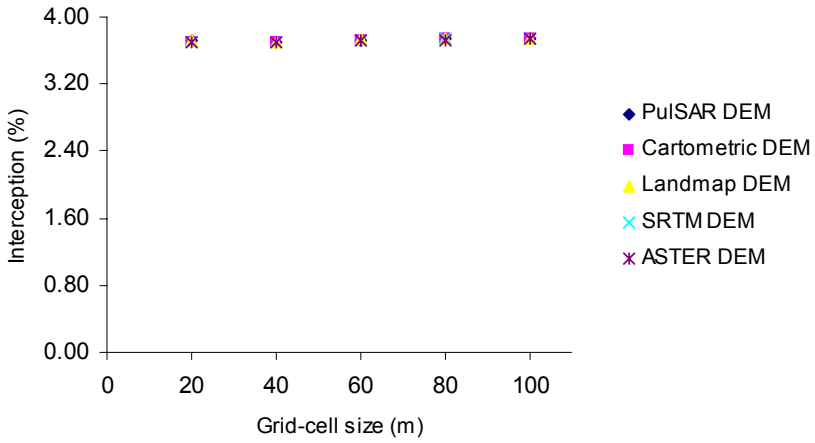

Figure 6.13: Effect of grid-cell size on interception

6.6.3 Infiltration

The infiltration was simulated using a single layer Green and Ampt model at three moisture conditions. It is expressed in terms of percentage of rainfall for comparison among DEMs. It was found that it increased for all DEM datasets as the grid-cell size was increased from 20 to 100 m at three AMCs (Figure 6.14). Table 6.7 shows the effect of resolution on infiltration listed in a descending order at three moisture conditions. Similarly, eleven result tables of effects of resolution on major hydrologic and erosion processes are given in Appendices E-14 through E-23.

There was a large increase of 9.35 per cent at high AMC and a little increase of 0.06 per cent at low AMC. At high AMC, the infiltration was maximum for the SRTM DEM dataset with an increase of 4.70 per cent and minimum for the PulSAR DEM dataset with an increase of 9.35 per cent when the grid-cell size was increased. Similarly, the infiltration was maximum for the SRTM DEM dataset at low and medium AMCs, and minimum for the PulSAR DEM at medium AMC and for the Landmap at low AMC. There was a slightly change in the infiltration at low AMC in all DEMs when the grid-cell size was increased. It was found that there was a large variation in

the infiltration at 20 m resolution among various DEMs at all AMCs (Table 6.7). It narrowed down at coarser resolutions. High infiltration in the SRTM and Cartographic DEMs was observed at all resolutions caused by the lower slope gradients which resulted in slope flattening and, hence, more infiltration.

6.6.4 Runoff Coefficient

The effect of resolution on the Hortonian surface runoff was studied at three antecedent moisture conditions. It was found that runoff coefficients decreased with an increase in grid-cell size at all three AMCs (Figure 6.15). The runoff coefficient was maximum for the PulSAR DEM dataset with a variability of 9.33, 2.97 and 0.24 per cent at high, medium and low moistures when the grid-cell size was increased (Appendix E - 12). Similarly, minimum runoff coefficient was observed for the SRTM DEM dataset with a variability of 4.67, 2.49 and 0.11 per cent reduction at high, medium and low moisture conditions when the grid-cell size was changed. There was a large variation in runoff coefficients at higher resolutions at high AMC, which narrowed down at larger grid-cell sizes. Similarly, the runoff coefficient has lower variations at medium and low moistures which further narrowed in each case. The highest and the lowest runoffs from the PulSAR DEM dataset and the SRTM DEM were caused by the highest and the lowest mean slope gradient respectively.

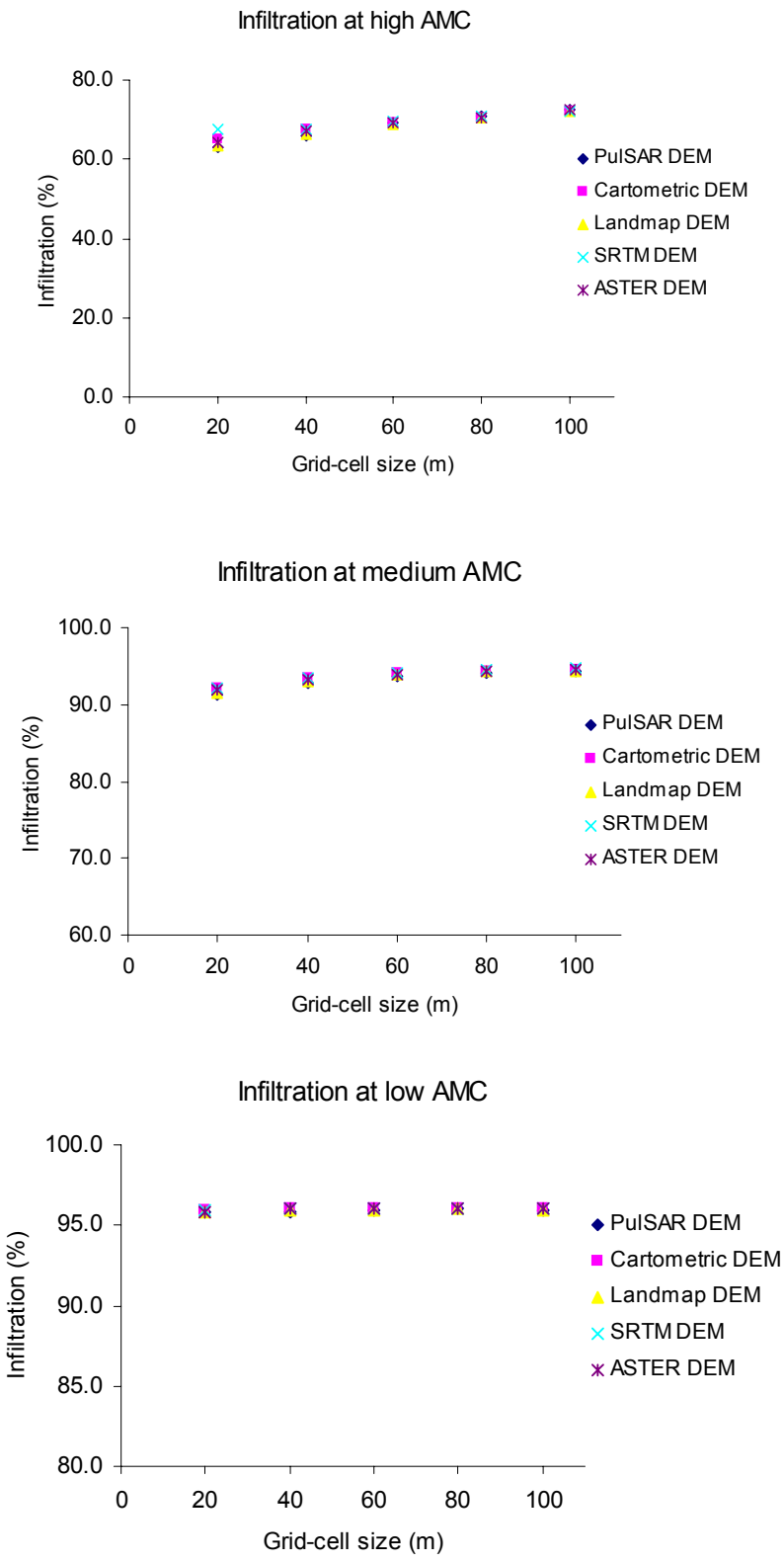

Figure 6.14: Effect of grid-cell size on infiltration at three AMCs

Table 6.7: Effect of grid-cell size on infiltration at three soil moisture conditions for five DEM datasets

DEM	AMC	Infiltration (per cent) Grid-cell size (m)				
		20	40	60	80	100
SRTM DEM	High	67.57	67.42	69.53	70.89	72.27
			(-0.15)	(1.96)	(3.32)	(4.70)
Cartometric DEM	,,	65.06	67.69	69.25	70.57	72.29
			(2.63)	(4.19)	(5.51)	(7.23)
ASTER DEM	,,	64.20	66.95	69.16	70.36	72.60
			(2.75)	(4.96)	(6.16)	(8.41)
Landmap DEM	,,	63.37	66.49	68.94	70.59	71.99
			(3.12)	(5.57)	(7.22)	(8.62)
PulSAR DEM	,,	63.04	66.11	69.20	70.82	72.39
			(3.07)	(6.16)	(7.78)	(9.35)
Difference among DEMs		4.53	1.31	0.59	0.53	0.61
SRTM DEM	Medium	92.19	93.50	94.11	94.46	94.66
			(1.32)	(1.92)	(2.27)	(2.48)
Cartometric DEM	,,	92.14	93.43	94.02	94.39	94.64
			(1.29)	(1.88)	(2.24)	(2.50)
ASTER DEM	,,	91.92	93.31	93.85	94.29	94.59
			(1.39)	(1.94)	(2.37)	(2.67)
Landmap DEM	,,	91.38	92.94	93.83	94.26	94.39
			(1.56)	(2.45)	(2.88)	(3.02)
PulSAR DEM	,,	91.29	92.72	93.60	94.17	94.26
			(1.43)	(2.31)	(2.88)	(2.96)
Difference among DEMs		0.90	0.78	0.51	0.29	0.40
SRTM DEM	Low	95.96	96.05	96.03	96.05	96.05
			(0.08)	(0.06)	(0.08)	(0.09)
Cartometric DEM	,,	95.91	96.01	96.00	96.01	96.03
			(0.10)	(0.09)	(0.10)	(0.11)
ASTER DEM	,,	95.87	96.01	95.99	96.00	96.03
			(0.14)	(0.12)	(0.14)	(0.16)
PulSAR DEM	,,	95.78	95.86	95.94	96.01	95.96
			(0.09)	(0.17)	(0.23)	(0.18)
Landmap DEM	,,	95.77	95.94	95.96	96.00	95.99
			(0.17)	(0.20)	(0.23)	(0.22)
Difference among DEMs		0.19	0.19	0.09	0.05	0.09

(Figures in parentheses show difference in per cent with respect to 20 m grid-cell size)

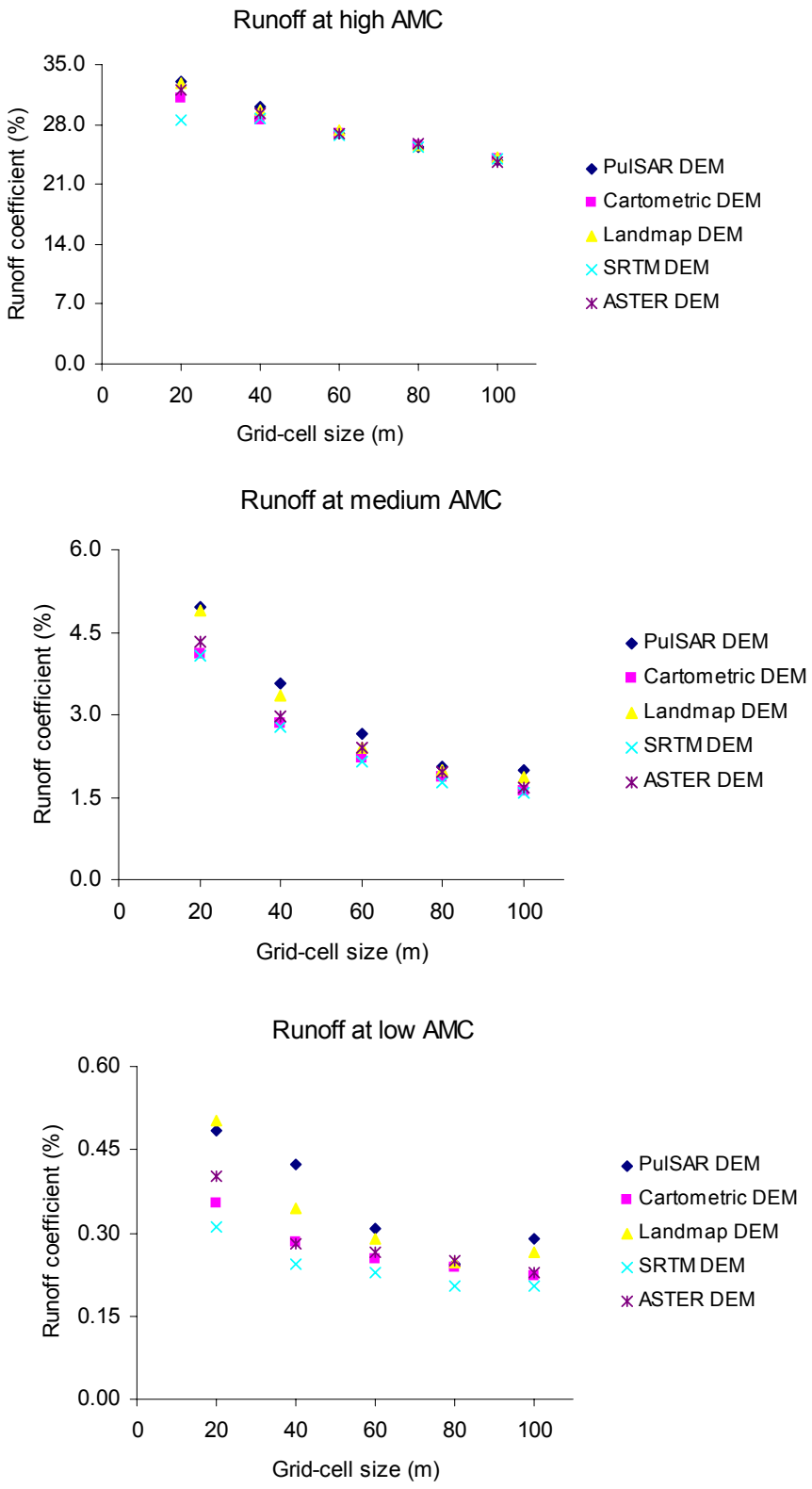

Figure 6.15: Effect of grid-cell size on runoff coefficient at three AMCs

6.6.5 Peak Discharge

The effect of increased catchment area on peak discharge at coarser resolutions was normalised by subtracting an equivalent percentage of increased area from the peak discharge. It was found that the normalised peak discharge decreased at all three moisture conditions as the grid-cell size was increased (Figure 6.16). At high AMC, the cartometric DEM dataset resulted in the highest peak discharge while the lowest peak discharge was observed for the ASTER DEM. At medium AMC, the Landmap and ASTER DEM datasets resulted in the highest and lowest peak discharge respectively (Appendix E-13). At low AMC, the Landmap and SRTM DEM datasets resulted in the highest and lowest peak discharge respectively. There was large variation at higher resolution which narrowed down at coarser resolution in all three moisture condition. This trend was observed with all five DEM datasets. The highest peak discharge in the Cartometric DEM at high moisture was caused by smooth topographic surface while it changed to the Landmap DEM at medium and low moistures which could be results of smoother surface.

6.6.6 Peak Time

The time to peak runoff decreased slightly with an increase of grid-cell size and increased drastically with a reduction in soil moisture content. The peak time was the highest and lowest for the Cartometric and Landmap DEM datasets at high and low moisture conditions while at medium AMC, the ASTER and Landmap DEM datasets resulted in the highest and lowest peak time respectively (Appendix E-14). More consistent results were observed at both high and medium AMCs while the results were more or less inconsistent at low moisture condition (Figure 6.17). The time to peak runoff could not be normalised as it depended on the travel length of runoff rather than catchment area.

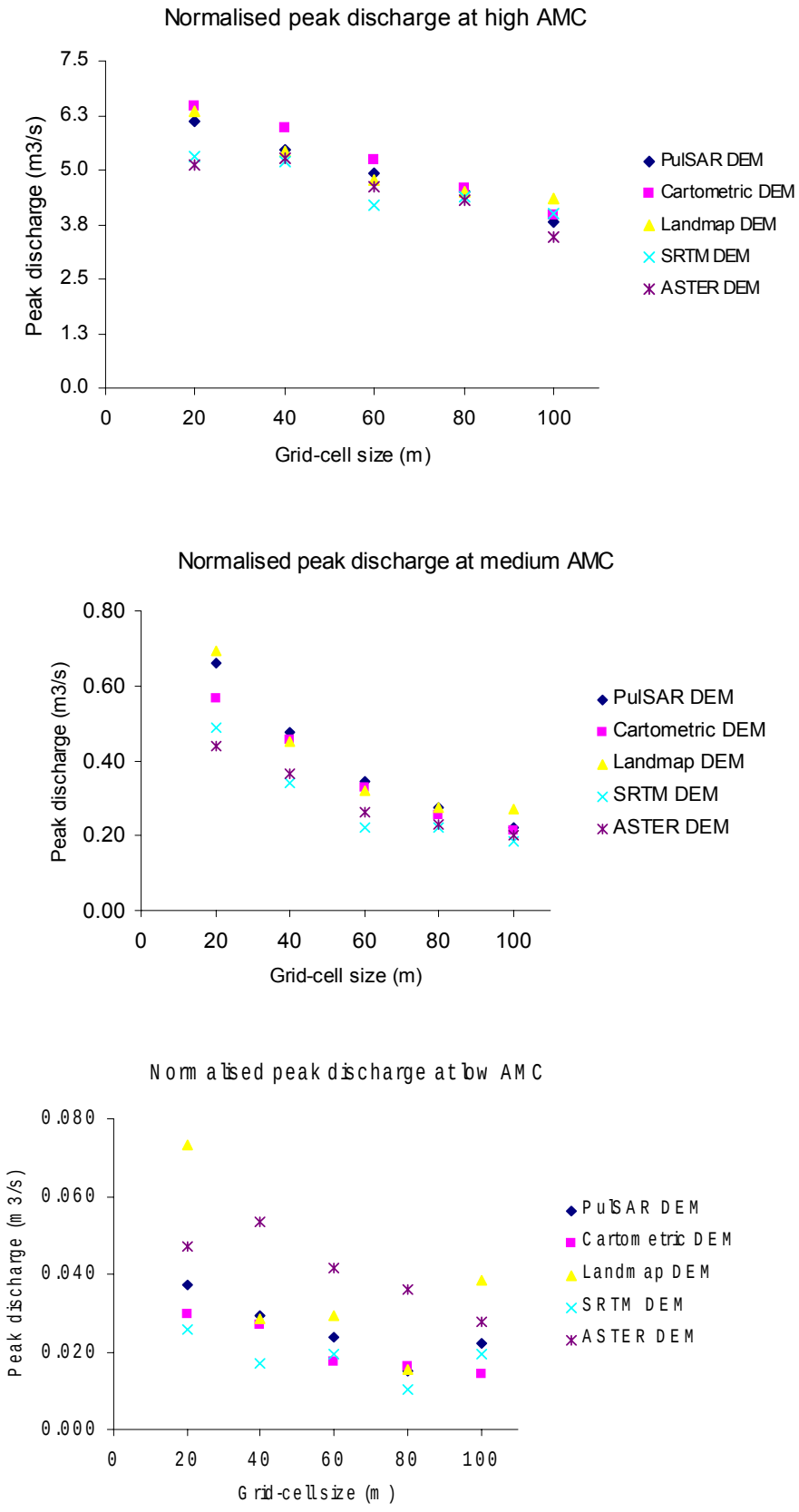

Figure 6.16: Effect of grid-cell size on normalised peak discharge at three AMCs

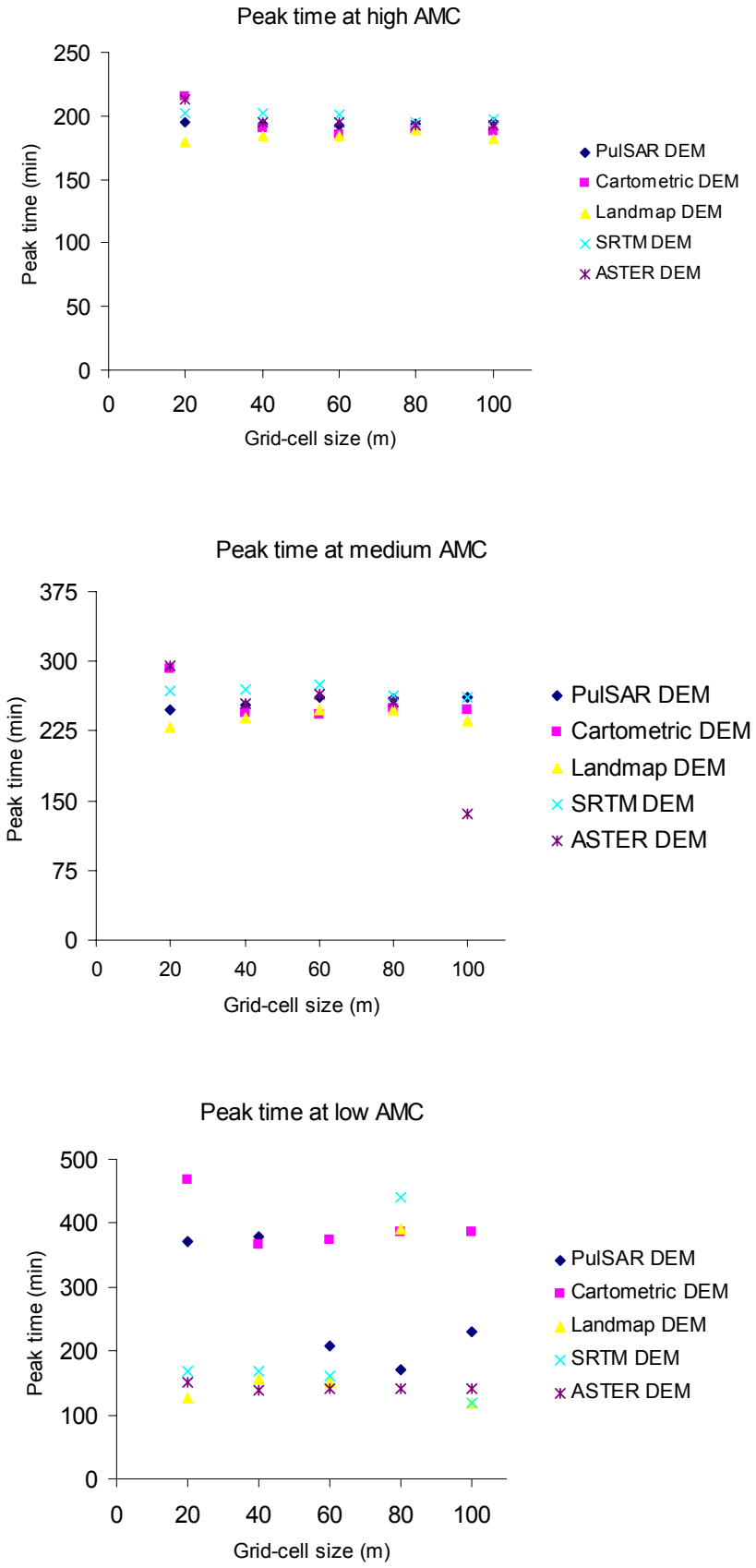

Figure 6.17: Effect of grid-cell size on peak time to runoff at three AMCs

6.6.7 Splash Detachment

Splash detachment by rainfall and leaf drips was modelled using a generalised erosion-deposition theory (Morgan et al, 1998; Smith et al, 1995). It was normalised for increased catchment area at lower resolutions. It increased with an increase of grid-cell size at high AMC, but this trend was not clearly observed at medium and low antecedent moisture conditions (Figure 6.18). The cartometric and SRTM DEM datasets produced the highest and lowest splash detachment respectively at high AMC. The SRTM DEM produced the highest splash erosion at medium and low moisture levels while the PulSAR DEM dataset produced the lowest splash erosion at medium and low moisture conditions (Appendix E-15). Higher splash detachment at higher moisture content was resulted because of slackening of soil particles by water. In some cases, there was decreasing trend of splash detachment at coarser resolutions at medium and low moisture conditions. In other words, mixed trends were observed at medium and low moisture conditions.

6.6.8 Flow Detachment

Simulation of soil detachment by flow was based on a same generalised erosion-deposition theory applied for splash detachment (Morgan et al, 1992; Smith et al, 1995). The normalised overland flow detachment decreased with an increase of grid-cell size at all three moisture conditions. The PulSAR and SRTM DEM datasets produced the highest and lowest flow detachment at all three moisture conditions (Figure 6.19). The highest and lowest reduction in detachment (73 and 59 per cent) was observed in the ASTER and SRTM DEM datasets at high moisture condition (Appendix E-16). At medium moisture, there was the lowest variability while there was higher variability at high and medium moisture contents. The higher moisture content in soil reduced the soil cohesion which resulted in higher flow detachment.

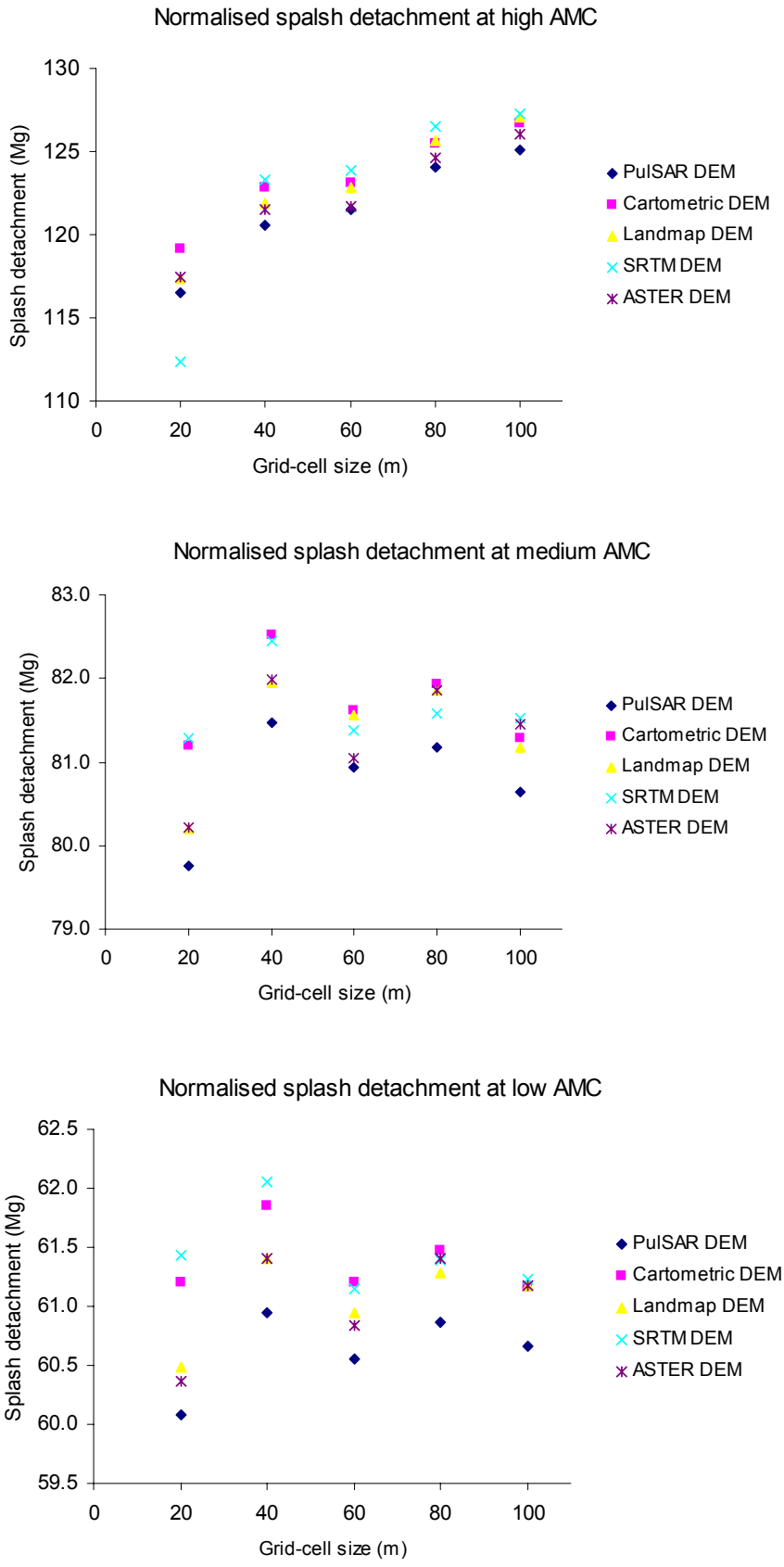

Figure 6.18: Effect of grid-cell size on normalised splash detachment at three AMCs

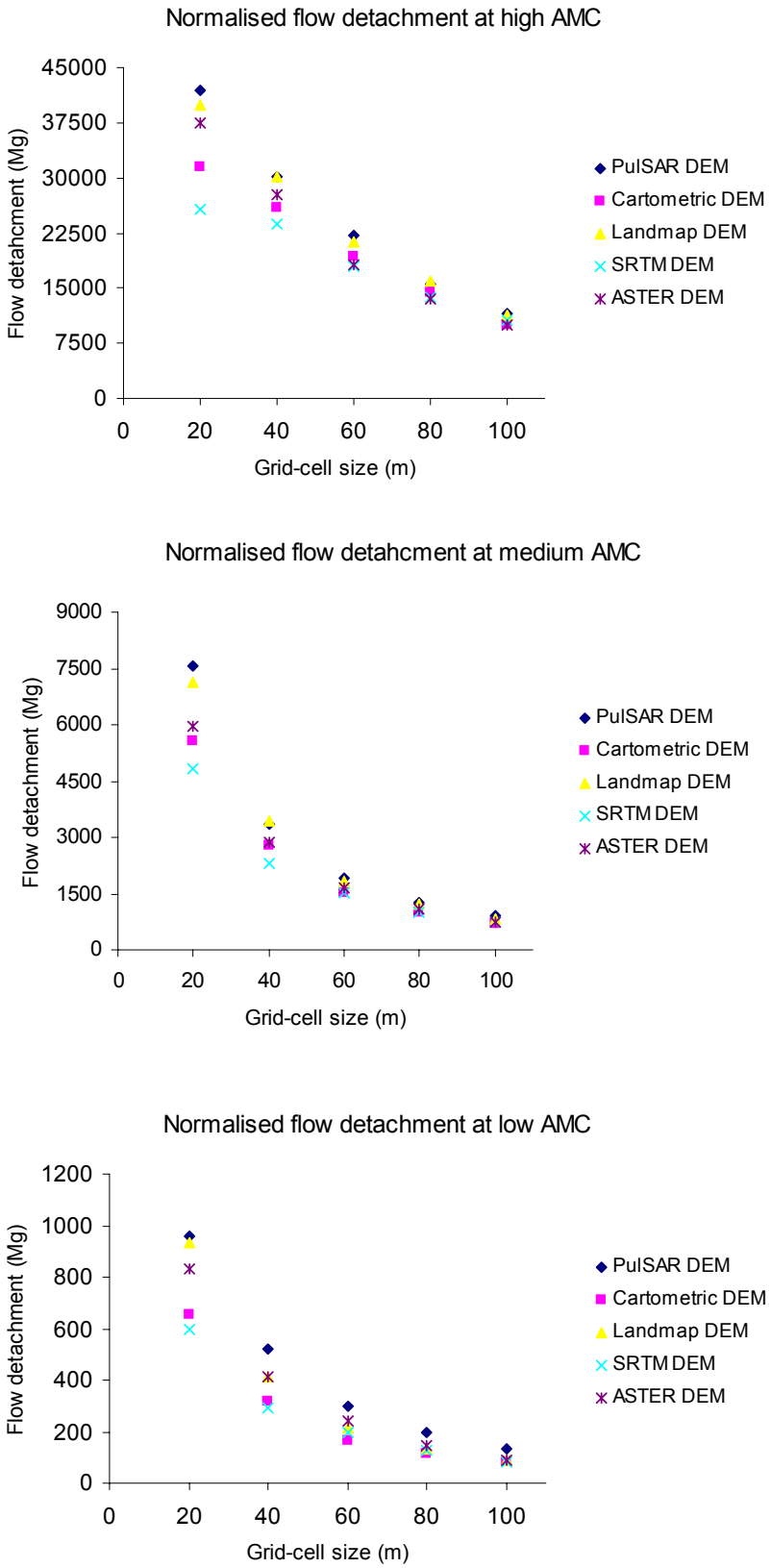

Figure 6.19: Effect of grid-cell size on normalised overland flow detachment at three AMCs

6.6.9 Overland Deposition

Overland deposition was modelled using an exponential decay function (Equation 2.36) discussed in Section 2.6, which simulates the effect of settling of particles slows down when they reach the bottom of the water layer on the surface. The deposition was based on runoff sediment concentration limiting. The sediment deposition on overland increased with an increase of grid-cell size for all DEM datasets at three moisture conditions (Figure 6.20). The PulSAR DEM dataset resulted in the highest deposition at three moisture conditions while the SRTM dataset produced the lowest sediment deposition at all moisture conditions (Appendix E-17). The results were quite consistent at all three moisture levels. The higher deposition in the PulSAR DEM dataset was caused by higher erosion which got deposited in the valley while lower deposition in the SRTM DEM dataset was caused by lower soil erosion because of lower slope gradient.

6.6.10 Channel Erosion

The effect of resolution on channel erosion at three moisture conditions was studied and the results were normalised. The normalised channel erosion decreased as the grid-cell size was increased at all moisture conditions. This trend was observed at medium and low moisture conditions but this trend was not strongly seen at high moisture level (Figure 6.21). The highest channel erosion was observed for the PulSAR DEM dataset at high AMC, for the ASTER DEM dataset at medium AMC and for the Landmap DEM dataset at low AMC respectively. The lowest channel erosion was observed for the SRTM DEM dataset at all moisture conditions (Appendix E-18). The higher soil moisture content resulted in higher runoff which led to higher channel erosion. Channel erosion depends on soil cohesion of the channel material and amount of flow to be handled in the model. Highest channel erosion in the PulSAR DEM, ASTER DEM and Landmap DEM datasets at high, medium and low moisture conditions respectively was caused by the higher slope gradient, which produced higher runoff leading to higher channel erosion although the channel cohesion remained same for these DEM datasets. The lowest erosion in the SRTM dataset at all moisture was caused by lower slope gradient leading to lower runoff.

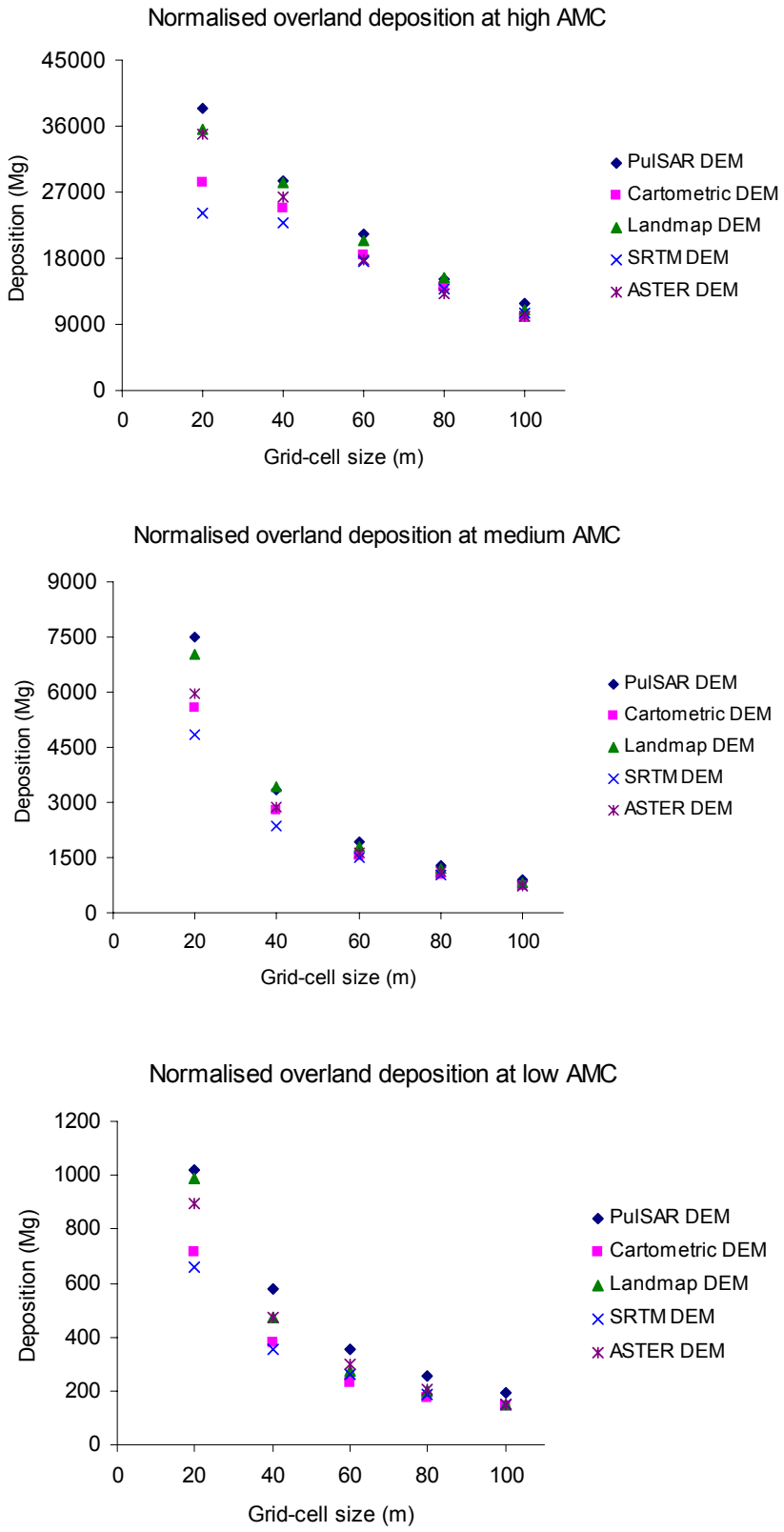

Figure 6.20: Effect of grid-cell size on normalised overland deposition at three AMCs

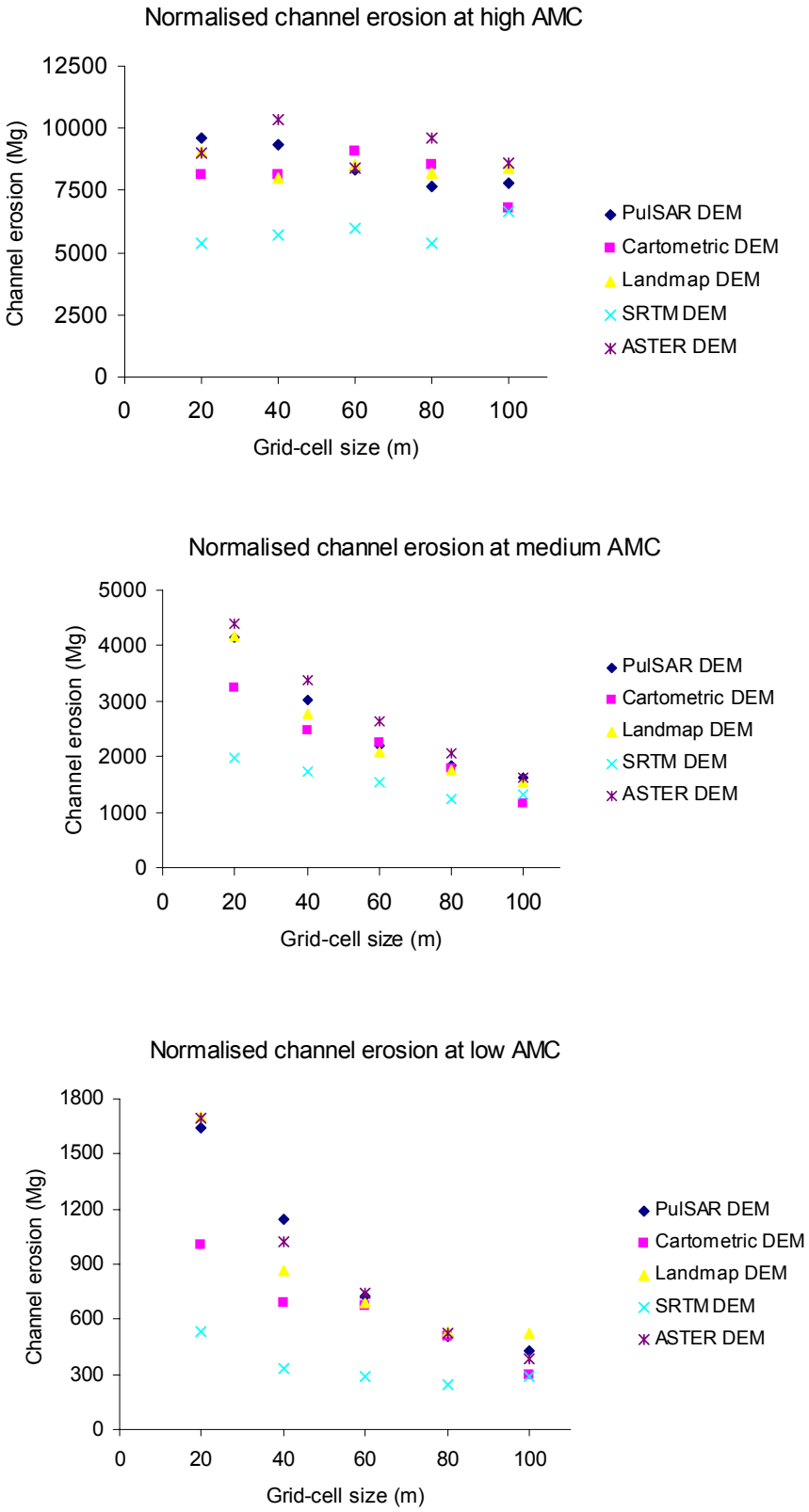

Figure 6.21: Effect of grid-cell size on channel erosion at three AMCs

6.6.11 Channel Deposition

Channel deposition was modelled on the basis of transport carrying capacity of the runoff in the channel. It was normalised for increased catchment area effect. It decreased at coarser grid-cell sizes for all five DEM datasets at all three moisture conditions (Figure 6.22). The highest and lowest channel depositions were found for the ASTER and SRTM DEM datasets respectively at high, medium and low moisture conditions (Appendix E-19).

6.6.12 Total Soil Loss

The effect of resolution on normalised total soil loss from the catchment at three moisture conditions was studied. It was found that it decreased at larger grid-cell sizes (Figure 6.23). The PulSAR DEM dataset at high AMC and the Landmap DEM dataset at medium and low AMCs produced the highest total soil erosion (Appendix E-20). The ASTER DEM dataset produced the lowest at all three moisture conditions. The ASTER DEM produced more inconsistent results at all moisture conditions while the SRTM produced inconsistent results at low moisture condition.

6.6.13 Average Soil Loss

Figure 6.24 shows the effect of resolution on average soil loss at three moisture conditions. It was found that it decreased as the grid-cell size was increased for all five DEM datasets at all three moisture conditions. The PulSAR DEM dataset produced the highest average soil loss at high moisture condition while the Landmap DEM resulted in the highest at medium and low moisture conditions. The ASTER produced the lowest average soil loss at all three moisture conditions, but its results were poor and inconsistent (Appendix E-21).

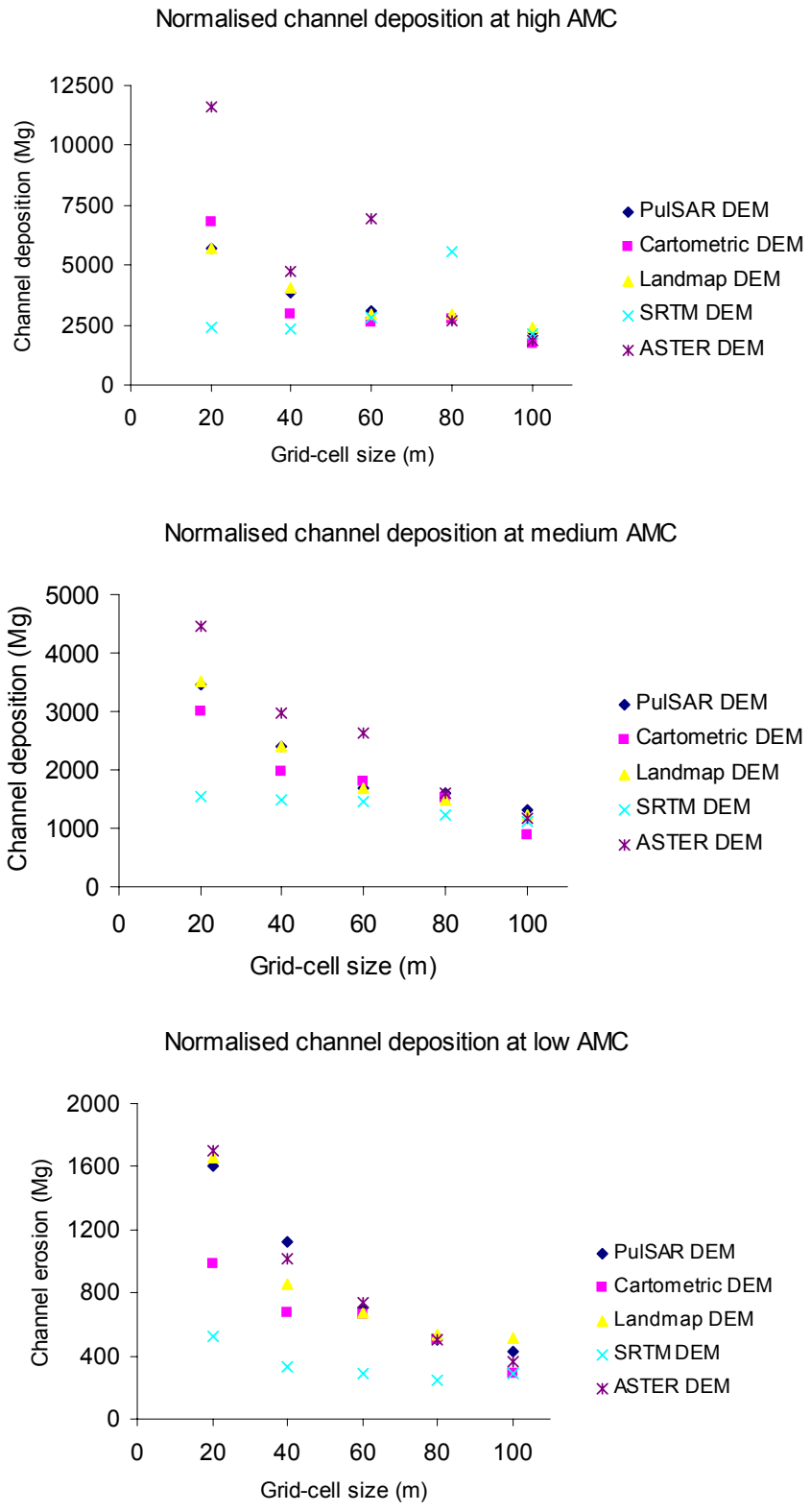

Figure 6.22: Effect of grid-cell size on channel deposition at three AMCs

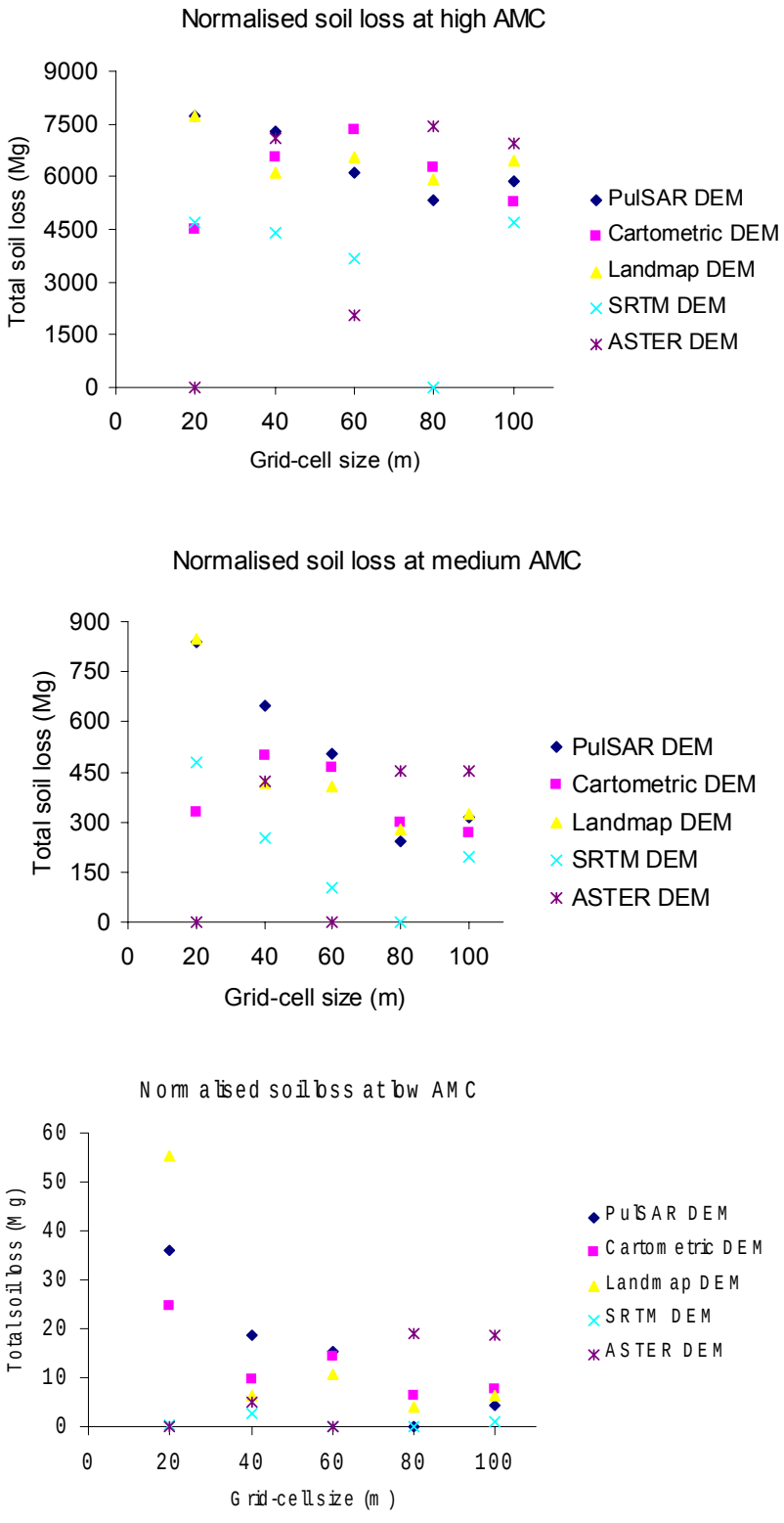

Figure 6.23: Effect of grid-cell size on total soil loss at three AMCs

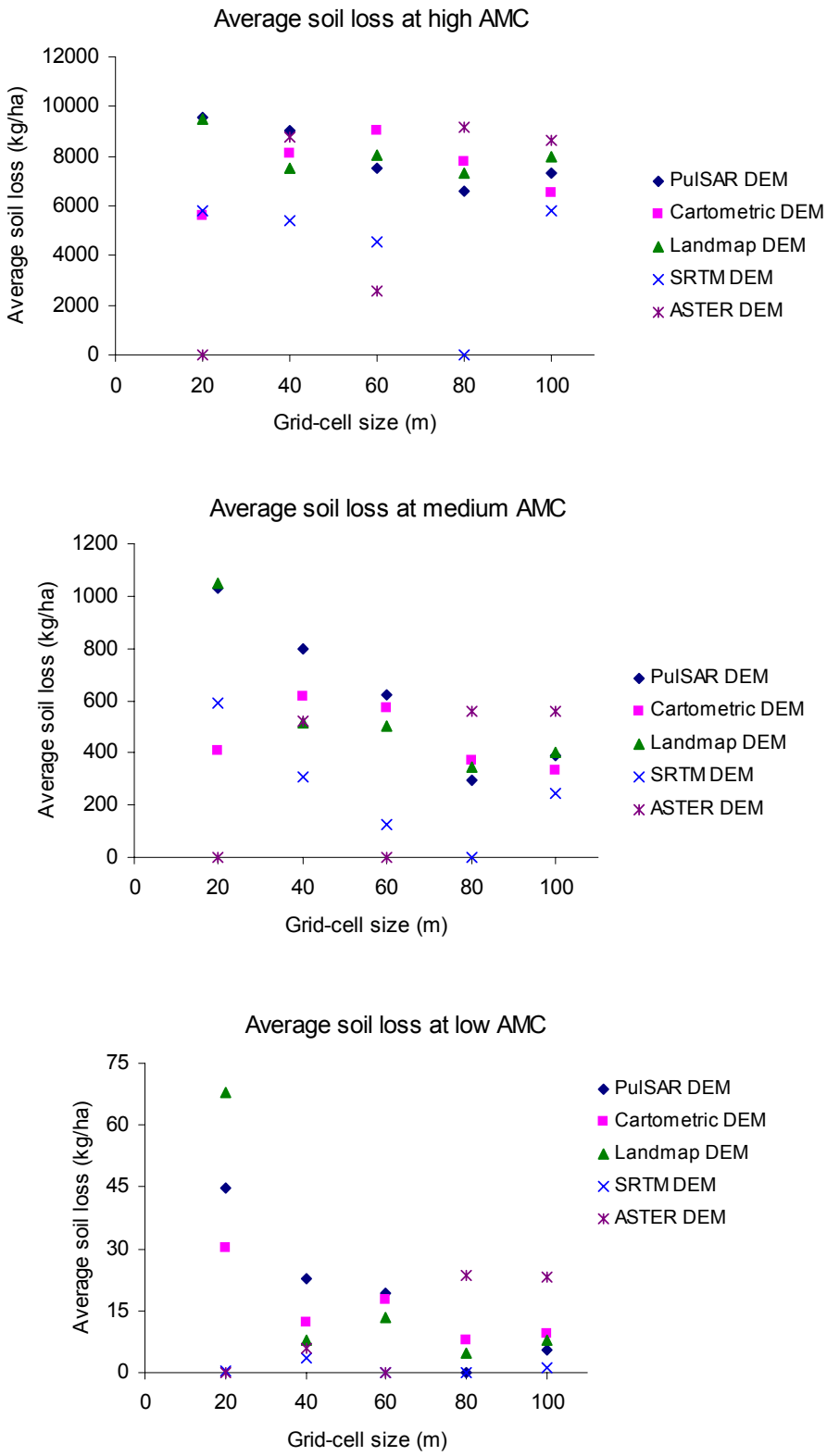

Figure 6.24: Effect of grid-cell size on average soil loss at three AMCs

6.7 Effects on Resolution on Spatio-Temporal Outputs

The effects of resolution on spatial distribution of erosion and deposition, time series outputs of hydrographs and sedigraph at the catchment outlet, and spatio-temporal outputs on major hydrologic and erosion processes were assessed for the storm event modelled using the PulSAR DEM dataset.

6.7.1 Erosion and Deposition

The spatial distribution of soil erosion and deposition was assessed at 20, 40, 60, 80 and 100 m grid-cell resolutions for the same storm event. It was found that erosion and deposition maps at 20 m resolution dataset were more spatially detailed to locate the priority area in the catchment, which may need attention (Figure 6.25 and Figure 6.26). Lesser details are available from spatial maps at larger grid-cell sizes such as 60, 80 and 100 m. The distribution of areas under various erosion classes at various resolution are given in Appendix E-22.

6.7.2 Hydrographs and Sedigraphs

Both peak discharge (Figure 6.27) and sediment discharge (Figure 6.28) decreased as the grid-cell size was increased from 20 to 100 m. Both time to peak discharge and to peak sediment discharge decreased slightly at coarser cell sizes. The shape of hydrographs and sedigraphs for various resolutions were symmetric, but the peak values at coarser resolutions were reduced (Appendix E-23). The peak discharge with 100 m resolution data was higher than that of the 80 m resolution data. This could be caused by errors propagated by resampling. Similar trend of higher sediment discharge at 100 m resolution was also observed in the sedigraph.

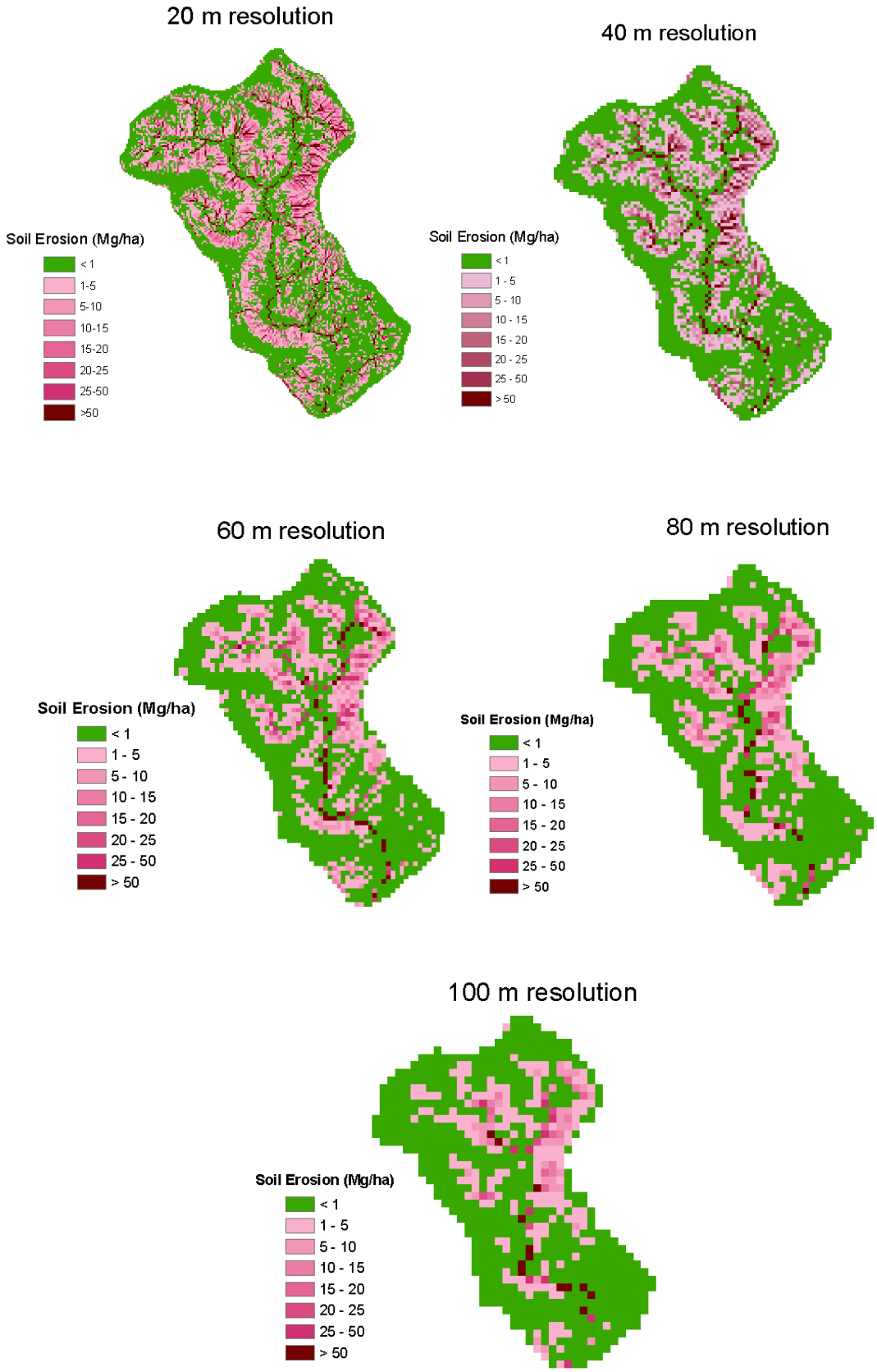

Figure 6.25: Effect of resolution on the distribution of soil erosion with 8 classes

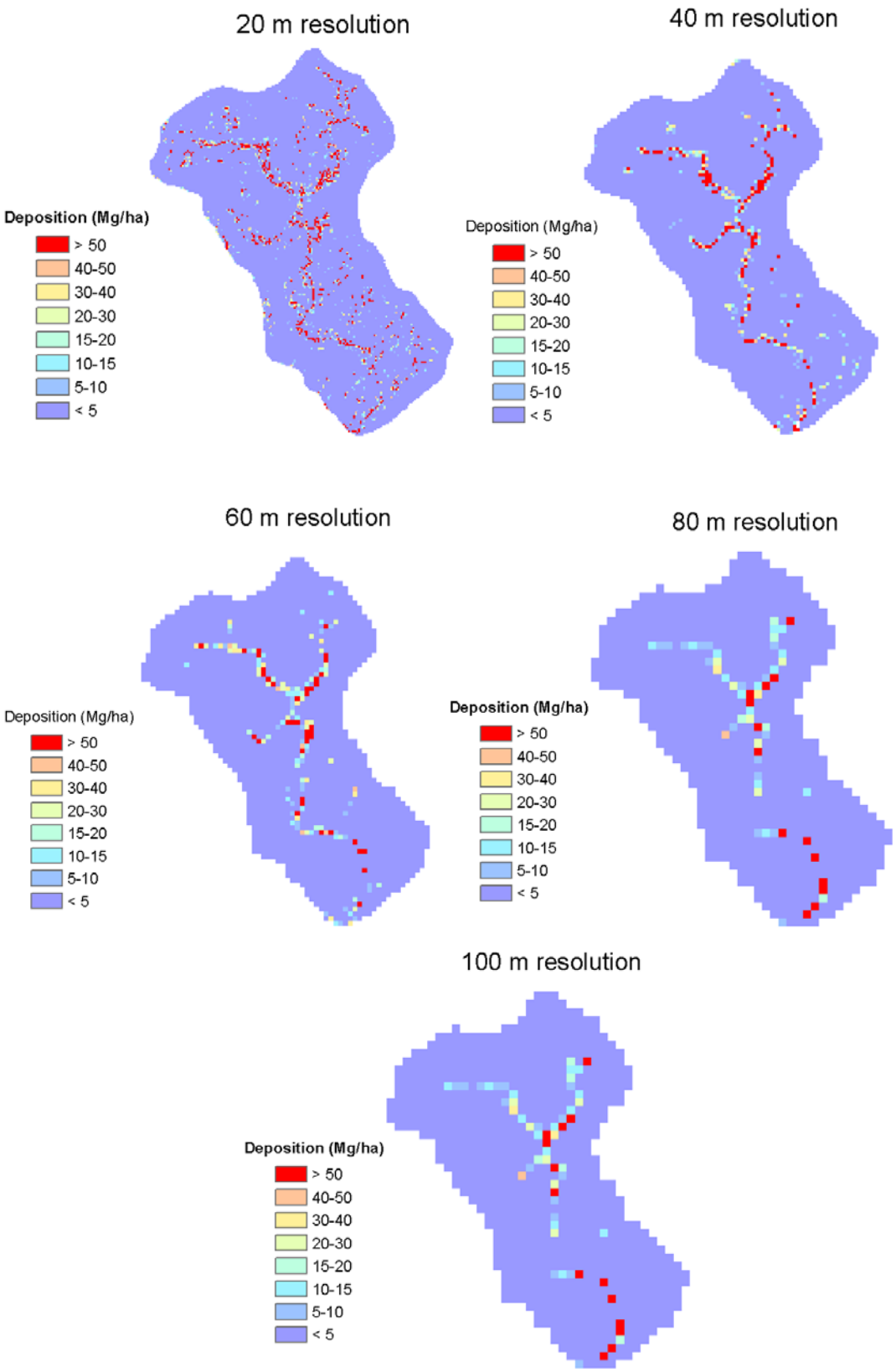

Figure 6.26: Effect of resolution on the distribution of sediment deposition with 8 classes

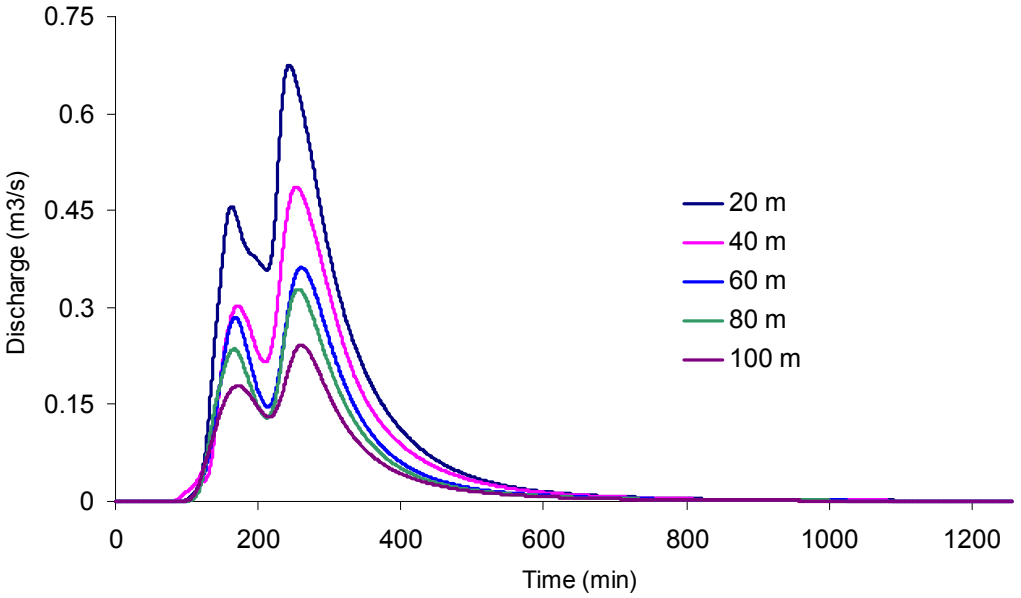

Figure 6.27: Effect of resolution on hydrographs at the catchment outlet

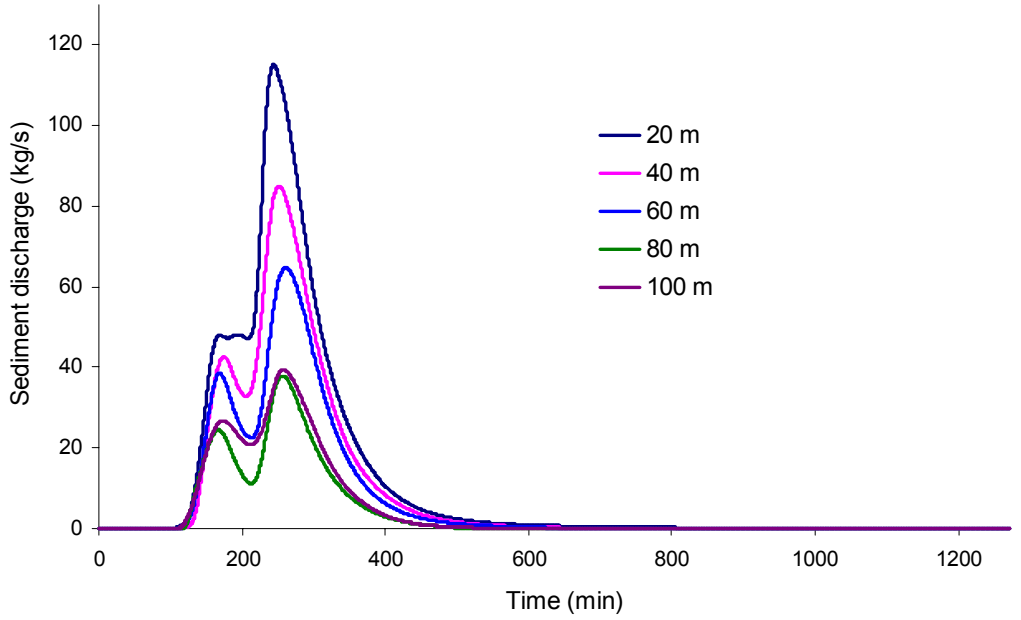

Figure 6.28: Effect of resolution on sediment discharge at the catchment outlet

6.7.3 Spatio-Temporal Outputs

Two thousand six hundred spatio-temporal maps on each major hydrologic and erosion processes such as infiltration, surface storage, runoff, runoff height, runoff velocity, erosion, deposition, suspended sediment concentration, and overland transport capacity were generated at every time-step for the storm event simulated. These processes were viewed in the Aguila dynamic visualisation environment to see the each process movement across the catchment. The efficiency of flow and sediment routing at each grid-cell size was observed. These provide visuals to see what is happening across the catchment at every time-step. These maps could not be attached to this chapter either in static or dynamic mode, but they are provided separately on an optical disk attached to the thesis for dynamic visualisation. A few AVI format video files are created for quick dynamic visualisation of spatial-temporal outputs and are provided on an optical disk under a 'video' folder.

6.8 Sensitivity Analysis for DEM Parameters

Three parameters derived from a DEM such as slope gradient, aspect (LDD) channel gradient were used in the model for an event simulation. Sensitivity analysis to decreasing trend of slope gradient was studied only with 20 m PulSAR DEM dataset because the value of slope gradient must be within 0.001 and 1. It was found that the infiltration, time to peak runoff and splash detachment were increased by 4.49, 38.38 and 6.11 per cent respectively when the slope gradient was reduced by 90 percent (Appendix E-24). Similarly, the runoff coefficient, peak discharge, flow detachment, overland deposition, channel erosion, channel deposition and total soil loss were reduced by 81.85, 89.73, 100.0, 98.87, 43.10, 33.71 and 90.92 per cent respectively when the gradient was reduced by 90 per cent. In other words, flattening of slope gradient produces lower runoff and sediment yield from a catchment (Figure 6.29). Sensitivity analysis of the LDD and channel gradient could not be studied because the LDD holds a directional value and the variation in channel gradient was quite small. Moreover, channel gradient did not have a significant effect on model outputs.

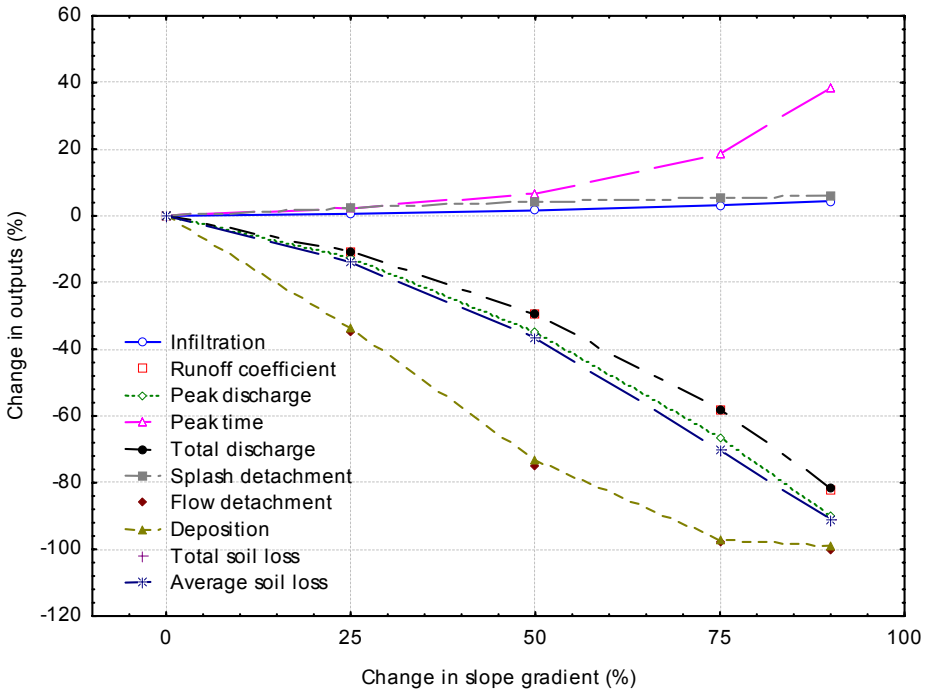

Figure 6.29: Model sensitivity to slope gradient at medium moisture level with 20 m PulSAR DEM dataset

6.9 Statistical Evaluation

Statistical evaluation is necessary to assess the performance of a spatially distributed and dynamic model for an event simulation. There are several statistical criteria used for performance evaluation discussed in the literature by Quinton (1994). For the Saltdean catchment, no statistical evaluation was carried out on model performance because there was no validation dataset available.

6.10 Propagation of Errors in Modelling

6.10.1 Overview

Distributed modelling consists of three stages: firstly, data collection which deals with collection of point or spatial data from various sources; secondly, creation of a GIS database of model input parameters; and thirdly, testing input values in a model. The errors can creep up at any of these stages. Errors in data is one aspect of error propagation in modelling while the uncertainly in model parameters and the mathematical expressions to represent processes in the model itself contribute to the

error in modelling results. The estimation of error propagation in erosion modelling was beyond the scope of the study. However, a brief overview of possible errors that might be introduced in the distributed erosion modelling is discussed. This will act as guidance for reliability of modelling results using LISEM.

6.10.2 Source of Errors in a GIS

The quality of key spatial data is fundamentally important to the reliability of modelling results. A GIS is principally based on the spatial entities and non-spatial attributes. The positional errors and attribute uncertainty are most important characteristics of all spatial databases. These errors are propagated and amplified by GIS operations, which adversely affect the potential application of GIS for extraction of distributed model parameters. The sources of errors in the spatial data are discussed in the literature by Burrough and McDonald (1998).

6.10.3 Error Propagation in Modelling

The quality of modelling results depends on the spatial data error and model error (Burrough et al, 1996). A successful distributed modelling is more dependent on data availability and its quality rather than by lack of process understanding and insight. Model prediction can be affected by uncertainty and errors in the values of coefficients and boundary conditions. The LISEM model assumes to have no residual error (Jetten, 2000), so most errors in prediction emanate from spatial data quality and model parameter extraction.

6.11 Guidelines for Spatial Variability on Catchment Scale Modelling

Various grid-cell sizes of an original resolution of the DEM directly influence runoff and erosion processes as the parameters are scale dependent. Increasing the grid-cell size from 20 to 100 m flattens the slope gradient and shortens the drainage length. Both have competing effect on the runoff and sediment flow routing. Over sampling of a coarse DEM at fine resolution does not add any more information, but it may introduce some kind of noise instead. Therefore, an appropriate resolution is necessary

to identify to optimisation of data collection and computer resources for catchment scale modelling.

Calibration is necessary to tune a physically based model with observed values to develop the confidence in modelling results. The model should at least be calibrated at a resolution to use for the prediction at other resolutions. In developing countires, observed data on runoff and sediment yield for a catchment are rarely available. In the absence of such observed dataset, a relative evaluation across various grid-cell sizes and DEM sources was carried out.

For a given catchment scenario at a single soil moisture level, there is always a single observed value of runoff, soil loss and peak discharge for a storm event. How these outputs are predicted with a reasonable accuracy using whatever resolution and whichever DEM needs to be examined. It was carried out for the runoff, average soil loss and peak discharge individually. These outputs were predicted for five DEMs at five resolutions each and are relatively compared against the Cartometric DEM as it is widely used in developing countries for the modelling purpose. To what extent these predictions could be improved using DEMs derived remote sensing against a cartometric DEM.

Comparison among various DEMs

The runoff was improved by 6-7, 19-21 and 37-42 per cent for the PulSAR DEM and Landmap DEM at high, medium and low moisture levels respectively as compared to the Cartometric DEM at 20 m resolution. Similarly, it was improved by 2, 5 and 14 per cent for the ASTER DEM; and was under predicted by 8, 1 and 12 percent for the SRTM DEM at high, medium and low moisture levels respectively (Figure 6.30). The PulSAR and Landmap DEMs improve the predictions because their slope gradients are inherently better than the Cartometric DEM. It was found that resampling of a coarse resolution SRTM DEM to smaller grid-cell sizes did not improve the prediction of runoff at all three moisture levels. At 100 m, runoff was over predicted as compared to an 80 m resolution. Therefore, a high resolution DEM should be resampled to 80 m grid cell size, but the resampling reduces the spatial variability drastically.

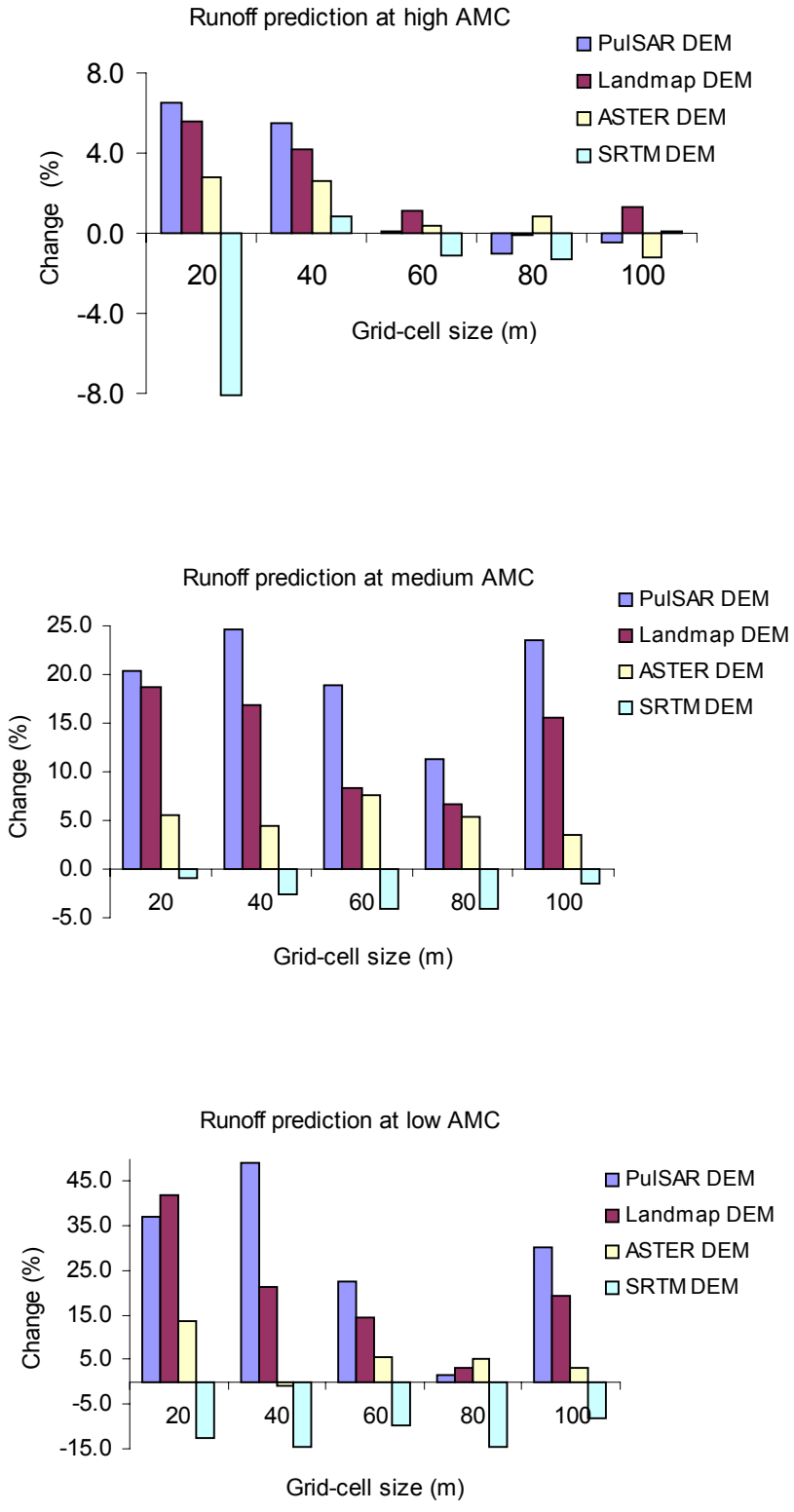

Figure 6.30: Runoff prediction as compared to the Cartometric DEM at three moisture levels

The average soil loss was improved by 71, 153-157 and 47-125 for the PulSAR DEM and Landmap DEM at high, medium and low moisture levels respectively as compared to the Cartometric DEM at 20 m resolution (Figure 6.31). Similarly, it was absolutely under predicted by 100, 100 and 100 per cent for the ASTER DEM; and was improved by 4, and 45, and under predicted by 98 for the SRTM DEM at high, medium and low moisture levels respectively. The ASTER DEM could not be used for the prediction of soil erosion because its results were poor at medium and low moisture levels. Both the PulSAR DEM and Landmap DEM are suitable for erosion modelling as they improve the prediction due to inherent better slope gradient mapped by remote sensing. The average soil loss at 80 m for the SRTM DEM was under predicted by 100 percent at all three moisture levels. The SRTM DEM predicts better at other grid-cell sizes than the original resolution. It emphasises that the released SRTM DEM contained artefacts, so it should either be filtered or resampled to smaller or larger grid-cell size to obtain a reasonable prediction. It should be used at original resolution for modelling in any case.

The peak discharge was under predicted by 2-5 per cent at high moisture level and was improved by 16-22 and 25-147 per cent at medium and low moisture levels for the PulSAR DEM and Landmap DEM (Figure 6.32). Similarly, the peak discharge was under predicted by 21 and 23 per cent and was improved by 58 per cent at high, medium and low moisture levels for the ASTER DEM. The peak discharge is under predicted by 18, 14 and 14 per cent for the SRTM DEM at high, medium and low moisture levels. The PulSAR and Landmap DEMs improve the prediction of peak discharge against the cartometric DEM. The SRTM DEM did not predict the peak discharge very well. The ASTER DEM still predicts well. Therefore, the ASTER DEM is reasonably good for the prediction of runoff only.

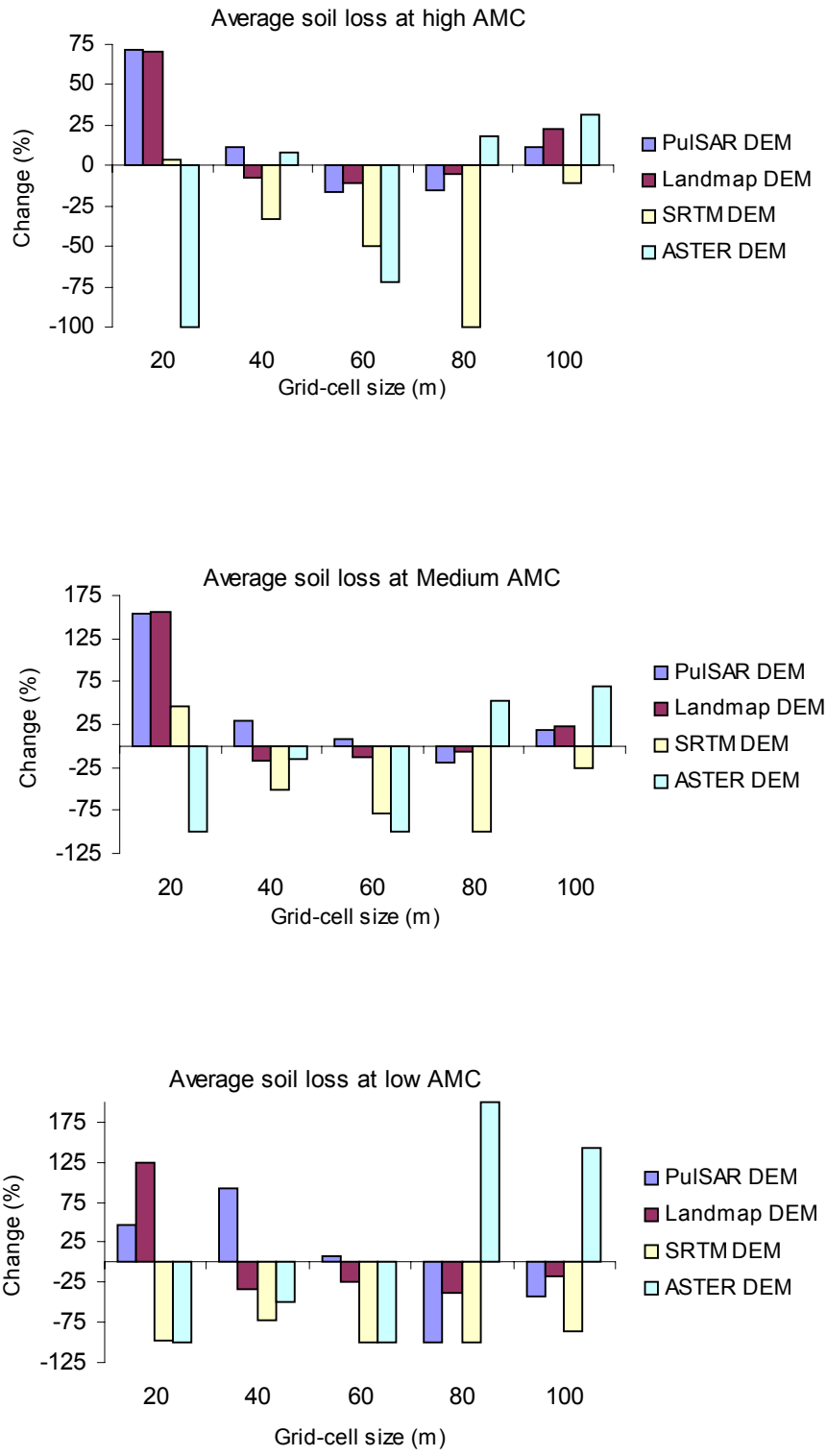

Figure 6.31: Prediction of average soil loss as compared to the Cartometric DEM at three moisture levels

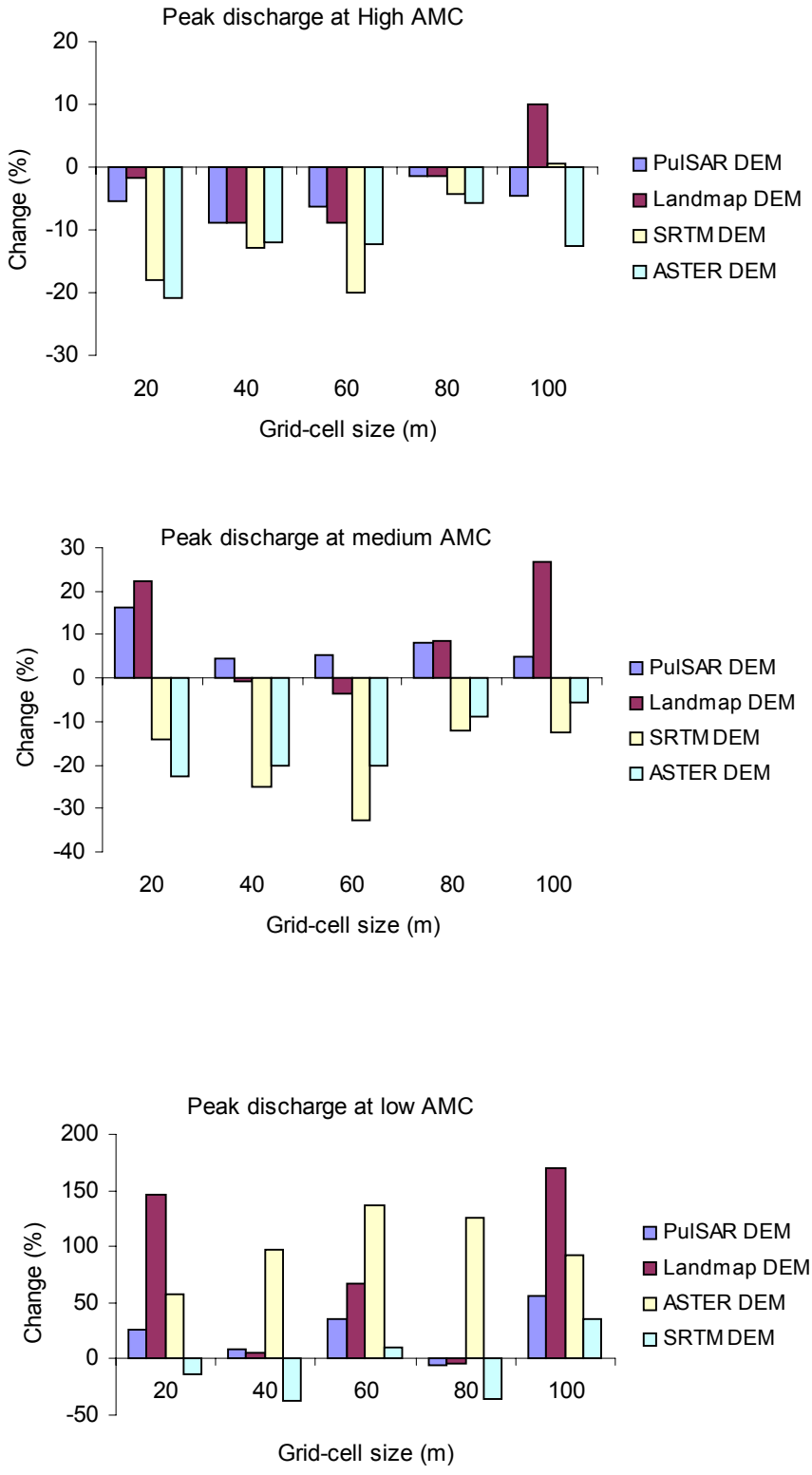

Figure 6.32: Prediction of peak discharge as compared to the Cartometric DEM at three moisture levels

Comparison among various resolutions

The runoff was reduced by 28, 40 and 60 per cent for the PulSAR DEM; by 26, 47 and 62 per cent for the Landmap DEM; by 26, 43 and 62 per cent for the ASTER DEM; 16, 35 and 61 per cent for the SRTM DEM; and by 23, 38 and 61 per cent for the Cartometric DEM at high, low and medium moisture levels respectively as compared to 20 m resolution (Figure 6.33). The PulSAR DEM, Landmap DEM and ASTER DEM have little more variability than the Cartometric DEM. At medium moisture, all DEMs show the same variability of around 60 per cent. The SRTM DEM has the lowest variability at high and low moisture levels. Higher runoff variability for the PulSAR dataset is caused by higher slope gradient. Lower variability for the SRTM is caused by lowest slope gradient. The ASTER DEM dataset has a medium variability at all three moisture levels.

The average soil loss at high moisture level was reduced by 24, 16, <1 and 18 per cent for the PulSAR DEM, Landmap DEM, SRTM DEM and Cartometric DEM respectively at 100 m grid-cell size as compared to 20 m resolution (Figure 6.34). Similarly, the average soil loss at medium moisture level was reduced by 62, 61, 59 and 19 per cent for the PulSAR DEM, Landmap DEM, SRTM DEM and Cartometric DEM. At low moisture level, average soil loss was reduced by 88, 88, 155 and 68 per cent for the PulSAR DEM, Landmap DEM, SRTM DEM and Cartometric DEM. The ASTER DEM produces poor results at 20 m resolution at all three moisture levels. The SRTM produces fairly well at medium moisture level.

The peak discharge was reduced by 38, 38, 31, 25, and 32 per cent at high moisture level; by 66, 61, 63, 62 and 54 per cent at medium moisture level; and by 40, 48, 41, 52, and 24 per cent at low moisture level for the PulSAR, Cartometric DEM, Landmap DEM, SRTM DEM and ASTER DEM respectively at 100 m grid-cell size as compared to 20 m resolution (Figure 6.35). The lowest runoff variability was observed at high moisture level among DEMs, highest at medium moisture level and medium at low moisture level. Lower variability is observed at smaller grid-cell sizes.

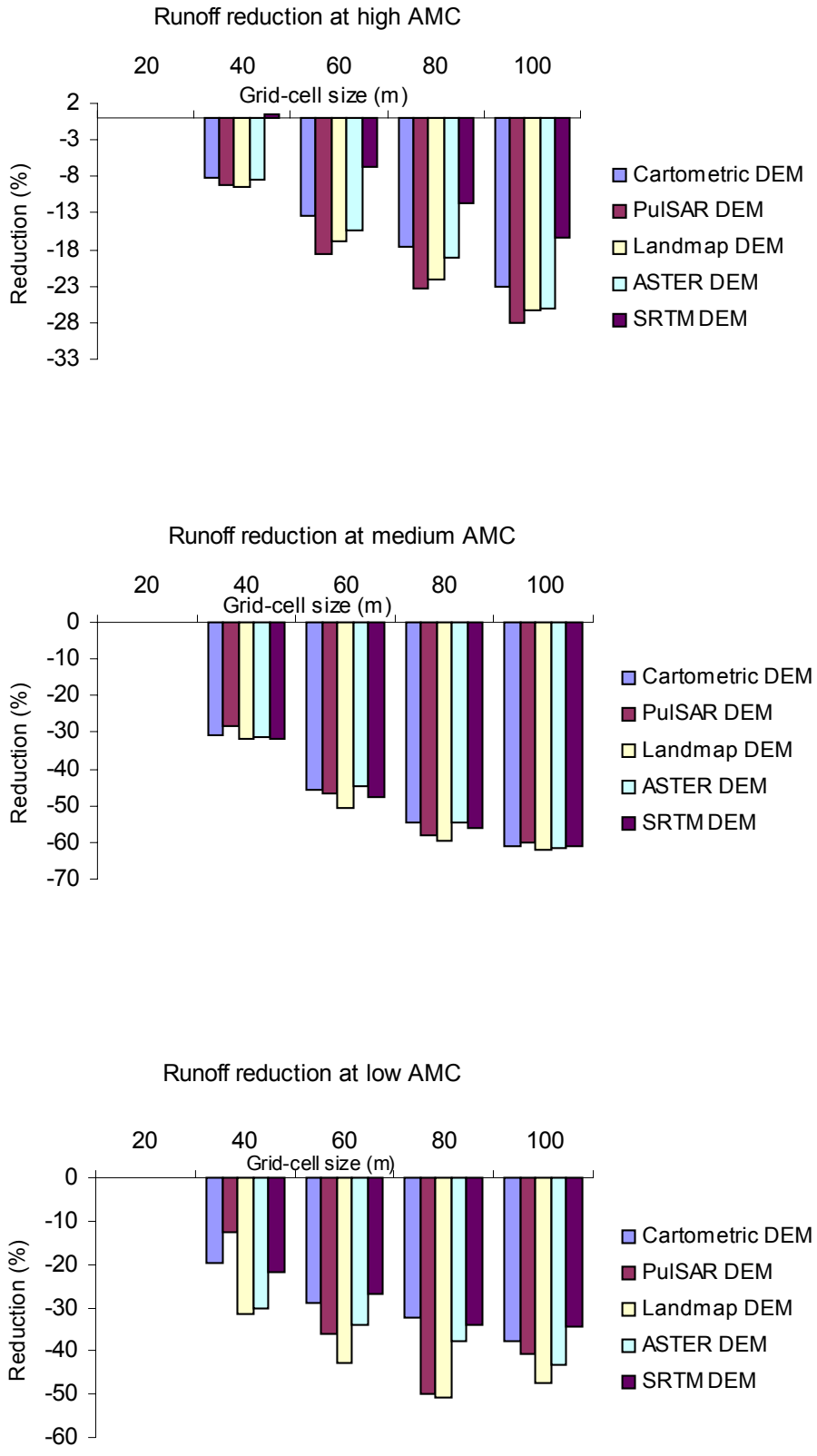

Figure 6.33: Change in runoff against 20 m grid-cell size at three AMC

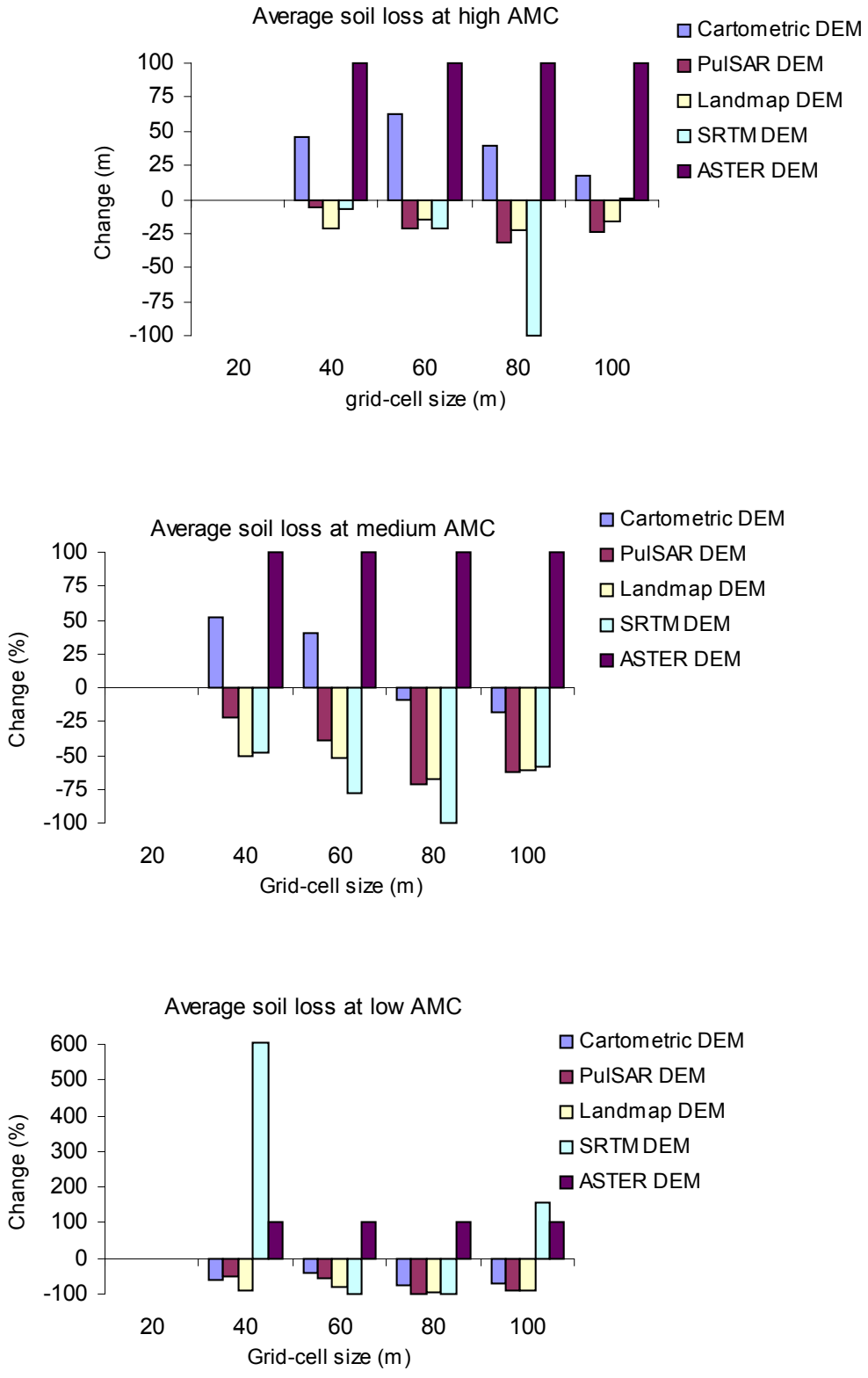

Figure 6.34: Change in average soil loss against 20 m grid-cell size at three AMC

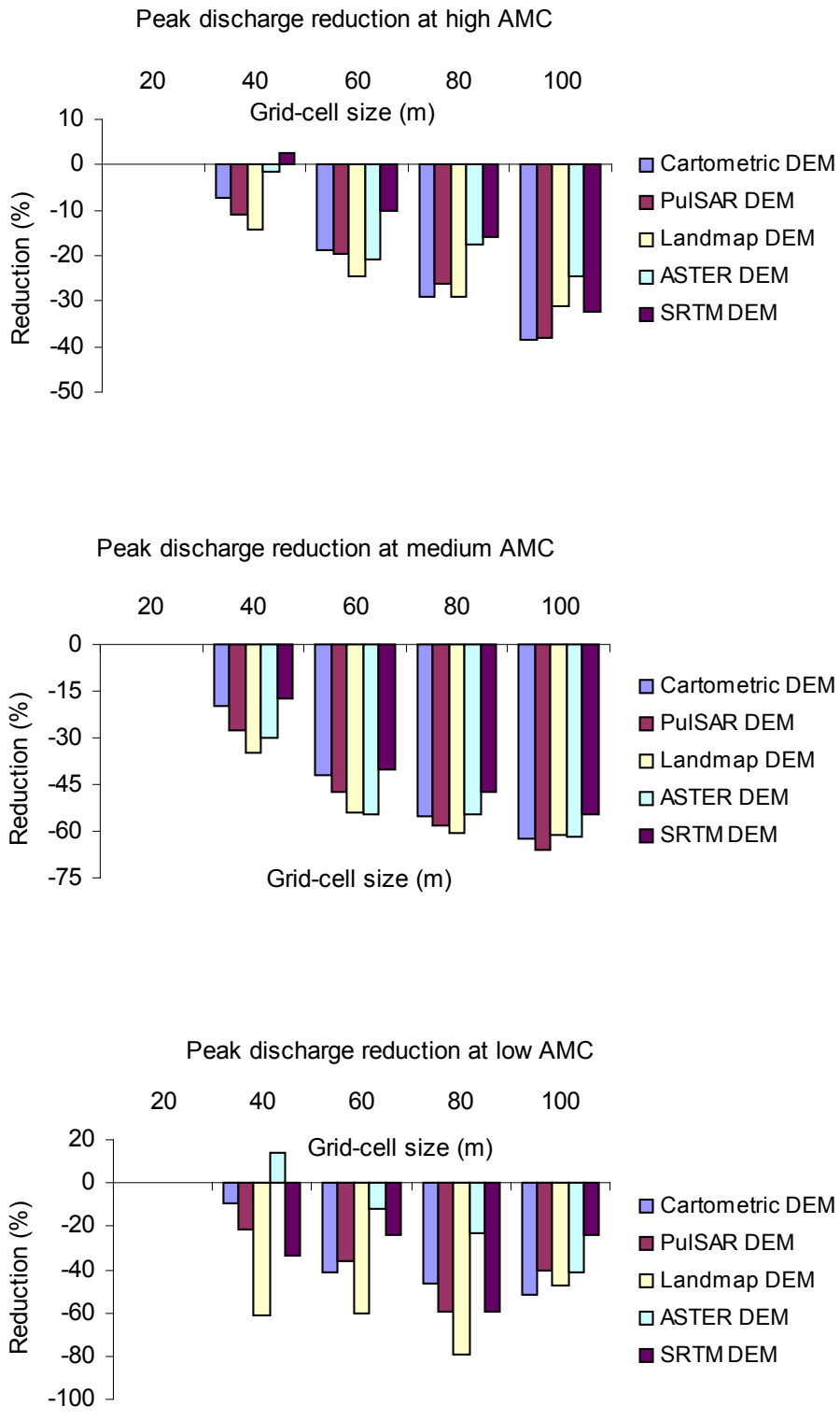

Figure 6.35: Change in peak discharge against 20 m grid-cell size at three AMC

6.12 Concluding Remarks

6.12.1 Discussion

The preceding sections of this chapter provide a comprehensive summary of effects of various grid-cell resolutions on dynamic modelling results for a storm event including sensitivity analysis and propagation of error in distributed modelling.

Key spatial data including three interferometric SAR DEMs, a cartometric DEM and an optical stereo DEM, a land use and land cover map and a soil map were resampled into five grid-cell resolutions. In additions to these datasets, crop, soil and surface parameters were estimated for possible field conditions assumed in the catchment in combination with the guidelines. Infiltration parameters for a single layer Green and Ampt model were extracted for the dominant soil series from the soil map of 1: 250 000 scale. These datasets were brought into PCRaster to create 25 LISEM databases of 30 parameters each for modelling the effects of various spatial representations on surface hydrologic and erosion processes.

The effects of grid-cell size on the slope gradient, drainage network and catchment area were studied. The mean slope gradient of the PulSAR DEM was the highest in all five 20 m resolution DEM datasets because no smoothing and filtering were performed deliberately while four other DEMs have undergone some level of smoothing and filtering during their production. The mean slope gradient of the PulSAR DEM reduced by 28 per cent as the grid-cell resolution was increased. This trend is supported by Vieux (2000). It is a result of cutting of hills and filling of valleys at larger resolutions by an aggregation scheme. The total drainage and channel lengths shortened at larger grid-cell sizes. At larger grid-cell sizes, the drainage network and channel length are short circuited because of cutting of hills and filling of valleys, thus, causing an overall shortening of the drainage network and channel length. The results indicate that the catchment area also increased by approximately 9 per cent as the grid-cell size was increased from 20 to 100 m for all DEM datasets. The effect of increased catchment area contribution on model outputs was normalised by subtracting an equivalent percentage of increased area from outputs to make a sensible comparison between different resolution outputs. An alternative way to address this issue is to

constrain the catchment area to approximately same area by excluding boundary cells manually (Molnár and Julien, 2000; Vieux, 2000). This approach could not be used because of limited functionality in PCRaster.

The effects of resolution on surface hydrologic and erosion processes at three moisture conditions were studied. The interception remained same for all DEM datasets at all three antecedent moisture conditions as the grid-cell size was increased. Interception is not influenced by the topography. Therefore, it is independent of grid-cell sizes of the DEMs. The change in the interception at coarser resolutions was insignificant (0.03 per cent) and it was purely caused by the rounding errors. The slight decrease in the interception at 40 m resolution in all DEMs was observed which could be caused by instability in the model algorithm.

The results indicate that the infiltration increases at coarser resolutions. Large variation in the infiltration at 20 m grid-cell resolution was observed in all DEM datasets. Its variability reduced from high to low soil moisture level as well as at coarser resolutions. Higher infiltration with lower variability was observed for the SRTM and cartometric DEM datasets at all moisture conditions. It was caused by slope flattening because of smoothing applied and hence, more infiltration. Lower infiltration with higher variability was observed for the PulSAR and Landmap DEM datasets because the Landmap DEM is a multipass DEM, which has undergone some level of smoothing during its production. The PulSAR DEM is an unfiltered DEM and has the highest slope gradient. Hence, it resulted in the lowest infiltration. The ASTER DEM has medium infiltration with medium variability at all three moisture conditions because it has medium slope gradient.

The runoff coefficient decreases with an increase of grid-cell size. Large variation in the runoff was observed at smaller grid-cell sizes and high moisture content for all DEM datasets. Its variability reduced from high to low soil moisture as well as at larger grid-cell size. Higher runoff with higher variability was observed for the PulSAR and Landmap DEM datasets at all moisture conditions. It was results of higher slope gradients and, hence, more runoff. Lower runoff with a lower variability was observed for the SRTM and Cartometric DEM datasets because of their lower slope gradients.

The ASTER DEM has medium runoff with medium variability at all three moisture conditions.

The peak discharge decreases as the grid-cell size is increased. A large variation in the peak discharge was observed at smaller grid-cell sizes and at high moisture content in all DEM datasets. Its variability reduced from high to low soil moisture as well as at coarser resolutions. Higher peak discharge with a higher variability was observed for the Cartometric and Landmap DEM datasets at high moisture content. Lower peak discharge with a lower variability was observed for the ASTER and SRTM DEM datasets. The PulSAR DEM has a medium peak discharge. At medium moisture, the Landmap DEM dataset produced the highest peak runoff while the ASTER DEM produced the lowest peak discharge. At low moisture condition, the Landmap DEM dataset produced the highest peak discharge while the ASTER DEM dataset produced the lowest. An inconsistent result was observed in the ASTER DEM at 40 m at high moisture condition.

The results suggest that the time to peak runoff decreases as the grid-cell size is increased. At high moisture content, the Cartometric and Landmap DEM datasets resulted in the highest and lowest peak time. The decreasing trend was observed for the Cartometric, SRTM and ASTER DEM while no definite trend appeared for the PulSAR and Landmap DEM datasets.

The results show that the splash detachment increases with an increase of moisture content and grid-cell size while the overland flow detachment and sediment deposition decreases at larger grid-cell sizes and at lower moisture conditions. The variability of splash detachment reduced from high to low soil moisture as well as at smaller grid-cell size. Higher splash detachment with a lower variability was observed for the Cartometric and ASTER DEM datasets at high moisture condition while the same was observed for the SRTM and Cartometric DEM datasets at medium and low moisture conditions respectively. It was caused by lower mean slope gradients. Lower splash detachment with a high variability was observed for the PulSAR and SRTM DEM datasets at high moisture and for the PulSAR at medium and low moisture conditions. Higher flow detachment and deposition with a higher variability was

observed for the PulSAR and Landmap DEM datasets at all moisture conditions while the lower splash detachment and deposition with a lower variability was observed for the cartometric and SRTM DEM datasets at all three moisture conditions.

The channel erosion decreases at larger grid-cell sizes and lower moisture levels. This trend was not observed at high moisture condition while it was strongly observed at medium and low moisture conditions. The channel deposition decreased at coarser grid resolutions and lower soil moisture levels for all the DEM datasets. The PulSAR, ASTER and Landmap DEM datasets produced the highest channel erosion at high, medium and low moisture conditions respectively. The SRTM has the lowest erosion with the largest variability at high moisture and the lowest erosion with the lowest variability at medium and low moisture conditions. The ASTER DEM has the highest deposition with the largest variability at all moisture conditions while the SRTM DEM has the lowest deposition with the lowest variability at all moisture conditions.

The results indicate that the total and average soil loss decreases at coarser grid-cell sizes and lower soil moisture levels. The total and average soil loss was higher for the PulSAR and Landmap DEMs and lower for the Cartometric and ASTER DEM datasets at all moisture conditions. The results from the ASTER DEM were inconsistent at 20 m resolution at all moistures and 40 m resolution at medium and low moisture levels. The SRTM produced inconsistent results at all the resolutions except at 40 m at low moisture conditions. The PulSAR, Landmap and Cartometric DEM datasets produced fairly good results. The total and average soil loss at 100 m resolution was always higher than that of the 80 m resolution. It could be caused by the error propagated by resampling. Therefore, 100 m resolution dataset is inadequate for representing spatial variability of the catchment characteristics for simulation of surface hydrologic and erosion processes from a storm.

It is also observed that smaller grid-cell size datasets produce detailed outputs on runoff and soil erosion, which are effective for identifying the exact location of sediment source and sink areas required for planning soil conservation measures. Larger grid-cell makes it difficult to identify the exact location of source and sink areas.

Sensitivity analysis provides an insight on model sensitivity to DEM derived parameters. The model sensitivity to the slope gradient was carried out. The results indicate that the infiltration, time to peak runoff and splash detachment are increased at lower slope gradients while the runoff coefficient, peak discharge, flow detachment, deposition, channel erosion and deposition, and total soil loss are reduced when the slope gradient is decreased. As the slope gradient is reduced, it produces lower runoff and sediment yield from a catchment. The LDD and channel gradient sensitivity could not be tested as it holds a directional data type. The variation in the channel gradient was quite small, so no sensitivity analysis was carried out.

The PulSAR and Landmap DEM datasets predict both runoff and soil erosion significantly better than the Cartometric DEM. Both show larger reductions in runoff and soil loss variability when the grid-cell sizes are increased. The ASTER DEM under predicts the average soil loss and is reasonably good for the prediction of runoff only. The SRTM DEM predicts better at other grid-cell sizes than the original resolution, which emphasises that the released SRTM DEM contained artefacts. Therefore, it should either be filtered or resampled to smaller or larger grid-cell size to obtain a reasonable prediction.

6.12.2 Conclusions

The influence of resolution on surface hydrologic and erosion processes at three antecedent moisture levels were analysed and the following conclusions were drawn:

- The mean slope gradient flattened as the grid-cell size was increased.
- Both total drainage length and channel length shortened at larger grid-cell sizes.
- The interception remained same at all resolutions and soil moisture levels.
- The infiltration increased as the grid-cell size was increased. The variation in the infiltration narrowed down at coarser grid-cell resolutions and at lower moisture levels. It indicates that the SRTM DEM dataset produced higher infiltration at all moisture levels because it has the lowest mean slope gradient by aggregation of 1 arc second to 3 arc second during production. The PulSAR and Landmap produced the lowest at high and medium, and low moisture levels because these

DEMs have higher mean slope gradient, which resulted in a quick drainage response.

- The runoff coefficient and peak discharge decreased with an increase in grid-cell size. Large variations at 20 m grid-cell resolution were observed in all the DEM datasets. It narrowed down at coarser resolutions in both cases.

- The splash detachment increased with an increase of grid-cell size at all antecedent moisture levels while the flow detachment and sediment deposition on overland decreased with an increase of grid-cell resolution at all moisture levels.

- The channel erosion at high moisture level has no definite trend but it decreased with an increase of grid-cell size at medium and low moisture levels while the channel deposition increased at larger grid-cell sizes for all the DEMs at three moisture levels.

- The total and average soil loss decreased at coarser grid-cell sizes. At high moisture level, a definite decreasing trend was observed for the PulSAR DEM dataset while no definite trend was observed for the other DEM datasets.

- Smaller grid-cell size datasets were found to be most suitable for identifying the exact location of sediment source and sink areas required for planning effective soil conservation measures.

- As the slope gradient was reduced in sensitivity analysis, the infiltration, time to peak runoff and splash detachment were increased while the runoff coefficient, peak discharge, flow detachment, deposition, channel erosion and deposition, and total soil loss were reduced. In other words, it produced lower runoff and sediment yield.

- The PulSAR and Landmap DEM datasets were found to be most suitable for improving the prediction of both runoff and soil erosion as compared to the Cartometric DEM. Guidelines presented highlight the role of remotely sensed derived DEMs for improving model predictions. These guidelines demonstrate the potential of this approach in developing countries.

7

Discussion, Conclusions and Recommendations for Future Study

In this chapter, a general discussion and conclusions on the influence of different resolutions of five DEMs on surface hydrologic and soil erosion processes at three antecedent soil moisture levels for a storm are summarised. Suitable guidelines identified for spatial variability at catchment scale modelling are also discussed. It also includes the recommendations for future study.

7.1 Introduction

Distributed soil erosion models require input parameters at an appropriate spatial scale (grid-cell size) for characterising the spatial variability of topography, vegetation and soil in a catchment. However, these models require a large number of input parameters, which can be derived from remotely sensed data and other spatial databases through a GIS. An embedded integration of erosion models within a GIS provides a powerful environment for modelling surface hydrologic and erosion processes at catchment scale. This integration avoids the programming of a database and display. In this context, the LISEM model was used with an aim to investigate the influence of different spatial representations of terrain, vegetation and soil on the performance of dynamic modelling on surface runoff and erosion processes in a GIS at catchment scale for an event in order to identify guidelines on catchment scale modelling.

The preceding chapters explain the procedures used to achieve the aim and objectives of the study, namely selection of a dynamic erosion model within a GIS, identification of rainstorm events, estimation of infiltration parameters, identification of land use and land cover, assessment of the public domain DEMs, generation of an InSAR DEM, creation of 25 LISEM databases at five resolutions and modelling the effects of resolution on surface hydrologic and erosion processes at three antecedent soil moisture levels for an event for the Saltdean catchment. All the previous chapters contain a comprehensive discussion and a set of conclusions corresponding to the findings of the each chapter. In this chapter, a general discussion and conclusions of the study are summarised and the recommendations for the further study are outlined.

7.2 General Discussion

Several issues on generation of key spatial data and input parameters and effects of resolution on modelling of surface hydrologic and erosion processes for a storm event were addressed in this study. The factors which affect the selection of a suitable model, the generation of key spatial data and input parameters, and modelling results are discussed individually below.

7.2.1 Selection of a Model Embedded within a GIS

LISEM was selected to study the effects of resolution on hydrologic and erosion processes for a storm because it allows spatial variability of input parameters at a resolution and its parameters have physical meaning. Moreover, it is developed for a European environment and catchment characteristics similar to the study catchment. Hence, it is applied and some parameter values from these catchments would be used. Since, it requires large amounts of input parameters and computational resources for a simulation, remote sensing and other spatial data have proved a cost effective alternative to parameterise the model.

The model simulates various options for infiltration, surface types, with or without channel, runoff or both runoff and soil loss to suit a variety of catchments in developing countries. It requires 24 parameters for a simple simulation. It could be applied for data poor catchments in developing countries by parameterising using remotely sensed and other spatial data. Being a physically-based model, it still contains

some empirical equations for process description such as transport capacity equation. PCRaster is a backbone of the LISEM model to create databases from various key spatial data. It does not have vector functionality and does not support widely used GIS data formats. It needs another supporting GIS for rasterisation of vector data and, projection and conversion of data into a GRID ASCII format for import. Despite all these limitations, PCRaster is a useful tool for dynamic and distributed erosion modelling.

7.2.2 Rainstorm and Its Distribution

A 6-hour storm segment of 30 October 2000 is used for the modelling study because of the limitation of computer disk space. The storm was a frontal storm, which covers a wider area and lasts for a couple of hours. The assumption of a uniform rainfall over the catchment due to single station rainfall data is largely valid for a frontal storm for the small catchment (~800 ha). Therefore, a single point rainfall data has provided a reasonable spatially representation of the storm over the catchment. A better spatial distribution of a storm would improve the reliability of model results.

The model is driven by the rainfall intensity and is more sensitive to shorter temporal resolution of the rainfall intensity. An hourly temporal resolution of the rainfall data is too coarse for assessing the temporal variability of a storm. This resolution of rainfall data is considered more or less representative for the frontal storm under the situation, but they are not ideal for modelling. The break point intensity data pairs of the storm could not be identified precisely from hourly data. This is one of the limitations of hourly data. The assumption of a constant intensity rainfall for a whole hour could rarely be valid for a frontal storm in reality. This assumption introduces a higher response from erosion and deposition processes in the model. Shorter temporal resolution storm data would be ideal for small catchments.

7.2.3 Infiltration Parameters

Infiltration parameters for a single layer Green and Ampt model were estimated from an available 1:250 000 scale NATMAP soil map using pedotransfer functions, described in Chapter 3. The soil associations in the map comprise a dominant and three to four associated soil series, which could not be spatially located by any means in soil

association polygons. Therefore, an assumption of the dominant soil series in each mapping polygon has largely reduced the spatial variability of infiltration parameters in the catchment. It affects the prediction of runoff and erosion in absolute quantity. For this study, the variability of parameters is not absolutely required. Higher spatial variability is better for model calibration and for comparison in absolute terms. Larger scale soil data would be better for assessing the spatial variability of infiltration parameters on hydrologic and erosion processes at catchment scale.

7.2.4 Land Use and Land Cover

Remote sensing is used for obtaining a reliable land use and land cover map close to a historic storm event. A hybrid classification procedure, described in Chapter 4, was successfully used to identify a land use and land cover map with an overall accuracy of 90 per cent from SPOT-1 data. There are a few significant problems with classification because of the spectral confusion caused by bare fields, farm buildings, urban areas and sea water; and grasslands in valleys and on slopes. These problems are further compounded by the untimely ground survey. Reliability of ground data is lessened during classification, which emphasises the importance of timely ground survey. NDVI data could not be used to derive the percentage ground cover and leaf area index for this study because of absence of field observations. Field observations are necessary to establish the relationship between NDVI and biophysical parameters.

The model relies on land use and land cover map for deriving crop and vegetation dependent parameters by reclassifying. Therefore, the classification accuracy would affect the parameter accuracy and hence, the model outputs.

7.2.5 Assessment of Public Domain DEMs

Landmap, ASTER and SRTM-3 DEMs are used to investigate their usefulness on model predictive capacity. These DEMs are described in Chapter 5. The Landmap DEM is of good quality DEM with a vertical accuracy of 6 m, which is suitable for modelling, but it still contains error in woodland and built-up areas in the catchment. The ASTER DEM is a relative height DEM and its quality could not be assessed precisely. Its vertical accuracy is assessed by a crude method. It has vertical accuracy similar to that of the Landmap DEM. Relative height does not affect slope gradient used in the model.

The SRTM-3 is a medium resolution unedited DEM and has a vertical accuracy of about 4 m. These DEM are not error free and do contain ground clutter and water body artefacts. How quality of these DEMs affects the modelling results are examined and discussed later.

7.2.6 Generation and Quality Assessment of InSAR DEMs

Spaceborne SAR interferometry is explored for generating high resolution DEMs from an ERS data pair in the context of developing countries, described in Chapter 5. PulSAR/InSAR Toolkit is successfully used to generate reliable InSAR DEMs. Processors used in this study had a major problem with data ingestion with data supplied by the I-PAF. It was realised that there is no exhaustive guideline for the selection of a quality data pair and a processor. Strategies for the selection of a quality data pair and a processor are outlined. Despite exhaustive ERS data search for a good data pair, a pair was selected for which no precision orbits data were available. This information is still not available from many sources. It emphasises the importance of guidelines for selection of a quality pair.

Quality assessment of the InSAR DEM reveals that it has a vertical accuracy (RMSE) of 20 m at 25 m grid-cell spacing. This large error is attributed to the non-availability of precision orbits data due to telemetry failure during the pair acquisition. This issue is not well addressed on the European Space Agency's website. It was known lately when precision orbit data was ordered. These data are necessary for precise geocoding. An attempt was made to rectify this systematic error using baseline refinement procedure through the ground control points. However, it could not be fully rectified and resulted in a vertical height error. Therefore, the necessity of precision orbit data for SAR data is emphasised for obtaining high quality InSAR DEMs. The model uses the slope gradient and aspect derived from a DEM, which are not influenced by systematic height error present in the InSAR DEM. On the quality assessment of an InSAR DEM against a reference drainage network, it found that InSAR DEMs are suitable at 1:25 000 or smaller scale for distributed modelling.

A photogrammetric DEM reveals on its quality assessment that it contains heavy clutter on the edges and holes in low tonal area because of the poor quality of

aerial photographs. It was timey consuming to edit such a DEM for removing clutter. It was learnt that the Sussex photography project was not intended for topographic mapping. This DEM could not be used as a validation DEM. It emphasises the need to select quality photograph pairs for an application. It was experienced in this study that InSAR DEM generation is less cumbersome than the optical stereo and radargrammetric DEM generation due to the presence of clouds and speckle respectively.

7.2.7 Creation of Different Spatial Representations

Five DEMs, a land use and land cover map and soil data each were resampled into five resolution datasets to derive input parameters at each resolution. All input parameters could not be extracted from these spatial data. Several crop, soil and surface parameters are required for the creation of a LISEM database. These parameters are generally not available in the developing world. They need to be estimated for possible field conditions assumed for the catchment at the time of a storm using guidelines. This requires some field observations to reclassify spatial data into parameter maps. These can be measured from the field observations for a future storm event. This kind of estimation may not yield an exact value, but it is representative for assumed conditions in the catchment. This is one of the limitations of the model application for a historic event. Moreover, an exact parameter value is not required for this study as it is concerned with model sensitivity to different resolutions and DEM sources. There are data import problem with PCRaster as it only supports data in GRID ASCII format. So every data needs to be converted to this format for which another supporting GIS is necessary.

7.2.8 Dynamic Erosion Modelling

Twenty-five LISEM databases with 30 parameters each were created and tested in the model for sensitivity analysis for different resolutions and DEMs. The model assumes no default parameter value. Everything should be defined for a simulation. It requires a large storage space as a single simulation of 1300 min at a 30 seconds time step produces spatio-temporal outputs of ~1.2 GB for a 20 m resolution dataset each for 8 sq km catchment. The model would have more limitations for catchments with larger

areas in terms of storage space and computing power. The model also over predicts the erosion and deposition.

7.2.9 Effects of Resolution on Hydrologic and Erosion Processes

As the grid-cell size increases, the slope gradient reduces and the drainage length shortens. It also increases the catchment area, which affects the hydrologic and erosion response for a storm caused by increased area contribution. It is normalised for area dependent processes.

The runoff coefficient decreases as the grid-cell size increases. Large variation in the runoff is observed at large grid-cell size at medium moisture level for all the DEM datasets with respect to 20 m resolution. Its variability is highest, medium and lowest at medium, low and high moisture levels. Higher runoff with higher variability is observed for the PulSAR and Landmap DEM datasets at all moisture levels. The PulSAR DEM dataset produces higher runoff than the Landmap DEM at high moisture level because the PulSAR DEM has higher slope than the Landmap DEM dataset. The Cartometric DEM has higher runoff variability than the SRTM DEM dataset but has lower than the PulSAR and Landmap DEMs because the Cartometric DEM dataset has a higher slope gradient than the SRTM DEM. The ASTER DEM dataset has medium runoff with medium variability at all three moisture levels.

The average soil loss decreases at larger grid-cell sizes and at lower soil moisture levels. The average soil loss is higher for the PulSAR and Landmap DEM datasets and lower for the Cartometric and ASTER DEM datasets at all moisture levels. The results from the ASTER DEM dataset are not consistent at 20 m resolution at all moistures and 40 m resolution at medium and low moisture levels. The SRTM datasets produces poor results at all the resolutions except at 40 m at low moisture level. The PulSAR, Landmap and Cartometric DEM datasets produce fairly good results. The average soil loss at 100 m resolution was always higher than that of the 80 m resolution. It could be caused by the error propagated by resampling. Therefore, 100 m resolution dataset is not fairly good for representing spatial variability of catchment characteristics for the simulation on surface hydrologic and erosion processes from a storm.

The normalised peak discharge decreases as the grid-cell size is increased. Large variations in the peak discharge were observed at small grid-cell size and at high moisture levels in all the DEM datasets. Its variability reduces from high to low at lower soil moisture levels and at larger grid-cell sizes. Higher peak discharge with a higher variability is observed for the Cartometric and Landmap DEM datasets at high moisture content. Lower peak discharge with a lower variability is observed for the ASTER and SRTM DEM datasets. The PulSAR DEM dataset has a medium peak discharge. At medium moisture, the Landmap DEM dataset produced the highest peak runoff while the ASTER DEM produced the lowest peak discharge. At low moisture level, the Landmap DEM dataset produced the highest peak discharge while the ASTER DEM dataset produced the lowest. A definite trend in peak discharge was observed in the ASTER DEM dataset at 40 m at high moisture level.

7.2.10 Guidelines for Spatial Variability on Catchment Scale Modelling

In developing countries, observed data on runoff and sediment yield for a catchment are rarely available. In such case, a relative evaluation across resolutions and DEMs can be carried out. In this study, a relative evaluation was carried out for the runoff, average soil loss and peak discharge individually. These outputs were predicted for five DEMs at five resolutions each and were relatively compared against the Cartometric DEM. To what extent these predictions could be improved using DEMs derived remote sensing against the Cartometric DEM.

Comparison against the Cartometric DEM

The prediction of runoff was considerably improved for the PulSAR DEM and Landmap DEM and was marginally improved for the ASTER DEM at three moisture levels against the Cartometric DEM at 20 m resolution. Conversely, it was under predicted for the SRTM DEM by 1-12 per cent at three moisture levels. The runoff was over predicted at 100 m as compared to an 80 m resolution. Hence, a high resolution DEM should be resampled to 80 m grid cell size to obtain reasonable results, but the resampling reduces the spatial variability drastically.

The average soil loss was significantly for the PulSAR DEM and Landmap DEM at all three moisture levels as compared to the Cartometric DEM at 20 m resolution. Conversely, it was poorly predicted for the ASTER DEM and it was reasonably predicted for the SRTM DEM at three moisture levels respectively. The ASTER DEM should not be used for the prediction of soil erosion because its results were poor at medium and low moisture levels. Both the PulSAR DEM and Landmap DEM are suitable for erosion modelling as they improve prediction due to inherently better slope gradient mapped by remote sensing. Average soil loss at 80 m for the SRTM DEM was under predicted absolutely at all three moisture levels. The SRTM DEM predicts better at other grid-cell sizes than the original resolution. It emphasises the need for removing artefacts from the DEM. The SRTM DEM should either be filtered or resampled to smaller or larger grid-cell size to obtain a reasonable prediction.

Comparison against various grid-cell sizes

The PulSAR DEM, Landmap DEM and ASTER DEM have shown little more variability in runoff than the Cartometric DEM. At medium moisture, all DEMs show the same variability of around 60 per cent. The SRTM DEM has the lowest variability at high and low moisture levels. Higher runoff variability for the PulSAR dataset is caused by higher slope gradient. Lower variability for the SRTM is caused by lowest slope gradient. The ASTER DEM dataset has a medium variability at all three moisture levels.

The PulSAR DEM has shown a higher variability in average soil loss than the Cartometric DEM whereas the Landmap DEM has shown a lower variability than the Cartometric DEM. At medium moisture, the PulSAR DEM, Landmap DEM and SRTM DEM show the same variability of around 59-61 per cent. At low moisture level, average soil loss was reduced by 88, 88, 155 and 68 per cent for the PulSAR DEM, Landmap DEM, SRTM DEM and Cartometric DEM. The ASTER DEM produces poor results at 20 m resolution at all three moisture levels. The SRTM produces fairly well at medium moisture level. The ASTER should not be used for the prediction of soil erosion.

7.3 Conclusions

The general conclusions are listed according to the objectives set out for this study in Chapter 1 as follows:

Objective 1

- SAR Interferometry has been tested for a study area in the UK and was found suitable for catchment scale topographic mapping despite atmospheric perturbations. A vertical accuracy of 20 m was achieved despite non-availability of precision orbital data for a tandem pair of 1997. The orbit error was translated into the systematic height error.
- InSAR DEM quality was also assessed independently against a reference drainage network from the 1:10 000 scale topographic maps. It was found that the InSAR DEM is suitable for the extraction of a drainage network at 1:25 000 or smaller scale.
- The strategies for selection of optimal single SAR data pairs with suitable SAR and InSAR processors are shown to be practicable and applicable for developing countries. Furthermore, DEM accuracy is shown to be improved with optimal strategies involving a single pair set.

Objective 2

- The quality assessment of the Landmap, ASTER DEM and SRTM DEMs were found to be less 6 m RMS error and thereby suitable for modelling.
- The usefulness of the public domain DEMs for distributed modelling was tested and it was found that the Landmap DEM results in reliable predictions of runoff and soil loss. The ASTER DEM predicts runoff reasonably and soil loss poorly, and the SRTM DEM was shown to under predict both runoff and soil loss as compared to the Cartometric DEM.

Objective 3

- The LISEM model was shown as a useful tool for predicting effects of resolution on surface runoff and erosion dynamics at the catchment scale for a heavy storm.

- A 6-hour intense storm of 30 October 2000 was used for the simulation study due to a limitation of computer disk storage. Although hourly rainfall data from a single raingauge station was found too coarse for assessing the spatial and temporal variability of the storm, it was considered representative for a frontal storm. It was not possible to locate precise break point rainfall intensity pairs of a storm from this hourly data.
- The spatial variability of infiltration parameters derived for a single layer Green and Ampt model from the 1:250 000 scale soil map using pedotransfer functions was shown to reduce considerably in the catchment.
- A large time lag between the image acquisition and field survey makes ground data less reliable during supervised classification. A statistically sound sampling scheme with a timely field survey is emphasised for reliable image classification.
- A hybrid classification approach was found to be the most effective solution for this study. Overall accuracy and Kappa coefficient of classification were satisfactory. Therefore, an eleven class thematic image was further reclassified to nine classes and was post-processed for model parameterisation.

Objective 4

- As the grid-cell size increases from 20 to 100 m for all the DEMs, the catchment area increases, the slope gradient flattens, and the drainage length shortens. Both slope gradient and drainage length demonstrated a competing effect on runoff and sediment routing.
- The runoff coefficient and peak discharge were seen to decrease with an increase in grid-cell size. Large variations at 20 m resolutions were observed in all the DEM datasets and reduced at larger grid-cell sizes in both cases.
- The average soil loss was shown to decrease at larger grid-cell sizes. At high moisture levels, a definite decreasing trend was observed for the PulSAR DEM dataset whilst no trend was observed for the other DEM datasets.

Objective 5

- PulSAR and Landmap DEM datasets were shown to improve the prediction of both runoff and soil erosion as compared to the Cartometric DEM. Guidelines are presented highlighting the role remotely sensed derived DEMs offer in improving model predictions. These guidelines demonstrate the potential of this approach in developing countries.
- Smaller grid-cell size datasets are shown as the most suitable for identifying the exact location of sediment source and sink areas, thereby facilitating the adoption of, for example, effective soil conservation measures.

7.4 Recommendations for Future Study

A series of future recommendations are made, including:

- A further study needs to be conducted with a better spatial and temporal distribution of the rainstorm particularly with a shorter temporal resolution rainfall data to improve the reliability of modelling results;
- A detailed study needs to be undertaken with larger scale soil data with more or less at a 1:50 000 scale with mapping unit as soil series to investigate the effect of soil variability on estimation of infiltration parameters. It would yield more realistic outputs and help in model calibration and validation;
- A further study with constrained similar catchment areas at various resolutions needs to be undertaken to investigate the influence of resolutions on surface hydrologic and erosion process and to compare with current results on normalisation issue;
- A detailed study with timely field survey needs to be undertaken to map the land use and land cover of the Eastern South Downs to improve classification accuracy. Using current multispectral sensors would improve the classification accuracy, providing improved spectral and spatial resolution;

- A detailed study with an ERS SAR raw data pair with the precision orbit data should be undertaken for deriving high resolution and quality InSAR DEMs with vertical accuracy on the order of metres for distributed modelling; and
- Further studies transferring this approach to other parts of the world, for instance developing countries, where land degradation has significant environmental and societal implications.

8

References

Ackermann, F. (1996) Techniques and strategies for DEM generation. *In:* C. Greve, ed. *Digital photogrammetry: An addendum to the manual of photogrammetr*y. Bethesda: American Society of Photogrammetry and Remote Sensing, 135-141

ADAS (1996a) *Landscape monitoring in the South Downs environmental sensitive areas (ESA), 1987–1995.* Unpublished report to Ministry of Agriculture, Fisheries and Food. (Accessed: 10 December 2003) http://www.defra.gov.uk/erdp/pdfs/esaspdfs/stage1/southlan.pdf

ADAS (1996b) *Environmental monitoring in the South Downs ESA, 1987–1995.* unpublished report to Ministry of Agriculture, Fisheries and Food. (Accessed: 10 December 2003) http://www.defra.gov.uk/erdp/pdfs/esaspdfs/stage1/southenv.pdf

Allmaras, R. R., Burwell, R. E., Larson, W. E. and Holt, R. F. (1966) Total porosity and random roughness of interrow zone as influenced by tillage. USDA Conservation Research Report, 7, as cited in Cremers, N. H. D. T., Van Dijck, P. M., De Roo, A. P. J. and Verzandvoort, M. A. (1996) Spatial and temporal variability of soil surface roughness and the application in hydrological and soil erosion modelling. *Hydrological Processes*, 10, 1035-1047

Anderson, J. R., Hardy, E. E., Roach, J. T. and Witmer, R. E. (1976) *A land-use and land cover classification system for use with remote-sensor data.* U. S. Geological Survey Professional paper 964, Washington: US Govt Printing Office. (Accessed: 17 February 2003) http://www.wsdot.wa.gov/environment/envinfo/docs/RSPrj_USGS_lulcclass.pdf

Aplin, P., Atkinson, P. M. and Curran, P. J. (1997) Fine spatial resolution satellite sensors for the next decade. *International Journal of Remote Sensing*, 18 (18), 3873-3881

Arya, L. M. and Paris, J. F. (1981) A physico-empirical model to predict the soil moisture characteristic from particle-size distribution and bulk density data. *Soil Science Society of America Journal*, 45, 1023-1030

Askne, J. and Hagberg, J. O. (1993) Potential of interferometric SAR for classification of land surfaces. *In: Proceedings of the Geoscience and Remote Sensing Symposium, 1993 (IGARSS '93) on Better Understanding of Earth Environment held at Tokyo from 18-21 August, 1993*, 3, 985-987

Aston, A. R. (1979) Rainfall interception by eight small trees. Journal of Hydrology, 42, 383-396 as cited in Jetten, V. (2002) *LISEM user manual, version 2.x. Draft version*. Utrecht Centre for Environment and Landscape Dynamics, Utrecht University, The Netherlands

Avery, B.W. (1990) *Soils of the British Isles*. Wallingford: CAB International

Axelsson, P. (1999) Processing of laser scanner data-algorithms and applications. *ISPRS Journal of Photogrammetry & Remote Sensing,* 54(2-3), 138-147

Bamler, R. (1992) A comparison of range-Doppler and wavenumber domain SAR focusing algorithms. *IEEE Transactions on Geoscience and Remote Sensing*, 30(4), 706-713,

Balmer, R. (1997) Digital terrain models from radar interferometry. *In*: D. Fritsch and D. Hobbie, eds., *Proccedings of Photogrammetric Week 97 , Heidelberg: Wichmann Verlag, 93-105.* www.ifp.uni-stuttgart.de/publications/phowo97/bamler.pdf (16 August 2003)

Bamler, R. (1999) The Shuttle Radar Topographic mission (SRTM): A worldwide 30 m resolution DEM from SAR interferometry in 11 days. *In:* D. Fritsch and R. Spiller, eds. *Proceedings of Photogrammetric week held at Wichmann Verlag, Heidelberg* http://www.ifp.uni-stuttgart.de/publications/phowo99/bamler.pdf (Accessed: 30 March 2004)

Barratt, G., Gaffney, V., Goodchild, H. and Wilkes, S. (2000) Survey at Wroxeter using carrier phase, differential GPS surveying techniques. *Archaeological Prospection*, 7, 133-143

Bayliss, A. (1999) *Catchment descriptors*. Flood Estimation Handbook (FEH), 5, Wallingford: Institute of Hydrology (Now CEH)

Beasley, D. B., Huggins, L. F., and Monke, E. J. (1980) ANSWERS: A model for watershed planning. *Transactions of the ASAE*, 23(4), 938-944

Beasley, D. B. and Huggins, L. F. (1981) *ANSWERS User's Manual*. Report No. EPA-905/9-82-001, U.S. Environmental Protection Agency, Region V, Chicago, Illinois: Purdue University, West Lafayette, Indiana

Belmans, C., Wesseling, J. G. and Feddes, R. A. (1983) Simulation model of the water balance of a cropped soil: SWATRE. *Journal of Hydrology*, 63, 271-286

Berry, J. K. (1993) Cartographic modelling: the analytical capabilities of GIS. *In:* M. F. Goodchild, B. Parks, and L. Steyaert, eds. *Environmental modelling with GIS*. New York: Oxford University Press, 58-74

Boardman, J. (1990). Soil erosion on the South Downs: a review. *In*: J. Boardman, I. D. L. Foster and J. A. Dearing, eds. *Soil Erosion on Agricultural Land*, Chichester: John Wiley & Sons, 87-105

Boardman, J. (1996) Soil erosion by water: problems and prospects for research. In: M. G. Anderson and S. M. Brooks, eds. Advances in Hillslope Processes, Chichester: John Wiley & Sons, (1), 489-505

Boardman, J. (2003) Soil erosion and flooding on the eastern South Downs, southern England, 1976-2001.*Transactions of the Institute of British Geographers*, 28 (2), 176-196

Boorman, D. B., Hollis, J. M and Lilly, A (1995) *Hydrology of soil types: a hydrologically-based classification of the soils of the United Kingdom*. Institute of Hydrology Report No.126, Wallingford: Institute of Hydrology (Now, CEH)

Bouwer, H. (1966) Rapid field measurement of air entry value and hydraulic conductivity of soil as significant parameters in flow system analysis. Water Resources Research, 2, 729-738 as cited in Rawls, W. J., Brakensiek, D. L. and Miller, N. (1983) Green-Ampt infiltration parameters from soil data. *ASCE Journal of Hydraulic Engineering*, 109 (1), 62-69

Brachet, G. (1986) SPOT: The first operational remote sensing satellite *In*: K. Szekield, ed. *Satellite remote sensing for resources development*. London: Graham & Trotman

Bradley, I. (2004) *Personal communication*, National Soil Resource Institute, Cranfield University at Silsoe

Brazier, R. (2004) Quantifying soil erosion by water in the UK: a review of monitoring and modelling approaches. *Progress in Physical Geography*, 28 (3), 340-365

Brooks, S. M. and McDonnell, R. A. (2000) Research advances in geocomputation for hydrological and geomorphological modelling towards the twenty-first century. *Hydrological Processes*, 14, 1899-1907

Brooks, R. H. and Corey, A. T. (1964) Hydraulic properties of porous media. Hydrology paper no 3, Colorado Sate University, Ft. Collins, Co 27 as cited in Vieux, B. E. (2000) *Distributed hydrologic modelling using GIS. Dordrecht*: Kluwer Academic Publishers

Burrough, P. A., van Rijn, R. and Rikken, M. (1996) Spatial data quality and error analysis issues: GIS functions and environmental modelling. *In:* M. F. Goodchild, L. T. Steyaert, B. O. Parks, C. Johnston, D, Maidment, M. Crane and S. Glendinning, eds. *GIS and environmental modelling: progress and research issue.* Fort Collins: GIS World Books, 29-34

Burrough, P. A. (1998) Dynamic modelling and geocomputation. *In:* P. A. Longley, S. M. Brooks, R. McDonnell, and B. Macmillan, eds*. Geocomputation: a Primer*. Chichester: John Wiley & Sons, 165-191

Burrough, P. A. and McDonnell, R. A. (1998) *Principles of geographical information systems*. 2nd edition, Oxford: Oxford University Press

Cafforio, C., Prati, C. and Rocca, E. (1991) SAR data focusing using seismic migration techniques, *IEEE Transactions on Aerospace and Electronic Systems*, 27 (2), 194-207

Campbell, J. B. (2002) *Introduction to remote sensing*. Third edition, London: Taylor and Francis

Carlson, T. N. and Ripley, D. A. (1997) On the relation between NDVI, fractional vegetation cover, and leaf area index. *Remote Sensing of Environment*, 62 (3), 241-252

Chao, W., Hong, Z., Guangdong, P. and Qingyou, Y. (1999) Retrieval of DEM from SIR-C data in Kunlun Mountain, West China. *In: Proceedings of the IGARSS '99 held at Hamburg, Germany from 28 June - 2 July, 1999*. IEEE 1999 International, 2, 1357 - 1359

Chen, D. and Stow, D. (2002) The effect of training strategies on supervised classification at different spatial resolution. *Photogrammetric Engineering & Remote Sensing*, 68(11), 1155-1161

Chitty, P. R. (2002) Personal communication, University of Sussex, Falmer, Brighton

Chow, V. T. (1964) *Handbook of applied hydrology: a compendium of water-resources technology.* New York: McGraw-Hill

Chow, V. T., Maidment, D. R. and Mays, L. W. (1988) *Applied hydrology*. New York: McGraw-Hill

Clark Lab (2004) IDRISI: *Image processing and GIS software*. http://www.idrisi.clarku.edu/IdrisiSoftware.asp?cat=2

CNES and Spot Image (1988) *SPOT user's handbook, volume I – reference manual*. No. SI/MR/88.0012a, Toulouse: CNES and Spot Image

CNES and MEDIAS (2004) *Incentive for the scientific use of Images from SPOT system (ISIS).* (Accessed: 20Aug 2004) http://medias.obs-mip.fr/isis/

Cochran, W. G. (1977) *Sampling techniques*. Third Edition, Wiley series in probability and mathematical statistics, New York: John Wiley & Sons

Cohen, A. (1995) *Digitizing options for hydrologic maps: scanning or hand digitizing*? U. S. Geological Survey, bulletin no. 2103 (4 January 2004) http://pubs.usgs.gov/bul/b2103/b.html

Collier, C. G. (1996) *Application of weather radar systems: a guide to uses of radar data in meteorology and hydrology*. 2nd edition, Chichester: Wiley-Praxis

Colombo, R., Bellingeri, D., Fasolini, D. and Marino, C. M. (2003) Retrieval of leaf area index in different vegetation types using high resolution satellite data. *Remote Sensing of Environment*, 86(1), 120-131

Congalton, R. G. and Green, K. (1999) *Assessing the accuracy of remotely sensed data*: principles and practices. Mapping science series, Boca Raton: Lewis Publishers

Congalton, R. G. (1991) A review of assessing the accuracy of classification of remotely sensed data, *Remote sensing of environment*, 37, 35-46

Congalton, R. G. and Mead, R. A. (1983) A quantitative method to test for consistency and correctness of photointerpretation. *Photogrammetric Engineering & Remote Sensing*, 49 (1), 69-74

Costantini, M. (1998) A novel phase unwrapping method based on network programming. *IEEE Transactions on Geoscience and Remote Sensing*, 36(3), 813-821

Curlander, J. C. and McDonough, R. N. (1991) *Synthetic aperture radar: systems and signal processing.* Chichester: John Wiley & Sons

Dammert, P. B. G. and Wegmüller, U. (1999) JERS InSAR DEM quality assessment for a boreal test site. *In: Proceedings of the IGRASS' 99 held at Honolulu from 28 June - 2 July 1999*, IEEE International, 4, 1930-1932

Daniel, C. and Tennant, K. (2001) DEM quality assessment. *In:* D. F. Maune, ed., *Digital elevation model technologies and applications: The DEM users manual*. Bethesda: American Society of Photogrammetry and Remote Sensing Publication, 395-440

DEFRA, NERC and the Met Office (2001) *To what degree can the October/November 2000 flood events be attributed to climate change*? DEFRA Technical Report FD2304, revised June 2001. CEH, Wallingford and the Met Office. (Accessed: 21 April 2004) http://www.defra.gov.uk/environ/fcd/floodincidents/fd2304r4.pdf

De Roo, A. P. J., Wesseling, C. G., Cremers, N. H. D. T., Offermans, R. J. E., Ritsema, C. J. and Oostindie, K. V. (1994) LISEM: a physically based hydrological and soil erosion model incorporated in a GIS. *In: Proceedings of the Fifth European Conference and Exhibition on Geographic Information Systems, EGI 94*, Utrecht: EGIS Foundation, 1994, 1,207-216 (Accessed: 14 May 2004) http://libraries.maine.edu/Spatial/gisweb/spatdb/egis/eg94023.html

De Roo, A. P. J., Wesseling, C. G. and Ritsema, C. J. (1996a) LISEM: a single-event physically based hydrological and soil erosion model for drainage basins. I: theory input and output. *Hydrological Processes*, 10, 1107-1117

De Roo, A. P. J., Offermans, R. J. E. and Cremers, N. H. D. T. (1996b) LISEM: a single-event physically based hydrological and soil erosion model for drainage basins. II: sensitivity analysis, validation and application. *Hydrological Processes*, 10, 1119-1126

De Roo, A. P. J. (1998) Modelling runoff and sediment transport using GIS. *Hydrological Processes*, 12, 905-922

De Roo, A. P. J. and Jetten, V. G. (1999) Calibrating and validating the LISEM model for two data sets from the Netherlands and South Africa. *Catena*, 37, 477-493

De Roo, A. P. J., Wesseling, C. G. and Van Deursen, W. P .A. (2000) Physically based river basin modelling within a GIS: The LISFLOOD model. *Hydrological Processes*, 14, 1981-1992

Davis , F. W., Quattrochi, D. A., Ridd, I. K., Lam, N. S. N., Walsh, S. J., Michaelsen, J. C., Franklin, J., Stow, D. A., Johannen, C. J. and Johnston, C. A. (1991) Environmental analysis using integrated GIS and remotely sensed data: Some research needs and priorities. *Photogrammetric Engineering & Remote Sensing*, 57(6), 689-697

Dillaha, T. (2004*) ANSWERS-2000*. (Accessed: 16 August, 2004) http://dillaha.bse.vt.edu/answers/

Di Luzio, M., Srinivasan R. and Arnold, J. G. (2004) A GIS-coupled hydrological model system for the watershed assessment of agricultural nonpoint and point sources of pollution. *Transactions in GIS*, 8(1), 113-136

Dowman, I. J., Chugani, K., Kitmitto, K., Muller, J. P. and Walker, A. H. (2000) Planimetric quality assurance of the Landmap mosaic: methods and results. *In: 26th Annual Conference of the Remote Sensing Society (RSS), University of Leicester, 12-14 September 2000* (Accessed: 21 February 2004) http://www.landmap.ac.uk/docs/RSS00_IJD_paperV2.pdf

Eineder, M and Holzner, J. (2000) Interferometric DEMs in Alpine Terrain – limits and options for ERS and SRTM. *In: Proceedings of the IGRASS' 2000 held at Honolulu from 24-28 July 2000*, IEEE, 7, 3210-3212

Endreny, T. A., Wood, E. F. and Lettenmaier, D. P. (2000) Satellite-derived digital elevation model accuracy: hydrological modelling requirements, *Hydrological Processes*, 14 (2), 177-194

Engel, B. A. (1996) Methodologies for development of hydrologic response units based on terrain, land cover and soils data. In: In: M. F. Goodchild, L. T. Steyaert, B. O. Parks, C. Johnston, D, Maidment, M. Crane and S. Glendinning, eds. GIS and environmental modelling: progress and research issues, Fort Collins: GIS World Books, 123-128

Engman, E. T. and Gurney, R. J. (1991) *Remote sensing in hydrology*. London: Chapman and Hall

ERDAS (2002) *ERDAS Imagine field guide*. Six Edition, Atlanta: ERDAS LLC and Leica Geosystems

ESA (2003) *ENVISAT radar altimetry tracks river levels worldwide*. Last update: 25 Sep 2003, European Space Agency. (Accessed: 30 March 2004) http://www.esa.int/export/esaSA/SEM7TF0P4HD_earth_0.html

ESA (2004) *SAR interferometry*. Document date 7 April 2004, Earthnet Online, European Space Agency.(Accessed: 8 April 2004) http://envisat.esa.int:80/rootcollection/eeo4.10075/002cb.html

Farr, T. G. and Kobrick, M. (2000) The Shuttle Radar Topography Mission: A Global DEM, *In: IGARSS Proceedings 2000, Honolulu, June 24-28, 2000*

Faulkner, D. (1999) *Rainfall frequency estimation*. Flood Estimation Handbook (FEH), 2, Wallingford: Institute of Hydrology (Now CEH)

Favis-Mortlock, D. and Boardman, J. (1995) Nonlinear responses of soil erosion to climate change: a modelling study on the UK South Downs. *Catena*, 25(1-4), 365-387

Favis-Mortlock, D. and Boardman, J. (1998) *Modelling soil erosion by water*. Berlin : Springer in cooperation with NATO Scientific Affairs Division,

Federal Geographic Data Committee, (1998a) *Geospatial positioning accuracy standards; part 3: national standard for spatial data accuracy*. FGDC-STD-007.3, Federal Geographic Data Committee. Washington, D.C. www.fgdc.gov/standards/status/sub1_3.html (Accessed: 18 February 2004)

Federal Geographic Data Committee (1998b) Content standards for digital geospatial metadata (version 2.0). FGDC-STD-001, Federal Geographic Data Committee, Washington, D.C. (Accessed: 18 February 2004) www.fgdc.gov/standards/status/csdgmovr.html

Flanagan, D. C. and Nearing, M. A. (1995) *USDA-Water erosion prediction project, hillslope profile and watershed model documentation*. NSERL Report -10, USDA-ARS National Soil Erosion Research Laboratory, West Lafayette, Indiana (Accessed: 10 May 2004) http://topsoil.nserl.purdue.edu/nserlweb/weppmain/docs/readme.htm

Flügel, W.-A. and Müschen, B. (2000) *Applied remote sensing and GIS integration for model Parameterization (ARSGISIP)*. Final Report, Contract No. ENV4-CT97-0396, Jena: Geographisches Institut, Annex D.2, V148-152 (Accessed: 16 August 2004) www.geogr.unijena.de/~arsgisip/arsgisip_final_pdf/annexes/a_pp117to152_rspool.pdf

Foody, G. M. (2002) Status of land cover classification accuracy assessment. *Remote Sensing of Environment*, 80, 185-201

Fuller, R. M., Smith, C. M., Sanderson, J. M., Hill, R. A. and Thomson, A. G. (2002) The UK Land Cover Map 2000: Construction of a parcel-based vector map from satellite images. *The Cartographic Journal*, 39 (1), 15-25

Gabriel, A. K. and Goldstein, R. M. (1988) Crossed orbit interferometry: theory and experiment results from SIR-B. *International Journal of Remote Sensing*, 9 (5), 857-872

Gabriel, A. K., Goldstein, R. M. and Zebker, H. A. (1989) Mapping small elevation changes over large areas: differential radar interferometry. Journal of Geophysical Research, 94(B7), 9183-9191 as cited in Rosen, P. A., Hensley, S., Joughin, I. R., Li, F. K., Madsen, S. N., Rodríguez, E. and Goldstein, R. M. (2000) Synthetic Aperture Radar Interferometry. In: *Proceedings of the IEEE*, 88(3), 333-382

Gao, J. (1997) Resolution and accuracy of terrain representation by grid DEMs at a micro-scale. *International Journal of Geographical Information Science*, 11 (2), 199-212

Gens, R. and van Genderen, J. L. (1996) SAR interferometry – issues, techniques and applications. *International Journal of Remote Sensing*, 17(10), 1803-1835

Gens, R. (1999) SAR interferometry: software, data format and data quality. *Photogrammetric Engineering & Remote Sensing*, 65(12), 1375-1378

Gens, R. (2003) Two-dimensional phase unwrapping for radar interferometry: developments and new challenges. *International Journal of Remote Sensing*, 24(4), 703-710

Ghiglia, D. C. and Pritt, M. D. (1998) *Two dimensional phase unwrapping: theory, algorithms and software*. Chichester: John Wiley & Sons

Goldstein, R. M., Zebker, H. A. and Werner, C. L. (1988) Satellite radar interferometry: two-dimensional phase unwrapping. *Radio Science*, 23 (4), 713-720

Goldstein, R. M. and Werner, C. L. (1998) Radar interferogram filtering for geophysical applications. *Geophysical Research Letters*, 25 (21), 4035-4038

Gooch, M. J. and Chandler, J. H. (1999) Failure prediction in automatically generated digital elevation models. *Computers and Geosciences,* 27 (8), 913-920

Govers, G. (1990) Empirical relationships on the transporting capacity of overland flow. *International Association of Hydrological Sciences Publication*, 189, 45-63

Govers, G. (1992) Evaluation of transporting capacity formulae for overland flow. *In:* A. J. Parsons and A. D. Abrahams, eds., *Overland flow: hydraulics and erosion mechanics*. London: University College London Press, 243-273

GRASS Team Development (2002) *GRASS GIS-simulation models*. (Accessed: 15 May 2004) http://grass.baylor.edu/modelintegration.html

Guyot, G. and Gu, X. (1994) Effect of radiometric corrections on NDVI-determined from SPOT-HRV and Landsat-TM data. *Remote Sensing of Environment*, 49(3), 169-180

Hanssen, R F. (2001) *Radar interferometry: data interpretation and error analysis*. Dordrecht: Kluwer Academic Publication

Henry, P and Dinguirard, M (1997) *SPOT data absolute calibration – a synthesis*. Technical report, Toulouse: Spot Image

Herland, E.-A. and Vuorela, A. (1997) Operational DEM generation by means of SAR interferometry. *In: Proceedings of the IGRASS' 97 on Remote Sensing - A Scientific*

Vision for Sustainable Development held at Singapore from 3-8 August 1997, IEEE, 3, 1344-1346

Hessel, R., Jetten, V., Baoyuanb, L., Yan, Z. and Stolte, J. (2003) Calibration of the LISEM model for a small Loess Plateau catchment. *Catena*, 54, 235-254

Heuvelink, G. B. M. (1998) *Error propagation in environmental modelling with GIS*. London: Taylor & Francis.

Hollis, J. M., Thanigasalam, P., Hallett, S. H., Mayr, T. R. and Jarvis, N. (1995) *SEISMIC: User manual*. Soil Survey and Land Research Centre, Cranfield University, Silsoe, UK

Hollis, J. M (2004) *Personal communication*, National Soil Resources Institute, Cranfield University at Silsoe

Holtan, H. N. (1961) A concept for infiltration estimates in watershed engineering. USDA-ARS Bulletin, 41-51, Washington, D C, 25, as cited in Mishra, S. K., Tyagi, J. V. and Singh, V. P. (2003) Comparison of infiltration models. *Hydrological Processes*, 17, 2629-2652

Hoyningen-Huene, J. V. (1981) Die Interzeption des Niederschlags in landwirtschaftlichen Pflanzenbeständen. Arbeitsbericht Deutscher Verband für Wasserwirtschaft und Kulturbau, DVWK, Braunschweig, 63 as cited in Jetten, V. (2002) LISEM user manual, version 2.x. Draft version. Utrecht Centre for Environment and Landscape Dynamics, Utrecht University, The Netherlands

Huang, Y. and Van Genderen, J. L. (1996) Comparison of several multilook processing procedures in InSAR processing for ERS-1 & 2 tandem mode. *In: Proceedings of Fringe 96: ESA workshop on applications of ERS SAR Interferometry from 30 Sept- 2 October,1996 held at Zurich* (Accessed: 23 March 2004) http://www.geo.unizh.ch/rsl/fringe96/papers/huang-genderen/

Hudson, W. D. and Ramm, C. W. (1987) Correct formulation of the Kappa coefficient of agreement. *Photogrammetric Engineering & Remote Sensing*, 53(4), 421-422

Hutson, J. L. and Cass, A.. (1987) A retentivity function for use in soil water simulation models. *Journal of Soil Science*, 38, 105-113

Ichoku, C., Karnieli, A., Arkin, Y., Chorowicz, J., Fleury, T. and Rudant, J-P. (1998) Exploring the utility potential of SAR interferometric coherence images. *International Journal of Remote Sensing*, 19 (6), 1147-1160

Jacobsen, K. (1998) Status and tendency of sensors for mapping. International Archives of *Photogrammetric Engineering & Remote Sensing*, 32(1) 124-130

Jarvis M. G., Allen, S. J., Fordham, J., Hazelden, A. J., and Sturdy, R. G. (1984) *Soils and their use in South East England.* Bulletin No.15, Herpenden: Soil Survey of England and Wales

Jarvis, N. J., Hollis, J. M., Nicholls, P. H, Mayr, T. R. and Evans, S. P. (1997) MACRO-DB: a decision support tool for assessing pesticide fate and mobility in soils. *Environmental Modelling & Software*, 12(2-3), 251-265

Jensen, J. R. (2000) *Remote sensing of the environment: an earth resource perspective.* Prentice Hall Series in GIS, New Jersey: Prentice Hall

Jetten, V. (2002) *LISEM user manual, version 2.x. Draft version*. Utrecht Centre for Environment and Landscape Dynamics, Utrecht University, The Netherlands

Jetten, V., Govers, G. and Hessel, R. (2003) Erosion models: quality of spatial predictions. *Hydrological Processes*, 17, 887-900

Jetten, V. (2004) *Personal communication*, University of Utrecht, The Netherlands

Jenson, S. K. and Domingue, J. O. (1988) Extracting topographic structure from digital elevation data for Geographic Information System Analysis. *Photogrammetric Engineering & Remote Sensing*, 54 (11), 1593-1600

Kamphorst, E., Jetten, V. G., Guerif, J., Pitkanen, J., Iversen, B., Douglas, J., and Paz Gonzales, A., (2000) Predicting depressional storage from soil surface roughness. *Soil Science Society of America Journal*, 64, 1749-1758

Kasser, M (2002) Use of scanners for the digitisation of aerial pictures. *In:* M. Kasser and V. Egels, eds. *Digital photogrammetry*. London: Taylor & Francis

Kervyn, F. (2001) Modelling topography with SAR interferometry - illustrations of a favourable and less favourable environment. *Computers and Geosciences*, 27(9), 1039-1050.

Kienzle, S. W. (2004) The effect of DEM raster resolution on first order, second order and compound terrain derivatives. *Transactions in GIS*, 8(1), 83-111

Kite, G. W. and Pietroniro, A. (1996) Remote sensing applications in hydrological modelling. *Hydrological Sciences Journal—des Sciences Hydrologiques*, 41(4) 563-592

Knisel, W. G. (1982) Systems for evaluating nonpoint source pollution: An overview. *Mathematics and Computers in Simulation*, 24 (2-3), 173-184

Konecny, G. (2002) *Geoinformation: remote sensing, photogrammetry and geographic information systems*. London: Taylor and Francis

Kramer, H. J. (2002) *Observation of the earth and its environment: survey of missions and sensors*. Fourth edition, Berlin: Springer-Verlag

Lal, R (2001) Soil degradation by erosion. *Land Degradation & Development*, 12, 519-539

Lanari, R., Fornaro, G., Riccio, D., Migliaccio, M., Papathanassiou, K. P., Moreira, J. R., Schwabisch, M., Dutra, L., Puglisi, G., Franceschetti, G. and Coltelli, M.(1996) Generation of digital elevation models by using SIR-C/X-SAR multifrequency two-pass interferometry: the Etna case study. *IEEE Transactions on Geoscience and Remote Sensing*, 34 (5), 1097-1114

Landmap (2003) *Landmap: satellite image and elevation maps of the UK*. (Accessed: 20 June 2004) http://www.landmap.ac.uk/download/100k_grids_selector_v2.htm

Landis, J. R., and Koch, G. G. (1977) The measurement of observer agreement for categorical data. Biometrics, 33, 159-174 as cited in De Silva, R. P. (1997) Spatio-temporal hydrological modelling with GIS for the Upper Mahaweli Catchment, Sri Lanka. PhD Thesis, Cranfield University, Silsoe

Leberl, F. W (1990) *Radargrammetric image processing*. Norwood: Artech House

Leberl, F. W (1998) Radargrammetry. *In:* F. M. Henderson and A. J. Lewis, eds. *Principles and applications of imaging radar*, Manual of remote sensing, third edition, volume 2, New York: John Wiley & Sons, 183-269

Levizzani, V., Amorati, R. and Meneguzzo, F. (2000) *A review of satellite-based rainfall estimation methods*. Deliverable 6.1, WP6, Multiple-Sensor Precipitation Measurements,

Integration, Calibration (MUSIC) and Flood Forecasting (Accessed: 20 April 2004) http://www.geomin.unibo.it/orgv/hydro/music/reports/D6.1_SatPrecEst.pdf

Li, F. K. and Goldstein, R. M. (1990) Studies of multibaseline spaceborne interferometric SAR. *IEEE Transactions on Geoscience and Remote Sensing*, 28(1), 88-97

Li, R., Stevens, M. A., and Simons, D. B. (1976) Solutions to the Green and Ampt infiltration equation. *Journal of Irrigation and Drainage Engineering*, 2, 239-248

Li, R., Zhou, R. G., Schmidt, N. J., Fowler, C. and Tuell, G. (2002) Photogrammetric processing of high-resolution airborne and satellite linear array stereo images for mapping applications. *International Journal of Remote Sensing*, 23(10), 4451-4473

Lightstone, L. (1996) Desktop SAR processing: No longer the best kept secret. *Earth Observation Magazine (EOM)*, March Issue. (Accessed: 21 March 2004) http://www.eomonline.com/Common/Archives/March96/lightstone.htm

Lillesand, T. M. and Kiefer, R. W. (1999) *Remote sensing and image interpretation.* Fourth Edition, New York: John Wiley & Sons

Limoine, F. G., Kenyon, S. C., Factor, J. K., Trimmer, R. G., Pavlis, N. K., Chinn, D. S., Cox, C. M., Klosko, S. M., . Luthcke, S. B, Torrence, M. H., Wang, Y. M., R. Williamson, G. E., Pavlis, C., Rapp, R. H. and Olson, T. R. (1998) The Development of the joint NASA GSFC and NIMA geopotential model, EGM96. NASA/TP-1998-206861, NASA Goddard Space Flight Center, Greenbelt, Maryland, 20771 USA, (Accessed: 3 November 2003) http://cddisa.gsfc.nasa.gov/926/egm96/egm96.html

Lin, Q., Vesecky, J. F. and Zebker, H. A. (1992) New approaches in interferometric SAR data processing. IEEE Transactions on Geoscience and Remote Sensing, 30 (3), 560-567

LISEM (2004) *Limburg Soil Erosion Model*. Faculty of Geosciences, Utrecht University, The Netherlands. (Accessed: 20 June 2004) http://www.frw.ruu.nl/lisem/

Mackay, H. (2002) Mapping Great Britain at one metre Z values. *The Ranger*, *the journal of the Defence Surveyors' Association*, Spring Issue, 21-24

Maidment, D. R. (1996) GIS and hydrologic modelling - an assessment of progress. In: Proceedings of the Third International Conference on GIS and Environmental Modelling held at Santa Fe, New Mexico from 22-26 January, 1996. (Accessed: 12 June 2004) http://www.ce.utexas.edu/prof/maidment/gishydro/meetings/santafe/santafe.htm

Main, J. D. (2000) Precise ground control is essential for spatial accuracy, *Imaging Notes*, 15(4), (Accessed: 12 March 2004) http://www.imagingnotes.com/julaug00/default.htm

Massonnet, D. and Rabaute, T. (1993) Radar interferometry: limits and potentials. *IEEE Transactions on Geoscience and Remote Sensing,* 31 (2), 455-464

Mather P. M. (1999) *Computer processing of remotely sensed images: an introduction.* Second edition, Chichester: John Wiley & Sons

Maune, D. F. (2001) *Digital elevation model technologies and applications: The DEM users manual.* Bethesda: American Society of Photogrammetry and Remote Sensing Publication

Mayes, J. (1997) South-East England. *In*: D. Wheeler and J. Mayes, eds. *Regional climates of the British Isles*. London: Routledge, 67-88

McBratney, A. B., Minasny, B., Cattle, S. R. and Vervoort, R. W. (2002) From pedotransfer functions to soil inference systems. *Geoderma*, 109, 41-73

Mercer J. B. (1995) SAR technologies for topographic mapping. *In*: D. Fritsch and D. Hobbie, eds., *Proccedings of Photogrammetric Week 95 , Heidelberg: Wichmann Verlag, 117-126*. (16 August 2003) http://www.ifp.uni-stuttgart.de/publications/phowo95/Mercer.pdf

Mercer, J. B., Thornton, S. and Tennant, K. (1998) Operational DEM production from airborne interferometry and from Radarsat stereo technologies. In: *Proceedings of ASPRS - RTI Annual Conference held at Tampa, Florida from 31 Mar-3April, 1998.* (Accessed: 20 March 2004) http://www.intermap.ca/PDF_files/asprs98.pdf

Mercer, J. B. (2001) Comparing LiDAR and IFSAR: what can you expect? *In:* D. Fritsch and Spiller, eds., *Proceedings of Photogrammetric Week 2001, Stuttgart* (Accessed: 15 August 2003) www.intermaptechnologies.com/PDF_files/paper_Stuttgart01_JBM3.pdf

Merriam, R. A. (1960) A note on the interception loss equation. Journal of Geophysical Research, 65, 3850-3851 as cited in De Roo, A. P. J., Wesseling, C. G. and Ritsema, C. J. (1996a) LISEM: a single-event physically based hydrological and soil erosion model for drainage basins. I: theory input and output. *Hydrological Processes*, 10, 1107-1117

Merriam, R. A. (1973) Fog drip from artificial leaves in a fog wind tunnel. Water Resources Research, 9, 1591-1598 as cited in Morgan, R. P.C., Quinton, J. N., Smith, R. E., Govers, G., Poesen, W. A., Auerswald, K., Chisci, G, Torri, D. and Styczen, M. E. (1998a) The European soil erosion model (EUROSEM): A dynamic approach for predicting sediment transport from field and small catchments. *Earth Surface Processes and Landform*, 23, 527-544

Mikhail, E. M., Bethel, J. S. and McGlone, J. C. (2001) *Introduction of modern photogrammetry*. New York: John Wiley & Sons

Molnár, K. and Julien, P. Y. (2000) Grid-size effects on surface runoff modelling. *Journal of Hydrologic Engineering*, 5 (1), 8-16

Morgan, R. P.C., Quinton, J. N., Smith, R. E., Govers, G., Poesen, W. A., Auerswald, K., Chisci, G, Torri, D. and Styczen, M. E. (1998a) The European soil erosion model (EUROSEM): A dynamic approach for predicting sediment transport from field and small catchments. *Earth Surface Processes and Landform*, 23, 527-544

Morgan R. P. C., Quinton, J. N., Smith, R. E., Govers, G., Poesen, J. W. A., Auerswald, K., Chisci, G., Torri, D., Styczen, M. E. and Folly, A. J. V. (1998b) *The European soil erosion model (EUROSEM): documentation and user guide*, version 3.6. Cranfield University, Silsoe

Moore, I. D. and Foster, G. R. (1990) Hydraulics and overland flow. *In:* M. G. Anderson and T. P. Burt, eds. *Process studies in hillslope hydrology*. Chichester: John Wiley & Sons, 215-254.

Moore, I. D., Grayson, R. B. and Ladson, A. R. (1991) Digital terrain modelling: a review of hydrological, geomorphological and biological applications. *Hydrological Processes*, 5, 3-30

Mualem, Y. (1976) A new model for predicting the hydraulic conductivity of unsaturated media. Water Resource Research, 12, 513-522, as cited in Jarvis, N. J., Hollis, J. M., Nicholls, P. H, Mayr, T. R. and Evans, S. P. (1997) MACRO-DB: a decision support tool for assessing pesticide fate and mobility in soils. *Environmental Modelling & Software*, 12(2-3), 251-265

Muller, J. P., Morley, J. G., Walker, A. H., Kitmitto, K., Mitchell, K. L., Chugani, K., Smith, A., Barnes, J., Keenan, R., Cross, P. A., Dowman, I. J. and Quarmby, N. (2000) The Landmap project for the automated creation and validation of multi-resolution orthorectified satellite image products and a 1" DEM of the British Isles from ERS tandem SAR interferometry. *In: 26th Annual Conference of the Remote Sensing Society, RSS, University of Leicester, 12-14 September 2000* (Accessed: 12 March 2004) http://www.landmap.ac.uk/docs/RSS00_JPM_paperV1.pdf

Müschen, B., Flugel, W.-A., Steinnocher, K., Fellah, K., Rodolfi, G., Colpaert, A., Krzywinski, K. and Quiel, F. (1999) Parameterising hydrological, erosion and solute transport models by application of remote sensing in the ARSGISIP project. *In: Proceedings of the IGARSS 99, June-2 July 1999*. IEEE International, 5 (28), 2554 - 2556

New, M., Todd, M., Hulme, M. and Jones, P. (2001) Precipitation measurements and trends in the twentieth century. *International Journal of Climatology*, 21 (15), 1899-1922

NSRI (2003) *Publications: maps and books, technical and research reports, digital data and software*. National Soils Resource Institute, Cranfield University, Silsoe (Accessed: 15 May 2004) http://www.silsoe.cranfield.ac.uk/nsri/services/publicationslist.pdf

NSRI (2004) *Digital soil information, NSRI soil data gateway*. National Soils Resource Institute, Cranfield University, Silsoe (Accessed: 10 July 2004) http://www.silsoe.cranfield.ac.uk/nsri/services/cf/nsriooi/information/intro.cfm

O'Callaghan, J. F. and Mark, D. M. (1984) The extraction of drainage networks from digital elevation data. Computer Vision, Graphics and Image Processing, 28 (6), 323-344 as cited in Tarboton, D. G. and Ames, D. P. (2001) Advances in the mapping of flow networks from digital elevation data. *In: Proceedings of the World Water and Environmental Resources Congress, 20-24 May 2001, Orlando, Florida*

Onstad, C. A. (1984) Depressional storage on tilled soil surfaces. *Transactions of ASAE*, 27, 729-732

Ordnance Survey (2004) *Land-form PROFILE: technical information and specifications*. (Accessed: 19 March 2004) http://www.ordnancesurvey.co.uk/oswebsite/products/landformprofile/techinfo.html

Ordnance Survey (2004) *National GPS Network Information: surveying with National GPS network*. Last update: 14 April 2004, Ordnance Survey (Accessed: 12 May 2004) http://www.gps.gov.uk/gpssurveying.asp#gpssurveying3

Osborn, T. J., Hulme, M., Jones, P. D. and Basnett, T. A. (2000) Observed trends in the daily intensity of United Kingdom precipitation. *International Journal of Climatology*, 20 (4), 347-364

Overton, D. E. (1964) Mathematical refinement of an infiltration equation for watershed engineering. ARS 41-99, U.S. Department of Agricultural Service, Washington, D. C. as cited in Mishra, S. K., Tyagi, J. V. and Singh, V. P. (2003) Comparison of infiltration models. *Hydrological Processes*, 17, 2629-2652

PCI Geomatics (2003) *Geomatica OrthoEngine User Guide, Version 9.1*. Richmond Hill: PCI Geomatics

Pebesma, E. J. and Wesseling, C. G. (1998) Gstat: a program for geostatistical modelling, prediction and simulation. *Computers & Geosciences*, 24 (1), 17-31.

PCRaster (1996) *PCRaster version 2 manual*. Department of Physical Geography, Utrecht University and PCRaster Environmental Software (Accessed: 10 May 2004) http://pcraster.geog.uu.nl/documentation/pcrman/book1.htm

Penna, N. T., Bingley, R. M. and Dodson, A. H. (2002) Single receiver heighting using the active stations of the GPS network of Great Britain. *Survey Review*, 36(283), 340-350

Peuquet, D. J. (1999) Time in GIS and geographical databases. *In:* P. A. Longley, M. F. Goodchild, D. J. Maguire and D. Rhind, eds., *Geographic information systems: principles and technical issues.* 1, New York: John Wiley & Sons, 91-103

Potts, A. S. and Browne, T. E. (1983) The climate of Sussex *In*: Geographical Editorial Committee eds, *Sussex: environment, landscape and society.* Gloucester: Alan Sutton, 88–106, as cited in Boardman, J. (2003) Soil erosion and flooding on the eastern South Downs, southern England, 1976-2001.*Transactions of the Institute of British Geographers*, 28(2), 176-196

Pullar, D. and Springer, D. (2000) Towards integrating GIS and catchment models. *Environmental Modelling and Software*, 15 (5), 451-459

Quinton, J. N. (1994) Validation of physically based erosion models with particular reference to EUROSEM. *In:* R. J. Rickson, ed. *Conserving soil resources- European perspectives*. Wallingford: CAB International, 300-313

Rawls, W. J. (1983) Estimating bulk density from particle size analysis and organic matter content. *Soil Science*, 135(2), 123-125

Rawls, W. J., Brakensiek, D. L. and Miller, N. (1983) Green-Ampt infiltration parameters from soil data. *ASCE Journal of Hydraulic Engineering*, 109(1), 62-69

Rauws, G. and Govers, G. (1988) Hydraulic and soil mechanical aspects of rill generation on agricultural soils. *Journal of Soil Science*, 39, 111-124 as cited in Jetten, V. (2002) *LISEM user manual, version 2.x. Draft version*. Utrecht Centre for Environment and Landscape Dynamics, Utrecht University, The Netherlands

Renschler, C. S. (2003) Designing geo-spatial interfaces to scale process models: the GeoWEPP approach. *Hydrological Processes*, 17, 1005–1017

Richards, J. A. and Jia, X. (1999) *Remote sensing digital image analysis: an introduction.* Third edition, Berlin: Springer-Verlag

Ritsema, C. J., Oostindie, K. V. and Stolte, J. (1996) Evaluation of vertical and later flow through agricultural loessial hillslopes using a two dimensional computer simulation model, *Hydrological Processes*, 10, 1091-1105

Rosen, P. A., Hensley, S., Joughin, I. R., Li, F. K., Madsen, S. N., Rodríguez, E. and Goldstein, R. M. (2000) Synthetic Aperture Radar Interferometry. In: *Proceedings of the IEEE*, 88(3), 333-382

Rosenfield. G. H. and Fitzpatrick-Lins, K. (1986) A coefficient of agreement as a measure of thematic classification. *Photogrammetric Engineering & Remote Sensing*, 52(2), 223-227

Rufino, G., Moccia, A. and Esposito, S. (1998) DEM generation by means of ERS tandem data. *IEEE Transactions on Geoscience and Remote Sensing*, 36 (6), 1905-1912

Sabins, F. F. (1997) *Remote sensing: principles and interpretation*. Third edition, New York: W. H. Freeman & Company

Sasowsky, K. C., Petersen, G. W. and Evans, B. M. (1992) Accuracy of SPOT digital elevation model and derivatives: utility for Alaska's North Slope. *Photogrammetric Engineering & Remote Sensing*, 58 (6), 815-824

Schmidt, J., Werner, M. V. and Michael, A. (1999) Application of the EROSION 3D model to the CATSOP watershed, The Netherlands. *Catena*, 37, 449-456

Schmidt, J (2000) *Soil erosion: Application of physically based models*. Berlin: Springer-Verlag

Schultz, G. A. (1998) Remote sensing in hydrology. *Journal of Hydrology*, 100, 239-265

Schutz, B. E. (2001) Laser altimetry and lidar from ICESat/GLAS. *In: Proceedings of IEEE IGRASS 2001 held at Sydney from 9-13 July 2001*, 3, 1016- 1019

Shine, J. A. and Wakefield, G. I. (1999) A comparison of supervised imagery classification using analyst-chosen and geostatistically-chosen training sets. *In:* J. Diaz, R. Tynes, D. Caldwell and J. Ehlen, eds. *GeoComputation CD-ROM: Proceedings of the 4th International Conference on GeoComputation, Fredericksburg, Virginia, 25-28 July 1999*. (Accessed: 27 November 2003) http://www.geocomputation.org/1999/044/gc_044.htm

Shortridge, A. M. (2001). Characterizing uncertainty in digital elevation models. *In*: C. T. Hunsaker, M. F. Goodchild, M. A. Friedl and T. J. Case, eds., S*patial uncertainty in ecology: implications for remote sensing and GIS applications*. Springer: New York, 238-257

Singh, V. P. (2002) *Computer models of watershed hydrology CD-ROM*. Highlands Ranch: Water resources publications

Small, D., Pasquali, P. and Fuglistaler, S. (1996) A comparison of phase to height conversion methods for SAR interferometry. *In: Proceedings of the IGARSS 96-Remote Sensing for a Sustainable Future on 27-31 May 1996*, IEEE International, 1, 342-344

Small, D. and Nüesch, D. (1996) Validation of Height Models from ERS Interferometry. *In: Proceedings of ESA-FRINGE' 96 Workshop held at Zürich, Switzerland from 30 September - 2 October 1996* (Accessed: 10 April 2004)

Smith, A. M. (1991) A new approach to range-Doppler SAR processing. *International Journal of Remote Sensing*, 12(2), 235-251

Smith, A. M. (2003) Personal communication, Phoenix Systems and Associates Ltd., Kingston-upon-Thames, Surrey

Smith, M. J., Smith, D. G. and Tragheim, D. G. (1997) DEMs and ortho-images from aerial photographs. *The Photogrammetric Record*, 15(90), 945-950

Smith, R. E., Goodrich, D. C. and Quinton, J. N. (1995) Dynamic, distributed simulation of watershed erosion: The KINEROS2 and EUROSEM models. *Journal of Soil and Water Conservation,* 50(5), 517-520

Smith, L. C., Alsdorf, D. E., Magilligan, F. J., Gomez, B., Mertes, L. A. K., Smith, N. D. and Garvin, J. B. (2000) Estimation of erosion, deposition, and net volumetric change caused by the 1996 Skeidararsandur Jokulhlaup, Iceland, from SAR interferometry. *Water Resources Research*, 36(6), 1583-1594

Smith, L. C. (2002) Emerging applications of interferometric synthetic aperture radar (InSAR) in geomorphology and hydrology. *Annals of the Association of American Geographers*, 92 (3), 385-398

Spot Image (1997) The *SPOT scene standard digital product format*.No. S4-ST-73-01-SI, Edition 1 - Revision 2, 97/11/17, Toulouse: Spot Image Inc.

Spot Image (2004) *Technical information*. (Accessed: 12 July 2004) http://www.spotimage.fr/html/_167_224_.php

Strahler, A. N. (1964) Quantitative geomorphology of drainage basins and channel networks. *In:* V. T. Chow, ed. *Handbook of Applied Hydrology: a compendium of water-resources* technology. New York: McGraw-Hill

Sui, D. Z. and Maggio, R. C. (1999) Integrating GIS with hydrological modelling: practices, problems, and prospects. *Computers, Environment and Urban Systems*, 23, 33-51

Sun, G. and Ranson, K. J. (1997) Digital elevation models from SIR-C interferometric and Shuttle Laser Altimeter (SLA) data. *In: Proceedings of IGARSS 97, Remote Sensing - A Scientific Vision for Sustainable Development*, IEEE International, 1, 460-462

Swain, P. H. and Davis, S. M. (1978) *Remote sensing: the quantitative approach*. New York: MacGraw-Hill

Takken, I., Beuselinck, L., Nachtergaele, J., Govers, G., Poesen, J, and Degraer, G. (1999) Spatial evaluation of a physically-based distributed erosion model LISEM. *Catena*, 37, 431-447

Taylor, J. C., Bird, A. C., Brewer, T. R., Keech, M. A., and Stuttard, M. J. (1991a) *Monitoring landscape change in the national parks- methodology*. Silsoe: Silsoe College

Taylor, J. C., Bird, A. C., Keech, M. A., and Stuttard, M. J. (1991b) *Monitoring landscape change in the national parks-main report*. Silsoe: Silsoe College

Taylor, J. C., Bird, A. C., Keech, M. A., and Stuttard, M. J., (1991c) *Monitoring landscape change in the national parks-application of satellite remote sensing*. Silsoe: Silsoe College

Taylor, J. C. and Eva, H. D. (1992) *Regional Inventories on Beds, Cambs and Northants (UK), 1992.* Final Report to CEC - JRC, Silsoe: Silsoe College, 70

Taylor, J. C. and Eva, H. D. (1997) *Comparison of crop area estimates using ground survey and remote*. Silsoe: Cranfield University, UK

Teillet, P. M., Staenz, K and Williams, D. J. (1997) Effects of spectral, spatial and radiometric characteristics of remote sensing vegetation indices of forested regions. *Remote Sensing of Environment*, 61, 139-149

Tomlin, C. D. (1990) Geographic information systems and cartographic modelling. Englewood Cliffs, New Jersey: Prentice-Hall as cited in PCRaster (1996) *PCRaster version 2 manual*. Department of Physical Geography, Utrecht University and PCRaster Environmental Software (Accessed: 10 May 2004) http://pcraster.geog.uu.nl/documentation/pcrman/book1.htm

Thomas, G. (1984) *Information manual for FILQUILT, REQUILT, and PIXCOUNT Turbo C++ programs.* Silsoe: Silsoe College, Cranfield University, UK

Tokunaga, M. (1997) DTM Accuracy derived from interferometry SAR. *In: Proceedings of the 18th Asian Conference on Remote Sensing (ACRS) 97 held at Malaysia from 20-24 October, 1997* (Accessed: 13 April 2004) http://www.gisdevelopment.net/aars/acrs/1997/ts6/ts6006.shtml

Tarboton, D. G. and Ames, D. P. (2001) Advances in the mapping of flow networks from digital elevation data. *In: Proceedings of the World Water and Environmental Resources Congress, 20-24 May 2001, Orlando, Florida*. (Accessed: 7 December 2003) http://www.engineering.usu.edu/cee/faculty/dtarb/asce2001.pdf

Toutin, T. (2000a) Evaluation of radargrammetric DEM from RADARSAT images in high relief areas. *IEEE Transactions on Geoscience and Remote Sensing*, 38(2), 782-789

Toutin, T. (2000b) Stereo-mapping with SPOT-P and ERS-1 SAR images. *International Journal of Remote Sensing*, 21(8), 1657–1674

Toutin, T. (2001) Elevation modelling from satellite visible and infrared (VIR) data. *International Journal of Remote Sensing*, 22(6), 1097-1125

Toutin, T (2002) DEM from stereo Landsat 7 ETM+ data over high relief areas. *International Journal of Remote Sensing*, 23(20), 2133–2139

Toutin, T. and Gray, A. L. (2000) State of the art of elevation extraction from satellite SAR data. *ISPRS Journal of Photogrammetry and Remote Sensing*, 55 (1), 13-33

Ungerer, M. J. (2000) Implementation of cellular automata models in a raster GIS dynamic modelling environment: an example using the Clarke Urban Growth Model. *In: 4th International Conference on Integrating GIS and Environmental Modelling (GIS/EM4): Problems, Prospects and Research Needs held at Banff, Alberta, from 2 - 8 September, 2000* (Accessed: 20 June 2004) http://www.colorado.edu/research/cires/banff/pubpapers/147/

U. S. Geological Survey (1997) *Standards for digital elevation models: part 3 – quality control*. National mapping programme, Technical instruction, National Mapping Division, U. S. Geological Survey (Accessed: 2 March 2004) http://rockyweb.cr.usgs.gov/nmpstds/acrodocs/dem/3DEM0897.PDF

U. S. Geological Survey (2003) *SRTM documentation*. Last update 11 May 2003 (Accessed: 2 March 2004) ftp://edcsgs9.cr.usgs.gov/pub/data/srtm/Documentation/SRTM_Topo.txt

U. S. Geological Survey (2004) *GTOPO30 documentation*. Last update: 5 January 2004, USGS-NASA Distributed Active Archive Center (Accessed: 6 March 2004) http://lpdaac.usgs.gov/gtopo30/README.asp

U. S. Geological Survey (2004) *ASTER digital elevation model*. (Accessed: 12 June 2004) http://edcdaac.usgs.gov/aster/ast14dem.asp

Van Deursen, W. P. A. (1995) Geographical information systems and dynamic models: development and application of a prototype spatial modelling language. Ph D Thesis, Utrecht University, The Netherlands, NGS Publication, 190 (Accessed: 10 May 2004) http://pcraster.geog.uu.nl/thesisWvanDeursen.pdf

Van Deursen, W. P. A. (1995) *Implementation of the RHINEFLOW in PCRaster*. (Accessed: 12 June 2004) http://rhine.geog.uu.nl/modelscript.html

Van Dijck, S. and Karssenberg, D. (2000) *EUROSEM in PC Raster*. (Accessed: 12 June 2004) www.geog.uu.nl/pcraster/runoff/eurosem/

Van Deursen, W. P. A. and Wesseling, C. G. (2004) *PCRaster Software*. PCRaster Environmental Software and Department of Physical Geography, University of Utrecht. (Accessed: 15 May 2004) http://pcraster.geog.uu.nl/index.html

Van Genuchten, M. Th. (1980) A closed-form equation for predicting the hydraulic conductivity of unsaturated soils. *Soil Science Society of America Journal*, 44, 892-898

Vieux, B. E. (2000) *Distributed hydrologic modelling using GIS*. Dordrecht: Kluwer Academic Publishers

Walker, A. H., Muller, J.-P., and Naden, P. S. (1999) High resolution interferometric SAR DEMs for hydrological network derivation. *In: Proceedings of the IEEE IGARSS 99 held at Hamburg from 28 June -2 July 1999*, IEEE International, 5, 2613-2615

Wehr, A. and Lohr, U. (1999) Airborne laser scanning - an introduction and overview. *ISPRS Journal of Photogrammetry and Remote Sensing*, 54(2-3), 68-82

Weibel, R. and Heller, M. (1991) Digital terrain modelling. *In:* D. J. Maguire, M. F. Goodchild and D. W. Rhind, eds. *Geographical information systems: principles and applications*. Harlow: Longman & Wiley, 2, 269-297

Werner, C. L., Wiesmann, A., Siegert , F. and Kuntz, S. (2000) JERS InSAR DEM generation for Borneo. *In: Proceedings of the IGRASS' 2000 held at Honolulu from 24-28 July 2000*. IEEE, 5, 2248-2250

Werner, M. v. (2002) *EROSION-3D: a computer-based model for the simulation of soil erosion by water, Vol. III, model basics: user manual*. Department of Soil Science and Water Protection, Fachgebiet Boden- und Gewässerschutz, Freiberg (Accessed: 12 June 2004) http://www.geog.fu-berlin.de/~erosion/manual_e/vol3/index.html

Wesseling, C. G., Van Deursen, W. P. A. and Burrough, P. A. (1996) A spatial modelling language that unifies dynamic environmental models and GIS. *In: Third International Conference/Workshop on Integrating GIS and Environmental Modelling held at Santa Fe, USA from 21-25 January'1996*. (Accessed: 20 May 2004) www.ncgia.ucsb.edu/conf/santa_fe_cdrom/sf_papers/wesseling_cees/santa_fe.html

Wesseling, C. G. (1997) *Specification of cross system format (CSF) version 2 format and API*. Department of Physical Geography, University of Utrecht

Williams, J. (1995) *Geographic information from space: Processing and application of geocoded satellite images*, Wiley Praxis series in remote sensing. Chichester: John Wiley & Sons and Praxis Publishing

Wise, S.M. (2000) Assessing the quality for hydrological applications of digital elevation models derived from contours. *Hydrological Processes*, 14, 1909-1929

Wolf, P. R. and Dewitt, B. A. (2000) *Elements of photogrammetry with applications in GIS*. Third edition, Boston: McGraw Hill

Wösten, J. H. M., Finke, P. A. and Jansen, M. J. W. (1995) Comparison of class and continuous pedotransfer functions to generate soil hydraulic characteristics. *Geoderma*, 66, 227-237

Wösten, J. H. M., Pachepsky, Y. A. and Rawls, W. J. (2001) Pedotransfer functions: bridging gap between available basic soil data and missing soil hydraulic characteristics. *Journal of Hydrology*, 251(3-4), 123-150

Xu, W. and Cumming, I. G. (1999) A region-growing algorithm for InSAR phase unwrapping. *IEEE Transactions on Geoscience and Remote Sensing*, 37 (1), 124-134

Young, R. A., Onstad, C. A., Bosch, D. D. and Anderson, W. P. (1989) AGNPS: A nonpoint source pollution model for evaluating agricultural watersheds. *Journal of Soil Water Conservation*, 44, 168-173

Zebker, H. (2000) Studying the earth with interferometric radar. *IEEE Computing in Science and Engineering*, 2 (3) 52-60

Zebker, H. A. and Goldstein, R. M. (1986) Topographic Mapping Derived from Synthetic Aperture Radar Measurements. Journal of Geophysical Research, 91, 4993-4999 as cited in Rosen, P. A., Hensley, S., Joughin, I. R., Li, F. K., Madsen, S. N., Rodríguez, E. and Goldstein, R. M. (2000) Synthetic Aperture Radar Interferometry. *In: Proceedings of the IEEE, 88(3), 333-382*

Zebker, H. A., Werner, C. L., Rosen, P. A. and Hensley, S. (1994) Accuracy of topographic map derived from the ERS-1 interferometric radar. *IEEE Transactions on Geoscience and Remote Sensing*, 32 (4), 823-836

Zebker, H. A., Rosen, P. A. and Hensley, S. (1997) Atmospheric effects in interferometric synthetic aperture radar surface deformation and topographic maps. *Journal of Geophysical Research- Solid Earth*, 102 (B4), 7547-7563

Appendix A

Appendix A-1: Input parameters for various categories and options in the model

Categories	Parameter	Map name	Unit
Catchment	Catchment area	AREA	
	Slope gradient in the direction of flow	GRAD	
	Local drain/overland flow direction	LDD	--
	Main catchment outlet	OUTLET	--
	Rain gauge influence zone	ID	--
Landuse & vegetation	Surface cover by vegetation & residues	PER	Fraction
	Leaf area index of the plant cover	LAI	m2/m2
	Plant height	CH	m
	Width of impermeable road	ROADWIDTH	m
	Width of grass strips	GRASSWID	m
Soil Surface	Random roughness	RR	cm
	Manning's roughness	N	--
	Fraction of grid-cell covered with crust	CRUSTFRC	Fraction
	Fraction of grid-cell compacted soil	COMPFRC	Fraction
	Fraction of grid-cell covered by stones	STONEFRC	Fraction
Erosion & deposition	Soil aggregate stability for splash erosion	AGGRSTAB	Number
	Cohesion of bare soil	COH	kPa
	Additional cohesion by plant roots	COHADD	kPa
	Median texture of the soil/suspended matter	D50	μm
Channel	LDD of main channel	LDDCHAN	--
	Channel width	CHANWIDT	m
	Channel cross section shape	CHANSIDE	--
	Slope gradient of channel bed	CHANGRAD	
	Manning's roughness of channel bed	CHANMAN	--
	Cohesion of channel bed	CHANCOH	kPa
Infiltration:			
Green-Ampt: One layer	Saturated hydraulic conductivity	KSAT1	mm/h
	Average suction at the wetting front	PSI1	cm
	Porosity	THETAS1	
	Initial moisture content	THETAI1	
	Depth	SOILDEP1	cm
Surface type	Saturated hydraulic conductivity of crusts	KSATCRST	mm/hr
	Saturated K of compacted areas	KSATCOMP	mm/h
	Saturated K of grass strips	KSATGRAS	mm/hr
Green-Ampt: Two layer	Saturated hydraulic conductivity	KSAT2	mm/h
	Average suction at the wetting front	PSI2	cm
	Porosity	THETAS2	
	Initial moisture content	THETAI2	
	Depth of a soil layer	SOILDE2	cm
Holtan model	Infiltration rate saturation	FC	mm/h
	Difference of initial and saturation rate	A	mm/h
	Soil moisture at field capacity	FP	
	Soil porosity	TP	cm3/cm3
	Depth of infiltration control zone	DF	mm
	Initial soil moisture content	ASM	--
	Coefficient of infiltration equation	P	--
SWATRE model	A large number of parameters (20)		

Appendix A-2: Model outputs with their data format for a storm event

Categories	Output	Format
Totals of an event	Main screen output and totals	JPEG
	Total result	CSV
	Erosion map	Map
	Deposition map	Map
Graphs for an event	Hyetograph, hydrograph and sedigraph at outlet	CSV
Spatio-temporal outputs	Surface storage	Map/Timeplot
	Infiltration	Map/Timeplot
	Runoff height (mm)	Map/Timeplot
	Water height (mm)	Map/Timeplot
	Runoff velocity	Map/Timeplot
	Runoff (l/s or l/s/m)	Map/Timeplot
	Erosion (ton/ha)	Ma/Timeplot
	Transport capacity	Map/Timeplot
	Deposition (ton/ha)	Map/Timeplot
	Sediment concentration (g/l)	Map/Timeplot

Appendix B

Appendix B - 1: Weather stations active during 2000 from the BADC archive

S. No	Station name	Area	Start date	End date	Latitude (Degree)	Longitude (Degree)
1.	Bexhill	East Sussex	01-01-1908	Current	50.837	0.467
2.	Brede	East Sussex	01-01-1988	Current	50.938	0.594
3.	Eastbourne	East Sussex	01-01-1886	Current	50.758	0.284
4.	Gatwick	East Sussex	01-01-1958	Current	51.151	-0.191
5.	Hastings	East Sussex	01-01-1934	Current	50.855	0.570
6.	Herstmonceux, West End	East Sussex	01-01-1992	Current	50.890	0.317
7.	Newhaven	East Sussex	01-01-1984	Current	50.781	0.058
8.	Plumpton	East Sussex	01-01-1954	Current	50.905	-0.069
9.	Wych Cross	East Sussex	01-06-1998	Current	51.064	0.033
10.	Bognor Regis	West Sussex	01-01-1898	Current	50.780	-0.676
11.	Littlehampton	West Sussex	01-10-1995	Current	50.826	-0.527
12.	Shoreham Airport	West Sussex	01-07-1983	Current	50.835	-0.289
13.	Thorney Island Saws	West Sussex	01-01-1984	Current	50.813	-0.921
14.	Wiggonholt	West Sussex	01-01-1995	Current	50.936	-0.492

Appendix B - 2: Hourly weather data format of 30 October 2000 including rainfall depth and intensity.

Date	Time	Temp In	Temp Out	Hi	Low	Heat DD	Cool DD	Chill DD	THI DD	Solar Rad	Energy	Bar	Wind Speed	Hi	Dir	Wind Chill	Wind Run	Rain	Rain Rate	Hum Out	Dew Point
30/10/00	0:00	19.4	12.6	12.7	12.6	0.2	0	0.5	0	0	0	993.8	14	32	SW	6.1	13	1.5	0.5	95	11.8
30/10/00	1:00	19.4	12.7	12.7	12.6	0.2	0	0.5	0	0	0	992.4	14	40	SW	6.2	13.2	0.8	0	95	11.9
30/10/00	2:00	19.3	12.7	12.7	12.6	0.3	0	0.5	0	0	0	990.4	13	35	SW	6.6	12.6	2.5	0.8	95	11.9
30/10/00	3:00	19.3	12.6	12.7	12.5	0.2	0	0.5	0	0	0	988.2	14	33	SW	6.1	13.2	1.8	0.3	95	11.8
30/10/00	4:00	19.3	12.6	12.8	12.6	0.2	0	0.4	0	0	0	986.2	15	35	SW	5.7	14.5	2.3	0.8	93	11.5
30/10/00	5:00	19.3	13	13.2	12.7	0.2	0	0.5	0	0	0	983.1	15	42	SSW	6.2	14.5	0.3	0	89	11.2
30/10/00	6:00	19.3	13.1	13.3	12.7	0.2	0	0.5	0	0	0	980.1	16	44	SSW	5.9	15.5	1.8	0.8	91	11.6
30/10/00	7:00	19.3	11.6	12.8	7.8	0.3	0	0.6	0	0	0	979.6	17	42	SSW	3.5	16.6	6.3	11.4	92	10.3
30/10/00	8:00	19.2	9.1	10	7.9	0.4	0	0.7	0	0	0	979.4	13	28	WSW	2	11.7	2	0.3	93	8.1
30/10/00	9:00	19.1	9.6	10.1	8.9	0.4	0	0.6	0	8	2.9	980.4	13	30	W	2.6	12.5	1.8	3	84	7.1
30/10/00	10:00	18.9	8.8	9.8	7.9	0.4	0	0.6	0	23	8.4	981.6	11	29	W	2.5	10.7	1.8	0.8	82	5.9
30/10/00	11:00	19.1	8.1	8.6	7.6	0.4	0	0.7	0	97	34.8	982.7	10	26	W	2.1	9.6	0.5	0.3	82	5.2
30/10/00	12:00	19.2	9.6	10.2	8.6	0.4	0	0.6	0	436	162.9	983.4	12	34	W	3.1	11.7	0.3	0	70	4.3
30/10/00	13:00	19.3	10	10.4	9.6	0.3	0	0.6	0	452	158.7	984.3	11	27	W	4.1	11.4	0	0	68	4.4
30/10/00	14:00	19.4	10.6	10.9	10.1	0.3	0	0.6	0	523	196.8	984.9	12	29	W	4.4	11.9	0	0	68	4.9
30/10/00	15:00	19.7	10.7	11.1	10.4	0.3	0	0.6	0	342	128.5	985.6	12	30	W	4.5	11.7	0	0	72	5.9
30/10/00	16:00	19.9	10.8	10.9	10.6	0.3	0	0.6	0	73	26.8	985.8	12	27	W	4.6	11.3	0	0	69	5.3
30/10/00	17:00	19.9	10.8	10.9	10.6	0.3	0	0.6	0	12	4.6	986.3	12	31	W	4.6	12.2	0	0	69	5.3
30/10/00	18:00	19.9	10.7	11	9.8	0.3	0	0.6	0	0	0	986.8	12	31	W	4.4	11.4	0	0	74	6.2
30/10/00	19:00	19.6	8.9	9.8	8.4	0.4	0	0.6	0	0	0	987	10	32	WSW	3.2	9	0.5	0.3	81	5.9
30/10/00	20:00	19.4	9.3	10	8.3	0.4	0	0.6	0	0	0	986.7	11	31	WSW	3.2	9.5	1	1.5	81	6.2
30/10/00	21:00	19.3	10.3	10.7	9.9	0.3	0	0.6	0	0	0	986.8	10	25	W	4.9	9.6	0	0	76	6.3
30/10/00	22:00	19.3	10.9	11.3	10.7	0.3	0	0.5	0	0	0	986.6	11	29	WSW	5.2	10.5	0	0	73	6.2
30/10/00	23:00	19.2	10.5	11.3	9.4	0.3	0	0.6	0	0	0	985.9	11	34	WSW	4.7	10.9	0.5	2.3	82	7.6

Appendix B - 3: Tentative dates for identifying possible heavy storms from daily rainfall data

Year	Sep	Rain (mm)	Oct	Rain (mm)	Nov	Rain (mm)	Dec	Rain (mm)	Jan	Rain (mm)
2001		0.3, 0.3, 5.6		1		0, 1.3, 0.3	0			0.8, 10.9, 9.1
	27	18	2	24.9	29	16.3			5	26.2
		3.3, 9.7		2, 0.8, 0.8						11.9, 0.5, 2
	30	17.5	7	14					26	30
			8	15						
2000		0, 0, 2.3		0, 9.1, 5.8		9.7, 3.8		0.3, 4.1, 2.5	0	
	1	36.8	9	25.1	2	18.5	1	21.8		
		0, 0, 0.3		9.1		2.5, 0.3		7.9, 1, 0.8		
	15	25.4	11	29.5	5	34.5	7	18.3		
		0, 0, 12.7	12	69.1	6	18.5		7.9, 12.2, 12.4		
	19	19.8		0.3, 7.6, 13.5			12	25.4		
			29	23.1						
			30	26.2						
1999		3.6, 0.3, 2.8		12.2, 5.3, 2.5	0			0.5, 5.1, 2.5	0	
	20	68.8	24	21.6			24	36.1		
		0.3, 2, 15						1.8		
	26	17.5					26	21.6		
	27	19.3								
1998		0.3, 6.4	1	16.8	0			1.3, 2.8		0.8, 7.1, 7.6
	3	13.7					23	17	1	15.5
	4	17.8						8.1	2	16
		0.3, 1.3, 0.8					25	12.4	3	13.2
	30	31.8					26	10.9		
1997	0			0, 0, 3.3		15.2, 6.9, 2		0, 0, 7.4	0	
			7	20.3	8	18	18	20.3		
			8	38.9	9	15.7				
			9	20.6	10	15.5				
				9.4		14, 2, 0.8				
			11	25.1	18	18.3				
						0, 0.3, 7.6				
					28	24.4				

Storm identification rules:

Rainfall on wet day should be more than 15mm and this should be preceded by one or two day(s) of rain with minimum 5mm.

Appendix B - 4: FEH parameters for the weather station and the Saltdean catchment

Parameter	Weather Station, Falmer	Saltdean
National Grid Ref	TQ 34600, 09000	TQ 38700, 04200
Grid Reference	534 600 m E; 109 000 m N	538 700 m E; 104 200 m N
Catchment descriptor		
AREA	8.71	6.92
FARL	1	1
PROPWET	0.34	0.34
ALTBAR	150	124
ASPBAR	170	171
ASPVAR	0.36	0.23
BFIHOST	0.967	0.957
DPLBAR	3.6	3.05
DPSBAR	117.9	164.2
LDP	5.99	5.27
RMED-1H	11.5	11.2
RMED-1D	37.9	36.5
RMED-2D	51.4	48.4
SAAR	928	862
SAAR4170	974	877
SPRHOST	5	5.9
URBCONC	0.639	-999999
URBEXT1990	0.014	0
URBLOC	0.114	-999999
Catchment average DDF parameter		
C	-0.026	-0.026
D1	0.383	0.382
D2	0.314	0.285
D3	0.423	0.41
E	0.313	0.311
F	2.481	2.458
1 km grid point DDF parameter		
C	-0.026	-0.026
D1	0.383	0.393
D2	0.315	0.282
D3	0.41	0.424
E	0.311	0.311
F	2.461	2.43

Appendix B - 5: Distribution and description of soil associations in the catchment

Map unit	Name	Area (m^2)	Area (%)	Soil description	Geology
342a	Upton 1	4046.5	0.05	Shallow silty over chalk	Chalk
343h	Andover 1	7157800	89.60	Shallow silty over chalk	Chalk
U343h	Andover 1	45.7	~ 0	Shallow silty over chalk	Chalk
581e	Marlow	827044	10.35	Deep loam to clay	Plateau and river terrace drift

Description of soil associations

Association	Simple description	Geology	Dominant soil
Andover 1	Shallow silty over chalk	Chalk	Shallow well drained calcareous silty soils over chalk on slopes and crests
Marlow	Deep loam to clay	Plateau and river terrace drift	Well drained fine loamy over clayey and clayey soils.

Map unit	Associated soil	Site characteristics	Land use
Andover 1	Deep calcareous and non-calcareous fine silty soils in valley bottoms	Striped soil patterns locally	Winter cereals and short term grassland with dairying and stock rearing; some woodland.
Marlow	Some coarse and fine loamy over clayey soils with slowly permeable sub soils and slight seasonal waterlogging.		Cereals and short term grassland; coniferous woodland on slopes.

Appendix B - 6: Soil series associations in the Saltdean catchment

Andover soil association

A) Shallow soils, chalk within 30 cm: silty

i) Brown topsoil : Andover
ii) Grey topsoil : Upton
iii) Dark, humose topsoil : Icknield

B) Deeper soils

a) Chalk within 80cm

i) Subsoil calcareous above 40cm : Panholes
ii) Subsoil non calcareous > 40cm : Garston

b) Chalk below 80cm

i) Subsoil calcareous above 80cm : Coombe or Millington
ii) Subsoil non calcareous > 80cm : Charity

Marlow soil association

A) Soil with reddish or red mottled subsoil

a) Loamy over clay

1) Unmottled

i) Fine loamy over clay : Marlow
ii) Fine silty over clayey : Carstens

2) Subsoil faintly mottled above 60 cm or distinctly mottled between 40 & 80 cm

i) Coarse loamy over clay : Berkhamsted
ii) Fine loamy over clayey : Hornbeam
iii) Fine silty over clayey : Batcombe

b) Clayey

i) Chalk within 80 cm : Winchester
ii) Chalk below 80 cm : Givendale

B) Other soils; Unmottled

i) Coarse loamy : Moulton
ii) Fine loamy : Frilsham

Appendix B-7a: Soil horizon data for the Andover soil series

Parameter/ Layer designation	Arable (AR)			Ley Grass (LE)			Permanent grass (PG)			Others (OT)			
	A	C	R	A	C	R	A	C	R	A	Bw1	C	R
Upper depth (cm)	0	25	50	0	25	50	0	25	50	0	10	25	50
Lower depth (cm)	25	50	150	25	50	150	25	50	150	10	25	50	150
Fine sand	9	Rubble	Rock	9	Rubble	Rock	9	Rubble	Rock	9	3	Rubble	Rock
Medium sand	4	Rubble	Rock	4	Rubble	Rock	4	Rubble	Rock	4		Rubble	Rock
Coarse sand	9	Rubble	Rock	9	Rubble	Rock	9	Rubble	Rock	9		Rubble	Rock
Total sand (%)	22	Rubble	Rock	22	Rubble	Rock	22	Rubble	Rock	22	13	Rubble	Rock
Total silt (%)	56	Rubble	Rock	56	Rubble	Rock	56	Rubble	Rock	56	68	Rubble	Rock
Total clay (%)	22	Rubble	Rock	22	Rubble	Rock	22	Rubble	Rock	22	19	Rubble	Rock
Organic carbon (%)	3.8	0.5	0.1	3.4	0.5	0.1	6.3	1	0.2	7.6	4.7	0.9	0.2
pH	7.7	Rubble	Rock	7.7	Rubble	Rock	7.5	Rubble	Rock	7.5	7.6	Rubble	Rock
Calculated bulk density (g/cm^2)	1.12			1.18			0.93			0.86	0.92		
Calculated particle density (g/cm^2)	2.59			2.59			2.55			2.52	2.57		
Calculated total pore space (%) vol	56.7			54.5			63.5			65.9	64.2		
Calculated (%) vol. water at 5 kPa	43.6			41.8			48.5			50.1	49.9		
Calculated (%) vol. water at 10 kPa	39.3			37.8			43.9			45.4	45.1		
Calculated (%) vol. water at 40 kPa	31.4			30.2			35.2			36.5	35.9		
Calculated (%) vol. water at 200 kPa	24.5			23.6			27.4			28.5	27.7		
Calculated (%) vol. water at 1500 ,,	18.9			18.2			21.1			22	21		
Calculated Ksat													
Sun-vertical (cm/day)	115.6			106.9			160.5			183.8	144.4		
Lateral (cm/day)	82			75.4			116.1			133.8	103.8		
Calculated saturated water content	0.4744			0.4329			0.6316			0.7038	0.6532		
Calculated residual water content	0.0875			0.0822			0.1122			0.1251	0.1058		
Calculated Van Genuchten Alpha	0.042			0.0423			0.0409			0.0405	0.0377		
Calculated Van Genuchten N	1.2426			1.2451			1.2361			1.2331	1.2371		
Calculated Van Genuchten M	0.1952			0.1968			0.191			0.189	0.1917		

Appendix B-7b: Soil horizon data for the Marlow soil series

Parameter/	Arable (AR)				Ley Grass (LE)				Permanent grass (PG)				Others (OT)			
Layer designation	A	E	Bt	C	A	E	Bt	C	A	E	Bt	C	A	E	Bt	C
Upper depth (cm)	0	25	50	110	0	25	50	110	0	25	50	110	0	10	50	110
Lower depth (cm)	25	50	110	150	25	50	110	150	25	50	110	150	10	50	110	150
Fine sand	21	12	16	7	21	12	16	7	21	12	16	7	21	12	16	7
Medium sand	14				14				14				14			
Coarse sand	6				6				6				6			
Total sand (%)	41	29	29	15	41	29	29	15	41	29	29	15	41	29	29	15
Total silt (%)	37	46	25	53	37	46	25	53	37	46	25	53	37	46	25	53
Total clay (%)	22	25	46	32	22	25	46	32	22	25	46	32	22	25	46	32
O C (%)	2.2	1	0.5	0.5	3.5	1	0.5	0.5	2.7	1	0.5	0.5	4.2	2	0.5	0.5
pH	6.7	5.4	5.7	5.7	5.9	5.4	5.7	5.7	6.3	5.4	5.7	5.7	5.6	5.4	5.7	5.7
Calculated bulk density (g/cm^2)	1.28	1.35	1.27	1.37	1.24	1.35	1.27	1.37	1.19	1.35	1.27	1.37	1.07	1.19	1.27	1.37
Calculated particle density (g/cm^2)	2.61	2.63	2.64	2.64	2.59	2.63	2.64	2.64	2.61	2.63	2.64	2.64	2.58	2.62	2.64	2.64
Calculated total pore space (%) vol	51	48.7	51.9	48.1	52.2	48.7	51.9	48.1	54.3	48.7	51.9	48.1	58.5	54.5	51.9	48.1
Calculated (%) vol. water at 5 kPa	37.9	38.3	44.3	41.7	38.3	38.3	44.3	41.7	40.4	38.3	44.3	41.7	43.3	40.6	44.3	41.7
Calculated (%) vol. water at 10 kPa	34	34.8	41.2	38.5	34.3	34.8	41.2	38.5	36.2	34.8	41.2	38.5	38.8	36.9	41.2	38.5
Calculated (%) vol. water at 40 kPa	27	28.4	35.3	32.3	27.2	28.4	35.3	32.3	28.7	28.4	35.3	32.3	30.7	30	35.3	32.3
Calculated (%) vol. water at 200 kPa	21	22.8	29.8	26.6	21.2	22.8	29.8	26.6	22.3	22.8	29.8	26.6	23.8	23.8	29.8	26.6
Calculated (%) vol. water at 1500 ,,	16.3	18.2	25.1	21.6	16.4	18.2	25.1	21.6	17.2	18.2	25.1	21.6	18.3	18.8	25.1	21.6
Calculated Ksat																
Sub vertical (cm d^{-1})	116	63.9	25.7	14.6	132.9	63.9	25.7	14.6	134.4	63.9	25.7	14.6	167.5	134.4	25.7	14.6
Lateral (cm/day)	82.3	43.1	15	7.1	95.2	43.1	15	7.1	96.3	43.1	15	7.1	121.4	96.3	15	7.1
Calculated saturated water content	0.3775	0.3444	0.4078	0.3538	0.3947	0.3444	0.4078	0.3538	0.4325	0.3444	0.4078	0.3538	0.5146	0.4158	0.4078	0.3538
Calculated residual water content	0.0698	0.0755	0.1199	0.0888	0.0746	0.0755	0.1199	0.0888	0.0761	0.0755	0.1199	0.0888	0.0881	0.0856	0.1199	0.0888
Calculated Van Genuchten Alpha	0.0546	0.0466	0.0485	0.0384	0.0544	0.0466	0.0485	0.0384	0.0541	0.0466	0.0485	0.0384	0.0534	0.0456	0.0485	0.0384
Calculated Van Genuchten N	1.2501	1.2319	1.1993	1.212	1.2553	1.2319	1.1993	1.212	1.2475	1.2319	1.1993	1.212	1.2461	1.2328	1.1993	1.212
Calculated Van Genuchten M	0.2001	0.1883	0.1662	0.1749	0.2034	0.1883	0.1662	0.1749	0.1984	0.1883	0.1662	0.1749	0.1975	0.1889	0.1662	0.1749

Appendix B-8a: Pedotransfer functions for estimating bulk density from particle size and organic carbon data

Acquire from property database:

Soil series stagno-grouping, soil series lithology code, land use, horizon code, clay %, silt %, sand %, org c %

At this stage it is necessary to set some default values in relation to the particle size and organic carbon data. This is to ensure that the PTF's will give sensible values for 'unusual' soil horizons with particle size or organic carbon content at the extreme ends of the UK soil population. Thus:

IF sand % is ≥93 %, SET clay % = 2 AND *silt % = 5*
ELSE
IF silt % is < 2% SET *silt % = 2*
ELSE
IF clay % is < 1% SET *clay % = 1*
ELSE
IF sand % is < 5% SET *sand % = 5*
ELSE
IF lithology code is 3 (B, C, D, Ef, Eg, Eh, Ei, F) AND horizon code is NOT A, O, O1, O2 or H, AND org c % is > 3.5
SET horizon code = A

In addition, because the PTF's use empirical regression equations derived from statistical analysis of SSLRC's existing datasets, it is dangerous to use them to predict bulk densities based on values which lie outside the range of data on which the regressions are based. Proctor compaction tests on topsoil and subsoil samples representing a range of textural classes suggest that bulk densities are unlikely to exceed values of 1.95 for any textures. It is therefore necessary to set a maximum value for bulk density predictions to ensure that soil horizons at the textural extremes of the UK soil population do not give unrealistically high predictions. Thus:

IF predicted bulk density ≥ 1.95 SET bulk density = 1.95

Then:

Compute: Bulk density (g/cm^3) D_b

D_b

IF horizon code is H then:

= 0.575

ELSE IF horizon code is O then:

= 0.593 - (0.00745 x org c %)

ELSE IF horizon code is O1 then:

= 0.554 - (0.00589 x org c %)

ELSE IF horizon code is O2 then:

= 0.553 - (0.00797 x org c %)

ELSE IF horizon code is A AND land use is arable

= 1.46 - (0.0254 x Log_eclay %) + (0.0279 x Log_esand %) - (0.261 x Log_eorg c %)

ELSE IF horizon code is A AND land use is ley

= 0.807 + (0.0989 x Log_eclay %) + (0.106 x Log_esand %) - (0.215 x Log_eorg c %)

ELSE IF horizon code is A AND land use is permanent grass

= 0.999 + (0.0451 x Log_eclay %) + (0.0784 x Log_esand %) - (0.244 x Log_eorg c %)

ELSE IF horizon code is A AND land use is other

= 0.870 + (0.071 x Log_eclay %) + (0.093 x Log_esand %) - (0.254 x Log_eorg c %)

ELSE IF horizon code is Bpodz

= 0.998 - (0.0702 x Log_esilt %) + (0.0798 x Log_esand %) - (0.131 x Log_eorg c %)

ELSE IF stagno-grouping is non-stagno AND lithology code is 1 (Ec)

= 0.7132 - (0.0336 x org c %)

ELSE IF stagno-grouping is non-stagno AND lithology code is 2 (Ea, Eb, Ed, Ee)

= 1.56 - (0.00124 x silt %) - (0.00372 x clay %) - (0.0668 x org c %)

ELSE IF stagno-grouping is non-stagno AND lithology code is 3 (B, C, D, Ef, Eg, Eh, Ei, F) AND horizon code is Eg

= 1.50 - (0.00067 x silt %) + (0.00262 x clay %) - (0.139 x org c %)

ELSE IF stagno-grouping is non-stagno AND lithology code is 3 (B, C, D, Ef, Eg, Eh, Ei, F) AND horizon code is E

= 1.54 - (0.000583 x silt %) - (0.00008 x clay %) - (0.162 x org c %)

ELSE IF stagno-grouping is non-stagno AND lithology code is 3 (B, C, D, Ef, Eg, Eh, Ei, F) AND horizon code is Bw1

= 1.55 - (0.00147 x silt %) - (0.00018 x clay %) - (0.209 x org c %)

ELSE IF stagno-grouping is non-stagno AND lithology code is 3 (B, C, D, Ef, Eg, Eh, Ei, F) AND horizon code is Bg1

= 1.47 - (0.00727 x silt %) + (0.00716 x clay %) - (0.082 x org c %)

ELSE IF stagno-grouping is non-stagno AND lithology code is 3 (B, C, D, Ef, Eg, Eh, Ei, F) AND horizon code is Bt

= 1.66 - (0.00069 x silt %) - (0.00827 x clay %) + (0.0123 x org c %)

ELSE IF stagno-grouping is non-stagno AND lithology code is 3 (B, C, D, Ef, Eg, Eh, Ei, F) AND horizon code is Btg

= 1.67 + (0.000751 x silt %) - (0.0105 x clay %) + (0.0316 x org c %)

ELSE IF stagno-grouping is non-stagno AND lithology code is 3 (B, C, D, Ef, Eg, Eh, Ei, F) AND horizon code is Bw2

= 1.54 - (0.00546 x silt %) + (0.00338 x clay %) - (0.160 x org c %)

ELSE IF stagno-grouping is non-stagno AND lithology code is 3 (B, C, D, Ef, Eg, Eh, Ei, F) AND horizon code is Bg2

= 1.69 + (0.0021 x silt %) - (0.00231 x clay %) - (0.505 x org c %)

ELSE IF stagno-grouping is non-stagno AND lithology code is 3 (B, C, D, Ef, Eg, Eh, Ei, F) AND horizon code is BC

= 1.49 - (0.00029 x silt %) + (0.00437 x clay %) - (0.314 x org c %)

ELSE IF stagno-grouping is non-stagno AND lithology code is 3 (B, C, D, Ef, Eg, Eh, Ei, F) AND horizon code is C

= 1.50 - (0.00059 x silt %) + (0.00085 x clay %) - (0.254 x org c %)

ELSE IF stagno-grouping is stagno AND lithology code is 6 (Ef)

= 0.618 + (0.095 x Log_esilt %) + (0.1 x Log_eclay %) + (0.0195 x Log_esand %)- (0.178 x Log_eorg c %)

ELSE IF stagno-grouping is stagno AND lithology code is 7 (Eg, Eh, Ei)

= -0.015 + (0.119 x Log_esilt %) + (0.102 x Log_eclay %) + (0.186 x Log_esand %)- (0.141 x Log_eorg c %)

ELSE IF stagno-grouping is stagno AND lithology code is 10 (Fh, Fi, Fj, Fk, Fl)

$= 1.96 - (0.0158 \times \text{Log}_e\text{silt \%}) - (0.154 \times \text{Log}_e\text{clay \%}) + (0.0102 \times \text{Log}_e\text{sand \%}) - (0.113 \times \text{Log}_e\text{org c \%})$

ELSE IF stagno-grouping is stagno AND lithology code is LUMP1 OR LUMP2 (B, C, D, Fa, Fb, Fc, Fd, Fe, Ff, Fg, Fm, Fn, Fo, Fp, Fq, Fr)

$= 2.37 - (0.246 \times \text{Log}_e\text{silt \%}) + (0.0266 \times \text{Log}_e\text{clay \%}) - (0.0178 \times \text{Log}_e\text{sand \%}) - (0.114 \times \text{Log}_e\text{org c \%})$

Appendix B-8b: Pedotransfer functions for deriving soil hydraulic properties from particle size, organic carbon and bulk density data

Acquire from property database:

Soil series lithology code, horizon code, clay %, silt %, sand %, org c %, bulk den.

At this stage it is necessary to set some default values in relation to the particle size and organic carbon data. This is to ensure that the PTF's will give sensible values for 'unusual' soil horizons with particle size or organic carbon content at the extreme ends of the UK soil population. Thus:

IF	sand % is ≥93 %,	SET clay % = 2 AND *silt % = 5*
ELSE		
IF	silt % is < 2%	SET *silt % = 2*
ELSE		
IF	clay % is < 1%	SET *clay % = 1*
ELSE		
IF	sand % is < 5%	SET *sand % = 5*
ELSE		
IF	pmlith is B, C, D, Ef, Eg, Eh, Ei, F AND horizon code is NOT A, O, O1, O2 or H, AND org c % is > 3.5 SET horizon code = A	

In addition, because the PTF's are based, at least in part, on theoretical relationships to mineral particle size distribution, it is necessary to exclude all non-mineral horizons comprising organic or carbonatic material, thin ironpans, or rock or rock rubble. Thus:

IF horizon code is O, O1, O2, H, or R, OR IF clay % is rock, rock rubble or thin ironpan OR IF pmlith is Ec SET 'value' = -1

Then compute:

Particle density (g/cm3)	PD
Total pore space (%vol)	TP
Water content at saturation (% vol)	θv_0
Water content at 5 kPa tension (% vol)	θv_5
Water content at 10 kPa tension (% vol)	θv_{10}

Water content at 40 kPa tension (% vol)	θv_{40}
Water content at 200 kPa tension (% vol)	θv_{200}
Water content at 1500 kPa tension (% vol)	θv_{1500}
Van Genuchten's 'alpha' parameter	VG α
Van Genuchten's 'en' parameter	VG n
Van Genuchten's residual water content (w/w)	VG θr
Van Genuchten's water content at saturation (w/w)	VG θs
Brook's Corey 'a' parameter	BC α
Brook's Corey 'b' parameter	BC β
Brook's Corey water content at saturation (vol fraction)	BC θvs
Saturated hydraulic conductivity (sub-vertical)	K_{sat}subvert
Saturated hydraulic conductivity (lateral)	K_{sat}lat

PD = ((2.65 * (100 - org c)) + org c) / 100

TP = [1 - (bulk den. / PD)] * 100

θv_0

If horizon code is A then:

= [(1.008 * clay %) + (0.988 * silt %) + (1.002 * sand %) - (38.989 * bulk den.) - (0.722 * org c %)]

If horizon code is E, B, BC, C then:

= [(1.035 * clay %) + (0.985 * silt %) + (0.916 * sand %) - (35.922 * bulk den) - (2.763 * org c %)]

θv_5

If horizon code is A then:

= [49.81 + (0.27 * clay%) + (0.11 * silt%) + (0.3 * org c%)] - (17.78 * bulk den)]

If horizon code is E, B, BC, C then:

= [42.16 + (0.34 * clay%) + (0.18 * silt%) + (0.22 * org c%)] – (16.97 * bulk den)]

θv_{10}

If horizon code is A then:

= [40.3 + (0.34 * clay%) + (0.13 * silt%) + (0.4 * org c%)] - (13.91 * bulk den)]

If horizon code is E, B, BC, C then:

= [30.86 + (0.4 * clay%) + (0.21 * silt%) + (1.26 * org c%)] – (12.46 * bulk den)]

θv_{40}

If horizon code is A then:

= [26.68 + (0.39 * clay %) + (0.13 * silt %) + (0.46 * org c %)] - (7.72 * bulk den)]

If horizon code is E, B, BC, C then:

= [22.05 + (0.47 * clay %) + (0.2 * silt %) + (0.93 * org c %)] – (9.56 * bulk den)]

θv_{200}

If horizon code is A then:

= [9.38 + (0.47 * clay %) + (0.11 * silt %) + (0.69 * org c %)]

If horizon code is E, B, BC, C then:

= [4.31 + (1.08 * clay %) - (0.0079 * clay $\%^{2}$)]

θv_{1500}

If horizon code is A then:

= [6.11 + (0.4 * clay %) + (0.05 * silt %) + (0.5 * org c %)]

If horizon code is E, B, BC, C then:

= [1.25 + (0.92 * clay %) - (0.0062 * clay $\%^{2}$)]

VG θ_r = θv_{1500} / 2 / bulk den / 100

VG θ_s = θv_0 / bulk den / 100

VG α = - 0.01926 + 0.438888 * [0.192526 * clay $\%^{-0.4}$ + 0.285901 * silt $\%^{-0.4}$ + 0.000157 * sand $\%^{1.4}$ + 0.012966 * bulk den.]

VG n = 1.08235 + 0.426943 * [0.628785 * clay $\%^{-0.4}$ + 2.16201 * silt $\%^{-1.6}$ + 0.00000000372 * sand $\%^{4}$ + 0.239019 * bulk den. *(org c % / clay $\%)^{0.2}$]

(Check that VGα is greater than 0!)

BC α = `-4.9840297533 + 0.0509226283*sand + 0.1575152771*silt + 0.1240901644*bd - 0.1640033143*oc - 0.0021767278*silt**2 + 1.438224E-05*silt**3 + 8.040715E-04*clay**2 + 0.0044067117*oc**2`

BC β = `-0.8466880654 - 0.0046806123*sand + 0.0092463819*silt - 0.4542769707*bd - 0.0497915563*oc + 3.294687E-04*sand**2 - 1.689056E-06*sand**3 + 0.0011225373*oc**2`

BC θvs = +0.2345971971 + 0.0046614221*sand +
0.0088163314*silt + 0.0064338641*clay -
0.3028160229*bd + 1.79762E-05*sand**2 -
3.134631E-05*silt**2

(Check that BC α and BC β are greater than 0!)

Saturated hydraulic conductivity (sub-vertical)

K_{sat}subvert

IF clay% <16, AND (silt% + (clay% * 2)) <31 AND (TP - $\theta_{v0.05}$) < 7.5, then:

= $0.4535 *(TP - \theta_{v0.05})^{1.03423}$

ELSE, IF clay% <16, AND (silt% + (clay% * 2)) <31

Then:

= $8.03578 - (6.7707 * [TP - \theta_{v0.05}]) + [0.833 * (TP - \theta_{v0.05})^2]$

ELSE, IF (TP - $\theta_{v0.05}$) < 4.0,

then:

= $0.14143 * EXP^{0.46944 * (TP - \theta_{v0.05})}$

ELSE:

= $5.8521 - (5.4125 * [TP - \theta_{v0.05}]) + [1.05138 * (TP - \theta_{v0.05})^2]$

Saturated hydraulic conductivity (lateral)

K_{sat}lat

IF clay% <16, AND (silt% + (clay% * 2)) <31 AND (TP - $\theta_{v0.05}$) < 7.5, then:

= $0.4535 *(TP - \theta_{v0.05})^{1.03423}$

ELSE, IF clay% <16, AND (silt% + (clay% * 2)) <31

then:

= $8.03578 - (6.7707 * [TP - \theta_{v0.05}]) + [0.833 * (TP - \theta_{v0.05})^2]$

ELSE, IF (TP - $\theta_{v0.05}$) < 5.5,

then:

= $0.14143 * EXP^{0.46944 * (TP - \theta_{v0.05})}$

ELSE:

= $3.155 - (4.639 * [TP - \theta_{v0.05}]) + [0.8143 * (TP - \theta_{v0.05})^2]$

Appendix C

Appendix C-1: Definitions of level-2 land use and land cover classes for the study area

Class	Sub class	Land use and land cover included
Arable	Bare soil	Bare soil, chalk exposed field, tilled land or planted field
	Harvested field	Harvested field with crop stubbles
	Set-aside	Set-aside with less five year crop rotation
	Ley grass	Grass leys for hay and silage and fodder crops
	Horticulture and vegetables	Horticulture and vineyard nursery, brassica, kale
Grassland		(Scattered tree crown cover ≤ 20%)
	Hill grazing land	Natural or marginal hill grassland used for sheep or cattle grazing
	Semi-improved	Less intensively management grassland
	Improved	Fully managed grassland including seeding, fertilising,
Dense scrub &	Hedges	Hedges or hedge line along fields
woodland	Gorse scrub - open	Gorse scrubs with less than 20 to 80% cover
	Gorse scrub - dense	Gorse scrub with cover ≥ 80 %
	Open woodland	Single or mixed woodland with 20 to 80% cover
	Dense woodland (plantation)	Single species woodland with crown cover
	Dense mixed woodland	Mixed woodland with crown cover ≥ 80%
Built-up land	Buildings	Large building and farmsteads
	Village	Village area including buildings, road, gardens and tress
	Urban area	Buildings, roads and trees
	Roads	Major roads more than 20 m wide
Open water	Inland water	Includes rivers, lakes, ponds and water courses with greater than 20 m wide
	Sea water	Sea water

Appendix C-2: Characteristics of the SPOT imaging sensors (reproduced from Spot Image, 2003)

Information	SPOT-1, 2 & 3	SPOT -4	SPOT-5
Launch date	Feb 86, Jan 90, Sep 93	24 Mar 1998	4 May 2002
Current state	SPOT-2 only in operation	Operational	Operational
Instruments	2 HRVs	2 HRVIRs	2 HRGs
Spectral Bands	XS	Xi	Xi
Band 1 (μm)	0.50 - 0.59	0.50 - 0.59	0.50 - 0.59
Band 2 (μm)	0.61 – 0.68	0.61 – 0.68	0.61 – 0.68
Band 3 (μm)	0.79 - 0.89	0.79 - 0.89	0.79 - 0.89
Band 4 (μm)	--	1.58 – 1.75	1.58 – 1.75
Pixel size (m)	20	20	10 & 5 in supermode (20 m for band 4)
Pan	0.51- 0.73 Pan	0.61 – 0.68 (Mono)	0.51- 0.73 Pan
Pixel size (m)	10 m	10 m	5 & 2.5 in supermode
Swath width	60 km	60 km	60 km
Onboard Compression	DPCH for PAN	DPCM (3/4) for both	
Normal life	3 years each	5 years	5 years
Altitude at equator	822 km	822 km	822 km
Inclination	98.7 degree	98.7 degree	98.7 degree
Attitude control	Earth-pointing	Earth-pointing	Earth-pointing & yaw axis controlled
Orbital period	101.4 min	101.4 min	101.4 min
Revolutions per day	14.2	14.2	14.2
Orbital revolutions per cycle	369	369	369
Orbital cycle	26 days	26 days	26 days

Appendix C-3: Availability of SPOT data from the SIRIUS archive

GRS	Date	SPOT id	Sensor ID	Resolution (m)	Cloud cover	Quality	Comment
033/247	5 May 2000	2	HRV-2	20 XS	No	OK	
,,	18June 2000	1	HRV-1	20 XS	No	OK	Selected
,,	18 June 2000	1	HRV-2	20 XS	No	OK	
033/247	15 Oct 2000	1	HRV-1	20 XS	Yes	Not OK	
,,	15 Oct 2000	1	HRV-2	20 XS	Yes	Not OK	
,,	17 Oct	4	HRVIR	10 Pan	Yes	Not OK	
,,	17 Oct	4	HRVIR	20 XS	Yes	Not OK	
	19 Oct	2	HRV-1	20 XS	Little	OK	
,,	19 Oct	2	HRV-2	20 XS	No	OK	
,,	26 Oct	1	HRV-1	20 XS	No	OK	Selected
,,	29 Oct	2	HRV	20 XS	Yes	Not OK	
,,	31 Oct	1	HRV	10 Pan	Yes	Not OK	
,,	4 Nov	1	HRV	10 Pan	No	OK	
032/247	30 May 2001	2	HRV	20 XS	Yes	Not OK	
033/247	25 June	4	HRVIR	20 Xs	No	Incomplete scene	
,,	3 July	1	HRV	20 XS	No	Incomplete scene	
032/247	30 July	4	HRVIR	10 Pan	No	Incomplete scene	
,,	30 July	4	HRVIR	20 XS	No	Incomplete scene	

Appendix C-4: Preprocessing levels and location accuracy of SPOT data

Standard preprocessing levels:

SPOT Scene products in the CAP format

- Level 0 – Raw data collected at sensor (NOT distributed for SPOT sensors)
- Level 1A - radiometrically corrected image data
- Level 1B - radiometrically and geometrically corrected image data
- Level 2 A - radiometric and geometric corrections applied and projected to a standard map projection (UTM, WGS 84) without ground control points (An entry level map product)

SPOTView Products in the DIMAP Format

- Level 2B (Precision) - radiometric and geometric corrections applied and projected to a standard map projection using ground control points for a better accuracy.
- Level 3 (Ortho) - radiometric and geometric corrections applied and projected to a standard map projection using GCPs and a DTM
- Level S - radiometric processing and geometric resampling for two scene registration
    - level S1 when one input scene is level 1B
    - level S2 when one input scene is level 2

Location accuracy of SPOT data

Satellite	Band	SPOT Scene				SPOTView	
		1A	1B	2A	2B	3 (ortho) with DEM	
						Reference3D	Other sources
SPOT 1-3	20 m XS 10 m Pan	350 m	350 m	350 m	30 m	15 m	30 m
SPOT-4	10m XS	350 m	350 m	350 m	30 m	15 m	30 m
SPOT-5	10 m XS 5 m XS 5 m Pan 2.5 m Pan	50 m	50 m	50 m	30 m	15 m	30 m

Appendix C-5: Scene acquisition parameters of the selected images

Parameter	26 October 2000	18 June 2000
Scene ID	1 033-247 00-10-26 11:01:40 1 X	1 033-246 00-06-18 11:00:33 1 X
K-J identification	033-247	033-246
Time	11:01:40	11:00:38
Instrument	HRV 1	HRV 1
Shift along track	0 0	6 1800
Preprocessing level	1B	1B
Spectral mode	XS	XS
Number of spectral bands	3	3
Spectral band indicator	XS1, XS2 and XS3	XS1, XS2 and XS3
Gain number	8, 8, 7	8, 8, 7
Absolute calibration gains (W/m2/sr/µm)	1.28757 1.02600 1.40646	1.28757 1.02600 1.40646
Scene orientation angle	11.5 degree	11.5 degree
Incidence angle	R17.2 degree	R17.2 degree
Sun azimuth angle	168.4 degree	151.4 ,,
Sun elevation angle	25.9degree	60.1 ,,
Number of lines	2994	2994
Number of pixels per line	3383	3382
Scene Centre Location:		
Latitude	50° 50' 28" N	50° 59' 56" N
Longitude	00° 06' 46" W	00° 03' 53" W
Pixels number	1711	1711
Line number	1497	1497
Cloud and snow cover:		
Scene cloud coverage	BBBBBBCC	AAAAAA**
Average cloud cover	B (10 per cent)	A (No cloud cover)
Sow cover	00000000	000000**
Average scene quality	E (Excellent)	E (Excellent)

(Note: * stands for missing segment)

Appendix C-6: SPOT CEOS data distribution format

The SPOT scene data are organised into a logical volume, which is stored on a single CD-ROM. A single CD-ROM logical volume includes five files in a sub directory in addition to a root directory catalogue file and quick look image(s):

- Volume Directory File (vold_01.dat)
- Leader File (lead_01.dat)
- Data Set File (imag_01.dat)
- Trailer File (trai_01.dat)
- Null Volume Directory File (null_01.dat)

Description of Level 1B Data Files

Record	Priority	No of records	Record length
`Volume Directory File`			
Volume descriptor record	Mandatory	1	360 bytes
Pointer record for the leader file	Mandatory	1	360 bytes
Pointer record for the imagery file	Mandatory	1	360 bytes
Pointer record for the trailer file	Mandatory	1	360 bytes
Text record	Mandatory	1	360 bytes
`Leader File`			
Leader file descriptor	Mandatory	1	3960 bytes
Header record	Mandatory	1	3960 bytes
Ancillary (ephemeris/attitude) record	Optional	1	3960 bytes
Ancillary (radiometric/calibration) Records	Optional	18	3960 bytes
Ancillary (histograms) records	Optional	3	3960 bytes
Ancillary (map projection) record	Optional	1	3960 bytes
Ancillary (GCPs) record		1	3960 bytes
Annotation record	Mandatory	1	3960 bytes
`Data Set File`			
File descriptor record	Mandatory	1	5400 bytes
Image data records	Mandatory	8982	5400 bytes
`Trailer File`			
Trailer file descriptor		1	1080 bytes
Trailer quality record		1	1080 bytes
Geometric transformation record		1	1080 bytes
`Null Volume Directory File`			
Null volume descriptor record	Mandatory	1	360 bytes

Appendix C-7 (a): Co-ordinates of 31 GCPs for geometric correction of 26 October sub image

GCP ID	X Image	Y Image	X Map	Y Map
1	2274.12	-1556.35	544323.0	102911.0
2	2202.18	-1344.18	543636.0	107355.0
3	2233.27	-1299.60	544433.0	108117.0
4	2293.55	-1254.53	545769.0	108787.0
5	2118.73	-1266.92	542263.0	109165.0
6	2047.75	-1105.44	541416.0	112568.0
7	1955.51	-1290.68	538984.0	109223.0
8	1814.01	-1462.02	535609.0	106359.0
9	1858.78	-1548.75	536167.0	104485.0
10	2002.19	-1632.06	538721.0	102345.0
11	1770.74	-1342.72	535175.0	108858.0
12	1632.40	-1337.98	532476.0	109437.0
13	1445.48	-1435.24	528465.0	108167.0
14	1451.11	-1231.06	529274.0	112163.0
15	1465.01	-1130.49	529915.0	114097.0
16	1239.07	-1492.25	524190.0	107740.0
17	1322.25	-1111.99	527153.0	114958.0
18	1076.67	-1591.27	520665.0	106340.0
19	980.76	-1238.03	520005.0	113657.0
20	1055.16	-1427.79	520812.0	109662.0
21	1054.84	-1340.87	521091.0	111367.0
22	1158.11	-1345.63	523126.0	110907.0
23	1596.33	-1564.08	530984.0	105097.0
24	1648.48	-1234.26	533160.0	111420.0
25	1936.64	-1531.92	537774.0	104563.0
26	1906.02	-1165.05	538442.0	111894.0
27	1925.59	-1452.82	537840.0	106158.0
28	2176.04	-1449.64	542768.0	105353.0
29	1311.05	-1224.59	526540.0	112788.0
30	2046.82	-1573.25	539788.0	103364.0
31	1294.61	-1029.59	526895.0	116669.0
			Total RMSE :	0.669

Appendix C-7 (b): Coordinates of 26 GCPs for geometric correction of 18 June sub image

GCP ID	X Image	Y Image	X Map	Y Map
1	2313.13	-2431.13	544320	102914
2	2239.38	-2222.38	543595	107254
3	2157.63	-2140.63	542271	109172
4	2086.88	-1979.88	541434	112576
5	2332.63	-2128.38	545761	108803
6	1809.88	-2218.13	535163	108849
7	1334.63	-1904.13	526901	116690
8	1361.88	-1986.63	527155	114959
9	1541.375	-2244.13	529791	109270
10	1484.88	-2311.38	528453	108134
11	1268.13	-2390.38	523912	107326
12	1122.63	-2451.88	520837	106611
13	1023.38	-2296.63	519424	110014
14	1021.13	-2113.38	520012	113638
15	1179.52	-2239.00	522701	110615
16	1089.22	-2547.51	519845	104851
17	1615.40	-2417.22	530645	105595
18	1671.54	-2213.32	532463	109420
19	1853.74	-2340.96	535607	106259
20	1898.49	-2423.84	536187	104475
21	2041.49	-2507.26	538706	102343
22	1976.35	-2406.37	537781	104559
23	2215.21	-2323.21	542773	105355
24	1994.09	-2165.38	538964	109240
25	1904.61	-2033.25	537659	112161
26	1661.30	-2106.72	532621	111554
			Total RMSE :	0.401

Appendix C-8: Selected ground segments in the unaligned systematic random scheme with their upper left corner co-ordinates

1 (2) 521 000 114 000	**2** (12) 270 000 112 000	**3** (9) 528 000 112 000	**4** (4) 535 000 114 000	**5** (14) 537 000 111 000	(16) X
6 (4) 523 000 110 000	**7** (3) 526 000 110 000	(14) 529 000 107 000 Urban	(13) 532 000 107 000 Urban	**8** (14) 537 000 107 000	**9** (3) 540 000 110 000
(10) Sea	(15) Sea	(1) 528 000 106 000 Urban	**10** (3) 534 000 106 000	**11** (7) 538 000 105 000	(8) X
Sea	Sea	Sea	Sea	(14) Sea	(6) Sea

Note:

First bold number on the left hand side in a block shows the segment ID of the selected sample.

Number in parentheses on the right hand side in the block shows the segment number selected randomly from a 16-segment block.

Appendix C-9: Survey form of a ground segment with the description of land use and land cover in the Eastern South Down

Site No. 11 Observer (s): DSB

Name of site: **Upper Saltdean** Date of survey: 7 May 2003

Segment no.: 11 Size of segment: 1 km x 1 km

Parcel ID	Land use and land cover	Crop/ surface condition	Remarks
1.	Semi-improved grassland	Poor cover	
2.	Arable land	Winter wheat	
3.	Semi-improved grassland	Poor cover	
4.	Arable land with patches of chalk visible	Spring wheat	
5.	Hill grazing grassland	Good cover	
6.	Open scrubs	Gorse etc	4 -5 m tall
7.	Dense scrubs	Gorse etc.	5 m tall
8.	Arable land	Winter wheat	
9.	Open scrub	Gorse	4-5 m tall
10.	Dense scrub	A patch of gorse	4-5 m tall

Appendix C-10: Accuracy of georeferencing of scanned segments

Segment ID	RMS error
1.	1.146
2.	0.563
3.	1.114
4.	0.960
5.	0.974
6.	0.979
7.	1.137
8.	0.739
9.	0.446
10.	0.686
11.	0.424
Average	0.833 (pixels)

(Details of a segment ID, please refer Appendix C.8.)

Appendix C-11: Aggregation of scheme classes during direct area estimation

Class	Aggregation of classes
Bare soil	10
Harvested fields with stubbles	11
Set-aside /fallow	12
Semi-improved grassland	20+21
Hill grazing grassland	22+23
Improved grassland	24+25
Open woodland	31+33
Dense woodland	32+34+35
Built-up land	40+41+42

(Class number stands for the level-2 class in the classification scheme Table 4.2)

Appendix C-12: Accuracy analysis of class estimates by direct area estimation approach

Class	Sum	Mean	Zc	y-mean sqr	1/(n(n-1))	Var (yc mean)	Sqrt(var)	SE (sq km)	SE in ha	95% CI	UCL	LCL
Bare soil	1.421	0.129	5596.168	0.240	0.009	0.002	0.047	10.650	1065.037	2087.472	3152.508	-1022.435
Harvested field	1.732	0.158	5683.382	0.399	0.009	0.004	0.060	13.737	1373.690	2692.433	4066.124	-1318.743
Set-aside/fallow	0.230	0.021	5673.136	0.048	0.009	0.000	0.021	4.774	477.390	935.684	1413.073	-458.294
Semi-improved	2.182	0.198	4526.640	0.449	0.009	0.004	0.064	14.584	1458.409	2858.482	4316.891	-1400.073
Rough grazing	1.651	0.150	3425.259	0.443	0.009	0.004	0.063	14.488	1448.768	2839.584	4288.352	-1390.817
Improved grass	0.950	0.086	1971.203	0.358	0.009	0.003	0.057	13.014	1301.416	2550.776	3852.192	-1249.360
Open woodland	0.754	0.069	1565.243	0.016	0.009	0.000	0.012	2.784	278.358	545.581	823.939	-267.224
Dense ,,	0.699	0.064	1449.452	0.018	0.009	0.000	0.013	2.953	295.308	578.805	874.113	-283.496
Built-up	1.381	0.126	2865.741	0.518	0.009	0.005	0.069	15.661	1566.115	3069.586	4635.702	-1503.471

(Note: UCL and LCL stand for upper and lower confidence limits)

Appendix C-13: Statistical properties of 40 cluster groups of the 26 October image

Case ID	Band 1		Band 2		Band 3	
	Mean1	Std Dev1	Mean2	Std Dev2	Mean3	Std Dev3
Case 1	35.813	1.916	16.950	2.114	23.245	3.224
Case 2	37.508	1.854	18.155	2.094	32.660	2.538
Case 3	39.306	1.845	19.280	1.859	40.087	1.950
Case 4	45.300	2.088	24.653	1.744	36.667	3.027
Case 5	39.372	1.615	18.892	1.435	46.641	1.676
Case 6	51.161	1.868	29.963	1.971	39.42	2.482
Case 7	39.595	1.623	18.712	1.391	51.725	1.361
Case 8	48.777	1.327	27.412	1.570	45.076	1.850
Case 9	56.602	2.22	35.065	2.087	45.417	2.811
Case 10	43.721	1.664	22.818	1.373	45.408	2.017
Case 11	44.096	1.495	22.801	1.367	51.321	1.598
Case 12	51.347	1.365	29.946	1.462	49.321	1.620
Case 13	41.150	1.543	19.783	1.385	56.15	1.292
Case 14	48.749	1.313	26.713	1.294	52.324	1.824
Case 15	52.932	1.629	30.514	1.646	54.777	1.758
Case 16	45.258	1.330	22.818	1.271	57.369	1.705
Case 17	61.988	2.326	40.742	2.454	53.24	2.780
Case 18	49.052	1.305	26.432	1.364	58.313	1.650
Case 19	52.247	1.520	29.582	1.744	62.239	1.977
Case 20	41.595	1.623	19.799	1.318	60.773	1.323
Case 21	45.529	1.229	22.565	1.242	63.769	1.800
Case 22	69.174	2.374	46.776	2.342	60.905	2.834
Case 23	48.995	1.261	25.825	1.369	65.358	1.860
Case 24	41.816	1.618	19.513	1.250	66.745	1.822
Case 25	58.148	2.587	34.684	2.526	61.332	3.012
Case 26	44.555	1.376	21.202	1.292	70.647	1.749
Case 27	50.879	1.451	28.044	1.606	70.661	1.911
Case 28	48.042	1.289	24.325	1.298	72.392	1.843
Case 29	42.126	1.779	19.078	1.293	75.513	2.053
Case 30	45.970	1.202	21.813	1.180	78.692	1.974
Case 31	49.437	1.316	25.419	1.500	78.627	2.162
Case 32	63.910	3.772	39.649	3.432	68.532	3.858
Case 33	43.112	1.787	19.187	1.117	83.858	2.296
Case 34	53.969	1.484	31.466	2.047	77.709	2.619
Case 35	76.258	3.091	52.386	3.233	67.102	2.873
Case 36	47.588	1.349	22.967	1.277	86.175	2.143
Case 37	52.463	2.004	27.883	1.652	87.091	3.040
Case 38	49.367	2.133	23.730	2.169	96.578	2.483
Case 39	45.779	1.615	20.856	1.451	92.676	2.349
Case 40	46.254	1.504	20.544	1.261	106.223	4.937

Appendix C-14: Regrouping 40 clusters into 11 classes

Case	Class		
	Ward's method and SED	Between Linkage and SED	Regrouping tool
Case 1	1	7	1
Case 2	1	6	2
Case 3	1	6	3
Case 4	2	9	3
Case 5	3	8	3
Case 6	2	9	3
Case 7	3	8	3
Case 8	2	9	3
Case 9	4	4	3
Case 10	3	8	3
Case 11	3	8	3
Case 12	4	5	3
Case 13	5	1	3
Case 14	4	5	3
Case 15	4	5	6
Case 16	5	1	3
Case 17	4	4	5
Case 18	5	1	7
Case 19	6	5	3
Case 20	5	1	3
Case 21	7	1	3
Case 22	8	10	3
Case 23	7	1	3
Case 24	7	1	8
Case 25	6	5	3
Case 26	7	1	3
Case 27	9	2	3
Case 28	7	1	3
Case 29	7	1	3
Case 30	10	2	3
Case 31	10	2	11
Case 32	6	11	3
Case 33	10	2	3
Case 34	9	2	3
Case 35	8	10	3
Case 36	10	2	9
Case 37	11	2	4
Case 38	11	3	3
Case 39	11	3	3
Case 40	11	3	10

(SED stands for squared Euclidean distance)

Appendix C-15: Signature separability of 11 classes with the Transformed Divergence and Jefferies-Matusita distance methods

	Transformed divergence distance										
Class	1	2	3	4	5	6	7	8	9	10	11
1	0										
2	1903	0									
3	2000	1952	0								
4	2000	1882	1545	0							
5	2000	2000	1939	1902	0						
6	2000	2000	1760	1985	1594	0					
7	2000	2000	2000	2000	2000	1895	0				
8	2000	2000	1953	2000	1991	1233	1606	0			
9	2000	2000	1998	1988	1429	1877	2000	2000	0		
10	2000	2000	2000	2000	1997	2000	2000	2000	1724	0	
11	2000	1926	1083	1245	1865	1871	2000	1998	1979	2000	0

Best average separability: 1893.03 and
Best minimum separability: 1082.75

	Jefferies-Matusita distance										
Class	1	2	3	4	5	6	7	8	9	10	11
1	0										
2	1365	0									
3	1414	1345	0								
4	1414	1296	1222	0							
5	1414	1414	1368	1358	0						
6	1414	1413	1286	1396	1213	0					
7	1414	1414	1414	1414	1414	1374	0				
8	1414	1414	1389	1414	1408	1079	1227	0			
9	1414	1414	1413	1409	1184	1367	1414	1414	0		
10	1414	1414	1414	1414	1411	1414	1414	1414	1267	0	
11	1414	1367	950	1059	1260	1331	1414	1412	1392	1414	0

Best average separability: 1358.94 and

Best minimum separability: 1082.75

Class	Name of class		
1	Arable2	2	Arable3
3	Arable4	4	Arable5
5	Arable fallow/set aside	6	Hill grazing grassland
7	Improved grassland	8	Semi-improved grassland
9	Open woodland and scrub	10	Dense woodland and scrub
11	Built-up land		

Appendix C-16: Calibration method of the SPOT HRV-1 sensor

For SPOT-1 HRV sensor, the complex model to describe instrument behaviour is expressed as:

$$x_{jmk} = A_k G_{mk} g_j L_{jk} + C_{jk}$$

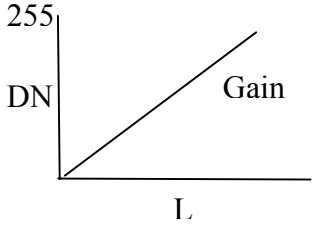

where x_{jmk} is the raw digital output, k identifies the spectral band, j is the pixel number along the spectral line, m is the onboard gain number. A_k is the absolute calibration coefficient, G_{mk} is the viewing gain coefficient, g_j is the pixel relative sensitivity (equalisation coefficient) and C_{jk} is the dark signal.

The equalisation process first determines the coefficients, C_{jk} and g_j, and then detector normalisation is carried out to compute level 1A data:

$$X_{jmk} = \frac{x_{jmk} - C_{jk}}{g_j} = A_k G_{mk} L_{jk}$$

For calibration of level 1B data, X_{jmk} is the digital numbers (DNs) and is expressed in simple equation:

$$DN = L_{0k} * A_{0k} * G_{mk}$$

or $L_{0k} = DN / (A_0 * G_{mk})$

where, L_{0k} is the radiance at sensor for a spectral band k, A_{0k} is the absolute calibration coefficient for a band k, and G_{mk} is the viewing gain coefficient for the band k

Gain coefficient is different for each sensor and is calculated with a very good accuracy from the following equations:

$G_{mk} = 1.3^{(m-3)}$ for SPOT-1
$G_{mk} = 1.5^{(m-2)}$ for SPOT-4

where m is the viewing gain number associated with the signal amplifiers and varies from 1 to 8 for SPOT system. The onboard gain number, m is given in the leader file (record 2, bytes 725-740)

G_{mk} and A_k coefficients should be determined independently for arriving at a more accurate equivalent radiance. The absolute calibration coefficients are estimated on a regular basis to account the change in detector sensitivity. This update coefficient table can be requested from the supplier and then coefficients for image acquisition date are interpolated from the table.
For 26 Oct 2000 image, gain coefficients were determined independently. Absolute calibration coefficients could not be determined; as coefficient table was not updated till the date of imagery acquisition so alternative method was adopted. In this method, a multiplication product

(A_k*G_{mk}) called absolute calibration gain was used and is directly supplied in the leader file (record 2, bytes 1765-2276). The accuracy of leader file supplied value is about 10%.
The final calibration equation can be expressed as:

$$L_{0k} = DN_k / A'_k$$

Where L_{0k} is the radiance measured at sensor for spectral band, k; A'_k is the absolute calibration gain for band k ($W^{-1}m^2$ sr μm) read directly from the leader file; and DN_k is the digital number for the band k.

Conversion of spectral radiance to exoatmospheric reflectance

The apparent reflectance, ρ_0, is related to the measured radiance, L_0 to the solar irradiance incident at the top of the atmosphere and is given as

$$\rho_0 = \frac{\pi * L_0 * d^2}{E_{sun} * Cos(SZ)}$$

where, ρ_0 is the exoatmospheric reflectance at the satellite (0-1), L_0 is the spectral radiance at sensor aperture in W m^{-2} $ster^{-1}$ μm^{-1} and d^2 is the square of the Earth-Sun distance in astronomical units (~149.6 x 10^6 km) and is expressed as:

$$d = (1 - 0.01674 \text{ Cos } (0.9856 (JD-4)))$$

where JD is the Julian Day of the image acquisition.

Note: The unit for the argument of the cosine function of 0.9856 x (JD-4) will be in degrees.

E_{sun} is the mean solar exoatmospheric irradiance in W m^{-2} μm^{-1} and SZ is the sun zenith angle in radians at time of scene acquisition. E_{sun} values can be obtained from the Spot Image website.

Table: Solar equivalent irradiances for SPOT –1 (watt/sq m/micrometres)

Band	Bandwidth	HRV-1	HRV-2
P/M	0.50-0.73	1680	1690
XS1	0.50-0.59	1855	1845
XS2	0.61-0.68	1615	1575
XS3	0.79-0.89	1090	1040

The zenith angle (SZ) is calculated by subtracting the sun elevation from 90° .

Appendix E

Appendix E-1: Average slope of the Saltdean catchment from a 20 m PulSAR DEM

Slope group (%)	Area (%)
≤ 5	10.2
5-10	21.5
10-15	23.3
15-20	17.4
20-25	10.9
25-30	7.2
30-35	4.2
35-40	2.3
40-45	1.3
45-50	0.6
> 50	1.2
Average slope	17.23

Appendix E-2: Catchment area and cumulative rainfall calculations by two LISEM versions

20 m resampled DEM	Original resolution	Catchment area (ha)		Cumulative rainfall (mm)	
		Ver 2.03	Ver 2.158	Ver 2.03	Ver 2.158
PulSAR DEM	25 m	811.160	832.050	16.601	16.184
Cartometric DEM	20 m	811.160	823.728	16.601	16.348
Landmap DEM	25 m	811.160	829.694	16.601	16.230
SRTM DEM	75 m	811.160	822.634	16.601	16.370
ASTER DEM	30 m	811.160	825.033	16.601	16.322

Appendix E-3: Rainfall intensity breakpoint pair file of the storm with a standard structure

RUU CSF TIMESERIE INTENSITY NORMAL 1
Raingauge_station_1 (time in min and rainfall intensity in mm/h)

0	0
60	0.8
120	11.4
180	0.3
240	3.0
300	0.8
360	0.3
420	0
750	0

Appendix E-4: Import and export of key spatial data to and from PCRaster

Creating a clone map of the Saltdean catchment using a 'mapattr' operator

mapattr <filename.map>

The following raster and geographic attributes of the Saltdean catchment are required to create a clone map at a 20 m grid-cell size, for an example:

No. of rows	: 229
No. of columns	: 179
Data type	: Scalar
Cell representation	: Small integer
Projection	: Y increases from bottom to top
X_ULC	: 536112.9
Y_ULC	: 107974.0
Cell length	: 20.0
Angle (degree)	: 0.0
File_id	: 0

Set the clone map as a global map using --clone function.

Import the ArcInfo GRID ASCII format data of DEM, landuse, soils, and raingauge base maps using an asc2map operator

asc2map [options] <ArcInfo GRID ASCII file> <PCRaster output file>

For an example,
asc2map --clone <clonemap file> -<data type> -a <GRID ASCII filename>
<PCRaster output file>

Export of a PCRaster map to a GRID ASCII format, for an example:

Map2asc –m < null value> -a <input file> <output file>

Appendix E-5: PCRaster script for the creation of a LISEM database from key spatial data

```
#! -f --matrixtable --lddin

binding # binding section
                  # Catchment key maps of various grid cell sizes

 dem = saltdemp20.map;         # InSAR DEM derived from an ERS SAR pair
 landuse = saltlusep20.map;    # Land use map from SPOT Data
 soil = saltsoilp20.map;       # National Soil map (NATMAP)
 rgauge=rgauge.map             # Raingauge location map

      mask = mask.map;         # Mask for the catchment area


                        # Catchment input tables
   utable1 = salt_utable.txt; #     Crop and soil parameter table
   utable2 = infil_utable.txt; # Infiltration parameter table


            #     CROP AND SOIL PARAMETER BASE TABLE
            #     ----------------------------------
            #  1 Surface cover (fraction)
            #  2 Crop and vegetation height (m)
            #  3 LAI (m2/m2)
            #  4 RR (cm)
            #  5 Manning's roughness coefficient, n (-)
            #  6 Aggregate stability (number)
            #  7 Soil cohesion (kPa)
            #  8 Additional cohesion by plant roots (kPa)
            #  9 Soil median texture, D50( μm)
            # 10 Road width (m)
            # 11 Grass width (m)
            # 12 Crust cover (m)
            # 13 Compacted soil (m)
            # 14 Stoniness (m)

            # INFILTRATION PARAMETER BASE TABLE
            # ---------------------------------
            # 15 Saturated hydraulic conductivity, ksat1 (mm/h)
            # 16 Average moisture section head, psi1 (cm)
            # 17 Saturated moisture content, (Porosity1) (cm3/cm3)
            # 18 Initial moisture content1 (cm3/cm3)
            # 19 Soil depth1 (cm)

                  # Input constants

    Chanwidth = 1.5; # Channel width
    Chanside = 1; # 1 for 45 degree side slope channel

      # INPUT PARAMETER MAPS

            # Catchment parameters

    Ldd = ldd.map;          # Local drain direction
    area = area.map;        # Catchment area based on an outlet(boolean)
```

```
    area1 = area1.map;      # Catchment area based on an outlet
    grad = grad.map;        # Slope map
    outlet = outlet.map;    # Location of outlets in the catchment
    id = id.map;            # Rainfall intensity distribution map

                  # Landuse and vegetation parameters
    per=per.map;
    ch=ch.map;
    lai=lai.map;
    roadwidt = roadwidt.map;
    grasswid=grasswid.map;

                  # Soil surface parameters
    rr=rr.map;
    mann=n.map;
    crustfrc=crustfrc.map;
    compfrc=compfrc.map;
    stonefrc=stonefrc.map;

                  # Soil erosion parameters

    aggrstab = aggrstab.map;
    coh = coh.map;
    cohadd = cohadd.map;
    D50 = d50.map;

                  # Channel parameters

   chanmask= chanmask.map;
   lddchan = lddchan.map;
   chanwidt = chanwidt.map;
   chanside = chanside.map;
   changrad = changrad.map;
   chanman = chanman.map;
   chancoh = chancoh.map;

      # Soil infiltration parameters: a single layer Green-Ampt model

    ksat1=ksat1.map;
    psi1=psi1.map;
    thetas1=thetas1.map;
    thetai1=thetai1.map;
    soildep1=soildep1.map;

      # Additional parameters for second layer G-A model (NOT USED)
            #   ksat2=ksat2.map;
            #   psi2=psi2.map;
            #   thetas2=thetas2.map;
            #   thetai2=thetai2.map;
            #   soildep2=soildep2.map;


areamap     # Areamap section of the script

    mask;   # Area map must exist along with base maps
            # or declare any base map as areamap

initial     # Initial section of the script
```

```
      # GENERATION OF THE LISEM DATABASE

      # Catchment parameters
report Ldd = lddcreate(dem, 1e20,1e20,1e20,1e20);
report outlet = pit(Ldd);
report area1 = catchment(Ldd, outlet); # Area based on outlet
 report area = boolean(area1);
 report grad = max(0.001, sin(atan(slope(dem)))); # grad > 0.001
 report id = spreadzone (rgauge, 0, 1); # Thiessen polygon
  #report id = spreadzone (rgauge,0,slope(dem))# by geomorphology

      # Land use and vegetation parameters
 report per = lookupscalar(utable1, 1, landuse);
 report ch = lookupscalar(utable1, 2, landuse);
 report lai = lookupscalar(utable1, 3, landuse);
 report roadwidt = lookupscalar(utable1, 10, landuse);
 report grasswid = lookupscalar(utable1, 11, landuse);

      # Soil surface parameters
report rr = lookupscalar(utable1, 4, landuse);
report mann = lookupscalar(utable1, 5, landuse);
report crustfrc= lookupscalar(utable1, 12, landuse);
report  compfrc = lookupscalar(utable1, 13, landuse);
report stonefrc = lookupscalar(utable1, 14, landuse);


      # Soil erosion parameters
 report aggrstab = lookupscalar(utable1, 6, landuse);
 report coh  = lookupscalar(utable1, 7, landuse);
 report cohadd  = lookupscalar(utable1, 8, landuse);
 report D50 = lookupscalar(utable1, 9, landuse);

      # Channel parameters
 report  chanmask =scalar(if(accuflux(Ldd,cellarea())gt  680000,1));
 report lddchan =lddcreate((dem*chanmask),1e20,1e20,1e20,1e20);
 report chanwidt = scalar( if (chanmask ne 0, Chanwidth));
 report chanside = scalar( if (chanmask ne 0, Chanside));
 report changrad =(grad*chanmask);
 report chancoh= ((coh + cohadd)*chanmask);
 report chanman= (mann*chanmask);

                  # option  chancoh=chanmask*scalar(Chancoh);
                  # option  chanman=chanmask*scalar(Chanman);

      # Parameters for a single layer GREEN and AMPT model
report ksat1 =   lookupscalar(utable2, 15, soil);
report psi1 =    lookupscalar(utable2, 16, soil);
report thetas1 =   lookupscalar(utable2, 17, soil);
report thetai1 = lookupscalar(utable2, 18, soil);
report soildep1 = lookupscalar(utable2, 19, soil);

# END
```

Appendix E-6: Batch file script for displaying a LISEM database

```
:: Batch file script for displaying a LISEM input parameter database
:: saltinput.bat <File name>
CLS
@echo off
echo          'LISEM DATABASE of the SALTDEAN CATCHMENT'
echo.
echo          Displaying LISEM input parameter maps, category wise
echo.
echo          RAINFALL Parameters: 2
echo.
echo            Rain intensity file, Raingage location and Rainzone map
echo.
echo Press any key to display:
pause > nul
echo          "Please close all map display to go next category"
echo.
     display id.map rgauge.map
pause > nul
echo.
echo          CATCHMENT Parameters : 4
echo.
echo            Catchment area, Gradient, LDD and Outlet
echo.
echo Press any key to display:
pause > nul
echo          "Please close all map display to go next category"
echo.
     display outlet.map ldd.map grad.map area.map
pause > nul
@echo off
echo.
echo          LAND USE AND VEGETATION Parameters: 5
echo.
echo            Surface cover, Plant height, LAI, Roadwidth and Grassstrip width
echo.
echo Press any key to display:
pause > nul
echo          "Please close all map display to display next category"
echo.
     display grasswid.map roadwidt.map lai.map ch.map per.map
pause > nul
@echo off
echo.
echo          SOIL SURFACE Parameters: 5
echo.
echo          Random roughness, Manning's roughness, crusted, compacted and stoniness
echo.
echo Press any key to display:
echo.
pause > nul
```

```
echo.
echo          "Please close all map display to go next category"
echo.
     display stonefrc.map compfrc.map crustfrc.map n.map  rr.map
pause > nul
@echo off
echo.
echo          SOIL EROSION Parameters: 4
echo.
echo          Aggregate stability, Cohesion, Additional cohesion and Median texture
echo.
echo Press any key to display:
pause > nul
echo          "Please close all map display to go next category"
echo.
     display d50.map cohadd.map coh.map aggrstab.map
Pause > nul
@echo off
echo.
echo          CHANNEL Parameters: 6
echo.
echo   LDD, width, Cross-section, Gradient, Manning's N and Cohesion of Main Channel
echo.
echo Press any key to display:
pause > nul
echo          "Please close all map display to go next category"
echo.
     display chancoh.map chanman.map changrad.map chanside.map chanwidt.map
lddchan.map
pause > nul
@echo off
echo.
echo          INFILTRATION Parameters – a single layer Green and Ampt Model: 5
echo.
echo  Saturated K, Front suction head, Initial and saturated moisture and soil depth
echo.
echo Press any key to display:
echo.
pause > nul
echo.
echo          "Please close all map display to EXIT"
echo.
     display soildep1.map thetas1.map thetai1.map psi1.map  ksat1.map
pause > nul
echo.
echo          'Ends'
echo.
```

Appendix E-7: Effect of resolution on the catchment area

DEM	Original resolution	Catchment area (hectares)				
		Grid-cell size (m)				
		20	40	60	80	100
PulSAR DEM	25 m	811.16	828.00	845.28	863.36	883.00
		(---)	(2.08)	(4.21)	(6.44)	(8.86)
Cartometric DEM	20 m	811.16	828.16	845.28	863.36	882.00
		(---)	(2.10)	(4.21)	(6.44)	(8.73)
Landmap DEM	25 m	811.16	828.32	845.28	863.36	885.00
		(---)	(2.12)	(4.21)	(6.44)	(9.10)
SRTM DEM	75 m	811.16	828.32	845.28	863.36	885.00
		(---)	(2.12)	(4.21)	(6.44)	(9.10)
ASTER DEM	30 m	811.16	828.32	845.28	862.08	885.00
		(---)	(2.12)	(4.21)	(6.28)	(9.10)

(Data in parenthesis show the change in catchment area in per cent)

Appendix E-8: Statistical properties of slope gradient maps of the Saltdean catchment

DEM	Minimum	Maximum	Mean	S. D.	Median	Mode
PulSAR DEM, 20 m	0.001	0.9203	0.1726	0.1170	0.1446	0.1051
Landmap DEM, 20 m	0.001	0.8992	0.1629	0.1109	0.1343	0.0782
Cartometric DEM 20 m	0.001	0.7663	0.1510	0.0811	0.1445	0.0010
SRTM DEM, 20 m	0.001	0.4797	0.1436	0.0803	0.1300	0.1057
ASTER DEM, 20 m	0.001	0.6772	0.1471	0.1007	0.1278	0.1093

Appendix E-9: Statistical properties of slope gradients of resampled PulSAR DEMs

DEM source	Minimum	Maximum	Mean	S. D.	Median	Mode
PulSAR DEM						
20 m	0.0010	0.9203	0.1726	0.1170	0.1446	0.1051
40 m	0.0044	0.5275	0.1492	0.0824	0.1332	0.1168
60 m	0.0010	0.4282	0.1397	0.0744	0.1279	0.0761
80 m	0.0044	0.3559	0.1312	0.0707	0.1211	0.0923
100 m	0.0023	0.3241	0.1236	0.0645	0.1141	0.1217

Appendix E-10: Drainage and channel lengths of five resampled PulSAR DEMs

DEM Parameter	Grid-cell size (m)				
	20	40	60	80	100
Drainage length (km)	479.790	244.773	165.919	126.796	101.226
Change (per cent)	Ref	-48.98	-65.42	-73.57	-78.90
Channel length (km)	7.125	6.913	6.835	6.368	6.170
Change (per cent)	Ref	-2.98	-4.08	-10.63	-13.41

Appendix E-11: Effect of resolution on interception at three AMCs

DEM	AMC	Interception (per cent)				
		Grid-cell size (m)				
		20	40	60	80	100
PulSAR DEM	High	3.72	3.69 (-0.03)	3.73 (0.01)	3.73 (0.02)	3.74 (0.02)
Landmap DEM	,,	3.72	3.70 (-0.02)	3.73 (0.02)	(3.74) (0.02)	(3.74) (0.02)
Cartometric DEM	,,	3.71	3.69 (-0.02)	3.73 (0.02)	3.73 (0.03)	3.74 (0.03)
SRTM DEM	,,	3.71	3.69 (-0.01)	3.73 (0.02)	3.73 (0.03)	3.73 (0.03)
ASTER DEM	,,	3.71	3.69 (-0.02)	3.73 (0.02)	3.73 (0.02)	3.73 (0.02)
PulSAR DEM	Medium	3.72	3.69 (-0.03)	3.73 (0.01)	3.74 (0.01)	3.74 (0.02)
Landmap DEM	,,	3.72	3.70 (-0.02)	3.73 (0.02)	3.74 (0.02)	3.74 (0.02)
Cartometric DEM	,,	3.71	3.69 (-0.02)	3.73 (0.02)	3.74 (0.03)	3.74 (0.03)
SRTM DEM	,,	3.71	3.69 (-0.01)	3.73 (0.02)	3.74 (0.03)	3.73 (0.03)
ASTER DEM	,,	3.71	3.69 (-0.02)	3.73 (0.02)	3.73 (0.02)	3.73 (0.02)
PulSAR DEM	Low	3.72	3.69 (-0.03)	3.73 (0.01)	3.74 (0.01)	3.74 (0.02)
Landmap DEM	,,	3.72	3.70 (-0.02)	3.73 (0.02)	3.74 (0.02)	3.74 (0.02)
Cartometric DEM	,,	3.71	3.69 (-0.02)	3.73 (0.02)	3.74 (0.03)	3.74 (0.03)
SRTM DEM	,,	3.71	3.69 (-0.01)	3.73 (0.02)	3.74 (0.03)	3.73 (0.03)
ASTER DEM	,,	3.71	3.69 (-0.02)	3.73 (0.02)	3.73 (0.02)	3.73 (0.02)

(AMC stands for antecedent soil moisture condition; Figures in parentheses show the difference in per cent with respect to the 20 m grid-cell size)

Appendix E-12: Effect of resolution on runoff coefficient at three AMCs

DEM	AMC	Runoff coefficient (per cent)				
		Grid-cell size (m)				
		20	40	60	80	100
PulSAR DEM	High	33.12	30.09 (-3.03)	26.97 (-6.15)	25.36 (-7.76)	23.80 (-9.33)
Landmap DEM	,,	32.82	29.71 (-3.11)	27.25 (-5.57)	25.60 (-7.22)	24.21 (-8.61)
ASTER DEM	,,	31.97	29.27 (-2.69)	27.03 (-4.93)	25.84 (-6.12)	23.60 (-8.36)
Cartometric DEM	,,	31.09	28.52 (-2.57)	26.94 (-4.15)	25.62 (-5.47)	23.90 (-7.19)
SRTM DEM	,,	28.59	28.77 (0.18)	26.64 (-1.95)	25.28 (-3.31)	23.92 (-4.67)
Difference among DEMs		4.53	1.57	0.61	0.56	0.61
PulSAR DEM	Medium	4.95	3.55 (-1.40)	2.64 (-2.31)	2.07 (-2.86)	1.98 (-2.97)
Landmap DEM	,,	4.88	3.33 (-1.55)	2.41 (-2.47)	1.98 (-2.90)	1.85 (-3.03)
ASTER DEM	,,	4.34	2.98 (-1.36)	2.39 (-1.94)	1.96 (-2.38)	1.66 (-2.68)
Cartometric DEM	,,	4.11	2.85 (-1.26)	2.23 (-1.89)	1.86 (-2.25)	1.60 (-2.51)
SRTM DEM	,,	4.07	2.78 (-1.30)	2.13 (-1.94)	1.78 (-2.29)	1.58 (-2.49)
Difference among DEMs		0.88	0.77	0.51	0.29	0.40
Landmap DEM	Low	0.50	0.35 (-0.16)	0.29 (-0.21)	0.25 (-0.26)	0.26 (-0.24)
PulSAR DEM	,,	0.49	0.42 (-0.06)	0.31 (-0.18)	0.24 (-0.24)	0.29 (-0.20)
ASTER DEM	,,	0.40	0.28 (-0.12)	0.27 (-0.14)	0.25 (-0.15)	0.23 (-0.17)
Cartometric DEM	,,	0.35	0.28 (-0.07)	0.25 (-0.10)	0.24 (-0.12)	0.22 (-0.13)
SRTM DEM	,,	0.31	0.24 (-0.07)	0.23 (-0.08)	0.20 (-0.11)	0.20 (-0.11)
Difference among DEMs		0.19	0.18	0.08	0.05	0.09

(Figures in parentheses show the difference in per cent with respect to the 20 m grid-cell size)

Appendix E-13: Effect of resolution on normalised peak discharge at three AMCs

DEM	AMC	Normalised peak discharge (m^3/s) Grid-cell size (m)				
		20	40	60	80	100
Cartometric DEM	High	6.449	5.968 (-7.45)	5.237 (-18.80)	4.566 (-29.20)	3.967 (-38.48)
Landmap DEM	,,	6.342	5.434 (-14.32)	4.774 (-24.72)	4.499 (-29.07)	4.362 (-31.22)
PulSAR DEM	,,	6.102	5.445 (-10.76)	4.913 (-19.48)	4.501 (-26.23)	3.790 (-37.89)
SRTM DEM	,,	5.291	5.208 (-1.56)	4.185 (-20.91)	4.367 (-17.47)	3.989 (-24.61)
ASTER DEM	,,	5.111	5.255 (2.81)	4.597 (-10.05)	4.305 (-15.78)	3.469 (-32.13)
Difference among DEMs		1.338	0.76	1.052	0.261	0.893
Landmap DEM	Medium	0.694	0.452 (-34.79)	0.318 (-54.13)	0.274 (-60.46)	0.269 (-61.23)
PulSAR DEM	,,	0.659	0.476 (-27.78)	0.346 (-47.42)	0.273 (-58.49)	0.223 (-66.20)
Cartometric DEM	,,	0.567	0.455 (-19.85)	0.329 (-41.96)	0.253 (-55.49)	0.212 (-62.58)
SRTM DEM	,,	0.489	0.342 (-30.08)	0.221 (-54.67)	0.222 (-54.53)	0.186 (-61.92)
ASTER DEM	,,	0.440	0.363 (-17.41)	0.263 (-40.25)	0.230 (-47.63)	0.200 (-54.44)
Difference among DEMs		0.254	0.134	0.125	0.052	0.083
Landmap DEM	Low	0.073	0.029 (-60.98)	0.029 (-60.00)	0.015 (-79.20)	0.038 (-47.63)
ASTER DEM	,,	0.047	0.053 (13.71)	0.041 (-11.79)	0.036 (-23.13)	0.028 (-41.36)
PulSAR DEM	,,	0.037	0.029 (-21.87)	0.024 (-36.24)	0.015 (-59.72)	0.022 (-40.25)
Cartometric DEM	,,	0.030	0.027 (-9.10)	0.018 (-40.90)	0.016 (-46.07)	0.014 (-52.02)
SRTM DEM	,,	0.026	0.017 (-33.67)	0.019 (-24.42)	0.010 (-59.46)	0.019 (-24.30)
Difference among DEMs		0.047	0.036	0.023	0.026	0.024

(Figures in parentheses show the change in per cent with respect to the 20 m grid-cell size)

Appendix E-14: Effect of resolution on time to peak runoff at three AMCs

DEM	AMC	Time to peak runoff (min)				
		Grid-cell size (m)				
		20	40	60	80	100
Cartometric DEM	High	215	190 (-11.63)	185.5 (-13.72)	189 (-12.09)	188 (-12.56)
ASTER DEM	,,	212.5	195 (-8.24)	195.5 (-8.00)	192.5 (-9.41)	192.5 (-9.41)
SRTM DEM	,,	202.5	202 (-0.25)	201.5 (-0.49)	195 (-3.70)	197 (-2.72)
PulSAR DEM	,,	194.5	194 (-0.26)	193 (-0.77)	193.5 (-0.51)	195.5 (0.51)
Landmap DEM	,,	179	184 (2.79)	184.5 (3.07)	188.5 (5.31)	181.5 (1.40)
Difference among DEMs		36	18	17	6.5	15.5
ASTER DEM	Medium	294.5	254.5 (-13.58)	264 (-10.36)	255.5 (-13.24)	135 (-54.16)
Cartometric DEM	,,	291.5	244.5 (-16.12)	242.5 (-16.81)	249.5 (-14.41)	248.5 (-14.75)
SRTM DEM	,,	267.5	270.5 (1.12)	275 (2.80)	263 (-1.68)	260.5 (-2.62)
PulSAR DEM	,,	247.5	253.5 (2.42)	261 (5.45)	259.5 (4.85)	260.5 (5.25)
Landmap DEM	,,	229	240 (4.80)	247 (7.86)	248.5 (8.52)	236 (3.06)
Difference among DEMs		65.5	30.5	32.5	14.5	125.5
Cartometric DEM	Low	467	367.5 (-21.31)	373 (-20.13)	385.5 (-17.45)	387 (-17.13)
PulSAR DEM	,,	371	378 (1.89)	207.5 (-44.07)	172 (-53.64)	231 (-37.74)
SRTM DEM	,,	169	169 (0.00)	160 (-5.33)	441.5 (161.24)	120 (-28.99)
ASTER DEM	,,	151	139.5 (-7.62)	141.5 (-6.29)	142 (-5.96)	140.5 (-6.95)
Landmap DEM	,,	126.5	156.5 (23.72)	152 (20.16)	391 (209.09)	120 (-5.14)
Difference among DEMs		340.5	228	231.5	142	267

(Figures in parentheses show the change in per cent with respect to the 20 m grid-cell size)

Appendix E-15: Effect of resolution on normalised splash detachment at three AMCs

DEM	AMC	Normalised splash detachment (Mg) Grid-cell size (m) 20	40	60	80	100
Cartometric DEM	High	119.125	122.807 (3.09)	123.122 (3.36)	125.503 (5.35)	126.743 (6.40)
ASTER DEM	,,	117.409	121.483 (3.47)	121.689 (3.65)	124.582 (6.11)	126.053 (7.36)
Landmap DEM	,,	117.361	121.855 (3.83)	122.800 (4.63)	125.645 (7.06)	127.116 (8.31)
PulSAR DEM	,,	116.471	120.580 (3.53)	121.468 (4.29)	124.018 (6.48)	125.141 (7.44)
SRTM DEM	,,	112.389	123.317 (9.72)	123.850 (10.20)	126.531 (12.58)	127.311 (13.28)
Difference among DEMs		6.736	2.737	2.382	2.513	2.17
SRTM DEM	Medium	81.284	82.455 (1.44)	81.387 (0.13)	81.582 (0.37)	81.517 (0.29)
Cartometric DEM	,,	81.192	82.512 (1.63)	81.618 (0.52)	81.927 (0.91)	81.292 (0.12)
ASTER DEM	,,	80.212	81.992 (2.22)	81.039 (1.03)	81.848 (2.04)	81.459 (1.56)
Landmap DEM	,,	80.206	81.954 (2.18)	81.570 (1.70)	81.850 (2.05)	81.171 (1.20)
PulSAR DEM	,,	79.759	81.463 (2.14)	80.930 (1.47)	81.183 (1.79)	80.633 (1.10)
Difference among DEMs		1.525	1.049	0.688	0.744	0.884
SRTM DEM	Low	61.430	62.052 (1.01)	61.153 (-0.45)	61.386 (-0.07)	61.229 (-0.33)
Cartometric DEM	,,	61.204	61.852 (1.06)	61.205 (0.00)	61.477 (0.45)	61.161 (-0.07)
Landmap DEM	,,	60.493	61.410 (1.52)	60.941 (0.74)	61.280 (1.30)	61.171 (1.12)
ASTER DEM	,,	60.359	61.408 (1.74)	60.844 (0.80)	61.406 (1.73)	61.176 (1.35)
PulSAR DEM	,,	60.076	60.943 (1.44)	60.555 (0.80)	60.862 (1.31)	60.665 (0.98)
Difference among DEMs		1.354	1.109	0.650	0.615	0.564

(Figures in parentheses show the change in per cent with respect to the 20 m grid-cell size)

Appendix E-16: Effect of resolution on normalised flow detachment at three AMCs

DEM	AMC	Normalised flow detachment (Mg)				
		Grid-cell size (m)				
		20	40	60	80	100
PulSAR DEM	High	42001.264	30247.442 (-27.98)	22150.606 (-47.26)	15561.842 (-62.95)	11528.069 (-72.55)
Landmap DEM	,,	39851.768	30231.437 (-24.14)	21196.235 (-46.81)	15906.520 (-60.09)	11338.827 (-71.55)
ASTER DEM	,,	37363.024	27643.116 (-26.01)	18222.833 (-51.23)	13508.976 (-63.84)	10081.267 (-73.02)
Cartometric DEM	,,	31404.470	26027.796 (-17.12)	19265.641 (-38.65)	14431.306 (-54.05)	9936.003 (-68.36)
SRTM DEM	,,	25698.914	23624.346 (-8.07)	18017.304 (-29.89)	13852.430 (-46.10)	10567.706 (-58.88)
Difference among DEMs		16302.35	6623.096	4133.302	2052.866	1592.066
PulSAR DEM	Medium	7545.203	3267.885 (-56.69)	1851.418 (-75.46)	1195.320 (-84.16)	823.266 (-89.09)
Landmap DEM	,,	7145.711	3373.476 (-52.79)	1745.970 (-75.57)	1129.827 (-84.19)	736.001 (-89.70)
ASTER DEM	,,	5946.397	2807.571 (-52.79)	1569.753 (-73.60)	1030.673 (-82.67)	655.077 (-88.98)
Cartometric DEM	,,	5581.460	2710.237 (-51.44)	1451.088 (-74.00)	931.674 (-83.31)	635.513 (-88.61)
SRTM DEM	,,	4824.312	2275.671 (-52.83)	1438.819 (-70.18)	953.709 (-80.23)	658.102 (-86.36)
Difference among DEMs		2720.892	1097.805	412.599	263.646	187.753
PulSAR DEM	Low	959.916	519.898 (-45.84)	296.176 (-69.15)	195.284 (-79.66)	134.575 (-85.98)
Landmap DEM	,,	931.430	412.917 (-55.67)	214.958 (-76.92)	136.064 (-85.39)	90.578 (-90.28)
ASTER DEM	,,	833.414	413.007 (-50.44)	240.587 (-71.13)	144.623 (-82.65)	90.643 (-89.12)
Cartometric DEM	,,	654.937	318.164 (-51.42)	167.548 (-74.42)	112.130 (-82.88)	83.113 (-87.31)
SRTM DEM	,,	597.433	293.123 (-50.94)	198.121 (-66.84)	127.876 (-78.60)	85.654 (-85.66)
Difference among DEMs		362.483	226.775	128.628	83.154	51.462

(Figures in parentheses show the change in per cent with respect to the 20 m grid-cell size)

Appendix E-17: Effect of resolution on normalised overland deposition at three AMCs

DEM	AMC	Normalised overland deposition (Mg)				
		Grid-cell size (m)				
		20	40	60	80	100
PulSAR DEM	High	-38327.648	-28593.434 (-25.40)	-21397.294 (-44.17)	-15238.761 (-60.24)	-11866.728 (-69.04)
Landmap DEM	,,	-35592.952	-28239.470 (-20.66)	-20348.227 (-42.83)	-15352.750 (-56.87)	-11071.471 (-68.89)
ASTER DEM	,,	-34871.256	-26339.577 (-24.47)	-17733.672 (-49.15)	-13142.296 (-62.31)	-10028.699 (-71.24)
Cartometric DEM	,,	-28282.208	-24768.797 (-12.42)	-18528.501 (-34.49)	-14122.568 (-50.07)	-9918.505 (-64.93)
SRTM DEM	,,	-24107.662	-22741.101 (-5.67)	-17605.516 (-26.97)	-13785.367 (-42.82)	-10538.473 (-56.29)
Difference among DEMs		14219.986	5852.333	3791.778	2210.454	1948.223
PulSAR DEM	Medium	-7489.385	-3323.337 (-55.63)	-1920.646 (-74.36)	-1275.366 (-82.97)	-911.717 (-87.83)
Landmap DEM	,,	-7039.188	-3421.308 (-51.40)	-1810.916 (-74.27)	-1205.871 (-82.87)	-810.363 (-88.49)
ASTER DEM	,,	-5965.761	-2878.433 (-51.75)	-1648.505 (-72.37)	-1110.573 (-81.38)	-734.833 (-87.68)
Cartometric DEM	,,	-5569.643	-2786.028 (-49.98)	-1530.040 (-72.53)	-1012.099 (-81.83)	-715.469 (-87.15)
SRTM DEM	,,	-4857.588	-2355.373 (-51.51)	-1518.534 (-68.74)	-1034.438 (-78.70)	-739.335 (-84.78)
Difference among DEMs		2631.797	1065.935	402.112	263.267	196.248
PulSAR DEM	Low	-1019.059	-580.699 (-43.02)	-356.661 (-65.00)	-256.107 (-74.87)	-195.336 (-80.83)
Landmap DEM	,,	-988.142	-472.243 (-52.21)	-274.703 (-72.20)	-197.137 (-80.05)	-151.065 (-84.71)
ASTER DEM	,,	-893.082	-474.115 (-46.91)	-301.362 (-66.26)	-205.914 (-76.94)	-151.697 (-83.01)
Cartometric DEM	,,	-715.815	-379.765 (-46.95)	-228.685 (-68.05)	-173.533 (-75.76)	-144.218 (-79.85)
SRTM DEM	,,	-658.823	-355.083 (-46.10)	-259.228 (-60.65)	-189.243 (-71.28)	-146.866 (-77.71)
Difference among DEMs		360.236	225.616	127.976	82.574	51.118

(Figures in parentheses show the change in per cent with respect to the 20 m grid-cell size)

Appendix E-18: Effect of resolution on normalised channel erosion at three AMCs

DEM	AMC	Normalised channel erosion (Mg)				
		Grid-cell size (m)				
		20	40	60	80	100
PulSAR DEM	High	9638.816	9344.245 (-3.06)	8316.964 (-13.71)	7641.308 (-20.72)	7828.750 (-18.78)
Landmap DEM	,,	9059.666	8013.812 (-11.54)	8532.064 (-5.82)	8202.614 (-9.46)	8432.342 (-6.92)
ASTER DEM	,,	9030.044	10381.601 (14.97)	8411.287 (-6.85)	9619.488 (6.53)	8615.111 (-4.60)
Cartometric DEM	,,	8106.593	8132.194 (0.32)	9042.363 (11.540	8549.292 (5.46)	6820.302 (-15.87)
SRTM DEM	,,	5361.450	5739.583 (7.05)	5986.773 (11.66)	5397.459 (0.67)	6675.768 (24.51)
Difference among DEMs		4277.366	3604.662	3055.59	4222.029	1939.343
ASTER DEM	Medium	4399.530	3383.696 (-23.09)	2639.633 (-40.00)	2046.999 (-53.47)	1607.942 (-63.45)
Landmap DEM	,,	4162.578	2776.681 (-33.29)	2086.501 (-49.870	1756.337 (-57.81)	1542.895 (-62.93)
PulSAR DEM	,,	4149.039	3016.276 (-27.30)	2189.494 (-47.23)	1848.603 (-55.45)	1624.295 (-60.85)
Cartometric DEM	,,	3245.540	2463.648 (-24.09)	2265.683 (-30.19)	1798.879 (-44.57)	1153.458 (-64.46)
SRTM DEM	,,	1982.995	1719.928 (-13.27)	1545.538 (-22.06)	1231.326 (-37.91)	1314.264 (-33.72)
Difference among DEMs		2416.535	1663.768	1094.095	815.673	470.837
Landmap DEM	Low	1705.983	862.937 (-49.42)	688.558 (-59.64)	533.512 (-68.73)	524.210 (-69.27)
ASTER DEM	,,	1695.106	1024.196 (-39.58)	738.944 (-56.41)	524.848 (-69.04)	383.045 (-77.40)
PulSAR DEM	,,	1639.451	1144.091 (-30.22)	721.545 (-55.99)	505.374 (-69.17)	427.234 (-73.94)
Cartometric DEM	,,	1005.345	687.894 (-31.58)	673.844 (-32.97)	510.993 (-49.170	299.064 (-70.25)
SRTM DEM	,,	529.312	333.947 (-36.91)	287.708 (-45.64)	246.155 (-53.50)	291.112 (-45.00)
Difference among DEMs		1176.671	810.144	451.236	287.357	233.098

(Figures in parentheses show the change in per cent with respect to the 20 m grid-cell size)

Appendix E-19: Effect of resolution on normalised channel deposition at three AMCs

DEM	AMC	Normalised channel deposition (Mg)				
		Grid-cell size (m)				
		20	40	60	80	100
ASTER DEM	High	-11637.144	-4719.526 (-59.44)	-6961.645 (-40.18)	-2693.871 (-76.85)	-1835.919 (-84.22)
Cartometric DEM	,,	-6828.500	-2951.779 (-56.77)	-2579.134 (-62.23)	-2719.245 (-60.18)	-1684.690 (-75.33)
Landmap DEM	,,	-5727.808	-4022.667 (-29.77)	-2967.062 (-48.20)	-2959.543 (-48.33)	-2385.503 (-58.35)
PulSAR DEM	,,	-5679.579	-3817.189 (-32.79)	-3085.495 (-45.67)	-2776.797 (-51.11)	-2210.532 (-61.08)
SRTM DEM	,,	-2376.189	-2366.588 (-0.40)	-2838.898 (19.47)	-5590.101 (135.25)	-2156.543 (-9.24)
Difference among DEMs		9260.955	2352.938	4382.511	2896.230	700.813
ASTER DEM	Medium	-4460.159	-2974.409 (-33.31)	-2641.825 (-40.77)	-1595.928 (-64.22)	-1159.487 (-74.00)
Landmap DEM	,,	-3500.606	-2394.296 (-31.60)	-1696.811 (-51.53)	-1485.465 (-57.57)	-1223.856 (-65.04)
PulSAR DEM	,,	-3447.102	-2393.445 (-30.57)	-1695.391 (-50.82)	-1609.988 (-53.29)	-1312.636 (-61.92)
Cartometric DEM	,,	-3007.780	-1969.977 (-34.50)	-1804.438 (-40.01)	-1501.277 (-50.09)	-888.364 (-70.46)
SRTM DEM	,,	-1550.888	-1472.718 (-5.04)	-1443.130 (-6.95)	-1232.170 (-20.55)	-1118.422 (-27.89)
Difference among DEMs		2909.271	1501.691	1198.695	377.818	424.272
ASTER DEM	Low	-1695.673	-1019.621 (-39.87)	-738.994 (-56.42)	-506.017 (-70.16)	-364.398 (-78.51)
Landmap DEM	,,	-1654.539	-858.583 (-48.11)	-678.924 (-58.97)	-529.828 (-67.98)	-518.484 (-68.66)
PulSAR DEM	,,	-1604.198	-1125.604 (-29.83)	-706.112 (-55.98)	-505.411 (-68.49)	-423.114 (-73.62)
Cartometric DEM	,,	-981.104	-678.426 (-30.85)	-659.540 (-32.78)	-504.758 (-48.55)	-291.383 (-70.30)
SRTM DEM	,,	-528.950	-331.267 (-37.37)	-287.752 (-45.60)	-246.174 (-53.46)	-290.129 (-45.15)
Difference among DEMs		1166.723	794.337	451.242	283.654	228.355

(Figures in parentheses show the change in per cent with respect to the 20 m grid-cell size)

Appendix E-20: Effect of resolution on normalised total soil loss at three AMCs

DEM	AMC	Normalised total soil loss (Mg)				
		Grid-cell size (m)				
		20	40	60	80	100
PulSAR DEM	High	7749.263	7301.612 (-5.78)	6106.285 (-21.20)	5311.592 (-31.46)	5880.795 (-24.11)
Landmap DEM	,,	7707.784	6104.882 (-20.80)	6535.760 (-15.21)	5922.495 (-23.16)	6441.269 (-16.43)
SRTM DEM	,,	4688.708	4379.470 (-6.60)	3683.526 (-21.44)	0.946 (-99.98)	4675.758 (-0.28)
Cartometric DEM	,,	4519.401	6562.149 (45.20)	7323.413 (62.04)	6264.297 (38.61)	5279.830 (16.83)
ASTER DEM	,,	1.382	7086.981 Too large	2060.395 Too large	7416.837 Too large	6957.762 Too large
Difference among DEMs		3229.862	2922.142	4475.365	2105.245	2282.004
Landmap DEM	Medium	848.622	416.481 (-50.92)	406.302 (-52.12)	276.680 (-67.40)	325.847 (-61.60)
PulSAR DEM	,,	837.400	648.832 (-22.52)	505.793 (-39.60)	239.749 (-71.37)	314.811 (-62.41)
SRTM DEM	,,	480.080	249.954 (-47.93)	104.073 (-78.32)	0.008 (-100.00)	196.128 (-59.15)
Cartometric DEM	,,	330.683	500.372 (51.31)	463.896 (40.28)	299.101 (-9.55)	266.429 (-19.43)
ASTER DEM	,,	0.012	420.360 Too large	0.064 419.70	453.014 Too large	450.158 Too large
Difference among DEMs		517.939	398.878	401.720	213.265	254.030
Landmap DEM	Low	55.211	6.436 (-88.34)	10.825 (-80.39)	3.891 (-92.95)	6.409 (-88.39)
PulSAR DEM	,,	36.158	18.623 (-48.50)	15.498 (-57.14)	0.000 (-100.00)	4.372 (-87.91)
Cartometric DEM	,,	24.529	9.714 (-60.40)	14.366 (-41.43)	6.308 (-74.28)	7.739 (-68.45)
SRTM DEM	,,	0.395	2.771 (602.16)	0.000 (-99.98)	0.000 (-99.99)	1.000 (153.29)
ASTER DEM	,,	0.000	4.844 Too large	0.001 599.29	18.942 Too large	18.768 Too large
Difference among DEMs		30.682	15.852	4.673	15.051	14.396

(Figures in parentheses show the change in per cent with respect to the 20 m grid-cell size)

Appendix E-21: Effect of resolution on average soil loss at three AMCs

DEM	AMC	Average soil loss (kg/ha) Grid-cell size (m) 20	40	60	80	100
PulSAR DEM	High	9553.31	9005.33 (-5.74)	7541.19 (-21.06)	6575.37 (-31.17)	7307.17 (-23.51)
Landmap DEM	,,	9502.17	7529.48 (-20.76)	8071.58 (-15.06)	7331.63 (-22.84)	8007.16 (-15.73)
SRTM DEM	,,	5780.25	5401.44 (-6.55)	4549.11 (-21.30)	1.17 (-99.98)	5812.45 (0.56)
Cartometric DEM	,,	5571.53	8093.39 (45.26)	9044.32 (62.33)	7754.75 (39.19)	6559.01 (17.72)
ASTER DEM	,,	1.70	8740.76 Too large	2544.56 Too large	9179.67 Too large	8649.22 Too large
Difference among DEMs		3981.78	3603.89	6499.76	2604.30	2836.70
Landmap DEM	Medium	1032.35	800.23 (-22.48)	624.65 (-39.49)	296.79 (-71.25)	391.17 (-62.11)
PulSAR DEM	,,	1046.18	513.67 (-50.90)	501.78 (-52.04)	342.51 (-67.26)	405.06 (-61.28)
SRTM DEM	,,	591.84	308.28 (-47.91)	128.53 (-78.28)	0.01 (-100.00)	243.81 (-58.81)
Cartometric DEM	,,	407.67	617.13 (51.38)	572.91 (40.53)	370.27 (-9.17)	330.98 (-18.81)
ASTER DEM	,,	0.02	518.45 Too large	0.08 420.66	560.69 Too large	559.59 Too large
Difference among DEMs		624.68	491.95	496.12	263.90	315.78
Landmap DEM	Low	68.06	7.94 (-88.34)	13.37 (-80.36)	4.82 (-92.92)	7.97 (-88.29)
PulSAR DEM	,,	44.58	22.97 (-48.47)	19.14 (-57.06)	0.00 (-100.00)	5.43 (-87.81)
Cartometric DEM	,,	30.24	11.98 (-60.38)	17.74 (-41.33)	7.81 (-74.18)	9.61 (-68.21)
SRTM DEM	,,	0.49	3.42 (602.49)	0.00 (-99.98)	0.00 (-99.99)	1.24 (155.42)
ASTER DEM	,,	0.00	5.97 Too large	0.00 616.67	23.44 Too large	23.33 Too large
Difference among DEMs		35.82	19.55	5.77	18.62	22.09

(Figures in parentheses show the change in per cent with respect to the 20 m grid-cell size)

Appendix E-22: Effect on resolution on distribution of soil erosion in the catchment

Erosion class (Mg)	Area under each class (per cent)				
	Grid-cell size (m)				
	20	40	60	80	100
< 1	86.21	74.90	71.08	71.39	72.25
1-5	0.00	8.73	15.63	18.31	19.03
5-10	0.00	4.91	6.30	4.08	3.62
10-15	5.73	3.81	1.02	1.48	1.13
15-20	0.00	1.06	1.49	1.19	0.79
20-25	1.99	1.53	0.85	0.82	0.57
25-50	2.20	1.97	1.66	1.19	1.13
>50	3.86	3.09	1.96	1.56	1.47

Appendix E-23: Effects of resolution on peak time and peak discharge of hydrograph and sedigraph

Resolution	Hydrograph			
	First peak		Second peak	
	Time (min)	Discharge (m3/s)	Time	Discharge
20	162.5	0.4559	243.5	0.6745
40	171.5	0.4333	253.5	0.4858
60	168.0	0.2856	261.0	0.3615
80	166.5	0.2356	256.5	0.3283
100	172.0	0.1787	260.5	0.2417
	Sedigraph			
20	193.5	48.128	244	115.065
40	174.5	42.578	251.5	84.955
60	169.0	38.482	261.5	64.734
80	167.0	24.464	256.5	37.879
100	173.5	26.683	258.0	39.440

Appendix E-24: Model sensitivity to slope gradient with the 20 m PulSAR DEM dataset at medium AMC

Process	Change in output variable (per cent)				
	Decrease in slope gradient (per cent)				
	0	-25	-50	-75	-90
Infiltration	(15.16)	0.61	1.63	3.20	4.49
Time to peak runoff	(247.5)	2.22	6.67	18.59	38.38
Splash detachment	(79.759)	2.26	3.99	5.35	6.11
Runoff coefficient	(4.95)	-10.96	-29.52	-58.23	-81.85
Peak discharge	(6.587)	-12.53	-34.99	-66.41	-89.73
Overland flow detachment	(7545.203)	-34.64	-74.66	-98.00	-100.00
Overland deposition	(-7489.380)	-33.62	-73.41	-96.87	-98.87
Channel erosion	(4149.039)	-1.15	-6.34	-20.47	-43.10
Channel deposition	(-3447.102)	-0.72	-2.55	-11.50	-33.71
Total soil loss	(837.400)	-13.91	-36.70	-70.24	-90.92
Average soil loss	(1032.350)	-13.91	-36.70	-70.24	-90.92

(Figures in parentheses show the true value obtained with no change in the slope gradient)

Appendix F

Appendix F-1: Content of the optical disk attached with the Thesis

Folder name	Description of the content
Model	LISEM model version 2.03
PCRaster	PCRaster GIS Professional version 2.0
Basemaps	Key spatial data of the Eastern South Downs,
25dbases	25 LISEM databases, a storm rainfall intensity file
PCRscript	PCRaster script files to create LISEM databases
Batch	Batch files to display the key spatial data and LISEM database
Outputs	Spatio-temporal output files for dynamic visualisation in Aguila
Video	AVI video files for viewing a single simulation